

Cover Page



Universiteit Leiden



The handle <http://hdl.handle.net/1887/44483> holds various files of this Leiden University dissertation

Author: Otten, Gilles

Title: Suppressing a sea of starlight : enabling technology for the direct imaging of exoplanets

Issue Date: 2016-11-29

Suppressing a Sea of Starlight

Enabling technology for
the direct imaging of exoplanets

Suppressing a Sea of Starlight

Enabling technology for
the direct imaging of exoplanets

Proefschrift

ter verkrijging van
de graad van Doctor aan de Universiteit Leiden,
op gezag van Rector Magnificus prof. mr. C. J. J. M. Stolker,
volgens besluit van het College voor Promoties
te verdedigen op dinsdag 29 november 2016
klokke 13:45 uur

door

Gilles Peter Paul Louis Otten
geboren te Meerssen
in 1987

Promotiecommissie

Promotor: Prof. dr. Christoph U. Keller

Co-promotores: Dr. Matthew A. Kenworthy
Dr. ir. Frans Snik

Overige leden: Prof. dr. N. J. Doelman
Prof. dr. H. V. J. Linnartz
Prof. dr. H. J. A. Röttgering
Prof. dr. I. A. G. Snellen
Dr. O. Absil (Université de Liège, België)
Dr. S. F. Pereira (TU Delft)

Dedicated to my parents, and Maria and Leon.

Dit proefschrift werd ondersteund door de Nederlandse Organisatie voor Wetenschappelijk Onderzoek (NWO) en het Leids Kerkhoven Bosscha fonds. This work is part of the research programme Instrumentation for the E-ELT, which is partly financed by NWO

© 2016 Gilles Otten

Contents

1	Introduction	1
1.1	The direct imaging of exoplanets	3
1.2	Challenges in direct imaging	7
1.2.1	The diffraction limit & Adaptive Optics	7
1.2.2	Seeing and speckles	10
1.3	Contrast enhancing techniques	11
1.3.1	PSF subtraction	11
1.3.2	Coronagraphs	13
1.4	Enabling technology for achromatic geometric phase elements	19
1.4.1	Achromatization with geometric phase elements	19
1.4.2	Accurate phase patterns	22
1.5	Work presented in this thesis	22
1.5.1	The vector Apodizing Phase Plate	22
1.5.2	Phase-Sorting Interferometry	25
1.6	Thesis outline	27
2	Laboratory demonstration of Phase Sorting Interferometry	41
2.1	Introduction	42
2.2	Laboratory setup	42
2.2.1	Wavefront sensor branch	42
2.2.2	Science camera branch	43
2.2.3	Data retrieval	44
2.3	Removing non-common path aberrations	44
2.3.1	“Coffee rings method”	45
2.3.2	Phase-sorting interferometry	46
2.3.3	Differential optical transfer function	47
2.3.4	Angel-Mach-Zehnder interferometer	49
2.3.5	Dialing out speckles	49
2.4	Conclusions and Future Work	50
3	Performance characterization of vector Apodizing Phase Plate coronagraph	55
3.1	Direct imaging of exoplanets	56
3.2	vAPP operating principle & manufacturing	58
3.2.1	Classical & vector phase	58
3.2.2	Fabrication of the vAPP prototype	60
3.3	Measuring the properties of the vAPP	61
3.4	PSF characterization	65

3.5	Conclusions & Outlook	73
3.A	Pupil measurement theory and setup	76
3.A.1	Pupil reconstruction	76
3.A.2	Pupil measurement setup & data reduction	78
3.A.3	Error propagation	80
3.B	PSF modeling theory	81
4	Vector Apodizing Phase Plate coronagraph: prototyping, characterization and outlook	91
4.1	Introduction	92
4.2	Vector Apodizing Phase Plate prototype	92
4.3	New opportunities	95
4.3.1	Integration of beam splitting	95
4.3.2	Aggressive phase patterns	97
4.3.3	360 degree suppression	98
4.4	Conclusion	99
5	First on-sky demonstration of the vector Apodizing Phase Plate on LBT/LMIRCam105	
5.1	Introduction	106
5.2	Principle of the grating-vAPP optic	106
5.3	Observations	108
5.3.1	Data reduction	109
5.4	On-sky performance of gvAPP	109
5.4.1	PSF modeling	109
5.4.2	Sensitivity maps & contrast curves	111
5.4.3	Detailed turbulence model	112
5.5	Conclusions	113
6	On-sky performance analysis of the vector Apodizing Phase Plate coronagraph on MagAO/Clio2	119
6.1	Introduction	120
6.2	The vAPP coronagraph for MagAO/Clio2	121
6.2.1	The grating-vAPP principle	121
6.2.2	Phase pattern design	122
6.2.3	Coronagraph optic specifications	122
6.3	Observations	126
6.3.1	Data reduction	127
6.3.2	Rotation, scaling & subtraction	128
6.4	Results: contrast curve	130
6.5	Discussion and conclusions	133
6.5.1	Future work	136

7 Outlook	143
7.1 Science observations with vAPP	143
7.1.1 NIR observations	143
7.1.2 Broad-band observations	143
7.1.3 The push towards shorter wavelengths	144
7.1.4 Binary observations with vAPP	144
7.1.5 Disk observations with 360 degree vAPP	145
7.2 Combining vAPP with complementary techniques	145
7.2.1 Focal plane wavefront sensing	145
7.2.2 Spectroscopy	145
7.2.3 Polarimetry	146
7.2.4 Instruments applying lessons learned	146
7.3 The vAPP in the ELT-era	146
7.3.1 European Extremely Large Telescope	147
 Nederlandstalige samenvatting	 153
 Gäölse saamevatting	 159
 English summary	 165
 Curriculum Vitae	 169
 Acknowledgments	 171
 List of acronyms	 173

1 | Introduction

Mankind has often philosophized about the existence of planets around other stars. It has been recorded as early as 300 BC when Epicurus argued, in a letter to his disciple Herodotus, that innumerable worlds must exist, both similar and dissimilar to ours (Laertius, 300). Later in the 17th century, Christiaan Huygens wrote in his philosophical treatise *Cosmotheoros* on the existence of planets around other stars, as well as seas, mountains, plants and animals on those planets¹. Using our modern view we can tackle this problem more scientifically. We can formulate more structured questions such as; how do planets form?; is our solar system normal or special?; how unique is our earth? and finally, the ultimate question; is there life elsewhere in the universe? To answer these questions we need to discover and study planets around other stars.

Planets around other stars (extrasolar/exoplanets) were first discovered in 1992 when Wolszczan and Frail discovered two low mass exoplanets around the pulsar PSR1257+12 based on periodic variations of the pulsar's pulse arrival times (Wolszczan and Frail, 1992). This long-expected confirmation proved that planets existed around other (albeit dead) stars. The hunt was on to find a planet around a solar-like star.

In 1995, Mayor and Queloz managed to detect radial velocity variations of the solar-type star 51 Pegasi that implied the presence of a planet of at least 0.47 Jupiter masses (M_{Jup}) (Mayor and Queloz, 1995), where there is a lower limit depending on the inclination of the orbit. In the following years more planets were discovered using the *radial velocity* (RV) technique (e.g. Marcy and Butler, 1996; Butler and Marcy, 1996) and it was evident that the first detected objects were mainly roughly Jupiter-mass planets at unexpectedly small Mercury-like orbits. The big question was how planets could be present at these locations. Quickly the realization came that the probability of such an object passing directly in front of its star as seen from Earth was about 10%. This transit would be seen as a small periodic decrease in the amount of light received from the parent star as the planet physically blocked part of the starlight.

The first planet detected using this *transit* method was HD 209458 b by Charbonneau et al. (2000); Henry et al. (2000), which was originally discovered with the radial velocity technique. This method allows for a relatively easy way of searching for exoplanets by monitoring the brightness of thousands of stars simultaneously. Within several years it has quickly become the most prolific planet detection method, especially with dedicated projects such as Kepler and Super-WASP. The detections of exoplanets through both RV and transit studies have raised questions on planet formation and migration (Udry et al., 2007), and has given us constraints on the occurrence of different types of planets (down to Earth radii) at different orbits around stars (Fressin et al., 2013).

Two other important techniques to discover exoplanets are microlensing (Gaudi, 2012) and astrometry. *Astrometry* is related to the RV method as it also uses the motion of the parent star to infer the presence of companions. The reflex motion of the star caused by the presence of a com-

¹http://www.staff.science.uu.nl/~gent0113/huygens/huygens_ct_en.htm

panion also has a transverse component that can be measured by accurately recording the position of the star in the plane of the sky. Previously, this technique was used to support several claimed detections of extrasolar planets. Most notoriously, the detection of two sub-Jupiter-mass planets around Barnard's star was presented by van de Kamp (1982) but later studies showed that these signals were spurious as planets have been excluded down to several Neptune masses (M. Kürster et al., 2003). A candidate was finally found with astrometry by Muterspaugh et al. (2010) orbiting in a binary system. This planet still has to be confirmed and it is unknown around which of the binary stars it orbits, thereby its properties are still ambiguous. A previously known exoplanet Gl876 b has also been confirmed with the Hubble Space Telescope (HST) through astrometry (Benedict et al., 2002). While this technique still has to discover its first official confirmed planet it is expected that the Gaia satellite, with its high astrometric precision, will detect thousands of Jupiter-mass objects within its lifetime (Perryman et al., 2014).

Micro lensing uses the effect that a massive object acts as a lens and distorts space-time around it. This lensing effect increases the amount of light that is received from a star behind the foreground star + planet combination. This brightening follows from Einstein's theory of general relativity and the magnification factor was consequently derived by Einstein (1936). Deviations from a simple lens can indicate the presence of a companion. The paper by Paczynski (1986) predicted that dark matter candidates could be found using this method by observing millions of stars for several years. Later, Mao and Paczynski (1991) wrote that exoplanets located at approximately the Einstein radius away from the star would be detectable in a similarly sized sample of stars. The first detection using the microlensing method was the $3 M_{\text{Jup}}$ planet OGLE 2003-BLG-235 b/MOA 2003-BLG-53 b by Bond et al. (2004).

The current discoveries with the major detection methods, with known mass and separation, are shown in Fig. 1.1. This plot includes discoveries made by the direct imaging technique that will be described in Section 1.1. Each of the methods has their advantages and disadvantages (see Table 1.1). Pulsar timing has led to the discovery of planets in a handful of cases, as the planets need to survive stellar death or otherwise form around a dead star. Microlensing candidates can only be studied during a single statistically unlikely event. Astrometry is expected to become routine with the astrometric performance of Gaia. The radial velocity and transit methods are currently the most prolific methods but are mainly sensitive to planets close to the star. The direct imaging method described in this paper overcomes many of these biases.

The previously mentioned detection methods are indirect ways of determining properties of the exoplanets such as period, radius and mass. Periods are easy to determine and can be translated into orbital radii with an estimate of the mass of the star. The radius is determined by measuring the amount of blocked light during a transit. A lower limit to the mass can be derived through radial velocity measurements. When combined with the radius of transiting planets this yields the density and therefore can give an indication of the bulk composition of the planet. Several methods are also sensitive to the properties of the planetary atmosphere, like wind speed (Snellen et al., 2010) and chemical abundances (Seager and Deming, 2010). For instance, the transit method can detect atmospheric features imprinted on the stellar light (Charbonneau et al., 2002) when the planet passes directly in front of its star. The presence of a spectral feature will appear as an apparent increase in the amount of blocked light and therefore derived radius of the planet. In the case of relatively hot planets, the thermal emission of the day-side of the planet can even be recorded during the secondary eclipse when the planet hides behind the star. The secondary eclipse probes the thermal radiation of the planet at the height in the atmosphere where it becomes

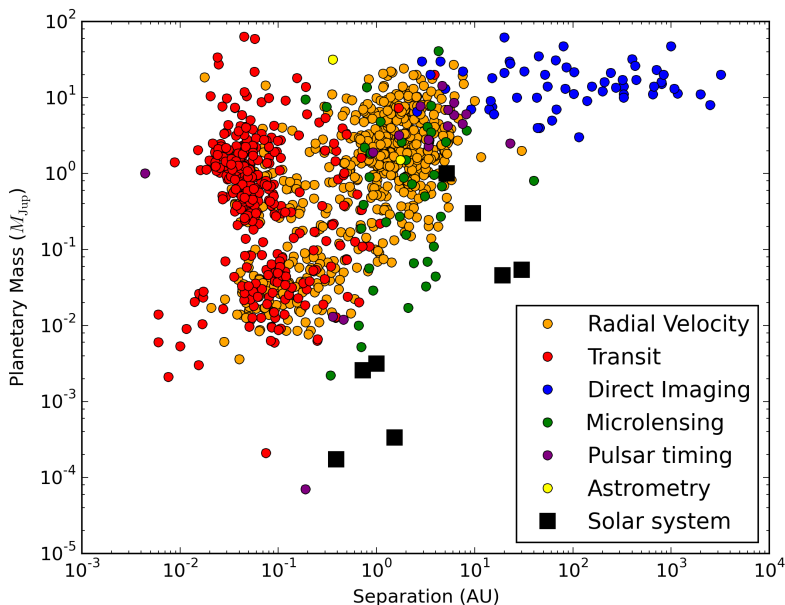


Figure 1.1: Mass versus separation plot for currently known extrasolar planets. This plot also includes some candidates that span the transition between planets and brown dwarfs. The official IAU definition of a planet has a cut-off at $13 M_{\text{Jup}}$. Source: www.exoplanet.eu (October 2015) and known solar-system values.

optically thin. Different wavelengths therefore probe different heights in the atmosphere and can be used to constrain atmospheric temperature/pressure profiles. Using the radial velocity method at high spectral resolution ($R \sim 100\,000$) it is also possible to probe the atmosphere by stacking the resolved spectral features of the planet using an atmospheric template (Snellen et al., 2010). The rotation rate of the known planet Beta Pictoris b was also determined with this technique (Snellen et al., 2014).

1.1 The direct imaging of exoplanets

The previously mentioned detection methods mostly depend on information derived from the light of the star and are therefore indirect ways of probing exoplanets. With *direct imaging*, the light of the planet itself is detected spatially resolved from the star, yielding a direct measurement of the thermal and/or reflected light of a planet. With enough spectral resolution and signal-to-noise, determination of atmospheric composition is possible. This makes it a very powerful technique for directly studying the atmospheres of planets. Furthermore, direct imaging does not require a full orbit of a planet around its star to confirm it is real.

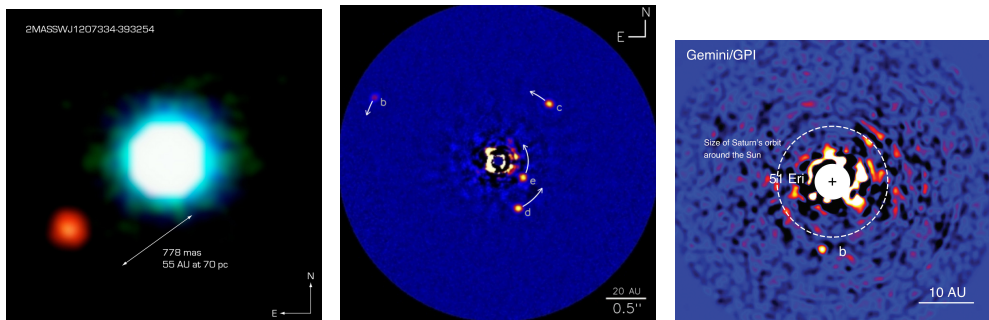
The technique of direct imaging is biased towards planets at larger separations from the star (5-1000 AU). This complements the other methods that are more sensitive to planets that are close

Table 1.1: Main exoplanet detection methods and their strengths and weaknesses.

	strength	weaknesses
Radial velocity	gives lower limit of mass, confirm transiting planets, atmospheric studies using high spectral resolution, sensitive to planets close to stars	sensitive to stellar oscillations, stellar type, magnetic activity and multiplicity, long periods require extensive monitoring
Transits	gives radius estimate, density of planets when combined with RV mass limits, atmospheric studies possible through spectroscopy or spectrophotometry, can probe Earth-like planets in habitable zone around select targets	inclination has to be close to 90 degrees, only measures relative radius, long periods require extensive monitoring, relatively short events that contain most information
Pulsar timing	sensitive down to small masses	dead systems, very rare occurrence
Microlensing	sensitive to Earth-like planets at several AU separation	one-time events, statistically unlikely, degeneracies
Astrometry	hardly depends on stellar type	requires well controlled systematics
Direct imaging	directly measures thermal and/or reflected planet light, does not require long baselines to confirm planet, allows direct atmospheric characterization	biased towards large, young planets at large separations, probes interesting (solar-system scale) separations only for nearest stars

to their star. Improvements in all detection methods will lead to overlapping areas of sensitivity that can be used to scrutinize the existing planet formation models and to further constrain the properties of the planet.

The first claimed directly imaged planet was 2M1207 b, a giant planet orbiting a brown dwarf (Chauvin et al., 2004); see Fig. 1.2a. Direct detections of other low mass companions have since followed (e.g., 1RXS J1609 b (Lafrenière et al., 2008), Fomalhaut b (Kalas et al., 2008), Beta Pictoris b (Lagrange et al., 2009), GJ 504 b (Kuzuhara et al., 2013), GU Piscium b (Naud et al., 2014), HD 106906 b (Bailey et al., 2014)). The list of detections even includes a planetary system of giant planets around HR8799, discovered by Marois et al. (2008, 2010); see Fig. 1.2b. Recently, the detection of 51 Eridani b was presented by Macintosh et al. (2015) that, depending on the formation history, may have a mass as low as $2 M_{\text{Jup}}$.



(a) 2M1207 b was the first directly imaged planet and is located around a brown dwarf. Discovered by Chauvin et al. (2004).

(b) HR 8799 is a directly imaged planetary system containing 4 giant planets. The 'b', 'c', 'd' planets were discovered by Marois et al. (2008) and the 'e' planet by Marois et al. (2010).

(c) 51 Eridani b is the least massive directly imaged planet to date. Assuming a hot-start formation model it may be as massive as $2 M_{\text{JUP}}$. Discovered by Macintosh et al. (2015).

Figure 1.2: A selection of famous directly imaged planets.

A major challenge in the direct imaging of planets is that the star is many orders of magnitude brighter than the planet. A planet is mainly detectable either through reflected or scattered starlight (in visible to near-infrared range), or by thermal radiation from the planet itself (in near-infrared to mid-infrared range). To show the order of magnitude of this problem; the ratio between the surface area of our Earth to that of the Sun is approximately 10 000. Combined with the average surface temperature of the Sun (5777K) and the Earth (287K) this means that the bolometric flux ratio between the Earth and the Sun is about $\sim 10^{-8}$ to 10^{-9} , although at select wavelengths the ratio becomes more favorable. The reflected light in the visible wavelength range from an Earth-like planet around a sunlike star is $\sim 10^{-10}$. A Jupiter-like planet around a Sun-like star will give a bolometric flux ratio of 10^{-7} . The reflected light of Jupiter-like planets in the visible range is even fainter at 10^{-8} (Traub and Oppenheimer, 2010).

This immense difference in brightness is often compared to trying to see a firefly next to a lighthouse (resp., 1/500 Candela and 2 million Candela or a factor of 10^{-9}). Without tackling the light of star, the planet will be an indistinguishably small bump next to the star, sitting in a sea of starlight. The origin of this sea of starlight will be explained in more detail later.

There are more factors that limit the detection of planets in direct imaging (e.g., atmospheric turbulence, instrumental wavefront changes, these will be explained in Section 1.2) and so current detections have been mostly limited to self-luminescent giant planets orbiting around young stars at relatively large separations. As the thermal emission of self-luminescent young planets peaks in the near-infrared it is logical that most of the previous planet detections were initially made in that wavelength regime. A spectrum can be taken of these directly imaged planets to detect atmospheric signals (e.g., Mohanty et al. (2007); Janson et al. (2010); Barman et al. (2011); Konopacky et al. (2013)). In the spectroscopic study of HR8799 c Konopacky et al. (2013) found signatures of both CO and H₂O and a C/O ratio higher than that of the parent star suggesting this planet formed using core accretion, in which a giant planet forms around a rocky core by rapidly accreting gas.

Even in the case of a non-detection, limits can be placed on the absence of companions down

to a certain magnitude of contrast. *Contrast* is defined as the brightness of a target with respect to its parent star at which it can be detected with a certain signal to noise ratio (typically $S/N = 5$ or equivalently a 5σ detection). Sometimes the term contrast is used when talking about normalized intensity profiles. The recent publication by Vigan et al. (2015) produced one of the highest contrasts measured to date by imaging Sirius with the newest generation of planet-finding instruments (VLT/SPHERE); see Fig. 1.3. While it did not find a new companion the study excludes their presence down to several M_{Jup} (equivalent to a 5σ contrast of $10^{-6.5}$ at 0.5 arcseconds in YJH -bands).

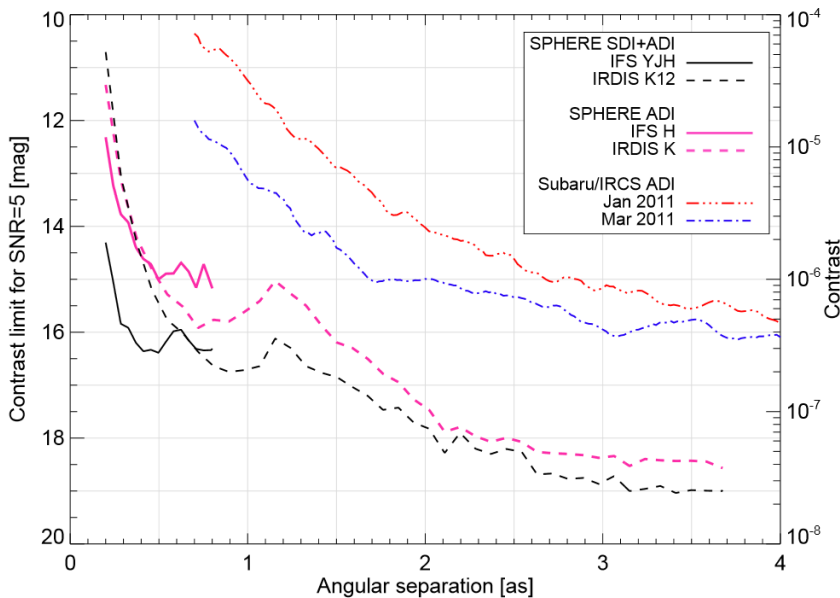


Figure 1.3: Contrast curve of the detection limit reached by direct imaging observations of Sirius. From Vigan et al. (2015).

To interpret the spectra and images many models exist, such as AMES-COND (Allard et al., 2001; Baraffe et al., 2003), AMES-DUSTY (Allard et al., 2001; Chabrier et al., 2000), BT-SETTL (Allard et al., 2012) and models by Burrows et al. (2004); Marley et al. (2007); Fortney et al. (2008); Morley et al. (2012); Morley et al. (2014a,b) amongst others. These models produce spectra dependent on the cooling history, mass, age, and metallicity, amongst other variables. By comparison with these models, multi-wavelength studies and spectra through direct imaging can constrain the planet's temperature, mass and atmospheric properties without depending on the completion of several orbits around the star as is the case with radial velocity studies. Furthermore it is possible to test the formation mechanism of the planet (disk instability versus core accretion).

In Fig. 1.4 we show the expected contrast ratio based on the thermal radiation between an F-type star and a planet with varying temperature. It is easily seen that observing in the near-infrared and especially at 4 – 5 micron is easier in terms of contrast and can probe lower temperatures and

less massive planets for a given contrast ratio. From the presence of spectral features we can infer atmospheric composition and constrain the formation history of the planet.

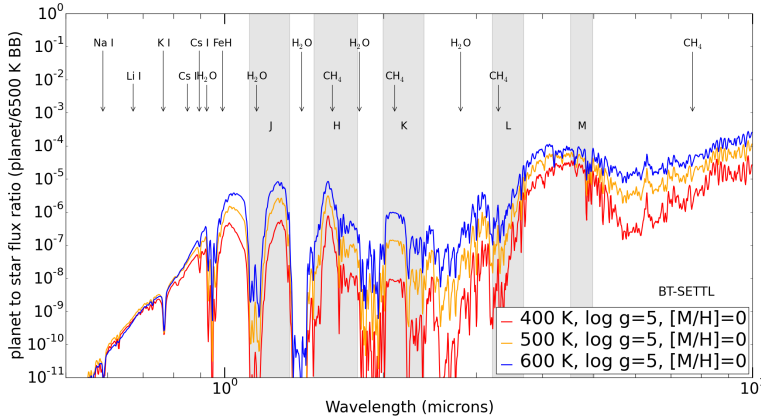


Figure 1.4: Flux ratio between planets and F-type stars based on the BT-SETTL models. Favorable contrast can be found in the near-infrared, especially in *L* and *M* band. Outside of the grey filter bands the Earth’s atmosphere is generally opaque due to water bands. Visible band filters are not shown but the atmosphere is mostly translucent between 350 nm and 1 micron.

1.2 Challenges in direct imaging

1.2.1 The diffraction limit & Adaptive Optics

Imaging point sources with a telescope with finite size results in images in which the point sources look like a central broad spot with rings surrounding it (*Point Spread Function* or PSF). This is due to a fundamental limit in spatial resolution due to the wave-like nature of light and the aperture of the telescope. A circular telescope with diameter D , observing at wavelength λ can only separate objects that are more than $1.22 \lambda/D$ apart (related to the width of the central spot); this is the Rayleigh Criterion. In the case of larger sources the finite aperture of the telescope produces images of the object plane that are blurred with this scale. The smallest spatial details are therefore lost. Improving the spatial resolution by increasing D is one of the main driving forces for building increasingly larger telescopes. The increase in diameter allows us to take sharper images. A nearly perfect PSF is shown in the top center frame of Fig. 1.5.

The diffraction limit is easily reached from space as there are fewer sources of optical aberrations. Observing from the ground is a different story, as our atmosphere is turbulent and produces a wavefront that varies in both time and space. Light at different parts of the pupil arrive at different times. This distorted wavefront creates an extended and time varying PSF that, when observed over time scales of a second, averages to a seeing disk with a width of approximately λ/r_0 , where r_0 (Fried parameter) is the typical size of the turbulence ($\sim 15 - 30$ cm in the optical range at

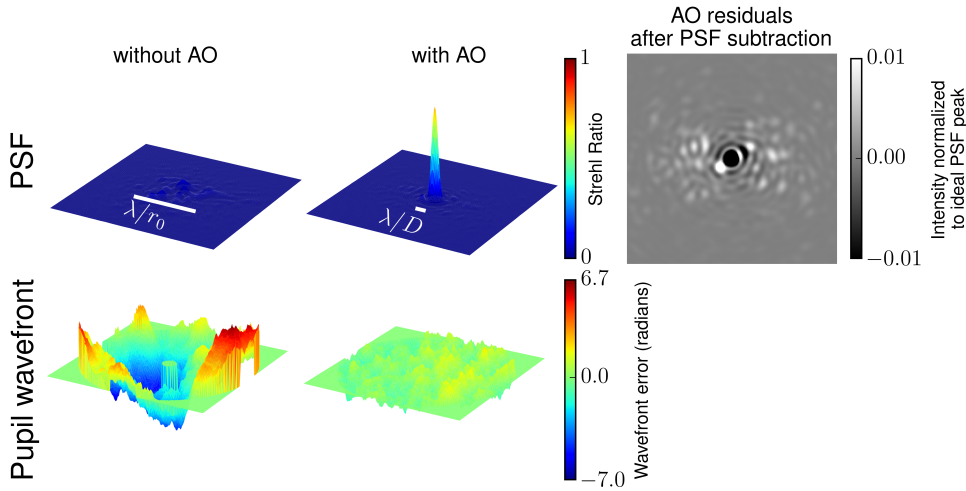


Figure 1.5: Top row shows simulated instantaneous monochromatic PSFs with and without Adaptive Optics (AO) and the typical spatial scales associated with them. The rightmost image shows the post-AO PSF with the ideal PSF subtracted (the residuals). The intensity for all PSFs is normalized to the peak of the ideal PSF. The residuals are atmospheric speckles, shown with a range of $\pm 10^{-2}$. The speckles are dominant along the horizontal wind direction. The pupil wavefront maps associated with the pre-AO and post-AO PSFs are seen below their respective PSFs in units of radians.

excellent astronomical sites). This means that a seeing limited telescope observing in the visible range will perform as well as a 15 – 30 cm telescope in terms of spatial resolution. The left-most column of images in Fig. 1.5 shows an instantaneous view of a seeing-limited PSF and its corresponding wavefront map.

While space-based direct imaging has many advantages, the biggest disadvantages are that it is expensive (~ 1 billion dollars) and the diameter of the telescope that can be launched is limited. On the ground, segmented mirrors can be built that are almost an order of magnitude larger in diameter and instruments can be easily serviced and upgraded. This comparison between ground-based and space-based direct imaging is also made in Table 1.2. In this thesis we focus on improvements in the ground-based direct detection of exoplanets to optimally use the high spatial resolution and light collecting area of the largest telescopes.

Adaptive Optics (AO) is the enabling factor that allows us to reach the diffraction limit from the ground for telescopes larger than r_0 . Current 6 – 10 meter class telescopes can reach solar-system scales around nearby stars when operating at the diffraction limit. Adaptive Optics actively measures the shape of the wavefront as it arrives at the *wavefront sensor* (WFS) and flattens the wavefront using a *deformable mirror* (DM) on timescales of milliseconds. It is important to note that a perfect PSF can not be fundamentally reached from the ground. An important indicator used for the post-AO image quality is *Strehl Ratio* (SR). The Strehl ratio is defined as the intensity of the PSF peak with respect to a theoretically perfect PSF. A simple closed-loop AO setup is seen in Fig. 1.6 with simulated PSFs with and without AO in the two left panels of Fig. 1.5.

When comparing the signal to noise ratio S/N (defined as the integrated flux within a certain

Table 1.2: Comparison between direct imaging from space and ground.

	advantage	disadvantage
space-based	10^{-9} raw contrast, no atmospheric aberrations, no transmission windows, relatively static diffraction limited PSF	limited diameter, hard to service/repair/upgrade, order of magnitude more expensive, limited lifetime
ground-based	easy to upgrade/repair/service, largest diameter technology can support	10^{-5} raw contrast, can only image in atmospheric transmission windows, seeing limited unless AO-capable

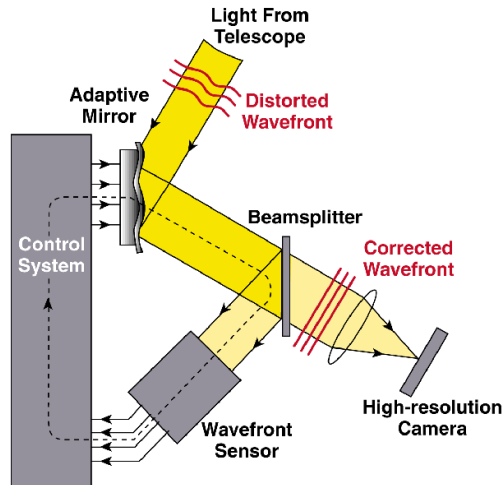


Figure 1.6: Schematic overview of typical closed-loop adaptive optics setup. The wavefront sensor measures the wavefront at a high rate (on the order of kHz) and sends commands to the deformable mirror to flatten the incoming wavefront. Note that the WFS can not see the wavefront errors in the branch towards the science camera. Image courtesy of Claire Max.

radius from the star and the variation of this flux measured across realizations) of a point source for diffraction limited telescopes versus seeing-limited telescopes we see that the S/N scales as respectively D^2 versus D . The amount of collected light remains the same but it is concentrated into an area that is smaller. Merely switching on the AO system significantly increases the S/N when imaging point sources from the ground. In the case of direct imaging, where faint targets sit in a variable halo of starlight with total intensity proportional to $1 - \text{Strehl Ratio}$, the improvement is even greater.

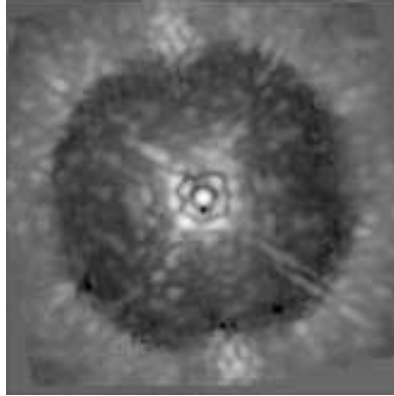


Figure 1.7: SPHERE monochromatic PSF at H-band, demonstrating the control radius of the deformable mirror (the darker circular region). From Vigan et al. (2015).

1.2.2 Seeing and speckles

An important source of noise in direct imaging is the presence of variable speckles (Racine et al., 1999; Hinkley et al., 2007). *Speckles* are planet-mimicking features that arise from uncorrected wavefront aberrations in the atmosphere and/or optical system. Speckles appear as modulations of intensity in the static diffraction structure of the PSF. These modulations are an important source of noise in direct imaging. Any planet is literally sitting in a sea of starlight. The rightmost PSF in Fig. 1.5 shows the residuals of a post-AO PSF after subtracting the ideal PSF from it. The point-like features at a level of 10^{-2} and lower are the speckles with a typical size on the order of a λ/D .

Atmospheric speckles

The Adaptive Optics system needs a finite time to respond and can only correct down to certain spatial scales dependent on the amount of actuators across the telescope pupil. This correction needs to be done on time scales of the order of $\tau_0 \sim \frac{r_0}{V_{\text{wind}}}$, where r_0 is coherence length or Fried parameter of the turbulence and V_{wind} is the wind speed. This means that the correction is not perfectly matched to the incoming distorted wavefront. This mismatch creates a wavefront that shows small residual variations, on small spatial scales. When looking at the PSF this means that a time varying cloud of λ/D -sized speckles remain and modulate the PSF. The variation of these speckles is a source of noise and, in many cases, larger than the photon noise contribution and consequently the most important limiting factor in detecting planets close to the star. The amount of variation is larger on top of the Airy rings which can be seen as pinned speckles. The limited amount of actuators also creates a control region with a radius $\frac{N\lambda}{2D}$, where N is the amount of actuators across the pupil. Outside of this radius AO correction will not be effective (see Fig. 1.7). An added effect of the finite response time combined with a dominant wind speed and direction creates a large uncorrected wavefront at the edge of the telescope. When looking at the PSF the unsensed edge projects a pronounced halo of speckles in the direction towards and away from the

wind.

Instrumental (non-common path) speckles

Another important limiting factor is the speckles created by uncorrected instrumental wavefront aberrations that slowly evolve in time. The cause of these quasi-static aberrations can be found in mechanical changes in the telescope and instrument due to factors such as flexing and thermal, pressure and gravity vector variations (Soummer et al., 2007). The wavefront sensor can not correct for these aberrations as they occur in the (non-common path) science arm of the instrument. This non-commonality can be seen in Fig. 1.6. These speckles also create a noise floor unless they are taken care of.

1.3 Contrast enhancing techniques

In order to get rid of the light of the star and the corresponding speckles while still minimizing the impact on the light of the planet, both optical and data-reduction techniques have been developed. We start with the data-reduction techniques.

1.3.1 PSF subtraction

One of the simplest ways to get rid of the starlight and some of the slowly varying speckles is by imaging a second star without a known companion (*Reference Differential Imaging*; RDI, Smith and Terrile (1984)). This second star can be used as a reference to subtract the starlight of the first object while keeping the planet intact. The reference object is not imaged simultaneously but before, after, or interleaved with the observations of the primary target. Due to the difference in time and telescope motions between the targets, wavefront changes build up that limit how well the starlight is subtracted. By using a local reference in both time and space this effect can be mitigated.

Simultaneous / Spectral Differential Imaging (SDI) is another way of removing the stellar light. The spectrum of a star and a planet have different absorption features and this can be leveraged to remove the starlight (Rosenthal et al., 1996; Racine et al., 1999; Marois et al., 2003; Lenzen et al., 2004). A large planet survey of 45 young and nearby stars (Biller et al., 2007) used this technique and specifically looked for Methane (CH_4) absorption on giant exoplanets following the predictions of Baraffe et al. (2003) for field brown dwarfs. The surprising lack of detections at this band showed that these massive planets do not follow the behavior of field brown dwarfs at cooler temperatures. More recently, successful SDI detections have been made at the Hydrogen α line (Close et al., 2014). This is a sign of the accretion of Hydrogen gas onto a forming planet.

With the *Spectral Deconvolution* technique (SD, Sparks and Ford, 2002) the spectral signature can also be used to effectively remove speckles as their angular distance from the star scales with wavelength while the distance of the planet to the star is fixed. This approach is taken as an extra correction step by the newest generation of dedicated planet finders (SPHERE, GPI), that contain Integral Field Units (IFUs) that carve up the image into tiny spectra (e.g., Mesa et al., 2015).

A third spectral diversity technique that can be used to improve the contrast while directly imaging planets is by Snellen et al. (2014) and uses the radial velocity shift of a planetary signature

at high spectral resolution ($R > 100\,000$) in order to resolve individual spectral lines. The signature of the planetary atmosphere can not be seen in an individual exposure. The data is therefore cross-correlated with template spectra. In the stacked data the atmospheric feature is above the noise floor and can be measured.

Polarization Differential Imaging (PDI) uses the fact that starlight is unpolarized while light reflecting off a planet is polarized up to a large fraction (Stam, 2003). By splitting the light according to their linear polarizations and taking the difference, the unpolarized starlight is canceled out while the light of the planet only partially cancels. This approach is often used by disk scientists to study debris disks around stars (Kuhn et al., 2001; Avenhaus et al., 2014). In the future it is expected that PDI will improve the detection of reflected light planets (Keller et al., 2010; Roelfsema et al., 2014).

Angular Differential Imaging (ADI) is a powerful technique that can be used to remove starlight and speckles without making modifications to a telescope (Marois et al., 2006). The angle of the instrument with respect to the telescope is fixed as much as possible and the sky (and therefore the planet) is let to rotate on the detector. As quasi-static speckles are associated with the telescope they remain at the same angles on the detector. This creates diversity that allows us to discriminate between (quasi-)static features and planets. By removing the median of the observations the starlight, and diffraction features and speckles associated with it are canceled while the rotating planet is minimally impacted. By derotating the images and stacking them the signal of a potential planet becomes even more significant. A schematic demonstration of ADI can be seen in Fig. 1.8.

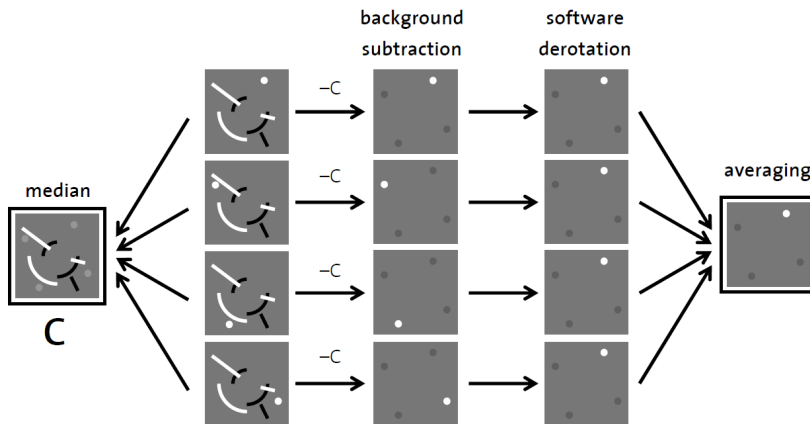


Figure 1.8: Schematic representation of ADI adapted from an image by Christian Thalmann (Roelfsema et al., 2014). A cube of images is taken at fixed parallactic angle. This means that the planet will seem to orbit around the star while features caused by the telescope and instrument are static (indicated above with white and black stripes/arcs). A median “C” can be subtracted to reduce the static features and afterwards the images are individually derotated and stacked to reveal the planet.

Variations of ADI that take time variations into account have been developed (e.g., LOCI, PCA). LOCI stands for *Locally Optimized Combination of Images* and was developed by Lafrenière et al. (2007). Variants of LOCI also exist (Marois et al., 2014; Wahhaj et al., 2015). The technique subdivides all frames into annular wedges and for every subregion optimally produces a reference by linearly combining the corresponding subregions from a PSF library. This library can also contain frames of the observations themselves. The optimal combination is made by performing a least-square fit to minimize the residual after subtraction. Note that in case the PSF library contains the target frames themselves, frames very close in time need to be excluded from the fit in order to minimize self-subtraction of the planet signal. ADI and LOCI made it possible to recover the planet HR8799 b in archival data taken with the HST in 1998 (Lafrenière et al., 2009); ten years before it was eventually discovered by Marois et al. (2008), also using ADI.

Principal Component Analysis (PCA) has also been recently used to improve PSF subtraction (Amara and Quanz, 2012; Soummer et al., 2012). PCA extracts principal components out of a PSF reference library using singular value decomposition or by projecting on a Karhunen-Loeve basis (KLIP algorithm). A linear combination of a limited amount of orthogonal basis components is then fitted and subtracted from each of the frames. The PCA basis construction, fitting and subtraction can also be performed on subsections of each of the frames. This was shown by Meshkat et al. (2014) to improve the contrast with respect to LOCI and a global optimization with PCA. While self-subtraction is a concern when the principal components are constructed from the target dataset, Meshkat et al. (2014) also showed that, in their case, including all frames actually improved the S/N the most.

1.3.2 Coronagraphs

An additional approach to improve the contrast can be taken by suppressing the starlight before it is captured by the detector. The reduction of starlight reduces the strength of the S/N -degrading speckles. This can be done using a *coronagraph*. These were originally developed by Bernard Lyot in 1939 for masking the disk of the sun in order to image the faint solar corona (hence the name) without having to wait for solar eclipses (Lyot, 1939). Coronagraphs not only improve the contrast between the star and the planet, by suppressing the intensity of the diffraction structure the noise contribution of the previously mentioned speckles is also reduced. At least four important quantities are used when talking about coronagraph performance: throughput, inner working angle, contrast and chromaticity. The *inner working angle* is the smallest angle at which a planet can be detected with $> 50\%$ throughput. A small inner working angle helps with optimally using the diffraction limit offered by the telescope. The *contrast* is the flux ratio with respect to the star for a significant point source companion detection (typically used is 5σ threshold). Higher contrast allows to image smaller, cooler and older planets. Finally the wavelength dependence or *chromaticity* of the coronagraph is important for broad-band imaging or spectroscopy. Due to factors outside of our control such as scintillation and atmospheric chromaticity² a raw contrast limit exists for 30 meter class telescopes that is on the order of 10^{-6} . This means that the raw contrast of a coronagraph operating from the ground does not have to be better than 10^{-6} . Another important aspect to consider about coronagraphs is whether they can handle complicated/obstructed pupils.

²<http://www.naoj.org/staff/guyon/04research.web/14hzplanetsELTs.web/content.html>

Focal-plane coronagraphs

The conceptually easiest type of coronagraph is the one that Bernard Lyot himself devised and uses an additional pupil and focal plane in the instrument. The Lyot (or *focal-plane*) coronagraph physically blocks the star in the additional focal plane with a small amplitude mask to get rid of the starlight. A Lyot stop sitting in the additional pupil plane cuts off the light at the edge of the pupil that diffracted around the focal-plane mask that would otherwise impact the contrast. Figure 1.9 shows a schematic representation of an optical setup with a focal-plane coronagraph.

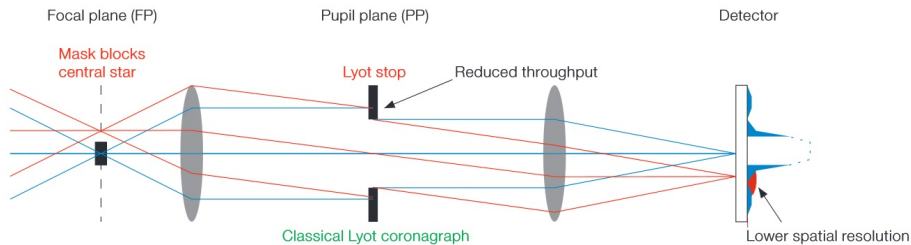


Figure 1.9: Schematic optical setup with focal-plane coronagraph. Focal-plane coronagraphs require both a focal-plane (mask) and focal-plane device (stop) in order to suppress the starlight. With permission from Matthew Kenworthy.

Since the first Lyot coronagraph, many types of focal-plane coronagraphs have been developed with either amplitude, phase or hybrid masks and stops with improved performance in terms of contrast, inner working angle and bandwidth. The original Lyot coronagraph could only improve in contrast by sacrificing inner working angle by making a larger blocking mask. By adjusting the optical elements in different planes of the instrument improvements can be made. For instance, the amplitude focal-plane mask can be altered with the Band-limited Lyot Coronagraph (Kuchner and Traub, 2002). The first pupil plane can also be used to preshape the PSF for higher contrast. This is the principle behind the Apodized Lyot Coronagraph (Soummer et al., 2003a) that uses an amplitude mask with an increasingly less transmissive edge to reduce the strength of the Airy rings. The Phase Induced Amplitude Apodization (PIAA) design achieves the same amplitude apodization but with no transmission loss (Guyon, 2003) and can be used with and without focal-plane mask.

By using a focal-plane phase mask with phase discontinuities to produce an amplitude singularity the on-axis stellar light can be diffracted to the edge or even outside of the Lyot pupil. In combination with a Lyot stop this removes the starlight from the optical system. The phase-based focal-plane mask improves the throughput and inner working angle with respect to the amplitude-based focal-plane masks. Beside radial phase designs like the Disk Phase Mask (Roddier and Roddier, 1997) and Dual Zone Phase Mask (Soummer et al., 2003b) azimuthal models like the Four-Quadrant Phase Mask (FQPM, Rouan et al., 2000) and 8 Octant Phase Mask (8OPM, Murakami et al., 2008) were developed to improve the chromatic behavior, contrast and IWA even further. Both the FQPM and 8OPM suffer from the problem that when a planet is crossing the phase discontinuities, the flux of the planet is also suppressed, leading to dead zones. The Annular Groove Phase Mask and the optical Vector Vortex Coronagraph use a smooth azimuthally varying phase gradient to overcome this effect and has been analytically proven to

(in theory) produce perfect rejection of on-axis light with a critically sized Lyot mask (Mawet et al., 2005). The Hybrid Lyot coronagraph uses a complex (both amplitude and phase) focal-plane mask to produce raw contrast in excess of 10^{-9} for space missions (Moody et al., 2008). An extension of the PIAA coronagraph (PIAACMC) also has a complex focal-plane mask to push the performance even closer to the theoretical limit of coronagraphs (Guyon et al., 2010).

The biggest issue that still remains with even the most advanced focal-plane coronagraphs is that they are sensitive to tip/tilt misalignments and vibrations. Vibrations are practically unavoidable as they are caused by crucial components related to the functioning of the telescope and instruments. Instruments need to be cooled using vacuum pumps to cryogenic temperatures, and wind pushing against the structure of the telescope can excite resonances in the telescope that can be seen as tip/tilt motion. Only with significant investments (such as a high accuracy multiple kHz tip/tilt correction stage) these vibrations no longer limit the performance of the focal-plane coronagraphs. These problems will only get worse when we move to even larger telescopes such as the European Extremely Large Telescope (E-ELT).

Pupil-plane coronagraphs

It is also possible to leave the core of the starlight largely intact and focus on suppressing starlight close to the core at a location where potential planets may occur. A phase and/or amplitude modification can be made to the light at the pupil of the telescope with a *pupil-plane coronagraph*. As the pupil-plane and focal-plane are connected through a Fourier transform, the pupil modification can be chosen in such a way that it alters the PSF of the telescope by highly suppressing the diffraction rings in a predefined region. The amount of starlight at the location of a potential planet will be reduced. See Fig. 1.10 for a schematic representation of the optical setup for such a type of coronagraph. Most importantly, by being located in the pupil of the telescope, the PSF is identical across the whole image plane and the contrast is therefore inherently insensitive to tip/tilt offsets and vibrations. All sources will be affected equally, including any planets. This means that pupil-plane coronagraphs also work for multiple stars. By choosing a modification that largely conserves the peak flux, the impact to the planet signal is minimized. The pupil modification can be either amplitude variations, phase variations or both. One example of pupil-plane coronagraphs are the shaped pupils of Kasdin et al. (2003); Kasdin et al. (2004) that use black and white regions of transmission that yields point-symmetric PSFs. Concepts using only phase were pioneered by (Yang and Kostinski, 2004; Kostinski and Yang, 2005) and perfected with the Apodizing Phase Plate (APP) (Codona and Angel, 2004; Codona et al., 2006; Kenworthy et al., 2007). Other important developments in phase designs have been made by Carlotti (2013); Ruane et al. (2015). These phase-only solutions allow one-sided dark holes near the PSFs. An important tradeoff for pupil-plane coronagraphs is the size of the suppressed PSF region, the required contrast and the effective throughput of the plate.

Coronagraphs have different advantages and disadvantages depending on their design. A comparison between focal-plane and pupil-plane coronagraphs is made in Table 1.3. The main advantage of the focal-plane coronagraphs is their theoretically high contrast performance. They are limited by vibrations and occupy multiple planes in an instrument which complicates the installation. Pupil-plane coronagraphs are insensitive to vibrations and only occupy one plane in a telescope. This greatly facilitates the installation into instruments.

A careful review of the then-known coronagraph designs by Guyon et al. (2006) showed

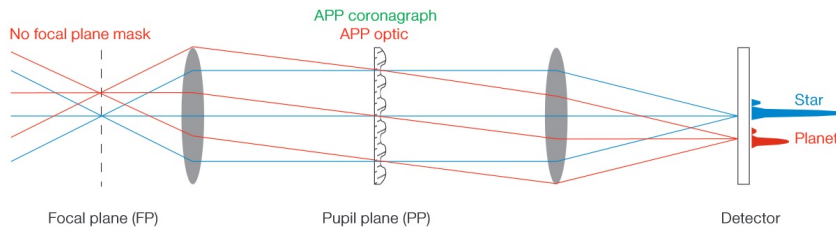


Figure 1.10: Schematic optical setup with pupil-plane coronagraph. Pupil-plane coronagraphs only require one optical element in the pupil plane to suppress the starlight in a predefined region. With permission from Matthew Kenworthy.

that many designs of coronagraphs are sensitive to the finite size of the star. The impact of this effect was generally ignored in coronagraphic simulations to simplify the calculations. Part of the coronagraph designs have to be excluded when considering this effect. The impact will only become more significant as the diffraction limit of the future ground-based telescopes continues to approach the angular sizes of nearby stars.

Many designs of coronagraphs also have an inner working angle that is relatively large ($3 - 4 \lambda/D$) and therefore do not optimally use the capabilities of the telescope in terms of angular resolution. A subset of coronagraph designs with inner working angles of $1 - 2 \lambda/D$ was summarized by Mawet et al. (2012) and distilled into multiple families of coronagraphs as seen in Fig. 1.11. The smaller inner working angle of these designs can be used to image planets closer to the star or to expand the study of planets towards stars that are farther away. Small inner working angle coronagraphs enable us to use the angular resolution of the largest telescopes to the fullest extent.

Apodizing Phase Plate

The *Apodizing Phase Plate* (APP) coronagraph is designed as a flux conserving, vibration insensitive pupil-plane coronagraph with small inner working angle (Codona et al., 2006; Kenworthy et al., 2007). Therefore, it combines the qualities needed to create a robust but powerful coronagraph. It uses a phase-only modification to the light in the pupil of the telescope. In the original APP the phase delay is created by physically varying the thickness Δx of a piece of high refractive index (n_{plate}) glass across the pupil, embedded in a medium with index n_{air} . The physical difference in distance traveled through the plate gives a varying phase delay $\Delta\phi$ to the light with wavelength λ (see Fig. 1.12 and Eq. 1.1).

$$\Delta\phi = 2\pi \frac{\Delta x}{\lambda} = 2\pi(n_{\text{plate}} - n_{\text{air}}) \frac{\Delta x}{\lambda} \quad (1.1)$$

Unfortunately this phase offset is chromatic, as light of different wavelengths will see a different phase offset. Deviating from the optimal wavelength generally degrades the contrast and limits the wavelength range at which the coronagraph can be used. The phase delay is typically diamond-turned into a substrate with high refractive index. The diamond-turning limits the spatial frequencies of the phase pattern. Discontinuous phase transitions are nearly impossible to

Table 1.3: types of coronagraphs and their (dis)advantages with examples. ALC: Apodized Lyot Coronagraph, DPM: Disk Phase Mask, DZPM: Dual Zone Phase Mask, FQPM: Four-Quadrant Phase Mask, 8OPM: Eight-Octant Phase Mask, OVC: Optical Vortex Coronagraph, VVC: Vector Vortex Coronagraph APP: Apodizing Phase Plate, PPA: Pupil Phase Apodization.

	amplitude	phase
focal plane	classical Lyot, ALC, band-limited, hybrid Lyot	DPM, DZPM, FQPM, 8OPM, OVC, VVC
pro	theoretically high contrast	theoretically high contrast
con	sensitive to vibrations, occupies multiple telescope planes, hard to align, stop blocks throughput and limits diameter and IWA	sensitive to vibrations, occupies multiple telescope planes, hard to install and align
pupil plane	shaped pupil	APP, PPA, PIAA
pro	achromatic by nature, insensitive to vibrations, single plane, single optic, easy to install and align, works on all sources	insensitive to vibrations, conserves total flux, single plane, single optic, easy to install and align, works on all sources in field of view, easy upgrade to non-coronagraphic instruments
con	reduced effective telescope area, reduced peak flux (even less than APP), larger inner working angle, light remains on focal plane	reduced peak flux, light remains on focal plane, generally limited angular workspace

manufacture in this way. Therefore, only low-order wavefront changes can be made and the amount of implementable phase designs is limited. Lastly, the spatially smooth antisymmetric coronagraphic phase designs only suppress one side of the star. This means that to image a full 360 degrees around the star a second dataset has to be taken after a rotation of the field by the derotator. See Fig. 1.13 for a typical phase pattern and PSF of the APP (Kenworthy et al., 2010).

Despite these caveats the APP has performed very well on-sky, both by characterizing known planets and discovering unknown companions. As an example, Quanz et al. (2010) imaged Beta Pictoris b in the NIR, thereby confirming the previous detections. They also combined their Narrow-band 4.05 micron photometry with previous L' measurements to get a $[L' - \text{NB4.05}]$ color of $-0.05 \pm 0.38 \text{ mag}$. A comparison of this color with models of cool field dwarfs suggests that the planet is comparable to a field dwarf with a spectral type of L4 and an effective temperature of 1700 Kelvin. Meshkat et al. (2015b) discovered a low-mass companion around HD 984 with an estimated mass on the order of $90 M_{\text{Jup}}$ at an angular separation of 0.19 arcseconds from the parent star. Furthermore, Meshkat et al. (2015a) used the APP extensively in a survey of stars with gapped debris disks (suggesting planet formation). The 5σ contrast reached with the APP by Meshkat et al. (2015c) is up to 10.6 magnitudes at 0.4 arcseconds in 2 hours of observation

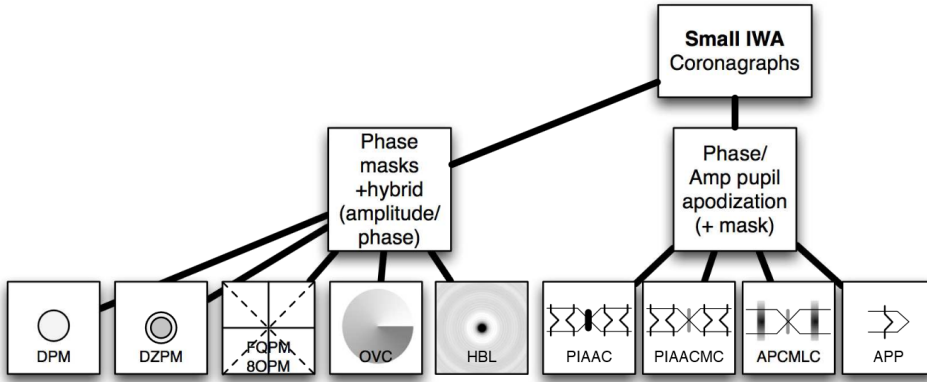


Figure 1.11: Figure with main types of coronagraphs with a small inner working angle, broken down into two families: phase-based focal-plane masks and pupil-plane apodizers. HBL: Hybrid Band-limited, PIAAC: Phase Induced Amplitude Apodization Coronagraph, PIAACMC: PIAA Complex Mask Coronagraph, APCMLC: Apodized Pupil Complex Mask Lyot Coronagraph. Adapted from Mawet et al. (2012).

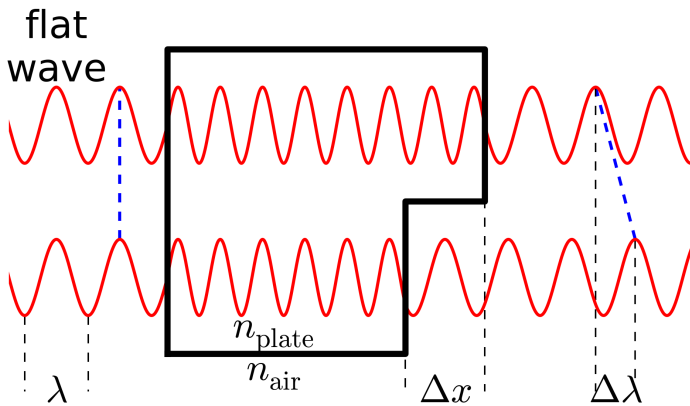


Figure 1.12: Phase generating principle behind Apodizing Phase Plate. A wave with wavelength λ picks up a phase delay $\Delta\phi$ with respect to another wave when it exits a high refractive index (n_{plate}) plate with a Δx path length difference. The medium around the plate has a refractive index of $n_{\text{air}} \approx 1$. The dependence of the phase on the wavelength and refractive indices makes this method chromatic. All polarization states are affected equally.

time around a star with $L' = 5$. APP images of two imaged planet can be seen in Figure 1.14.

The limitations of the APP (its chromaticity, single-sided dark hole and phase pattern constraints) can be resolved by switching from classical phase to geometric phase methods. This will be detailed in the following section.

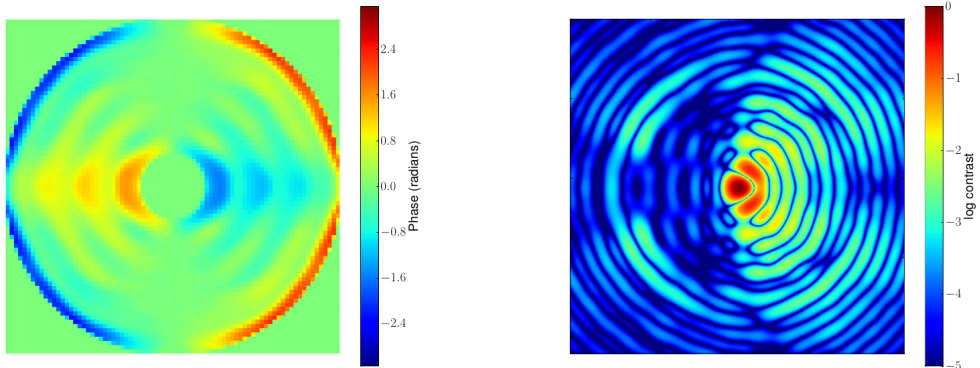


Figure 1.13: Left panel: An example of an antisymmetric phase pattern of the Apodizing Phase Plate coronagraph applied in the pupil plane. Right panel: Corresponding theoretical log-scaled PSF, normalized to its peak flux showing the D-shaped region with suppressed Airy rings.

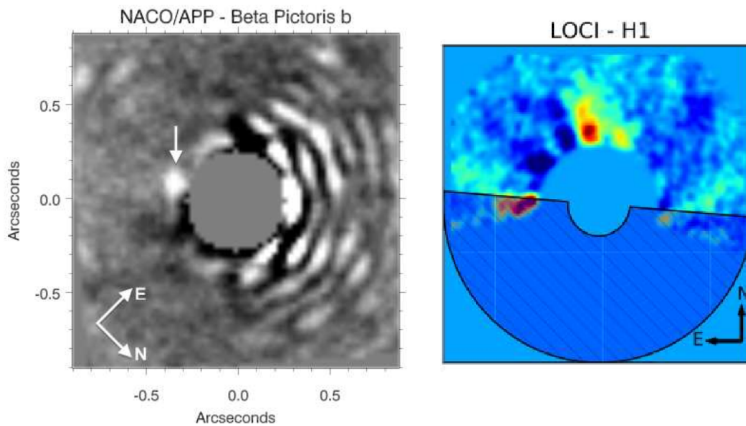


Figure 1.14: The left-hand side shows the APP detection of Beta Pictoris b at 4.05 microns narrow-band by Quanz et al. (2010). The right-hand side shows the detection of HD100546 b in *L*-band by Quanz et al. (2013).

1.4 Enabling technology for achromatic geometric phase elements

1.4.1 Achromatization with geometric phase elements

A different way of generating phase is based on retarding optics where the refractive index is dependent on the angle between the incoming linear polarization and the optic axis of the retarder. A beam of light which is not parallel to the optic axis will experience a different refractive index

for orthogonal components when going through a birefringent optic. In practice, these optical elements are often made with the optic axis parallel to the front surface of the optic. The uniaxial materials used to construct retarders have a different index of refraction along the optic axis than in the plane perpendicular to the optic axis. The axis with the smallest refractive index is commonly referred to as the fast axis, and similarly, the axis with the highest refractive index is called the slow axis. An unpolarized beam of light can be decomposed into two components with orthogonal linear polarizations. These two components of a beam of light pick up a different phase delay depending on whether they travel along the fast or slow axis. The amount of phase delay between the components (or retardance) depends on the wavelength, and thickness and birefringent properties of the optic.

The effect of a half-wave retarder (where the delay between components is exactly half of a wavelength) on a linearly polarized ray with an angle θ with respect to the fast axis is a rotation by 2θ with respect to a ray that travels along the fast axis. Similarly, a circular polarized ray of light receives a phase delay relative to a beam with the opposite circular polarization. This is the geometric or Pancharatnam-Berry phase, first used by Pancharatnam (1956) in the context of polarized light and later rediscovered by Berry (1984) in the context of quantum mechanics. As we are generally only interested in the relative phase, the phase equation becomes the one in Eq. 1.2.

$$\phi = \pm 2\theta \quad (1.2)$$

The retarder therefore flips the handedness of the circularly polarized beam and (depending on the handedness) the beam picks up either a positive or negative phase as can be seen in Fig. 1.15.

A phase pattern is no longer encoded in a physical path difference but encoded in the orientation of the fast axis of a half-wave retarder. This geometric phase is therefore not dependent on the wavelength but proportional to the orientation angle of the fast axis. However, there is a chromaticity associated with the retardance of the optic. In the case where the retardance is not exactly half-wave the emerging light also has a second component with a phase that is not dependent on the fast axis orientation. In extreme cases, a zero-wave plate consists of a beam with no added phase, while in the case of a perfect half-wave plate 100% of the beam has the required phase added. The intermediate cases produce a mixture of the two extremes. In the course of this thesis, in cases where the beam ideally has picked up a geometric phase, the component without a phase is commonly referred to as *leakage term* as it is generally unwanted.

While normal retarding optics have a $1/\lambda$ dependence on their retardance they can be relatively easily achromatized by stacking multiple retarding optics with slightly different orientations or birefringent properties following Pancharatnam (1955). In this way half-wave retardance can be approximated across a large wavelength range which minimizes the leakage term.

Achromatic linear retarders are easy to manufacture as the patterns are simple and therefore require only rotational alignment between layers to produce an approximately constant retardance. This becomes more difficult when the retarder is patterned as in coronagraphs and consequently the X-Y alignment between layers becomes critical, as was demonstrated by the work of Mawet (2010). A higher tolerance on the bandwidth and achromaticity requires more layers and further complicates the manufacturing.

Self-aligning *Multi-Twist Retarders* (MTR) overcome this problem. These use layers of bire-

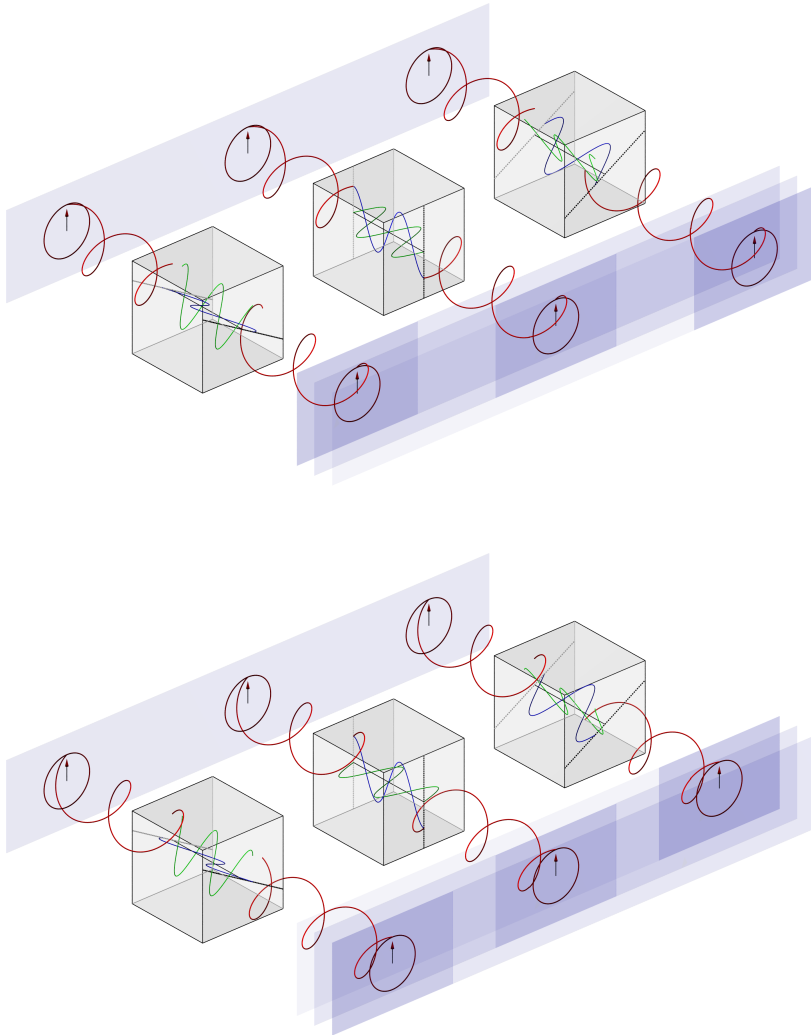


Figure 1.15: Phase generating principle of half-wave retarders. The panels show how a circularly polarized wave is decomposed into orthogonally polarized components. The component propagating along the slow axis picks up a phase delay of half a wave with respect to the other component. The two rows show different handedness of polarization. The leftmost half-wave retarder has a fast axis orientation θ of +60 degrees while the rightmost half-wave retarder has a fast axis orientation of -60 degrees. Depending on the angle of the fast axis (dashed line on retarder face) the emerging beam is delayed by twice that angle with respect to the case of where the angle is 0° (middle column of retarders). The handedness flip naturally emerges as well as the sign flip on the phase. This effect is the same regardless of the wavelength as long as the retardation is exactly half-wave.

fringing liquid crystals as a retarding medium (the polarization modifying properties of liquid crystals have been known since the 19th century, Reinitzer (1888)). A first layer of liquid crystals is deposited on a substrate with a certain fast axis orientation. Multiple liquid crystal layers with varying birefringent properties (e.g., twists) and thicknesses are deposited on top of this initial layer. Due to the elongated shape of the liquid crystals every consecutive layer aligns itself to the pattern on the previous layer (see Fig. 1.16) (Komanduri et al., 2013). To generate 100% bandwidth about 3 layers are required.

1.4.2 Accurate phase patterns

The constraint on the smoothness of the phase pattern can be relaxed by locally setting the fast axis of the retarder. With the liquid crystal based retarders this can be done with a polarized UV source with a beamwidth of the order of 10 microns (see Fig. 1.17). This *direct-write* approach allows almost any phase pattern and can therefore be used for a wide range of applications, ranging from lenses and gratings to q -plates (Miskiewicz and Escuti, 2014; Kim et al., 2015; Gao et al., 2015).

Within astronomy simple linear phase ramps can be used to produce polarization gratings (PGs, Escuti et al., 2006; Oh and Escuti, 2008; Packham et al., 2010), which generate two spectrally dispersed polarized copies of the imaged target (see Fig. 1.18). Complex patterns like a Vector Vortex Coronagraph (Mawet et al., 2009) and Apodizing Phase Plate coronagraph can also be made using such a scanning UV beam.

1.5 Work presented in this thesis

1.5.1 The vector Apodizing Phase Plate

The *vector Apodizing Phase Plate* (vAPP) was developed to overcome the limitations of the Apodizing Phase Plate using the patterned half-wave retarder introduced in Section 1.4 to create an achromatic phase delay (Snik et al., 2012).

When circularly polarized light hits a half-wave retarder with a certain fast axis orientation, the polarization state flips and a phase delay is added to the light. The opposite handedness of polarization will also flip states but pick up a negative phase delay. Unpolarized light can be interpreted to be composed of equal amounts of orthogonal linear and circular states. Therefore unpolarized light (such as starlight) can be decomposed into two opposite circularly polarized beams of light. As the phase design of Fig. 1.13 is antisymmetric these opposite circular polarizations will produce PSFs with dark holes on either side. The phase of the light depends only on the fast axis orientation of the retarder and is therefore achromatic. This means that selecting a different wavelength will impose the same phase to the light. If the retarder is not half-wave at all wavelengths part of the light will travel through the plate unaltered, leaking the original PSF on top of the coronagraph PSFs. This reduces the efficiency but as mentioned before retarders can be achromatized easily with a Pancharatnam design (Pancharatnam, 1955; Komanduri et al., 2013) which can reduce the impact to an acceptable level.

The vAPP is designed as a patterned half-wave retarder where the fast axis orientation is chosen to be exactly half of the required phase. Due to the nature of the retarder this will impart exactly

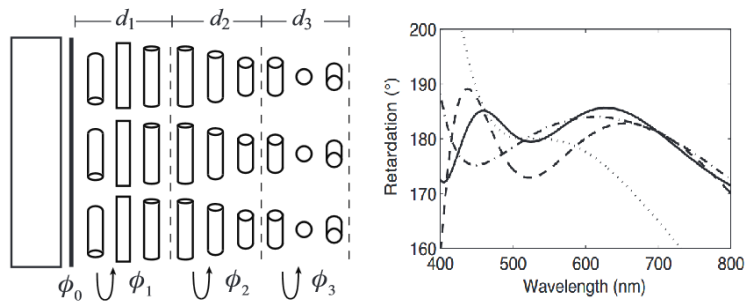


Figure 1.16: Left: schematic representation of an achromatic multi-twist retarder. The substrate and initial alignment layer are seen on the left-hand side. Subsequent multiple self-aligning layers with different thickness d and birefringent properties ϕ produce an achromatic half-wave retardance. Several representative retardance curves of MTRs with quasi-achromatic half-wave retardance are shown on the right. Adapted from Komanduri et al. (2013).

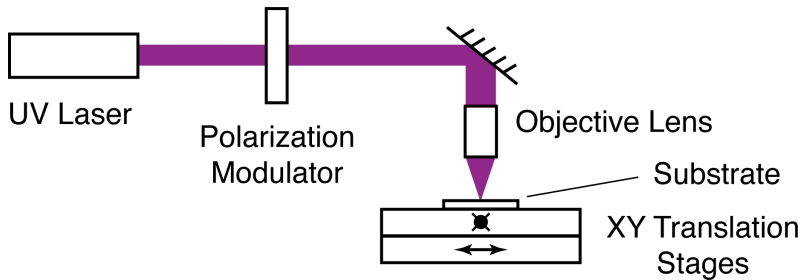


Figure 1.17: Schematic setup of direct writing tool used by Miskiewicz and Escuti (2014). A polarized UV laser is used to align the first liquid crystal layer on a substrate. The sample is translated underneath the polarized UV spot with an adjustable angle of polarization to vary the fast axis as a function of position.

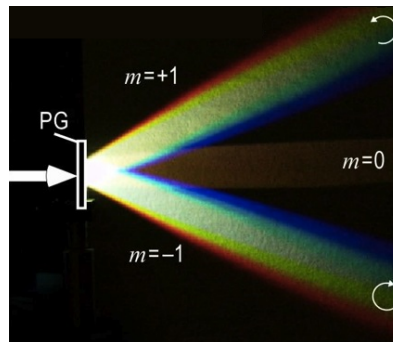


Figure 1.18: Effect of a polarization grating on an unpolarized beam of white light. The beam is split into two main beams that have orthogonal circular polarization states and a third 'leakage' beam that is unaltered and depends on the retardance of the PG. The splitting angle of the two main beams is dependent on wavelength and therefore the two beams are spectrally dispersed. Image courtesy of Geometric-Phase Photonics Lab, NCSU

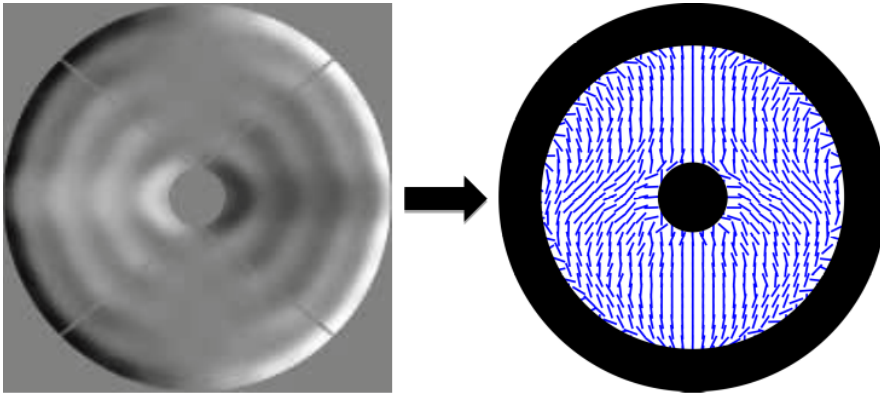


Figure 1.19: The required APP phase is no longer encoded in physical path length differences but as the orientation of the fast axis of a retarder. This figure shows an example with the APP phase pattern. Image courtesy of Frans Snik.

the right phase delay to the light as it passes through the coronagraph. Using a laser writing tool this patterning can be done with high spatial resolution on the order of 10 microns (Miskiewicz and Escuti, 2014). The retarder is manufactured to be approximately half-wave (to within a certain tolerance) within the required wavelength range. After splitting according to the circular polarization state with a quarter-wave plate and a Wollaston prism, two beams with opposite phases are formed. By focusing these beams with a lens we get two images of the same source with PSFs with opposite phases. For the default APP PSF this means that we get two PSFs with dark holes on opposite sides of the star as seen in Fig. 1.20. The coverage is now 360 degree in one shot, the coronagraph is achromatic in phase (see Fig. 1.21) and the phase design itself can be more complicated, thereby overcoming the limitations of the APP coronagraph.

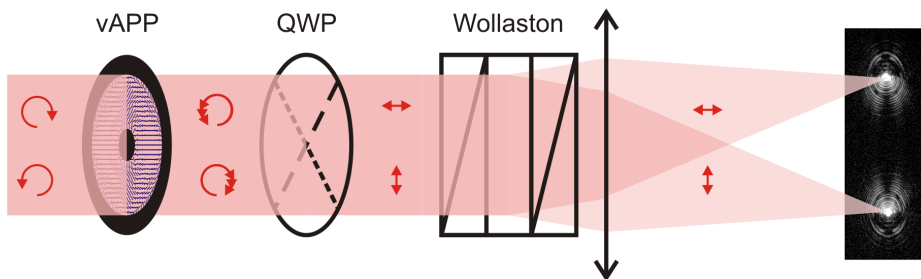


Figure 1.20: The operational principle of the vector Apodizing Phase Plate coronagraph. A patterned half-wave plate converts input circular polarizations into their opposite handedness with an extra phase delay added. One circular polarization accrues a positive phase pattern while the opposite polarization receives a negative phase. A QWP plate at 45 degrees and a Wollaston prism then splits the beam based on the circular polarization, while a camera lens images complementary PSFs on the camera (Snik et al., 2012).

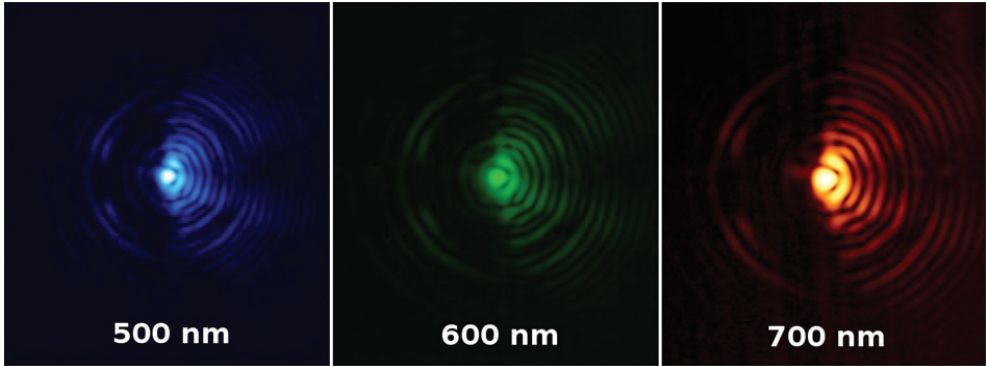


Figure 1.21: Laboratory measurements of PSF of vAPP taken at three different wavelengths demonstrating the achromatic nature of the technology. The shape of the PSF and the darkness in the dark hole stays consistent while the size scales with λ/D as expected. See Chapter 3 for a detailed characterization of the optic.

The aforementioned techniques in this introduction are stepwise improvements to seeing-limited imaging. It starts with Adaptive Optics to enable diffraction limited imaging from the ground. This massively improves the contrast that can be achieved by increasing the peak flux and stabilizing the PSF. Afterwards, the vAPP coronagraph creates a suppressed region close to the star. These improvements are shown in Fig. 1.22 as step 1 through 3. By getting rid of the stellar light in this region the residual noise after PSF subtraction will be reduced which is of course the crucial improvement needed to enhance the detection and characterization of exoplanets. To show the sensitivity of the coronagraph we show the 5σ point source sensitivity around a bright star in steps 4 and 5, which is based on data taken in this thesis with MagAO on Magellan at 3.94 microns. Step 4 only includes the APP + ADI while step 5 also has an extra PSF subtraction step explained in Chapter 6.

1.5.2 Phase-Sorting Interferometry

Quasi-static aberrations are important contrast-limiting factors. While part of their influence can be reduced by using advanced PSF subtraction techniques like LOCI and PCA, and PSF suppressing coronagraphs it is better if they are corrected in real-time within the instrument. Phase Sorting Interferometry (PSI) is a technique developed by Codona et al. (2008) and expanded by Codona and Kenworthy (2013) to use the wavefront information on residual atmospheric speckles to interferometrically probe the complex amplitude of quasi-static speckles on the science detector. Because the quasi-static speckles have lifetimes that are considerably longer than the atmospheric speckles and the average integration time of the science camera they can be reconstructed and corrected based on the wavefront sensor telemetry and the science camera image cubes. After constraining the phase and amplitude for each speckle the deformable mirror can be adjusted to create a conjugated speckle to remove it. Alternatively, this information can be used in a post-processing step to create an improved PSF model for PSF subtraction.

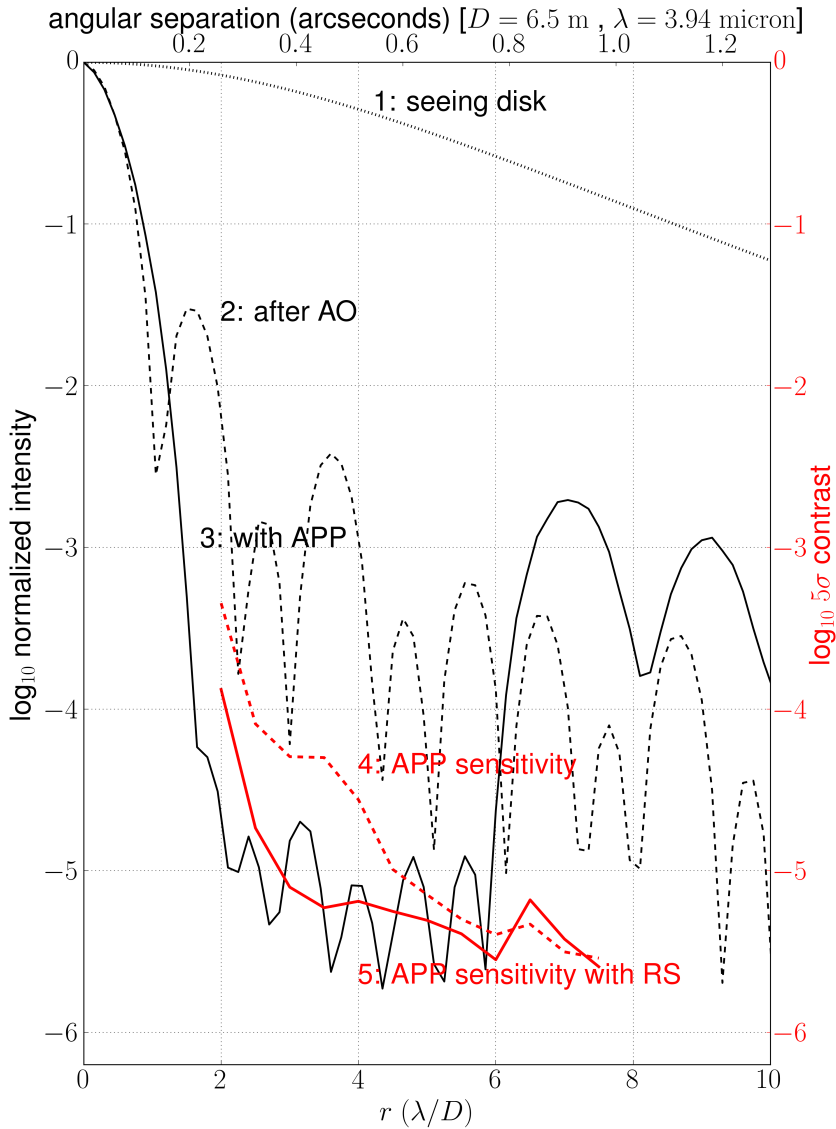


Figure 1.22: Development of the normalized intensity and 5σ contrast after implementing different correction steps. Starting with 1: a 1 arcsecond FWHM seeing disk that is created after taking a long exposure with normal atmospheric turbulence in the optical band. For graphs 2 through 5 we assume a high performance AO system is operational. Graph 2 shows the intensity profile of a diffraction limited PSE. Graph 3 shows the same but after adding the APP coronagraph to the optical system. The 5σ point source detection sensitivity after ADI is shown in Graph 4 and the sensitivity after Rotation and Subtraction (RS) + ADI is shown in Graph 5. This reduction process will be explained in more detail in this thesis.

1.6 Thesis outline

Chapter 2

Part of instrumental aberrations are unsensed by the wavefront sensor. These unsensed aberrations create quasi-static speckles that limit the contrast that can be achieved. In Chapter 2 we present the AO laboratory testbed at Leiden Observatory and the techniques we propose to use to test the impact of the time synchronization between the wavefront sensor and science camera, the achromaticity of the atmosphere and other limiting factors on the PSI focal-plane wavefront reconstruction technique. The AO setup has two separate laser sources to simulate starlight at two distinct frequencies. Depending on the wavelength the light is either sent to a wavefront sensor or a science camera using a dichroic mirror, as is commonly done in direct imaging instruments. This setup can be used to test the performance of the previously mentioned PSI method in conjunction with coronagraphs such as vector Apodizing Phase Plates, Lyot coronagraphs and VVCs. The phase solutions given by the PSI method can be compared with independent phase solutions coming from the differential Optical Transfer Function (dOTF) method and a phase-stepping interferometer. This setup enables us to rapidly prototype high-contrast imaging techniques and has since been used to characterize the first visible band vAPP prototypes. This chapter is based on Otten et al. (2012).

Chapter 3

The concept of the vAPP was first introduced by Snik et al. (2012) and an initial narrow-band prototype was shown to produce two complementary PSFs with dark holes. In Chapter 3 the first achromatic vAPP prototype based on a three-layer multi-twist retarder was tested. We have performed both pupil and PSF measurements of the achromatic vAPP at multiple wavelengths in the visual band (400-800 nm). We recorded the intensity of the coronagraph pupil between parallel and crossed polarizers at different position angles. We used pupil measurements to reconstruct the three important parameters of the coronagraph as a function of position: transmission, retardance and fast axis orientation. Based on a Mueller matrix representation of the coronagraph in its measurement setup these properties could be constrained. These three parameters were applied in a PSF model based on Jones calculus and compared to PSF measurements taken in the same bands. The intensity profile of the forward model and the reality were in agreement with an average normalized intensity ratio of $10^{-3.8}$ measured from 2 to $7 \lambda/D$. While the coronagraph performed within specifications it was concluded after analyzing the different coronagraph properties that the most detrimental impact to the contrast was caused by the offset from half-wave retardance, which causes light of the original PSF to leak through. This can be resolved by either filtering the leakage with polarizing filters or producing a retarder with improved half-wave behavior, for instance by adding more retarding layers. This chapter is based on work presented in Otten et al. (2014b).

Chapter 4

The principle of the vector Apodizing Phase Plate coronagraph presented in Snik et al. (2012) and Otten et al. (2014b) works in the lab but is harder to implement in an instrument than the single

optic regular APP as it requires an achromatic beamsplitter and quarter-wave plate that need to be carefully aligned. Furthermore, one of the conclusions of Chapter 3 is that the vAPP's performance is limited by the offset from half-wave retardance of the coronagraph, creating leakage terms that deteriorate the contrast of the coronagraphic PSFs. While the leakage can be suppressed by filtering polarization states, this complicates the installation into instruments even more. Chapter 4 shows that a phase ramp (i.e., a polarization grating phase pattern) added to the vAPP's phase pattern can reduce the complexity and increase the robustness of the coronagraph. The included phase ramp creates a splitting based on the circular polarization states, thereby eliminating the quarter-wave plate and Wollaston prism. The coronagraphic PSFs are moved away from the non half-wave leakage term. This eliminates the impact that the retardance has on the contrast ruining leakage. This design is called the grating-vAPP (gvAPP). The robustness of the gvAPP comes at a cost because spectral smearing in one dimension limits the width of an individual filter to approximately 5%. However, thanks to liquid-crystal achromatization one gvAPP device can be used with narrow-band filters throughout a large wavelength range. We also present a manufactured vAPP design that can suppress a 360 degree annular region around the star. This phase pattern is so extreme that it can not be manufactured using conventional diamond turning manufacturing techniques. The validity of the phase design is tested in a laboratory setup and shows a rearrangement of the light in such an annular area. This chapter is based on work presented in Otten et al. (2014a).

Chapter 5

In Chapter 5 we present the first on-sky results with the narrow-band gvAPP coronagraph on the Large Binocular Telescope. These results show that the vAPP coronagraph can be taken within a few months from concept to installation and works in the near-infrared (4 microns) under cryogenic conditions as expected. The phase ramp that was added in the design works as predicted by keeping the leakage PSF away from the coronagraphic PSFs. Our analysis shows however that the first light measurements taken at 4.05 microns narrow-band are limited in performance by a pupil misalignment and a significant amount of wavefront error in the form of astigmatism. Our PSF simulation shows that the measured performance can be explained by the combined impact of both factors. The pupil alignment issue can be solved by realigning the pupil before taking the observations and the wavefront error can be dialed out using the deformable mirror of the instrument.

Chapter 6

In Chapter 6 we present the first on-sky results with the gvAPP coronagraph at MagAO/Clio2. This coronagraph is optimized to work at an extremely broad wavelength range from 2 to 5 microns and also includes a phase grating to separate the coronagraphic and leakage PSFs. We demonstrate that the two PSFs can be combined to perform an even better PSF subtraction, especially in the speckle halo close to the star. The apparent limitations seen at the LBT are not present in this coronagraph and instrument combination, and it achieves an unprecedented contrast close to the star. After rotating, optimally scaling one PSF, and subtracting it from the other PSF we see a contrast improvement by 1.46 magnitudes at $3.5 \lambda/D$. Applying regular Angular Differential Imaging as a final step, the MagAO gvAPP coronagraph delivers a 5σ Δ mag contrast

of 8.3 ($= 10^{-3.3}$) at $2 \lambda/D$, 10.8 ($= 10^{-4.3}$) at $2.5 \lambda/D$, 12.2 ($= 10^{-4.8}$) at $3.5 \lambda/D$, and 12.5 ($= 10^{-5}$) at $4.5 \lambda/D$, all measured at $3.9 \mu\text{m}$ in 1.5 hours of observing time. Compared to other coronagraphs on current 6 – 10 meter telescopes the vAPP performs up to 2 magnitudes better inward of $5 \lambda/D$. These results can also be seen at a glance in Fig 1.22. These numbers improve with more advanced PSF subtraction methods like PCA. This work is to be submitted to ApJ.

We conclude the scientific part of the thesis with an outlook on future work and scientific possibilities with the vAPP in Chapter 7.

References

- Allard, F., Hauschildt, P. H., Alexander, D. R., Tamanai, A., and Schweitzer, A. (2001). The Limiting Effects of Dust in Brown Dwarf Model Atmospheres. *ApJ*, 556:357–372.
- Allard, F., Homeier, D., and Freytag, B. (2012). Models of very-low-mass stars, brown dwarfs and exoplanets. *Philosophical Transactions of the Royal Society of London Series A*, 370:2765–2777.
- Amara, A. and Quanz, S. P. (2012). PYNPOINT: an image processing package for finding exoplanets. *MNRAS*, 427:948–955.
- Avenhaus, H., Quanz, S. P., Meyer, M. R., Brittain, S. D., Carr, J. S., and Najita, J. R. (2014). Hd100546 multi-epoch scattered light observations. *The Astrophysical Journal*, 790(1):56.
- Bailey, V., Meshkat, T., Reiter, M., Morzinski, K., Males, J., Su, K. Y. L., Hinz, P. M., Kenworthy, M., Stark, D., Mamajek, E., Briguglio, R., Close, L. M., Follette, K. B., Puglisi, A., Rodigas, T., Weinberger, A. J., and Xompero, M. (2014). HD 106906 b: A Planetary-mass Companion Outside a Massive Debris Disk. *ApJ*, 780:L4.
- Baraffe, I., Chabrier, G., Barman, T. S., Allard, F., and Hauschildt, P. H. (2003). Evolutionary models for cool brown dwarfs and extrasolar giant planets. The case of HD 209458. *A&A*, 402:701–712.
- Barman, T. S., Macintosh, B., Konopacky, Q. M., and Marois, C. (2011). Clouds and Chemistry in the Atmosphere of Extrasolar Planet HR8799b. *ApJ*, 733:65.
- Benedict, G. F., McArthur, B. E., Forveille, T., Delfosse, X., Nelan, E., Butler, R. P., Spiesman, W., Marcy, G., Goldman, B., Perrier, C., Jefferys, W. H., and Mayor, M. (2002). A Mass for the Extrasolar Planet Gliese 876b Determined from Hubble Space Telescope Fine Guidance Sensor 3 Astrometry and High-Precision Radial Velocities. *ApJ*, 581:L115–L118.
- Berry, M. V. (1984). Quantal Phase Factors Accompanying Adiabatic Changes. *Royal Society of London Proceedings Series A*, 392:45–57.
- Biller, B. A., Close, L. M., Masciadri, E., Nielsen, E., Lenzen, R., Brandner, W., McCarthy, D., Hartung, M., Kellner, S., Mamajek, E., Henning, T., Miller, D., Kenworthy, M., and Kulesa, C. (2007). An Imaging Survey for Extrasolar Planets around 45 Close, Young Stars with the Simultaneous Differential Imager at the Very Large Telescope and MMT. *ApJS*, 173:143–165.
- Bond, I. A., Udalski, A., Jaroszyński, M., Rattenbury, N. J., Paczyński, B., Soszyński, I., Wyrzykowski, L., Szymański, M. K., Kubiak, M., Szewczyk, O., Żebruń, K., Pietrzyński, G., Abe, F., Bennett, D. P., Eguchi, S., Furuta, Y., Hearnshaw, J. B., Kamiya, K., Kilmartin, P. M., Kurata, Y., Masuda, K., Matsubara, Y., Muraki, Y., Noda, S., Okajima, K., Sako, T., Sekiguchi,

- T., Sullivan, D. J., Sumi, T., Tristram, P. J., Yanagisawa, T., Yock, P. C. M., and OGLE Collaboration (2004). OGLE 2003-BLG-235/MOA 2003-BLG-53: A Planetary Microlensing Event. *ApJ*, 606:L155–L158.
- Burrows, A., Sudarsky, D., and Hubeny, I. (2004). Spectra and Diagnostics for the Direct Detection of Wide-Separation Extrasolar Giant Planets. *ApJ*, 609:407–416.
- Butler, R. P. and Marcy, G. W. (1996). A Planet Orbiting 47 Ursae Majoris. *ApJ*, 464:L153.
- Carlotti, A. (2013). Apodized phase mask coronagraphs for arbitrary apertures. *A&A*, 551:A10.
- Chabrier, G., Baraffe, I., Allard, F., and Hauschildt, P. (2000). Evolutionary Models for Very Low-Mass Stars and Brown Dwarfs with Dusty Atmospheres. *ApJ*, 542:464–472.
- Charbonneau, D., Brown, T. M., Latham, D. W., and Mayor, M. (2000). Detection of Planetary Transits Across a Sun-like Star. *ApJ*, 529:L45–L48.
- Charbonneau, D., Brown, T. M., Noyes, R. W., and Gilliland, R. L. (2002). Detection of an Extrasolar Planet Atmosphere. *ApJ*, 568:377–384.
- Chauvin, G., Lagrange, A.-M., Dumas, C., Zuckerman, B., Mouillet, D., Song, I., Beuzit, J.-L., and Lowrance, P. (2004). A giant planet candidate near a young brown dwarf. Direct VLT/NACO observations using IR wavefront sensing. *A&A*, 425:L29–L32.
- Close, L. M., Follette, K. B., Males, J. R., Puglisi, A., Xompero, M., Apai, D., Najita, J., Weinberger, A. J., Morzinski, K., Rodigas, T. J., Hinz, P., Bailey, V., and Briguglio, R. (2014). Discovery of H α Emission from the Close Companion inside the Gap of Transitional Disk HD 142527. *ApJ*, 781:L30.
- Codona, J. L. and Angel, R. (2004). Imaging Extrasolar Planets by Stellar Halo Suppression in Separately Corrected Color Bands. *ApJ*, 604:L117–L120.
- Codona, J. L. and Kenworthy, M. (2013). Focal Plane Wavefront Sensing Using Residual Adaptive Optics Speckles. *ApJ*, 767:100.
- Codona, J. L., Kenworthy, M. A., Hinz, P. M., Angel, J. R. P., and Woolf, N. J. (2006). A high-contrast coronagraph for the MMT using phase apodization: design and observations at 5 microns and 2 λ/D radius. In *Society of Photo-Optical Instrumentation Engineers (SPIE) Conference Series*, volume 6269 of *Society of Photo-Optical Instrumentation Engineers (SPIE) Conference Series*.
- Codona, J. L., Kenworthy, M. A., and Lloyd-Hart, M. (2008). A novel WFS technique for high-contrast imaging: Phase Sorting Interferometry (PSI). In *Society of Photo-Optical Instrumentation Engineers (SPIE) Conference Series*, volume 7015 of *Society of Photo-Optical Instrumentation Engineers (SPIE) Conference Series*, page 5.
- Einstein, A. (1936). Lens-Like Action of a Star by the Deviation of Light in the Gravitational Field. *Science*, 84:506–507.

- Escuti, M. J., Oh, C., Sánchez, C., Bastiaansen, C., and Broer, D. J. (2006). Simplified spectropolarimetry using reactive mesogen polarization gratings. In *SPIE Optics+ Photonics*, pages 630207–630207. International Society for Optics and Photonics.
- Fortney, J. J., Lodders, K., Marley, M. S., and Freedman, R. S. (2008). A Unified Theory for the Atmospheres of the Hot and Very Hot Jupiters: Two Classes of Irradiated Atmospheres. *ApJ*, 678:1419–1435.
- Fressin, F., Torres, G., Charbonneau, D., Bryson, S. T., Christiansen, J., Dressing, C. D., Jenkins, J. M., Walkowicz, L. M., and Batalha, N. M. (2013). The false positive rate of kepler and the occurrence of planets. *The Astrophysical Journal*, 766(2):81.
- Gao, K., Cheng, H.-H., Bhowmik, A. K., and Bos, P. J. (2015). Thin-film pancharatnam lens with low f-number and high quality. *Opt. Express*, 23(20):26086–26094.
- Gaudi, B. S. (2012). Microlensing surveys for exoplanets. *Annual Review of Astronomy and Astrophysics*, 50:411–453.
- Guyon, O. (2003). Phase-induced amplitude apodization of telescope pupils for extrasolar terrestrial planet imaging. *A&A*, 404:379–387.
- Guyon, O., Martinache, F., Belikov, R., and Soummer, R. (2010). High Performance PIAA Coronagraphy with Complex Amplitude Focal Plane Masks. *ApJS*, 190:220–232.
- Guyon, O., Pluzhnik, E. A., Kuchner, M. J., Collins, B., and Ridgway, S. T. (2006). Theoretical Limits on Extrasolar Terrestrial Planet Detection with Coronagraphs. *ApJS*, 167:81–99.
- Henry, G. W., Marcy, G. W., Butler, R. P., and Vogt, S. S. (2000). A Transiting “51 Peg-like” Planet. *ApJ*, 529:L41–L44.
- Hinkley, S., Oppenheimer, B. R., Soummer, R., Sivaramakrishnan, A., Roberts, Jr., L. C., Kuhn, J., Makidon, R. B., Perrin, M. D., Lloyd, J. P., Kratter, K., and Brenner, D. (2007). Temporal Evolution of Coronagraphic Dynamic Range and Constraints on Companions to Vega. *ApJ*, 654:633–640.
- Janson, M., Bergfors, C., Goto, M., Brandner, W., and Lafrenière, D. (2010). Spatially resolved spectroscopy of the exoplanet hr 8799 c. *The Astrophysical Journal Letters*, 710(1):L35.
- Kalas, P., Graham, J. R., Chiang, E., Fitzgerald, M. P., Clampin, M., Kite, E. S., Stapelfeldt, K., Marois, C., and Krist, J. (2008). Optical Images of an Exosolar Planet 25 Light-Years from Earth. *Science*, 322:1345–.
- Kasdin, N. J., Vanderbei, R. J., Littman, M. G., Carr, M., and Spergel, D. N. (2004). The shaped pupil coronagraph for planet finding coronagraphy: optimization, sensitivity, and laboratory testing. In Mather, J. C., editor, *Optical, Infrared, and Millimeter Space Telescopes*, volume 5487 of *Society of Photo-Optical Instrumentation Engineers (SPIE) Conference Series*, pages 1312–1321.
- Kasdin, N. J., Vanderbei, R. J., Spergel, D. N., and Littman, M. G. (2003). Extrasolar planet finding via optimal apodized-pupil and shaped-pupil coronagraphs. *The Astrophysical Journal*, 582(2):1147.

- Keller, C. U., Schmid, H. M., Venema, L. B., Hanenburg, H., Jager, R., Kasper, M., Martinez, P., Rigal, F., Rodenhuis, M., Roelfsema, R., Snik, F., Verinaud, C., and Yaitskova, N. (2010). Epol: the exoplanet polarimeter for epics at the e-elt. In *Proc. SPIE*, volume 7735, pages 77356G–77356G–13.
- Kenworthy, M. A., Codona, J. L., Hinz, P. M., Angel, J. R. P., Heinze, A., and Sivanandam, S. (2007). First On-Sky High-Contrast Imaging with an Apodizing Phase Plate. *ApJ*, 660:762–769.
- Kenworthy, M. A., Quanz, S. P., Meyer, M. R., Kasper, M. E., Lenzen, R., Codona, J. L., Girard, J. H., and Hinz, P. M. (2010). An apodizing phase plate coronagraph for VLT/NACO. In *Ground-based and Airborne Instrumentation for Astronomy III*, volume 7735 of *Proc. SPIE*, page 773532.
- Kim, J., Li, Y., Miskiewicz, M. N., Oh, C., Kudenov, M. W., and Escuti, M. J. (2015). Fabrication of ideal geometric-phase holograms with arbitrary wavefronts. *Optica*, 2(11):958–964.
- Komanduri, R. K., Lawler, K. F., and Escuti, M. J. (2013). Multi-twist retarders: broadband retardation control using self-aligning reactive liquid crystal layers. *Opt. Express*, 21(1):404–420.
- Konopacky, Q. M., Barman, T. S., Macintosh, B. A., and Marois, C. (2013). Detection of carbon monoxide and water absorption lines in an exoplanet atmosphere. *Science*, 339(6126):1398–1401.
- Kostinski, A. B. and Yang, W. (2005). Pupil phase apodization for imaging of faint companions in prescribed regions. *Journal of Modern Optics*, 52:2467–2474.
- Kuchner, M. J. and Traub, W. A. (2002). A Coronagraph with a Band-limited Mask for Finding Terrestrial Planets. *ApJ*, 570:900–908.
- Kuhn, J. R., Potter, D., and Parise, B. (2001). Imaging polarimetric observations of a new circumstellar disk system. *The Astrophysical Journal Letters*, 553(2):L189.
- Kuzuhara, M., Tamura, M., Kudo, T., Janson, M., Kandori, R., Brandt, T. D., Thalmann, C., Spiegel, D., Biller, B., Carson, J., Hori, Y., Suzuki, R., Burrows, A., Henning, T., Turner, E. L., McElwain, M. W., Moro-Martín, A., Suenaga, T., Takahashi, Y. H., Kwon, J., Lucas, P., Abe, L., Brandner, W., Egner, S., Feldt, M., Fujiwara, H., Goto, M., Grady, C. A., Guyon, O., Hashimoto, J., Hayano, Y., Hayashi, M., Hayashi, S. S., Hodapp, K. W., Ishii, M., Iye, M., Knapp, G. R., Matsuo, T., Mayama, S., Miyama, S., Morino, J.-I., Nishikawa, J., Nishimura, T., Kotani, T., Kusakabe, N., Pyo, T.-S., Serabyn, E., Suto, H., Takami, M., Takato, N., Terada, H., Tomono, D., Watanabe, M., Wisniewski, J. P., Yamada, T., Takami, H., and Usuda, T. (2013). Direct Imaging of a Cold Jovian Exoplanet in Orbit around the Sun-like Star GJ 504. *ApJ*, 774:11.
- Laertius, D. (300). Lives and opinions of eminent philosophers, book 10, section 45.
- Lafrenière, D., Jayawardhana, R., and van Kerkwijk, M. H. (2008). Direct Imaging and Spectroscopy of a Planetary-Mass Candidate Companion to a Young Solar Analog. *ApJ*, 689:L153–L156.

- Lafrenière, D., Marois, C., Doyon, R., and Barman, T. (2009). HST/NICMOS Detection of HR 8799 b in 1998. *ApJ*, 694:L148–L152.
- Lafrenière, D., Marois, C., Doyon, R., Nadeau, D., and Artigau, É. (2007). A New Algorithm for Point-Spread Function Subtraction in High-Contrast Imaging: A Demonstration with Angular Differential Imaging. *ApJ*, 660:770–780.
- Lagrange, A.-M., Gratadour, D., Chauvin, G., Fusco, T., Ehrenreich, D., Mouillet, D., Rousset, G., Rouan, D., Allard, F., Gendron, É., Charton, J., Mugnier, L., Rabou, P., Montri, J., and Lacombe, F. (2009). A probable giant planet imaged in the β Pictoris disk. VLT/NaCo deep L'-band imaging. *A&A*, 493:L21–L25.
- Lenzen, R., Close, L., Brandner, W., Biller, B., and Hartung, M. (2004). A novel simultaneous differential imager for the direct imaging of giant planets. In Moorwood, A. F. M. and Iye, M., editors, *Ground-based Instrumentation for Astronomy*, volume 5492 of *Society of Photo-Optical Instrumentation Engineers (SPIE) Conference Series*, pages 970–977.
- Lyt, B. (1939). The study of the solar corona and prominences without eclipses (George Darwin Lecture, 1939). *MNRAS*, 99:580.
- M. Kürster, M. Endl, F. Rouesnel, S. Els, A. Kaufer, S. Brilliant, A. P. Hatzes, S. H. Saar, and W. D. Cochran (2003). The low-level radial velocity variability in barnard's star (= gj 699). *A&A*, 403(3):1077–1087.
- Macintosh, B., Graham, J. R., Barman, T., De Rosa, R. J., Konopacky, Q., Marley, M. S., Marois, C., Nielsen, E. L., Pueyo, L., Rajan, A., Rameau, J., Saumon, D., Wang, J. J., Patience, J., Ammons, M., Arriaga, P., Artigau, E., Beckwith, S., Brewster, J., Bruzzone, S., Bulger, J., Burningham, B., Burrows, A. S., Chen, C., Chiang, E., Chilcote, J. K., Dawson, R. I., Dong, R., Doyon, R., Draper, Z. H., Duchêne, G., Esposito, T. M., Fabrycky, D., Fitzgerald, M. P., Follette, K. B., Fortney, J. J., Gerard, B., Goodsell, S., Greenbaum, A. Z., Hibon, P., Hinkley, S., Cotten, T. H., Hung, L.-W., Ingraham, P., Johnson-Groh, M., Kalas, P., Lafreniere, D., Larkin, J. E., Lee, J., Line, M., Long, D., Maire, J., Marchis, F., Matthews, B. C., Max, C. E., Metchev, S., Millar-Blanchaer, M. A., Mittal, T., Morley, C. V., Morzinski, K. M., Murray-Clay, R., Oppenheimer, R., Palmer, D. W., Patel, R., Perrin, M. D., Poyneer, L. A., Rafikov, R. R., Rantakyro, F. T., Rice, E. L., Rojo, P., Rudy, A. R., Ruffio, J.-B., Ruiz, M. T., Sadakuni, N., Saddlemyer, L., Salama, M., Savransky, D., Schneider, A. C., Sivaramakrishnan, A., Song, I., Soummer, R., Thomas, S., Vasisht, G., Wallace, J. K., Ward-Duong, K., Wiktorowicz, S. J., Wolff, S. G., and Zuckerman, B. (2015). Discovery and spectroscopy of the young jovian planet 51 eri b with the gemini planet imager. *Science*, 350(6256):64–67.
- Mao, S. and Paczynski, B. (1991). Gravitational microlensing by double stars and planetary systems. *ApJ*, 374:L37–L40.
- Marcy, G. W. and Butler, R. P. (1996). A Planetary Companion to 70 Virginis. *ApJ*, 464:L147.
- Marley, M. S., Fortney, J. J., Hubickij, O., Bodenheimer, P., and Lissauer, J. J. (2007). On the Luminosity of Young Jupiters. *ApJ*, 655:541–549.

- Marois, C., Correia, C., Galicher, R., Ingraham, P., Macintosh, B., Currie, T., and De Rosa, R. (2014). GPI PSF subtraction with TLOCI: the next evolution in exoplanet/disk high-contrast imaging. In *Adaptive Optics Systems IV*, volume 9148 of *Proc. SPIE*, page 91480U.
- Marois, C., Lafrenière, D., Doyon, R., Macintosh, B., and Nadeau, D. (2006). Angular Differential Imaging: A Powerful High-Contrast Imaging Technique. *ApJ*, 641:556–564.
- Marois, C., Macintosh, B., Barman, T., Zuckerman, B., Song, I., Patience, J., Lafrenière, D., and Doyon, R. (2008). Direct Imaging of Multiple Planets Orbiting the Star HR 8799. *Science*, 322:1348–.
- Marois, C., Nadeau, D., Doyon, R., Racine, R., and Walker, G. A. H. (2003). Searching for Faint Companions with the TRIDENT Differential Simultaneous Imaging Camera. In Deming, D. and Seager, S., editors, *Scientific Frontiers in Research on Extrasolar Planets*, volume 294 of *Astronomical Society of the Pacific Conference Series*, pages 103–106.
- Marois, C., Zuckerman, B., Konopacky, Q. M., Macintosh, B., and Barman, T. (2010). Images of a fourth planet orbiting HR 8799. *Nature*, 468:1080–1083.
- Mawet, D. (2010). Presentation. *Spirit of Lyot*.
- Mawet, D., Pueyo, L., Lawson, P., Mugnier, L., Traub, W., Boccaletti, A., Trauger, J. T., Gladysz, S., Serabyn, E., Milli, J., Belikov, R., Kasper, M., Baudoz, P., Macintosh, B., Marois, C., Oppenheimer, B., Barrett, H., Beuzit, J.-L., Devaney, N., Girard, J., Guyon, O., Krist, J., Mennesson, B., Mouillet, D., Murakami, N., Poyneer, L., Savransky, D., Vérinaud, C., and Wallace, J. K. (2012). Review of small-angle coronagraphic techniques in the wake of ground-based second-generation adaptive optics systems. In *Society of Photo-Optical Instrumentation Engineers (SPIE) Conference Series*, volume 8442 of *Society of Photo-Optical Instrumentation Engineers (SPIE) Conference Series*.
- Mawet, D., Riaud, P., Absil, O., and Surdej, J. (2005). Annular groove phase mask coronagraph. *The Astrophysical Journal*, 633(2):1191.
- Mawet, D., Serabyn, E., Liewer, K., Hanot, C., McEldowney, S., Shemo, D., and O’Brien, N. (2009). Optical Vectorial Vortex Coronagraphs using Liquid Crystal Polymers: theory, manufacturing and laboratory demonstration. *Optics Express*, 17:1902–1918.
- Mayor, M. and Queloz, D. (1995). A Jupiter-mass companion to a solar-type star. *Nature*, 378:355–359.
- Mesa, D., Gratton, R., Zurlò, A., Vigan, A., Claudi, R. U., Alberici, M., Antichi, J., Baruffolo, A., Beuzit, J.-L., Boccaletti, A., Bonnefoy, M., Costille, A., Desidera, S., Dohlen, K., Fantinel, D., Feldt, M., Fusco, T., Giro, E., Henning, T., Kasper, M., Langlois, M., Maire, A.-L., Martínez, P., Moeller-Nilsson, O., Mouillet, D., Moutou, C., Pavlov, A., Puget, P., Salasnich, B., Sauvage, J.-F., Sissa, E., Turatto, M., Udry, S., Vakili, F., Waters, R., and Wildi, F. (2015). Performance of the VLT Planet Finder SPHERE. II. Data analysis and results for IFS in laboratory. *A&A*, 576:A121.

- Meshkat, T., Bailey, V. P., Su, K. Y. L., Kenworthy, M. A., Mamajek, E. E., Hinz, P. M., and Smith, P. S. (2015a). Searching for Planets in Holey Debris Disks with the Apodizing Phase Plate. *ApJ*, 800:5.
- Meshkat, T., Bonnefoy, M., Mamajek, E. E., Quanz, S. P., Chauvin, G., Kenworthy, M. A., Rameau, J., Meyer, M. R., Lagrange, A.-M., Lannier, J., and Delorme, P. (2015b). Discovery of a low-mass companion to the F7V star HD 984. *MNRAS*, 453:2378–2386.
- Meshkat, T., Kenworthy, M. A., Quanz, S. P., and Amara, A. (2014). Optimized Principal Component Analysis on Coronagraphic Images of the Fomalhaut System. *ApJ*, 780:17.
- Meshkat, T., Kenworthy, M. A., Reggiani, M., Quanz, S. P., Mamajek, E. E., and Meyer, M. R. (2015c). Searching for gas giant planets on Solar system scales - a NACO/APP L-band survey of A- and F-type main-sequence stars. *MNRAS*, 453:2533–2539.
- Miskiewicz, M. N. and Escuti, M. J. (2014). Direct-writing of complex liquid crystal patterns. *Opt. Express*, 22(10):12691–12706.
- Mohanty, S., Jayawardhana, R., Huélamo, N., and Mamajek, E. (2007). The Planetary Mass Companion 2MASS 1207-3932B: Temperature, Mass, and Evidence for an Edge-on Disk. *ApJ*, 657:1064–1091.
- Moody, D. C., Gordon, B. L., and Trauger, J. T. (2008). Design and demonstration of hybrid Lyot coronagraph masks for improved spectral bandwidth and throughput. In *Space Telescopes and Instrumentation 2008: Optical, Infrared, and Millimeter*, volume 7010 of *Proc. SPIE*, page 70103P.
- Morley, C. V., Fortney, J. J., Marley, M. S., Visscher, C., Saumon, D., and Leggett, S. K. (2012). Neglected Clouds in T and Y Dwarf Atmospheres. *ApJ*, 756:172.
- Morley, C. V., Marley, M. S., Fortney, J. J., and Lupu, R. (2014a). Spectral variability from the patchy atmospheres of t and y dwarfs. *The Astrophysical Journal Letters*, 789(1):L14.
- Morley, C. V., Marley, M. S., Fortney, J. J., Lupu, R., Saumon, D., Greene, T., and Lodders, K. (2014b). Water clouds in y dwarfs and exoplanets. *The Astrophysical Journal*, 787(1):78.
- Murakami, N., Uemura, R., Baba, N., Nishikawa, J., Tamura, M., Hashimoto, N., and Abe, L. (2008). An Eight-Octant Phase-Mask Coronagraph. *PASP*, 120:1112–1118.
- Muterspaugh, M. W., Lane, B. F., Kulkarni, S. R., Konacki, M., Burke, B. F., Colavita, M. M., and Shao, M. (2010). The Phases Differential Astrometry Data Archive. III. Limits to Tertiary Companions. *AJ*, 140:1631–1645.
- Naud, M.-E., Étienne Artigau, Malo, L., Albert, L., Doyon, R., Lafrenière, D., Gagné, J., Saumon, D., Morley, C. V., Allard, F., Homeier, D., Beichman, C. A., Gelino, C. R., and Boucher, A. (2014). Discovery of a wide planetary-mass companion to the young m3 star gu psc. *The Astrophysical Journal*, 787(1):5.
- Oh, C. and Escuti, M. J. (2008). Achromatic diffraction from polarization gratings with high efficiency. *Opt. Lett.*, 33(20):2287–2289.

- Otten, G. P., Kenworthy, M. A., and Codona, J. L. (2012). Laboratory demonstration and characterization of phase-sorting interferometry. In *SPIE Astronomical Telescopes+ Instrumentation*, pages 84469F–84469F. International Society for Optics and Photonics.
- Otten, G. P., Snik, F., Kenworthy, M. A., Miskiewicz, M. N., Escuti, M. J., and Codona, J. L. (2014a). The vector apodizing phase plate coronagraph: prototyping, characterization and outlook. In *Proc. SPIE*, volume 9151, pages 91511R–91511R–10.
- Otten, G. P. P. L., Snik, F., Kenworthy, M. A., Miskiewicz, M. N., and Escuti, M. J. (2014b). Performance characterization of a broadband vector apodizing phase plate coronagraph. *Opt. Express*, 22(24):30287–30314.
- Packham, C., Escuti, M., Ginn, J., Oh, C., Quijano, I., and Boreman, G. (2010). Polarization gratings: A novel polarimetric component for astronomical instruments. *Publications of the Astronomical Society of the Pacific*, 122(898):pp. 1471–1482.
- Paczynski, B. (1986). Gravitational microlensing by the galactic halo. *ApJ*, 304:1–5.
- Pancharatnam, S. (1955). Achromatic combinations of birefringent plates. *Proceedings of the Indian Academy of Sciences - Section A*, 41(4):137–144.
- Pancharatnam, S. (1956). Generalized theory of interference, and its applications. part i. coherent pencils. In *Proceedings of the Indian Academy of Sciences, Section A*, volume 44, pages 247–262. Indian Academy of Sciences.
- Perryman, M., Hartman, J., Bakos, G. Á., and Lindegren, L. (2014). Astrometric Exoplanet Detection with Gaia. *ApJ*, 797:14.
- Quanz, S. P., Amara, A., Meyer, M. R., Kenworthy, M. A., Kasper, M., and Girard, J. H. (2013). A Young Protoplanet Candidate Embedded in the Circumstellar Disk of HD 100546. *ApJ*, 766:L1.
- Quanz, S. P., Meyer, M. R., Kenworthy, M. A., Girard, J. H. V., Kasper, M., Lagrange, A.-M., Apai, D., Boccaletti, A., Bonnefoy, M., Chauvin, G., Hinz, P. M., and Lenzen, R. (2010). First results from very large telescope naco apodizing phase plate: 4 um images of the exoplanet beta pictoris b. *The Astrophysical Journal Letters*, 722(1):L49.
- Racine, R., Walker, G. A. H., Nadeau, D., Doyon, R., and Marois, C. (1999). Speckle noise and the detection of faint companions. *Publications of the Astronomical Society of the Pacific*, 111(759):pp. 587–594.
- Reinitzer, F. (1888). Beiträge zur kenntniss des cholesterins. *Monatshefte für Chemie und verwandte Teile anderer Wissenschaften*, 9(1):421–441.
- Roddier, F. and Roddier, C. (1997). Stellar Coronagraph with Phase Mask. *PASP*, 109:815–820.
- Roelfsema, R., Bazzon, A., Schmid, H. M., Pragt, J., Gisler, D., Dominik, C., Baruffolo, A., Beuzit, J.-L., Costille, A., Dohlen, K., Downing, M., Elswijk, E., de Haan, M., Hubin, N., Kasper, M., Keller, C., Lizon, J.-L., Mouillet, D., Pavlov, A., Puget, P., Salasnich, B., Sauvage,

- J.-F., and Wildi, F. (2014). The ZIMPOL high contrast imaging polarimeter for SPHERE: system test results. In *Society of Photo-Optical Instrumentation Engineers (SPIE) Conference Series*, volume 9147 of *Society of Photo-Optical Instrumentation Engineers (SPIE) Conference Series*, page 3.
- Rosenthal, E. D., Gurwell, M. A., and Ho, P. T. P. (1996). Efficient detection of brown dwarfs using methane-band imaging. *Nature*, 384:243–244.
- Rouan, D., Riaud, P., Boccaletti, A., Clenet, Y., and Labeyrie, A. (2000). The four-quadrant phase-mask coronagraph. i. principle. *Publications of the Astronomical Society of the Pacific*, 112(777):pp. 1479–1486.
- Ruane, G. J., Huby, E., Absil, O., Mawet, D., Delacroix, C., Carlomagno, B., and Swartzlander, G. A. (2015). Lyot-plane phase masks for improved high-contrast imaging with a vortex coronagraph. *ArXiv e-prints*.
- Seager, S. and Deming, D. (2010). Exoplanet Atmospheres. *ARA&A*, 48:631–672.
- Smith, B. A. and Terrile, R. J. (1984). A circumstellar disk around beta pictoris. *Science*, 226(4681):1421–1424.
- Snellen, I. A. G., Brandl, B. R., de Kok, R. J., Brogi, M., Birkby, J., and Schwarz, H. (2014). Fast spin of the young extrasolar planet β Pictoris b. *Nature*, 509:63–65.
- Snellen, I. A. G., de Kok, R. J., de Mooij, E. J. W., and Albrecht, S. (2010). The orbital motion, absolute mass and high-altitude winds of exoplanet HD209458b. *Nature*, 465:1049–1051.
- Snik, F., Otten, G., Kenworthy, M., Miskiewicz, M., Escuti, M., Packham, C., and Codona, J. (2012). The vector-APP: a broadband apodizing phase plate that yields complementary PSFs. In *Society of Photo-Optical Instrumentation Engineers (SPIE) Conference Series*, volume 8450 of *Society of Photo-Optical Instrumentation Engineers (SPIE) Conference Series*.
- Soummer, R., Aime, C., and Falloon, P. E. (2003a). Stellar coronagraphy with prolate apodized circular apertures. *A&A*, 397(3):1161–1172.
- Soummer, R., Dohlen, K., and Aime, C. (2003b). Achromatic dual-zone phase mask stellar coronagraph. *A&A*, 403(1):369–381.
- Soummer, R., Ferrari, A., Aime, C., and Jolissaint, L. (2007). Speckle noise and dynamic range in coronagraphic images. *The Astrophysical Journal*, 669(1):642.
- Soummer, R., Pueyo, L., and Larkin, J. (2012). Detection and characterization of exoplanets and disks using projections on karhunen-loève eigenimages. *The Astrophysical Journal Letters*, 755(2):L28.
- Sparks, W. B. and Ford, H. C. (2002). Imaging Spectroscopy for Extrasolar Planet Detection. *ApJ*, 578:543–564.
- Stam, D. M. (2003). Polarization spectra of extrasolar planets. In Fridlund, M., Henning, T., and Lacoste, H., editors, *Earths: DARWIN/TPF and the Search for Extrasolar Terrestrial Planets*, volume 539 of *ESA Special Publication*, pages 615–619.

- Traub, W. A. and Oppenheimer, B. R. (2010). Direct imaging of exoplanets.
- Udry, S., Fischer, D., and Queloz, D. (2007). A Decade of Radial-Velocity Discoveries in the Exoplanet Domain. *Protostars and Planets V*, pages 685–699.
- van de Kamp, P. (1982). The planetary system of barnard’s star. *Vistas in Astronomy*, 26:141 – 157.
- Vigan, A., Gry, C., Salter, G., Mesa, D., Homeier, D., Moutou, C., and Allard, F. (2015). High-contrast imaging of Sirius A with VLT/SPHERE: looking for giant planets down to one astronomical unit. *MNRAS*, 454:129–143.
- Wahhaj, Z., Cieza, L. A., Mawet, D., Yang, B., Canovas, H., de Boer, J., Casassus, S., Ménard, F., Schreiber, M. R., Liu, M. C., Biller, B. A., Nielsen, E. L., and Hayward, T. L. (2015). Improving signal-to-noise in the direct imaging of exoplanets and circumstellar disks with MLOCI. *A&A*, 581:A24.
- Wolszczan, A. and Frail, D. A. (1992). A planetary system around the millisecond pulsar PSR1257 + 12. *Nature*, 355:145–147.
- Yang, W. and Kostinski, A. B. (2004). One-sided Achromatic Phase Apodization for Imaging of Extrasolar Planets. *ApJ*, 605:892–901.

2 | Laboratory demonstration of Phase Sorting Interferometry

Abstract

Non-common path (NCP) errors that lie downstream from the wavefront sensor (WFS) in an AO setup can not be directly corrected by the WFS and end up altering the science images by introducing quasi-static speckles. These speckles impose limits to the direct imaging of exoplanets, debris disks and other objects for which we require high contrast. Phase-sorting interferometry (PSI) uses WFS residuals as interferometric probes to the speckles. With the retrieved amplitude and phase the deformable mirror can be adjusted to remove the speckles. Previously PSI has been demonstrated to correct -to first order- the non-common path error on-sky at the MMTO in Arizona. We present an AO laboratory testbed and the techniques used to determine the properties of PSI; the influence of the time synchronisation between WFS and science camera, the achromaticity of the atmosphere and other limiting factors. Furthermore we test the performance of the PSI method when coronagraphs such as apodizing phase plates, Lyot masks and 4QPMs are introduced to the setup. Lastly this setup enables us to rapidly prototype high-contrast imaging techniques.

2.1 Introduction

Quasi-static speckles are an important limiting factor in reaching the contrast level required for the direct imaging of extrasolar planets (Hinkley et al., 2007; Martinez, P. et al., 2012). Even if the wavefront sensor (WFS) could perfectly correct the wavefront, the science camera will see a slightly different optical path which will introduce a non-common path (NCP) aberration. Imperfections in the optics and telescope structure are therefore not corrected. A quasi-static background halo appears in the focal plane together with planet-like speckles. The timescale of the NCP aberration (on the order of seconds to minutes) (Hinkley et al., 2007) isn't fast enough to statistically average into a removable background nor is it static enough to remove using techniques like angular differential imaging (ADI) (Marois et al., 2006) and local optimization of combined images (LOCI) (Lafrenière et al., 2007). One promising technique to characterise the non-common path aberrations is phase-sorting interferometry (Codona et al., 2008) (PSI). In this work we present the adaptive optics test bench at Leiden Observatory and the techniques that we will use to test the validity and limits of phase-sorting interferometry. The NCP aberration retrieval with PSI will be cross-checked against measurements taken with a modified Mach-Zehnder interferometer and the differential optical transfer function technique (dOTF). The goal is to use a coronagraph and phase-sorting interferometry as a demonstrator for high contrast imaging with large telescopes LBT, VLT and E-ELT and reach a contrast in the lab of 10^{-5} at $2\lambda/D$ using only science images.

2.2 Laboratory setup

An adaptive optics setup is used to characterize the non-common path aberrations (see Figure 2.1). Two different lasers are used in the setup; a 5 mW polarised red laser at 633 nm and a 0.5 mW polarised green laser at 543 nm. This reflects the current design of adaptive optic systems on telescopes where the wavefront sensor is fed by the visible part of the telescope beam while the instrument receives the longer (near-)infrared part. The two laser beams are combined with a beamsplitter and cleaned using a spatial filter consisting of a 20 mm microscope objective and 10 micron pinhole. This pinhole is reimaged onto a 20 mm pupil stop where the beam is distorted by a atmospheric turbulence plate. To correct the wavefront a liquid crystal spatial light modulator (SLM) is used. The SLM used was manufactured by Boulder Non-linear Systems and has a 512 by 512 pixel grid with 15 micron pitch. The previously mentioned pupil stop was reimaged as a 4 mm spot on the SLM. After the SLM the two different wavelengths were split using a dichroic into a wavefront sensor and a science camera branch.

2.2.1 Wavefront sensor branch

Within the wavefront sensor branch, the pupil is reimaged to 20 mm and passes through a 20 by 20 mm micro-lens array with a focal length of 40 mm and a pitch of 300 microns. The spots are then demagnified by a factor of 3 and imaged onto a Lumenera Lu125M 1280×1024 pixel CMOS camera with 6.7 micron sized pixels. The PSFs of the focal plane spots are therefore approximately 5 pixels across and 15 pixels apart.

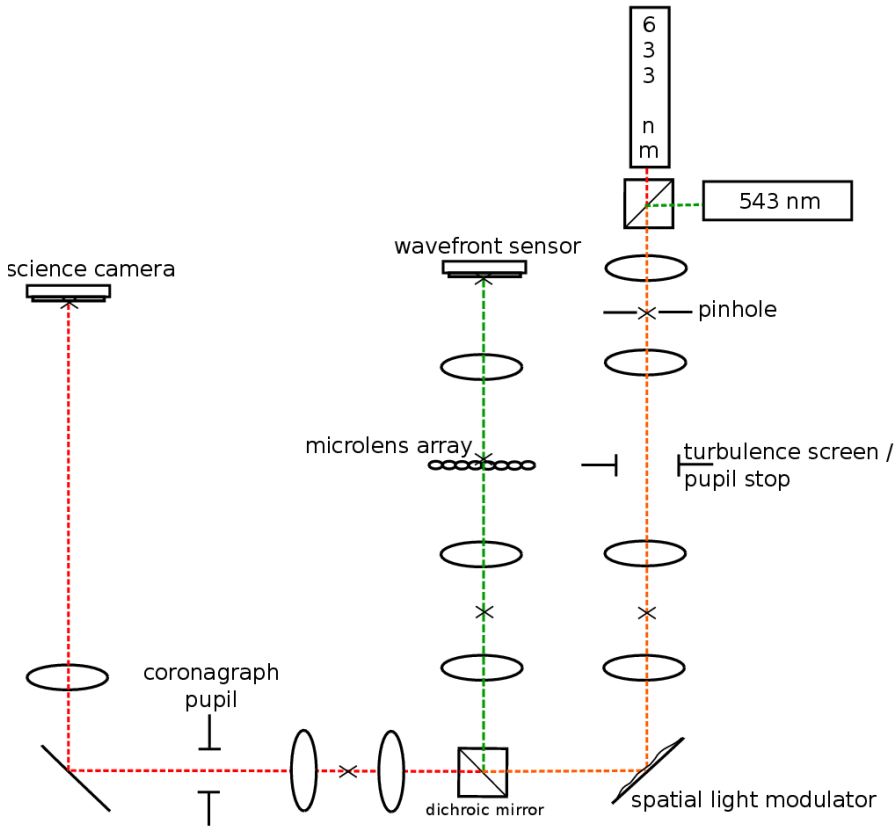


Figure 2.1: Schematic of the adaptive optics test bench. On the right, the 2 lasers, the spatial filter and turbulence screen. In the middle is the wavefront sensor branch and on the left is the science camera branch.

2.2.2 Science camera branch

The reimaged pupil in the science camera branch has a diameter of 6 mm. The size of this pupil was chosen to match the size of the two coronagraphs that are available in our lab; The Apodizing Phase Plate (Codona et al., 2006; Kenworthy et al., 2007) (APP) and the Vector-APP prototype (Snik et al., 2012). With a 1000 mm lens the 6 mm pupil is focused onto a SBIG ST2000XM CCD camera. The chip has 1600×1200 pixels and 7.4 micron sized pixels. This converts into a full width half-maximum (FWHM) at 633 nm of 129 microns or approximately 17 pixels.

To convert the setup to an interferometer an extra path is added behind the coronagraph as can be seen in Figure 2.2. The interferometer gives an independent determination of the non-common path aberrations.

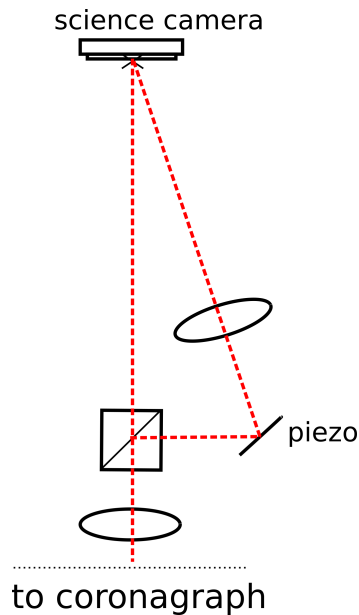


Figure 2.2: Modification of test bench that enables focal plane phase retrieval using the Modified Mach-Zehnder method described in Section 2.3.4. Part of the light is diverted using a beamsplitter and magnified. The magnification smooths the phase so it can be used as a flat phase reference to the PSF that contains NCP aberrations. The piezo element is used to step through a full wavelength of optical path difference in order to retrieve the phase and amplitude for each individual pixel in the focal plane.

2.2.3 Data retrieval

Both cameras and the SLM can be controlled using modules in IDL. A stack of 20 images was obtained to test the performance of the setup without a turbulence plate and coronagraph and is seen in Figure 2.3.

2.3 Removing non-common path aberrations

The non-common path aberrations can be represented as a complex field in the pupil plane of the coronagraph. This field is added to the pupil field generated by the optics upstream of the dichroic splitter, and it includes the aberrations introduced by all the optics from the dichroic through to the science camera focal plane. This complex field can be decomposed as a series of sinusoidal ripples with a given amplitude, phase and orientation in the pupil plane. Each wave then transforms to a speckle in the science camera focal plane.

In order to confirm that the PSI method can correctly retrieve the NCP aberrations, the following four methods will be used to retrieve the NCP as a check of mutual consistency. The focus of these consistency tests will be the performance of the phase-sorting interferometry.

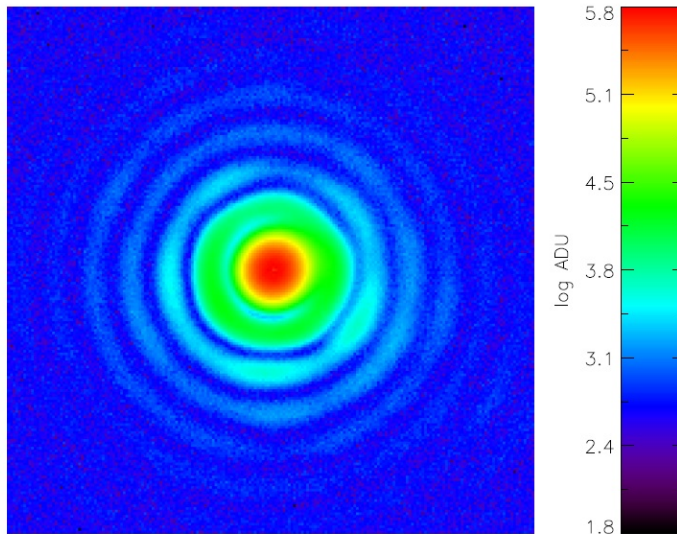


Figure 2.3: Stack of 20 exposures at the science camera of the point spread function with no turbulence plate and no coronagraph in the beam. Some astigmatism can be seen.

2.3.1 "Coffee rings method"

The key to PSI is the synchronization of the WFS telemetry and the science camera images. Short exposures typical of thermal infrared observations (100ms or less) show intensity variations along all the diffraction structures in the science images. If the WFS frames taken at the same time as the science camera frame are identified, a WFS wavefront can be reconstructed and Fourier transformed to produce a complex field at the science camera focal plane. The difference between this complex field and the intensity measurement at the focal plane is due to the NCP. These quantities can be represented by vectors in the complex plane (see Figure 2.4) as the WFS vector (the green line) and the as yet unknown NCP vector (five possibilities represented by the blue lines). The science camera only gives the intensity, which is the amplitude squared of the electric field in the science camera focal plane. Because the amplitude is known but the phase is not, we can represent it in the complex plane with a circle with its radius equal to the amplitude (indicated in red). The WFS vectorially adds to the NCP to give a point on the red circle. Multiple exposures give new realizations for the science camera amplitude and the WFS vector, providing enough diversity to solve for the correct NCP for that pixel in the science camera focal plane (see Figure 2.5). This assumption is valid for small amplitude changes which are achieved when observing at Strehl ratios higher than 0.8. Note that the overlapping circular intensity constraints look like coffee rings left behind by a coffee mug (ergo, the colloquial name of this section).

To correct the difference in exposure times between science camera and WFS the complex image of the WFS is integrated to the same exposure time as the science camera. The quasi-

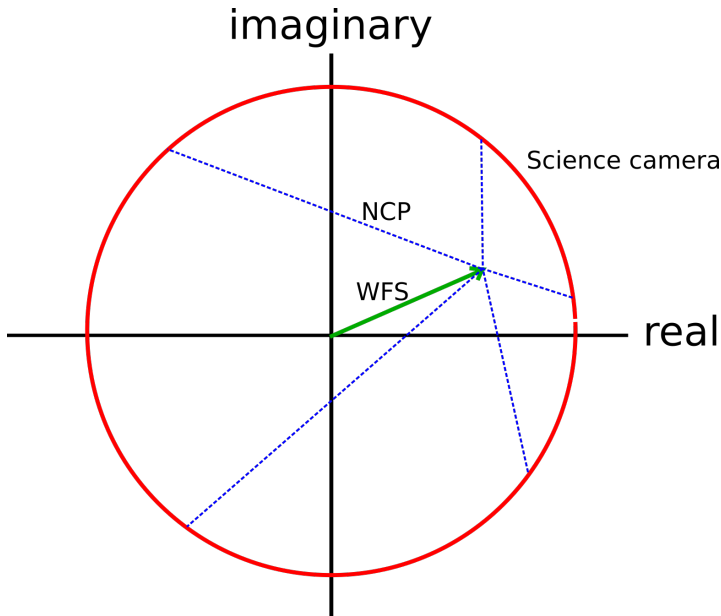


Figure 2.4: Determining NCP aberrations with the “coffee rings” method. In green is the wavefront sensor vector derived from the WFS telemetry. In red is the amplitude seen by the science camera. The difference between these two is the non-common path aberration (seen in blue as five potentially correct solutions). One image alone isn’t enough to constrain the NCP.

static speckles vary on the order of seconds to minutes. Because the atmospheric speckles move in amplitude and phase on much shorter timescales, the time integrated vector arrow will move around the complex plane and gives multiple constraints on the non-common path aberrations. For a Shack-Hartmann WFS, there is an unknown scaling factor between the reconstructed phase screen and the true incident wavefront phase. To compensate for this difference a gain factor is introduced to the WFS vector that is assumed to be fixed for each pixel and only introduces one extra degree of freedom.

2.3.2 Phase-sorting interferometry

Similarly, when the residuals of the atmospheric speckles vary, they occasionally have the correct phase to null out a quasi-static speckle. Because we know the phase of the atmospheric speckles we can plot for a single pixel in multiple frames the intensity and the phase. If this is done on timescales shorter than the timescale of the quasi-static speckle an image will slowly build up where the intensity is lowest out of phase and highest in phase. In Figure 2.6 data can be seen from the CLIO imager at the 6.5 meter MMT which demonstrates this. The phase of the quasi-static speckle can easily be seen in Figure 2.6, the amplitude on the other hand is a combination of the amplitude of the quasi-static speckle and the amplitude of the static halo. Luckily the statistics of the science images can be used to quantify the contribution of the static halo.

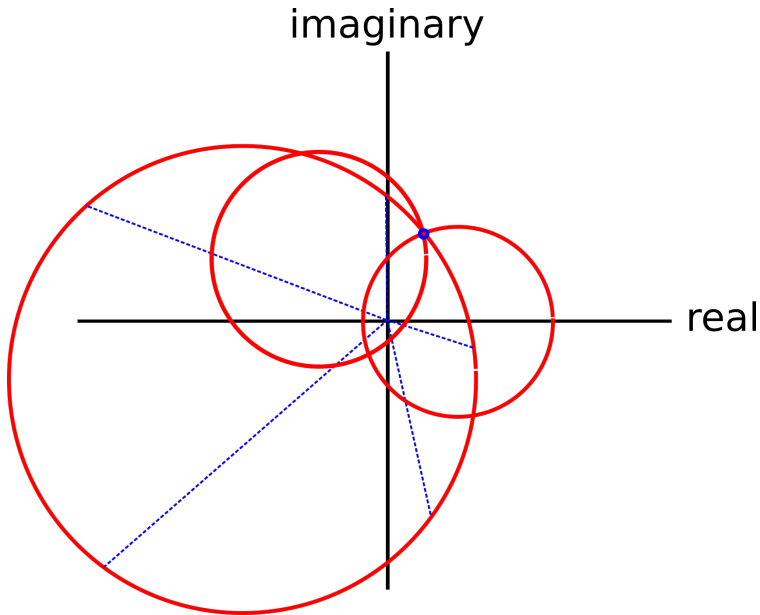


Figure 2.5: Taking the difference between the amplitude circle and the WFS vector is similar to translating the circle over the length of the WFS vector. When multiple measurements are taken in a short timespan, the NCP aberration doesn't change. The WFS vector and science camera intensity do change. Therefore although the circles will move around they will have a common point of intersection and this shows the true vector (complex number) of the NCP error.

Instead of building and fitting the image as seen in Figure 2.6 for each individual pixel it is also possible to construct a software-based phase-stepping interferometer (Codona et al., 2008). We construct four empty images as large as the science camera image. The intensities of each pixel taken at the science camera are added to one of these four images I_X according to the WFS phase that that pixel has. Each of the four images spans a phase range of $\pi/2$ centered around $\{0, \pi/2, \pi, 3 \cdot \pi/2\}$. We also have 4 images N_X that are incremented by one each time a pixel is added to one of the 4 phase maps. After gathering enough statistics we can construct a complex image ξ using Equation 2.1.

$$\xi = \left(\frac{I_0}{N_0} - \frac{I_{180}}{N_{180}} \right) + i \cdot \left(\frac{I_{90}}{N_{90}} - \frac{I_{270}}{N_{270}} \right) \quad (2.1)$$

The phase of this complex image ξ is equal to the phase of the NCP aberration. The amplitude is equal to the RMS of the WFS halo multiplied by the amplitude of the NCP aberrations.

2.3.3 Differential optical transfer function

A method developed by (Codona, 2012) describes the full complex field retrieval through the use of optical transfer functions (OTF). Two images are taken in focus at the science camera, one image with a fully illuminated pupil and one where a small pointlike piece is blocked. The

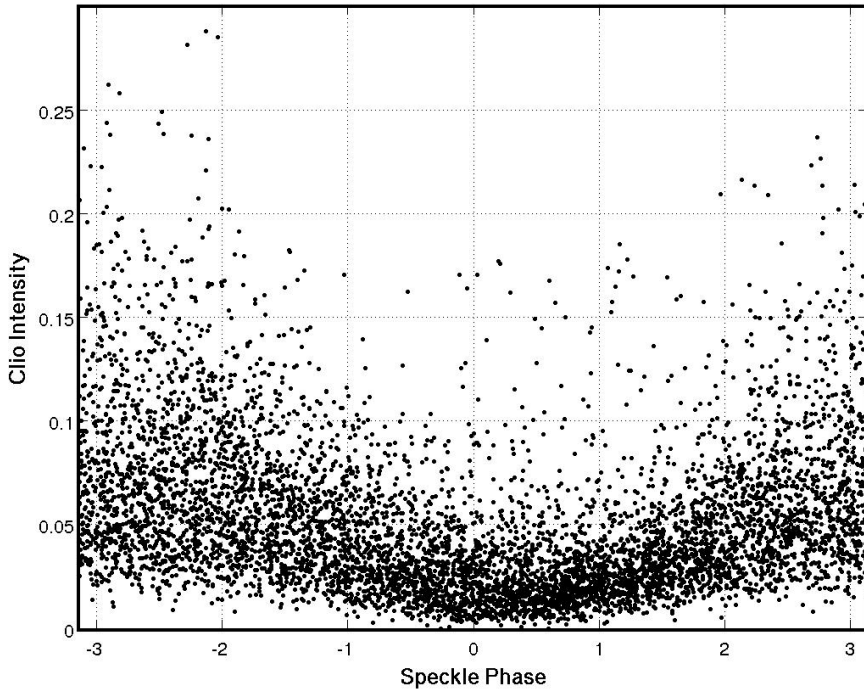


Figure 2.6: MMT data for a single pixel in the first Airy ring of a 7th magnitude star imaged with the infrared CLIO detector (Sivanandam et al., 2006). It can be seen that for this pixel the minimum of intensity is located at a WFS speckle phase of about 0.3 radians (Codona and Kenworthy, 2013).

blocking can be done by inserting a sharp object at the edge of the pupil. The OTFs of both images are made by taking the Fourier transform of their respective PSFs. The difference between the two OTFs is equal to the convolution of the difference between the two pupils (\sim delta peak) and the complex pupil field. The phase of this complex differential optical transfer function (dOTF) is equal to the phase of the pupil as seen from the science camera. To get a good signal-to-noise ratio on the dOTF and its phase a lot of light is needed which makes this method unpractical for most on-sky applications. However because this method only requires two images it is a quick method of determining aberrations in an optical setup. Especially because the supply of light can be easily tuned in a test bench.

The dOTF method was applied to the test bench at Leiden Observatory in order to retrieve the pupil phase map. In order to create a delta-like disturbance in the pupil the sharp tip of a metal file was inserted at the edge of it. The previously described method was used to calculate the dOTF which can be seen in Figure 2.7 and shows that our current system has a Strehl ratio of 83%.

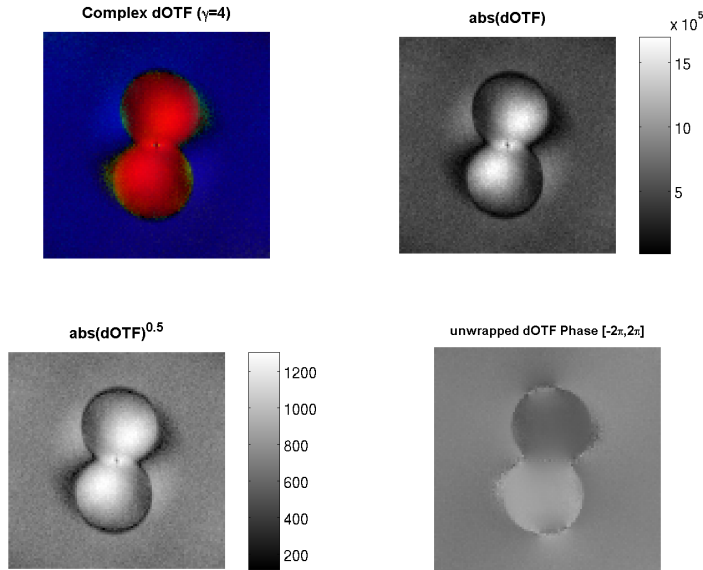


Figure 2.7: Top left shows the complex dOTF where brightness indicates amplitude and color indicates phase. In order to reduce the contrast the brightness in this frame has been scaled with a power law with $\gamma = 4$. Top right frame shows amplitude component of the dOTF. This amplitude is the amplitude map of the pupil. Lower right frame shows phase map in radians.

2.3.4 Angel-Mach-Zehnder interferometer

Another method to derive the non-common path aberration is to build an Angel-Mach-Zehnder interferometer (Codona and Angel, 2004) (see Figure 2.2). An image of the beam is taken away using a beamsplitter, magnified several times to smoothen and flatten the phase of the central portion of the beam and directly recombined with the rest of the light on the science camera. Due to the image magnification of the Airy core the phase of the reference beam will become uniform in phase, the eventual PSF on the science camera interferes with the magnified core and creates fringes. After stepping through a full wavelength of path length in the reference beam, the fringe pattern shifts after each step and can be converted back to the phase difference between the two paths.

2.3.5 Dialing out speckles

When we know the amplitude, phase and position of each of the quasi static speckles we can add sine waves with the deformable mirror (DM) that will destructively interfere with each speckle and perform speckle nulling, creating higher contrasts that will ultimately lead to 10^{-5} at separations

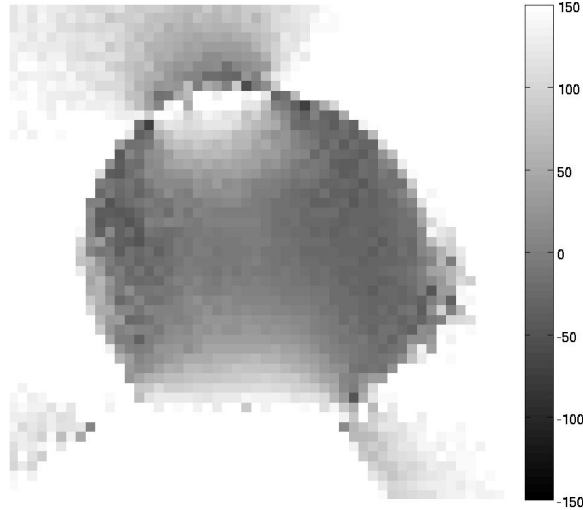


Figure 2.8: Optical path difference map in nanometers derived from the phase map shown in Figure 2.7 by dividing through 2π and multiplying by the wavelength $\lambda = 633$ nm, equivalent to a Strehl ratio of 83%. Some astigmatism can be seen in the retrieved phase map which is also seen in PSF image in Figure 2.3.

of $1 - 2\lambda/D$ (limited by servo-lag and shot noise ¹).

2.4 Conclusions and Future Work

We have described the layout of our optical testbed in Leiden Observatory, and have shown the first results of characterizing our optical performance with the application of dOTF in our system, which gives a Strehl of 83%. We are aiming for a Strehl of greater than 90%, representative of Strehls expected on the next generation of 35m class telescopes with instruments such as METIS, MICADO and EPICS.

Our close range goals include getting PSI working in the Leiden Optical Testbed, then introducing an APP coronagraph designed to work in the visible band at 820nm. The goal is to get 10^{-5} contrast at the smallest inner working angles, consistent with the expected performance of wavefront sensors on E-ELTs (Guyon et al., 2012). The addition of the Angel-Mach-Zehnder provides a consistency check between the PSI and the dOTF methods, where the PSI and AMZ provide a complete complex pupil field solution, and the dOTF can provide partial complex field solutions (limited by the overlap region introduced by the perturbation).

One of the long-term goals of the Leiden Optical Testbed is to demonstrate PSI with a coronagraph and to produce a set of software packages to implement PSI on current AO-enabled

¹<http://www.naoj.org/staff/guyon/04research.web/14hzplanetsELTs.web/content.html>

telescopes. The software library is expected to be coded in Python. PSI can provide reconstructed science PSFs for each science camera frame, but ultimately it can act as an additional anti-halo server to provide real time focal plane wavefront sensing at current telescopes with no additional hardware cost.

Acknowledgments

The authors would like to thank Remko Stuik for his help and support. This work is part of the research programme Instrumentation for the E-ELT, which is partly financed by the Netherlands Organisation for Scientific Research (NWO).

References

- Codona, J. L. (2012). Theory and application of differential OTF (dOTF) wavefront sensing. In *Society of Photo-Optical Instrumentation Engineers (SPIE) Conference Series*, volume 8447 of *Society of Photo-Optical Instrumentation Engineers (SPIE) Conference Series*.
- Codona, J. L. and Angel, R. (2004). Imaging extrasolar planets by stellar halo suppression in separately corrected color bands. *The Astrophysical Journal Letters*, 604(2):L117.
- Codona, J. L. and Kenworthy, M. (2013). Focal Plane Wavefront Sensing Using Residual Adaptive Optics Speckles. *ApJ*, 767:100.
- Codona, J. L., Kenworthy, M. A., Hinz, P. M., Angel, J. R. P., and Woolf, N. J. (2006). A high-contrast coronagraph for the MMT using phase apodization: design and observations at 5 microns and 2 λ/D radius. In *Society of Photo-Optical Instrumentation Engineers (SPIE) Conference Series*, volume 6269 of *Society of Photo-Optical Instrumentation Engineers (SPIE) Conference Series*.
- Codona, J. L., Kenworthy, M. A., and Lloyd-Hart, M. (2008). A novel WFS technique for high-contrast imaging: Phase Sorting Interferometry (PSI). In *Society of Photo-Optical Instrumentation Engineers (SPIE) Conference Series*, volume 7015 of *Society of Photo-Optical Instrumentation Engineers (SPIE) Conference Series*.
- Guyon, O., Martinache, F., Cady, E. J., Balasubramanian, K., Belikov, R., Clergeon, C. S., and Mateen, M. (2012). How ELTs will acquire the first spectra of rocky habitable planets. In *Society of Photo-Optical Instrumentation Engineers (SPIE) Conference Series*, volume 8447 of *Society of Photo-Optical Instrumentation Engineers (SPIE) Conference Series*.
- Hinkley, S., Oppenheimer, B. R., Soummer, R., Sivaramakrishnan, A., Lewis C. Roberts, J., Kuhn, J., Makidon, R. B., Perrin, M. D., Lloyd, J. P., Kratter, K., and Brenner, D. (2007). Temporal evolution of coronagraphic dynamic range and constraints on companions to vega. *The Astrophysical Journal*, 654(1):633.
- Kenworthy, M. A., Codona, J. L., Hinz, P. M., Angel, J. R. P., Heinze, A., and Sivanandam, S. (2007). First On-Sky High-Contrast Imaging with an Apodizing Phase Plate. *ApJ*, 660:762–769.
- Lafrenière, D., Marois, C., Doyon, R., Nadeau, D., and Artigau, É. (2007). A New Algorithm for Point-Spread Function Subtraction in High-Contrast Imaging: A Demonstration with Angular Differential Imaging. *ApJ*, 660:770–780.
- Marois, C., Lafrenière, D., Doyon, R., Macintosh, B., and Nadeau, D. (2006). Angular Differential Imaging: A Powerful High-Contrast Imaging Technique. *ApJ*, 641:556–564.

- Martinez, P., Loose, C., Aller Carpentier, E., and Kasper, M. (2012). Speckle temporal stability in xao coronagraphic images. *A&A*, 541:A136.
- Sivanandam, S., Hinz, P. M., Heinze, A. N., Freed, M., and Breuninger, A. H. (2006). Clio: a 3-5 micron AO planet-finding camera. In *Society of Photo-Optical Instrumentation Engineers (SPIE) Conference Series*, volume 6269 of *Society of Photo-Optical Instrumentation Engineers (SPIE) Conference Series*.
- Snik, F., Otten, G., Kenworthy, M., Miskiewicz, M., Escuti, M., Packham, C., and Codona, J. (2012). The Vector-APP: a Broadband Apodizing Phase Plate that yields Complementary PSFs. *ArXiv e-prints*.

3 | Performance characterization of a broadband vector Apodizing Phase Plate coronagraph

Abstract

One of the main challenges for the direct imaging of planets around nearby stars is the suppression of the diffracted halo from the primary star. Coronagraphs are angular filters that suppress this diffracted halo. The Apodizing Phase Plate coronagraph modifies the pupil-plane phase with an anti-symmetric pattern to suppress diffraction over a 180 degree region from 2 to 7 λ/D and achieves a mean raw contrast of 10^{-4} in this area, independent of the tip-tilt stability of the system. Current APP coronagraphs implemented using classical phase techniques are limited in bandwidth and suppression region geometry (i.e. only on one side of the star). In this chapter, we introduce the vector-APP (vAPP) whose phase pattern is implemented through the vector phase imposed by the orientation of patterned liquid crystals. Beam-splitting according to circular polarization states produces two, complementary PSFs with dark holes on either side. We have developed a prototype vAPP that consists of a stack of three twisting liquid crystal layers to yield a bandwidth of 500 to 900 nm. We characterize the properties of this device using reconstructions of the pupil-plane pattern, and of the ensuing PSF structures. By imaging the pupil between crossed and parallel polarizers we reconstruct the fast axis pattern, transmission, and retardance of the vAPP, and use this as input for a PSF model. This model includes aberrations of the laboratory set-up, and matches the measured PSF, which shows a raw contrast of $10^{-3.8}$ between 2 and 7 λ/D in a 135 degree wedge. The vAPP coronagraph is relatively easy to manufacture and can be implemented together with a broadband quarter-wave plate and Wollaston prism in a pupil wheel in high-contrast imaging instruments. The liquid crystal patterning technique permits the application of extreme phase patterns with deeper contrasts inside the dark holes, and the multilayer liquid crystal achromatization technique enables unprecedented spectral bandwidths for phase-manipulation coronagraphy.

3.1 Direct imaging of exoplanets

The detection of planets around stars in our galaxy is one of the most exciting recent discoveries in astronomy. The first planets were not detected directly but through their effect on their parent star. The very first discovery of an exoplanet by Wolszczan and Frail (1992) involved a planet around a pulsar, and the first exoplanet detected around a solar type star was through the radial velocity (RV) reflex motion of the parent star 51 Peg (Mayor and Queloz, 1995). These massive, short-period planets implied that some of them would transit their parent star, and one such planet was found to transit its parent star, HD209458b (Charbonneau et al., 2000). After the discovery of this so-called Hot-Jupiter many more transiting planets have been found, with as most prolific contributor being the transit mission Kepler (Borucki et al., 2009) that has detected over 2300 planetary candidates so far (Batalha et al., 2013). For both RV and transit searches the observing efficiency decreases sharply with increasing orbital period. Direct imaging of extrasolar planets is required to study solar-system-like exoplanets. In addition to direct detections, high-contrast imaging methods allow for the characterization of exoplanetary atmospheres through photometry (variability implying clouds) and spectroscopy, and are not restricted to the transit window of the planet. The most prominent success story for direct imaging is the 4-planet system around HR8799 (Marois et al., 2008; Marois et al., 2010; Oppenheimer et al., 2013), for which the chemical composition of HR8799 c implies a core accretion formation mechanism (Konopacky et al., 2013).

Direct imaging is highly challenging because of the large contrast between the star and the planet (typically 10^{-9} for visible light reflected from the Sun by Jupiter to $\sim 10^{-4}$ for direct thermal emission from young gas giant planets in formation), the small angular separation between the star and the planet (typically 1 arcsecond or less), and the effects of diffraction of the stellar light due to the finite size of the telescope. The diffraction halo of the primary star (the point spread function - PSF) at the location of the planet can be several decades brighter than the planet itself. Contrast from the ground is furthermore limited by a halo of speckles created by imperfect Adaptive Optics (AO) correction of atmospheric turbulence and optical aberrations that are not corrected by the AO system as they are not sensed by the wavefront sensor. Removing the diffraction halo by telescope modeling or observing a nearby reference star is not effective because the optics of the telescope changes as a function of time, and hence the resulting PSF is variable at the pertinent levels of contrast. The speckles that result from incorrect PSF subtraction are similar in shape to the planets that are the target of our search. Several differential techniques for improving PSF subtraction have been developed and are used to obtain roughly an additional order of magnitude in suppression: Angular Differential Imaging (Marois et al., 2006; Lafrenière et al., 2007; Amara and Quanz, 2012; Meshkat et al., 2014), Spectral Differential Imaging (Vigan et al., 2010), Spectral Deconvolution (Sparks and Ford, 2002) and Polarimetric Differential Imaging for scattered light sources (see Avenhaus et al. (2014) for a recent example).

The intensity of the speckles is related to the telescope wavefront error and the intensity of the diffraction structure at the location of the planet (Bloemhof, 2003). By suppressing the diffraction structure from the central star the effect of the intensity of the corresponding speckles is also reduced. Coronagraphs are angular filters designed to reject light from the direction of the star while transmitting as much light as possible from the direction of the planet. Originally developed for the study of the solar corona (Lyot, 1939), several different designs have been considered for use in direct imaging of exoplanets (for recent comprehensive reviews see Guyon (2005); Mawet et al.

(2012)). New-generation coronagraphs such as the Apodizing Phase Plate and Annular Groove Phase Mask coronagraph have been in use at near-infrared wavelengths in ground-based telescopes (Quanz et al., 2010; Mawet et al., 2013). Out of the wide family of coronagraphic designs, those which use focal-plane amplitude and/or phase masks to suppress the on-axis starlight are sensitive to both the finite angular size of the star and tip-tilt vibrations within the telescope structure. Coronagraphs which modify the complex amplitude of the pupil plane only are not susceptible to these problems. Modifications of the pupil through amplitude apodization (Kasdin et al., 2004; Carlotti, 2013) and phase apodization (Codona and Angel, 2004; Yang and Kostinski, 2003, 2004; Guyon et al., 2005) are possible and can provide a combination of large suppression of starlight and high throughput of the light of a planet at small angular separations from the central star. In Yang and Kostinski (2004) the theory of pupil apodization in one dimension was developed and extended for square apertures. Pupil apodization over circular apertures was further developed in Kostinski and Yang (2005) with iterative Gerchberg-Saxton algorithms, clearing out regions in the focal plane at typically $5 \lambda/D$ and larger. Codona and Angel (2004) and Kenworthy et al. (2007) developed and realized phase coronagraphs at smaller inner working angles. The largest advantages of pupil-plane over focal-plane coronagraphs are the small inner working angle, easy accommodation of complex pupil shapes (segments/spiders) and its insensitivity to tip-tilt variations. One disadvantage of a stand-alone pupil-plane coronagraph is that all the stellar light still reaches the detector, which leads to dynamic range issues.

The original Apodizing Phase Plate (APP) (Kenworthy et al., 2007; Codona et al., 2006) introduces a phase variation across the telescope pupil by varying the thickness of a plate as a function of position in the pupil, and has been used successfully to directly image exoplanets (e.g. Quanz et al. (2010)). For the APP these thickness variations are typically diamond-turned into a substrate with a high refractive index. The two limiting factors for this APP design are (1) it is inherently chromatic and (2) it only delivers 180 degrees field of suppression. However, the implementation of phase control through the *vector phase* solves these two problems, and enables an improved version of the APP coronagraph, which is the subject of this paper. The much improved performance for the vector Apodizing Phase Plate (vAPP) is achieved with a combination of liquid crystal techniques: The phase pattern can be written in a photo-alignment material (Yaroshchuk and Reznikov, 2012) with a direct-write scanning system (Miskiewicz and Escuti, 2014). Broad-band performance is achieved by applying multiple layers of self-aligning liquid crystals (multi-twist retarders; MTR), that together yield an achromatized retardance (Komanduri et al., 2013), which extends the efficiency of the inherently achromatic vector-phase application over a large wavelength range.

In this paper we present the characterization of the first vAPP prototype, which creates dark holes in two complementary PSFs over a broad wavelength range (500–900 nm). In Section 3.2 we describe the principle behind the vAPP. In Section 3.3 we directly characterize the manufactured optic through narrowband imaging at multiple wavelengths. Using these measurements we then model the PSF in the focal plane in Section 3.4 and compare it with measurements of the PSF in the laboratory. We present our conclusions and provide outlooks for future improvements in Section 3.5.

3.2 vAPP operating principle & manufacturing

3.2.1 Classical & vector phase

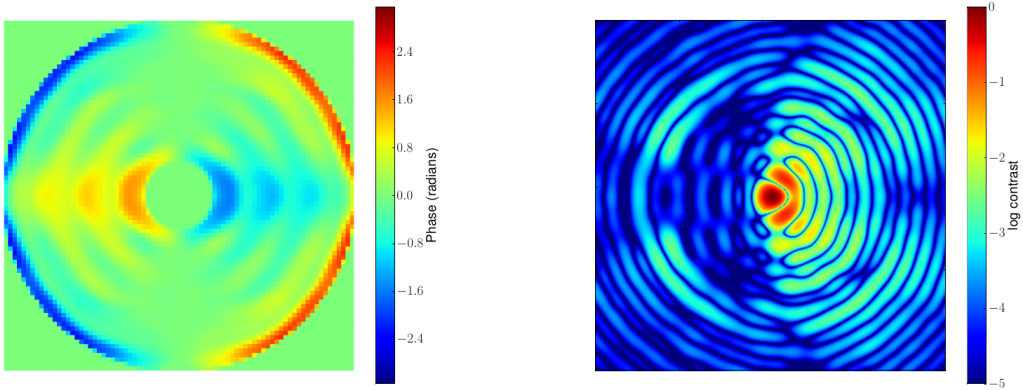


Figure 3.1: Left panel: The anti-symmetric phase pattern of the Apodizing Phase Plate coronagraph that is used in the vAPP prototype. Right panel: Corresponding theoretical log-scaled PSF, normalized to its peak flux.

The APP coronagraph uses optical path differences to induce a phase change as a function of position across the pupil. One such phase pattern is shown in Fig. 3.1. In this case, a phase pattern $\Delta\phi$ is introduced by varying the thickness Δx of a high refractive index material. The expression relating $\Delta\phi$ to Δx is given in Eq. (3.1) where λ is the wavelength, n_{plate} is the refractive index of the coronagraph and $n_{\text{air}} \approx 1$.

$$\Delta\phi = \frac{2\pi}{\lambda} (n_{\text{plate}}(\lambda) - n_{\text{air}}(\lambda)) \Delta x \quad (3.1)$$

This phase is clearly chromatic with a $1/\lambda$ term and a dispersion term for the glass.

The vAPP coronagraph instead makes use of the geometric phase, also sometimes called the vector phase, which is a manifestation of the Pancharatnam-Berry phase (Pancharatnam, 1956; Berry, 1987). This approach was previously used for focal-plane phase masks like the 4QPM (with quartz/MgF₂ achromatic waveplates) by Mawet et al. (2006), the 8OPM (with photonic crystals) by Murakami et al. (2010), the Vector Vortex Coronagraph by Mawet et al. (2009), and introduced for the vAPP by Snik et al. (2012). The vector phase arises when a circularly polarized beam passes through a half-wave retarder and is converted into circularly polarized light of the opposite handedness. While the circular polarization handedness flip is independent from the half-wave retarder's axis orientation, the absolute phase of the emergent beam is directly determined by it. In this way, even a perfectly flat optic can induce a phase pattern. Moreover, as the phase is only determined by the fast axis orientation, it is inherently achromatic.

The electric components of a beam of polarized light can be described by a Jones vector $\mathbf{E} = \begin{pmatrix} E_x \\ E_y \end{pmatrix}$. Using the Jones formalism to express the effect of a half-wave plate (HWP) with a

fast axis oriented at θ_{HWP} on circular polarization states we can write

$$\mathbf{E}_{\text{out}} = \mathbf{J}_{\text{rot}}(-\theta_{\text{HWP}}) \mathbf{J}_{\text{HWP}} \mathbf{J}_{\text{rot}}(\theta_{\text{HWP}}) \mathbf{E}_{\text{in,circular},\pm} \quad (3.2)$$

where the rotation matrix is

$$\mathbf{J}_{\text{rot}}(\theta) = \begin{pmatrix} \cos \theta & \sin \theta \\ -\sin \theta & \cos \theta \end{pmatrix}, \quad (3.3)$$

the Jones matrix of the HWP

$$\mathbf{J}_{\text{HWP}} = \begin{pmatrix} \exp(-i\pi/2) & 0 \\ 0 & \exp(i\pi/2) \end{pmatrix}. \quad (3.4)$$

Adopting circularly polarized input states

$$\mathbf{E}_{\text{in,circular},\pm} = \frac{1}{\sqrt{2}} \begin{pmatrix} 1 \\ \pm i \end{pmatrix} \quad (3.5)$$

gives us

$$\mathbf{E}_{\text{out}} = -\frac{i}{\sqrt{2}} \begin{pmatrix} 1 \\ \mp i \end{pmatrix} \exp(\mp i 2 \theta_{\text{HWP}}), \quad (3.6)$$

which shows that the input circular polarization has flipped its sign and received a phase delay equal to

$$\Delta\phi = \mp 2 \theta_{\text{HWP}}. \quad (3.7)$$

It can be seen that the expression of the vector phase has a positive or negative phase depending on the handedness of the circularly polarized light, and is independent of wavelength. If the retarder is not perfectly half-wave, the handedness-flip is incomplete and leakage terms emerge (Mawet et al., 2009).

Unpolarized light can be decomposed into equal components of the orthogonal circular polarization states, and therefore half of the light accrues a positive phase while the other half receives a negative phase. Since the APP phase pattern is anti-symmetric, the negative phase corresponding to opposite circular polarization yields a point-reflected PSF compared to the PSF of the positive phase. This can be easily understood by looking at the properties of the Fourier transform. The sign flip of the phase pattern is equivalent to the complex conjugation of the electric field pattern in the pupil. The Fourier transform of the two pupil functions yields electric field structures in the focal plane that are point-reflected ($[x, y] \rightarrow [-x, -y]$) complex conjugates. The PSFs (square of the modulus of the electric field pattern in the focal plane) for the two circular polarization states therefore exhibit point-reflection symmetry. In the case of an anti-symmetric pupil phase pattern, the two PSFs are mirror-symmetric. Therefore, if the light is split based on the handedness of the emerging beam we obtain two distinct images of the same source but with opposite sides cleared out. Figure 3.2 shows a sketch of the vector APP coronagraph. In this case, the beam-splitting according to circular polarization states is achieved by introducing a quarter-wave plate (QWP) and Wollaston prism behind the vAPP. The QWP converts the circular polarizations into linear polarizations that are split by the Wollaston prism.

We use liquid crystal techniques to create the desired pattern retarder, which has a retardance close to half-wave over a large wavelength range. While a single layer of in-plane, uniaxial nematic

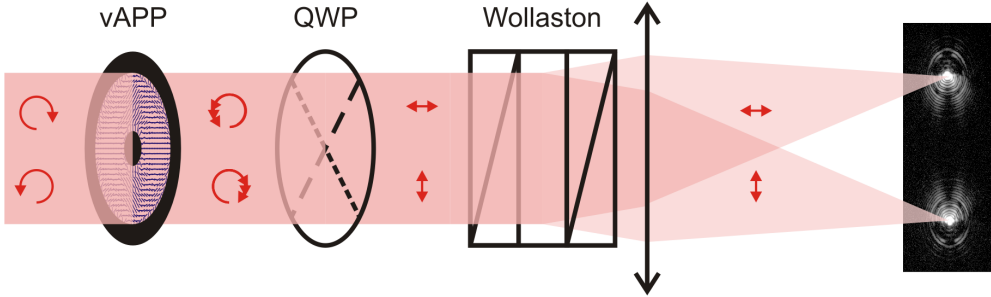


Figure 3.2: The operational principle of the vector Apodizing Phase Plate coronagraph. The vAPP is a patterned half-wave plate that converts input circular polarizations into their opposite handedness with an extra phase delay added. One circular polarization accrues a positive phase pattern while the opposite polarization receives a negative phase. A QWP plate at 45 degrees converts these circular into linear polarization states. The Wollaston prism then splits the beam based on the linear polarizations, while a camera lens images complementary PSFs on the camera. The log-scaled grey-scale image on the right-hand side of the image shows an example of these PSFs as measured in the lab.

liquid crystal formed into the vAPP pattern produces output waves with phase following Eq. (3.7), it nevertheless has a very chromatic retardance, i.e., proportional to $1/\lambda$. This means that only a narrow band of wavelengths will experience a half-wave retardance, even approximately. At other wavelengths, the large deviations from half-wave retardance create leakage of the original PSF. An achromatized half-wave retarder can be created by coating multiple layers of chiral liquid crystals, each with its own thickness and helical twist (Komanduri et al., 2013). This static thin film with multiple sublayers is called a Multi-Twist Retarder (MTR). In addition to its broadband performance, the other key advantage of this birefringent film is that the local fast axis of each layer spontaneously self-aligns to the fast axis of the prior layer, implying that only one patterning step for a single photoalignment material is needed. Furthermore, in this work, we direct-write the vAPP fast axis orientation pattern using a scanned laser spot, a direct-write lithography technique (Miskiewicz and Escuti, 2014), which has the advantageous feature of being able to record *any* phase pattern.

3.2.2 Fabrication of the vAPP prototype

The vAPP prototype characterized in this paper is made on a substrate (Schott D263 glass) with a diameter of 25.4 mm and a thickness of 1.1 mm. The first layer applied to the glass is a linearly photo-polymerized polymer (LPP, Yaroshchuk and Reznikov (2012)), which defines the local optical axis orientation for subsequent layers and therefore the fast axis of the whole device. A linearly polarized UV laser (325 nm) encodes the APP phase as a position-dependent fast axis orientation pattern into the LPP layer with a spatial resolution of 25 microns. The angle of polarization varies with a rotating half-wave plate (Miskiewicz and Escuti, 2014) in order to locally enforce the polymerization direction to follow the required phase pattern (see Fig. 3.1). Note that a factor of two in angle is applied to the phase pattern, cf. Eq. 3.7. After the curing of the LPP, successive layers of liquid crystal form the achromatized, patterned half-wave retarder. The multilayer design compensates for the chromaticity of individual layers by a combination of varying thick-

nesses, twists and birefringences. For our prototype, we use three total layers (i.e., a 3TR design, Komanduri et al. (2013)) of liquid crystal polymers and cure each layer with a UV LED source. The properties of the individual MTR layers are given by $[\theta_1 = 70^\circ, d_1 = 1.45 \mu\text{m}, \theta_2 = 0^\circ, d_2 = 3 \mu\text{m}, \theta_3 = -70^\circ, d_3 = 1.45 \mu\text{m}]$ where θ_i denotes the local fast axis orientation and d_i the thickness of each layer. In more detail; the process involves spin-coating successive layers of a mixture containing polymerizable liquid crystal monomers and potentially chiral dopants within a solvent, and results in a solid cross-linked polymer film. Further details of the design method and fabrication principles are found in Komanduri et al. (2013). An end-cap glass plate with a broadband anti-reflection coating is added.

The multilayer liquid crystal structure creates a retardance that is designed to be approximately half-wave between 500 and 900 nanometers. To minimize the leakage of the regular PSF to a level comparable to the theoretical contrast of the coronagraph we specify a maximum retardance offset. By comparing the contrast in a 135 degree wedge from 2 to 7 λ/D for the normal PSF and the theoretical APP PSF for the adopted phase pattern we see that we can tolerate a leakage of 7.3%. The intensity of the leakage term as a function of the retardance offset $\Delta\delta$ is approximately $\sin^2(\Delta\delta/2)$ (Snik et al., 2012), and from this we derive that the maximum retardance offset that can be tolerated is $\Delta\delta = 0.55$ radians. The MTR design for the vAPP prototype is selected to fall within this requirement (see Fig. 3.8). A coronagraph design with improved contrast will have a stronger requirement on the retardance offset. For instance, a design with a 10 times better theoretical contrast requires a maximum retardance offset of 0.17 radians, and/or the application of leakage filtering with circular polarization filters on either side of the vAPP (Mawet et al., 2009; Snik et al., 2014).

While the MTR design used for the vAPP prototype is optimized to create an approximately half-wave retardance across a broad wavelength range, the fast axis zero point is left unconstrained. The effect of the zero point is a global rotation of the fast axis and therefore a harmless global piston offset of the phase of the emergent beam as a function of wavelength. The dependance of the zero point on the wavelength is derived from the theoretical 3-layer MTR Mueller matrices and is shown in Fig. 3.3. This feature creates a paradoxically colorful appearance when viewing the broadband vAPP prototype in between polarizers (see Fig. 3.4).

An amplitude mask is made using a substrate with the same specification as is used for the patterned liquid crystal. A layer of opaque (black) resist, with a transmissive annulus with an inner diameter of 1.1 mm and outer diameter of 5.5 mm is applied to this substrate. The transmission of this mask is measured to be lower than $10^{-5.5}$. This amplitude mask is manually aligned to the other substrate under a microscope and bonded with optical glue. The completed optic can be seen in Fig. 3.4.

3.3 Measuring the properties of the vAPP

Detailed characterization of the broadband optical behavior (i.e., transmission, retardance, and fast axis) of the vAPP is necessary not only to verify if the plate is functioning according to specifications, but also to identify solutions to perfect the current design and reach the performance needed to accommodate more complex coronagraphs. The vAPP prototype is inserted in between rotatable polarizers, and a lens re-images the pupil plane onto a detector, see Fig. 3.5. For details about this setup see Appendix 3.A.2. By recording images for different (crossed, parallel) config-

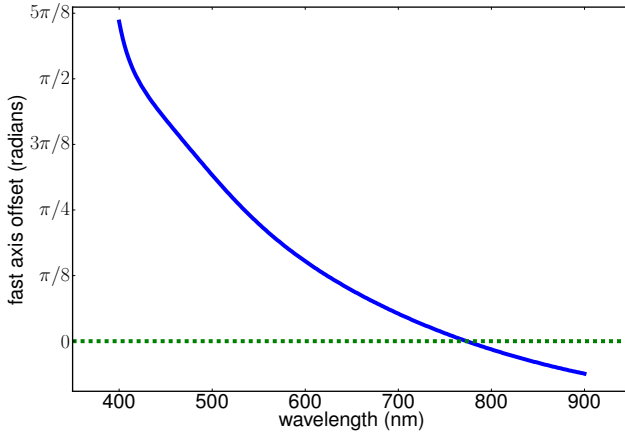


Figure 3.3: Theoretical fast axis offset as a function of wavelength for the vAPP prototype. This apparent fast axis rotation is derived from the theoretical MTR Mueller matrix, and is used to offset the polarizers in the measurements of the phase pattern.

urations of the polarizers, and application of a Mueller matrix model (see Appendix 3.A.1), the transmission, retardance and fast axis patterns are derived for a range of narrow-band filters from 500 to 800 nm.

The measured phase pattern at 750 nm, and the difference between the reconstructed phase map of the pupil and the input phase map of Fig. 3.1 can be seen in Fig. 3.6. The reconstructed phase map (i.e. two times the retarder axis orientation pattern) is remarkably similar to the input pattern although small, local deviations can be discerned. Especially at the 270 degree and 150 degree clock-wise positions two peculiar phase deviations can be seen. These are due to dust specks that landed on the substrate during manufacturing and locally created a thicker layer of polymers. The pile-up of polymers causes an offset in retardance and phase.

The non-zero residuals in the phase shown in Fig. 3.6 are partially caused by measurement errors. The fuzzy edges that trace out some of the phase pattern are evidence of this. The phase folds back at the extremes of the arccosine function in Eq. (3.20), where the derivative of the arccosine is large and a small change in the ratio can cause a big difference in phase. Measurement noise is therefore very pronounced at these locations. Furthermore, there is a small phase jump at this location. Simulations of the end-to-end measurement trace this phase jump back to a 1% residual background value in the original images. The use of a (well-calibrated) complete Mueller matrix imaging polarimeter would reduce such issues, although some degeneracies would remain. In addition to these spurious effects, the phase pattern appears to have a small ($\ll 0.1$ radians) real deviation from the specified pattern (see Fig. 3.17 in the Appendix). This may be caused by instrumental polarization issues in the direct-write system.

The retardance and transmission maps are shown in Fig. 3.7 together with the corresponding histograms. A hint of the phase pattern can be seen in the retardance map, because it is reconstructed simultaneously with the phase map. Simulations show that this is caused by a shift of a few pixels between the four recorded images that are used to compute this map. This shift is

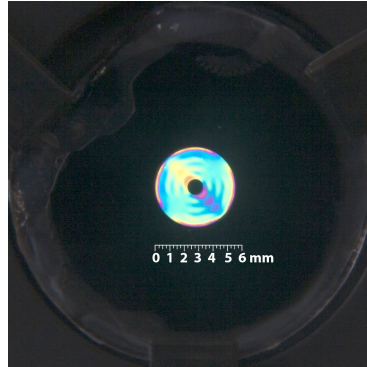


Figure 3.4: The vAPP prototype seen between crossed polarizers. The colors are due to the global rotational offset of the fast axis as a function of wavelength.

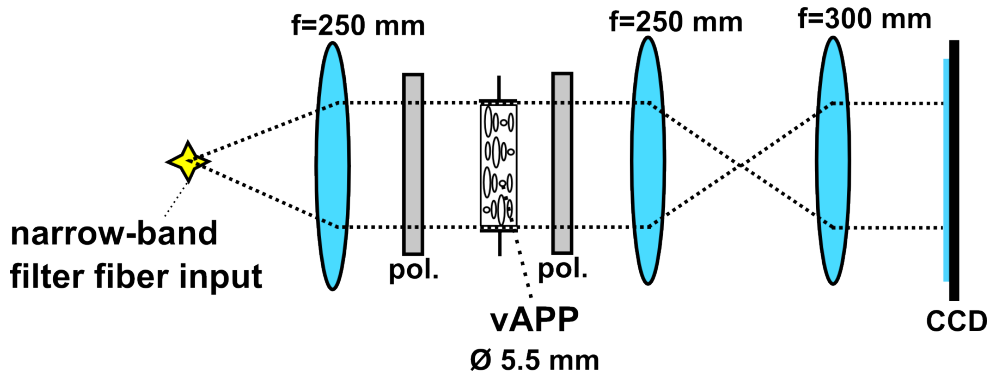


Figure 3.5: Layout of the pupil measurement setup of the vAPP. The vAPP is placed between linear polarizers and its surface is re-imaged onto a CCD. The intensity images of the vAPP taken at different polarizer angles are used to reconstruct the fast axis, retardance and transmission of the optic as described in Appendix 3.A.1. The setup is described in more detail in Appendix 3.A.2.

caused by the different orientations of the polarizers that are required to derive the retardance and phase maps (see Appendix 3.A.1). The polarizer is slightly tilted on purpose to remove reflection ghosts that would otherwise bias the characterization. Furthermore, the average of the measured retardance map is offset from the theoretically expected value for the 3TR design. Simulations using the Mueller matrix model in Appendix 3.A.1 show that this is caused by the propagation of noise in the recorded images.

The transmission map shows a gradient across the pupil but does not show any print-through of the phase pattern. A global gradient of light going from a flux ratio of 1.25 to 0.75 across the pupil is seen in the topleft panel of Fig. 3.7. To investigate the cause of this gradient we divide the APP pupil image by a flat field image created by removing the vAPP optic. Inspection of this image shows no gradients in transmission across the APP optic to within 1%. We conclude that the gradient seen in the pupil transmission image is caused by an asymmetric illumination of the pupil.

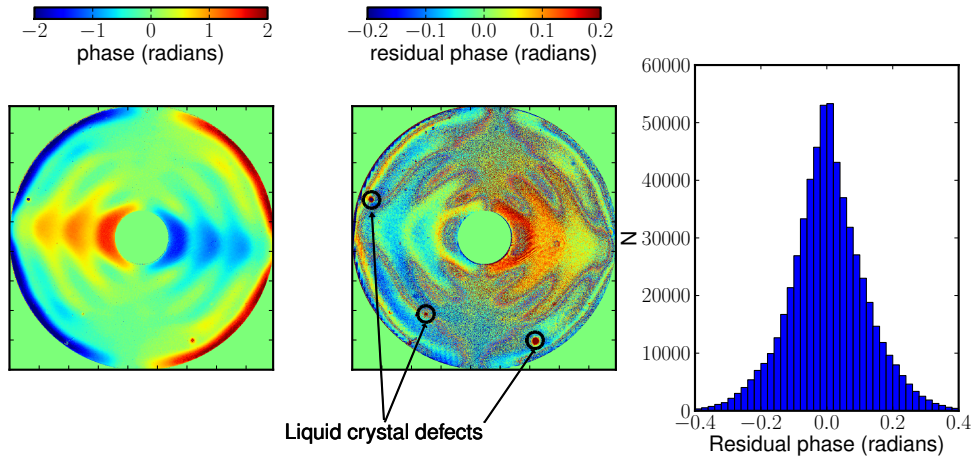


Figure 3.6: Left panel: Reconstructed phase (i.e., two times the retarder axis orientation) map of vAPP. Middle panel: Difference between reconstructed phase of vAPP and target phase pattern used for manufacturing. Small irregularities can be seen in the map. Some regions of the plate have a peculiar phase pattern due to dust specks present on the substrate during manufacturing. The dust specks locally create a thicker layer of liquid crystals. Right panel: Histogram of phase residuals.

Amplitude variations can be seen at several locations on the pupil image. The long black fringes are scratches in the cover window of the CCD and the circular fringes are from dust specks on the lenses located close to the vAPP. These effects can be corrected by improving the optical setup. Other amplitude effects are in the coronagraph itself and have to be solved in the manufacturing step. For instance, the small circles on this image are air bubbles and dust specks in the glue that binds the amplitude mask to the coronagraph.

Finally in the lower left of the coronagraph image a small indentation is seen where the transmission is substantially lower. This seems to be a patch of resist that is sticking out of the amplitude mask. In the phase and retardance reconstruction the static amplitude variations are removed automatically. In the PSF reconstruction presented in Sect. 3.4 it is shown that these amplitude variations do not have a significant impact on the performance of the coronagraph.

Figure 3.8 presents the measured offsets from half-wave retardance as a function of wavelength for the two different reconstruction techniques detailed in Appendix 3.A.1. The retardance values are measured as an average across the entire device. Because the retardance reconstruction in Eq. (3.19) has a degeneracy, we plot the offset from half-wave retardance, which is the factor that determines leakage of the original PSF. The 3-layer design approximates half-wave retardance for the specified spectral range of 500–900 nm to within 0.3 radians or 17.2 degrees. The measurements of retardance as a function of wavelength well match the expected performance. The purple dots in Fig. 3.8 represent the systematic error offset due to the photon noise (see Appendix 3.A.3), and are a lower bound for the measurement error of the retardance offset. The large systematic error at 800 nm is caused by the very low photon efficiency of the used detector. At 750 nanometers both method A and B give significantly lower retardance offsets than the prediction. At 500 and 600 nm, the two employed methods do not agree, which is likely caused by fluctuations in the light source.

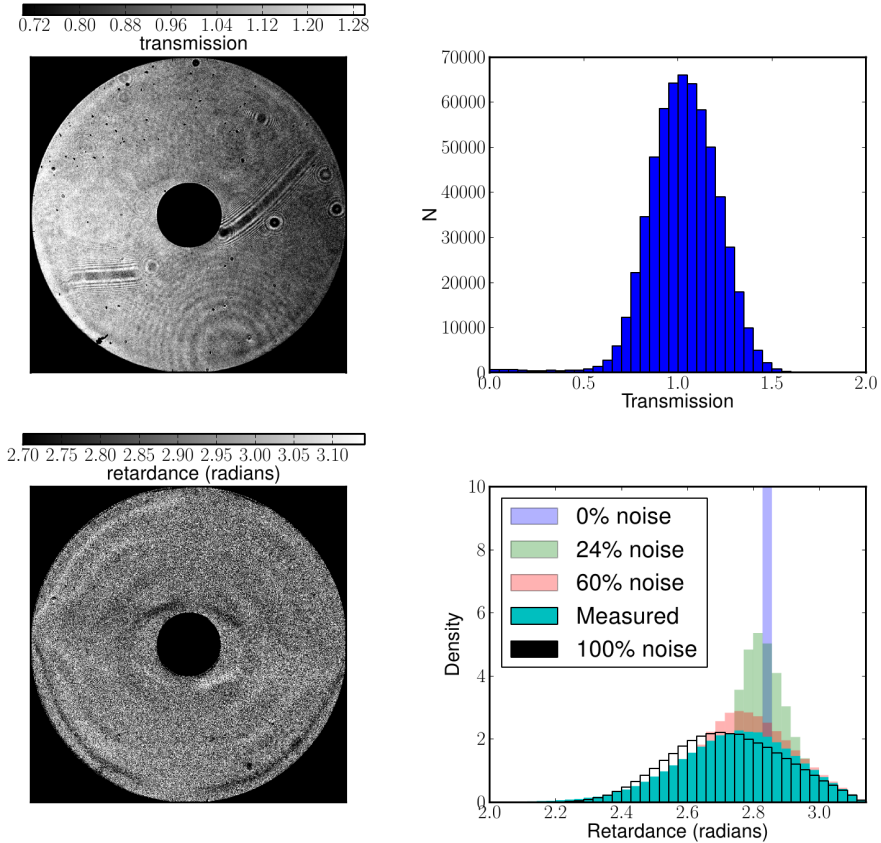


Figure 3.7: Upper panel: Measured transmission map at 750 nm. The transmission includes effects caused by the optical setup. Lower panel: Reconstructed retardance map at 750 nm. The right hand side shows the corresponding histograms. The histogram of the retardance also shows the expected simulated histograms assuming a retardance that matches the theoretical value given by the MTR design. Different amounts of Gaussian noise were injected, where 100% corresponds with the measured noise in the recorded images. This noise offsets the peak and skews the distribution.

3.4 PSF characterization

In directly imaging exoplanets, where the halo of the primary star dominates the flux at the location of the planet, it is important to know the intensity as a function of angular separation away from the central star. This is expressed in an azimuthally averaged radial light profile called a contrast curve. The contrast curve is typically normalized to unity at the location of the star and the angular separation expressed in units of diffraction width λ/D , with D the diameter of the pupil aperture. From this contrast curve the sensitivity of a coronagraph for a given observation can be calculated. We therefore model the theoretical PSF of the vAPP as a function of wavelength based on the results of the pupil-plane measurements presented in the previous Section and compare it to laboratory PSF measurements.

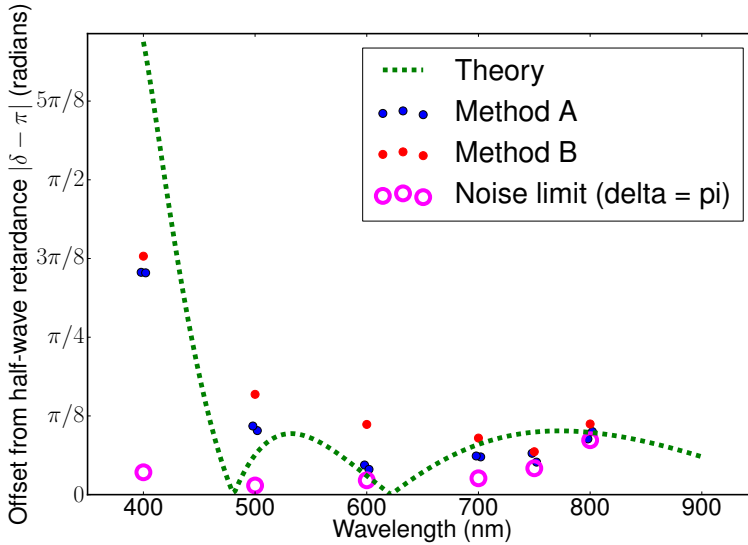


Figure 3.8: Measured offset of the retardance from π radians as a function of wavelength. Denoted in red and blue circles are the two different reconstruction methods. Method A uses 4 pairs of images to solve for both the fast axis and the retardance while method B only looks the antisymmetry axis in pairs of images. Overplotted in a dashed green line is the theoretical retardance curve for a 3-layer MTR. The pink circles represent the noise limit of the retardance measurement using the noise and flux of the real images to retrieve the retardance of a HWP that is exactly half-wave. This noise limit is not included in the theoretical retardance curve. At 750 and especially 800 nm it is seen that these dots roughly overlap with these limits which shows these values are only an upper limit.

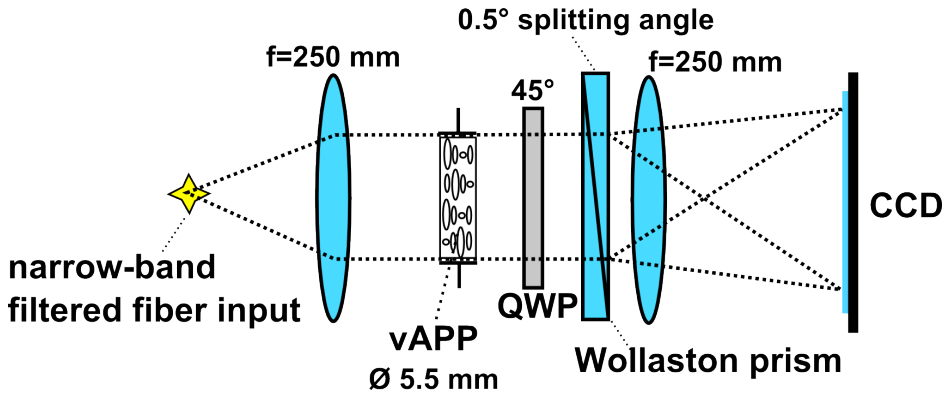


Figure 3.9: Layout of the PSF measurement setup. The working principle is the same as seen in Fig. 3.2. The vAPP is re-imaged onto the detector by a lens of $f = 250$ mm. By splitting the two circular polarizations with a QWP at 45 degrees and a Wollaston prism with a 0.5 degree splitting angle, two PSF spots with complementary dark holes are recorded in the focal plane.

In order to measure the PSF of the vAPP we use the laboratory setup shown in Fig. 3.9. The optics from the fiber to the vAPP are identical to the pupil imaging setup in Fig. 3.5. As a point

source we use a Thorlabs SM600 fiber that is single mode between 550 and 800 nm and has a mode field diameter that is significantly smaller than the optical resolution of the setup. This point source is re-imaged onto the pupil using a 2'' achromatic lens Thorlabs $f = 250$ mm lens. Behind the vAPP, a combination of an “achromatic” (i.e., Quartz/MgF₂) Thorlabs quarter-wave plate (AQWP05M-600) and a Wollaston prism splits the two circular polarization states into two beams angularly separated by 0.5 degrees. A $f = 250$ mm lens forms two PSF images on the CCD camera (SBIG ST2000XM). This optical setup is similar to the way a vAPP would be implemented in a science camera on a telescope. With approximately 500 mm between the Wollaston prism and the CCD, the separation of the two complementary PSFs is 4.36 mm. Both PSFs are simultaneously imaged on the CCD. At 400 nanometers the FWHM of the PSF is about 22 microns, and with the 7.4 micron pixel size this means the PSF is always Nyquist-Shannon sampled with at least 3 pixels per diffraction element. We require images with high dynamic contrast of at least 10^{-4} to characterize the vAPP PSFs. The dynamic range of the camera is limited to approximately 2.5×10^{-3} . We therefore combine images with different exposure times and construct a high dynamic range (HDR) image. Images are taken at five different exposure times (i.e., 10, 100 milliseconds, 1, 10 and 30 seconds). For each exposure time 10 images are taken and median combined after subtracting the master bias. To obtain HDR images we start with the median combined frame that has the shortest exposure time (i.e., 10 milliseconds) and replace the pixels of this image with exposure-time corrected values of the pixels that are in the linear regime of the next longest exposed median combined image. This procedure is repeated iteratively with increasingly longer integrations. After assembling these HDR images, the Left beam and Right beam PSFs are extracted by using a square box of 140 by 140 pixels centered on the pixel with the highest value in the core of each PSF. The background is estimated by taking the mean value of a rectangular region (100 by 200 pixels) located between the two PSFs and subtracted from both PSF images. Even at the longest wavelength of 800 nm this background region is located at $\sim 25\lambda/D$ from the central core of both of the PSFs and the contribution of the PSF halo to the flux in this region is negligible. Each individual PSF is then normalized by its peak flux. These measurements are repeated at wavelengths from 500 to 800 nanometers at 50 nm intervals with 10 nm wide filters. Figure 3.10 presents the Left and Right beams of the PSFs at increasing wavelengths. The coronagraph shows consistent performance across all wavelengths, which demonstrates its broadband performance. The contrast inside the dark hole barely varies with wavelength, and therefore the dominating chromatic effect is the fundamental growth of the diffraction pattern with wavelength. This means that for imaging through broadband filters, the inner working angle is only limited by the longest transmitted wavelength. Figure 3.11 presents the contrast curve for 750 nm by taking azimuthal averages of normalized Left and Right beam PSFs. The flux at a given radius r is calculated by taking the mean over a region defined between radius r and $r + \Delta r$ and an angular separation 135 degrees wide in the dark hole.

In order to model the PSFs of the vAPP, we require a formalism that can account for relative phase in the pupil plane so that we can calculate the intensity (i.e., the square of the amplitude) in the final focal plane using Fraunhofer diffraction theory. The Mueller-Stokes theory cannot account for this, so we use the Jones formalism instead, as the split beams are 100% polarized. The PSF model is detailed in Appendix 3.B. Using the measured phase pattern, retardance and transmission of the plate, the QWP retardance δ_{QWP} from the Thorlabs specifications, and the model described in Appendix 3.B we reconstruct the expected PSFs. The reconstructed PSFs are normalized to their peak flux to enable comparison with lab measurements of the PSFs in

Figs. 3.11, 3.12 and 3.13.

Figure 3.11 shows the contrast profile of Left and Right beam PSFs, which are extremely similar. The measurements show a contrast degradation of typically 0.5 decades with respect to the ideal curve. Inside the dark hole the contrast curve reconstruction agrees with the measured Left and Right beam PSFs at all angular distances, apart from 2 and 7 λ/D . To establish which of the leakage terms and other degrading terms is most detrimental we consider in Fig. 3.12 the effect of the individual properties on the contrast, and model the PSF for each property separately while keeping the other two theoretically perfect. This demonstrates that, by itself, the retardance has the largest impact on the contrast in the dark hole of the prototype, as it immediately leads to leakage of the original PSF. We also calculate the impact of improving only one of the three properties that we have characterized (see Fig. 3.13). Again our conclusion is that improving the retardance in subsequent plate manufacture or filtering leakage terms (Mawet et al., 2009; Snik et al., 2014) will improve the average contrast by 0.35 decades between 2 and 7 λ/D towards the ideal.

A residual discrepancy between measurements and reconstruction is observed in Fig. 3.11. We attribute these differences at these angular separations to low-order wavefront aberrations in the re-imaging optics, variations in thickness of the vAPP substrate and the Wollaston prism. In Figure 3.13 we show that injecting 0.15 radians RMS of third-order spherical aberrations results in excellent agreement of the model with the measured curve at these angular scales. Such wavefront aberrations can be corrected in a telescope (for at least one PSF) by offsetting the deformable mirror.

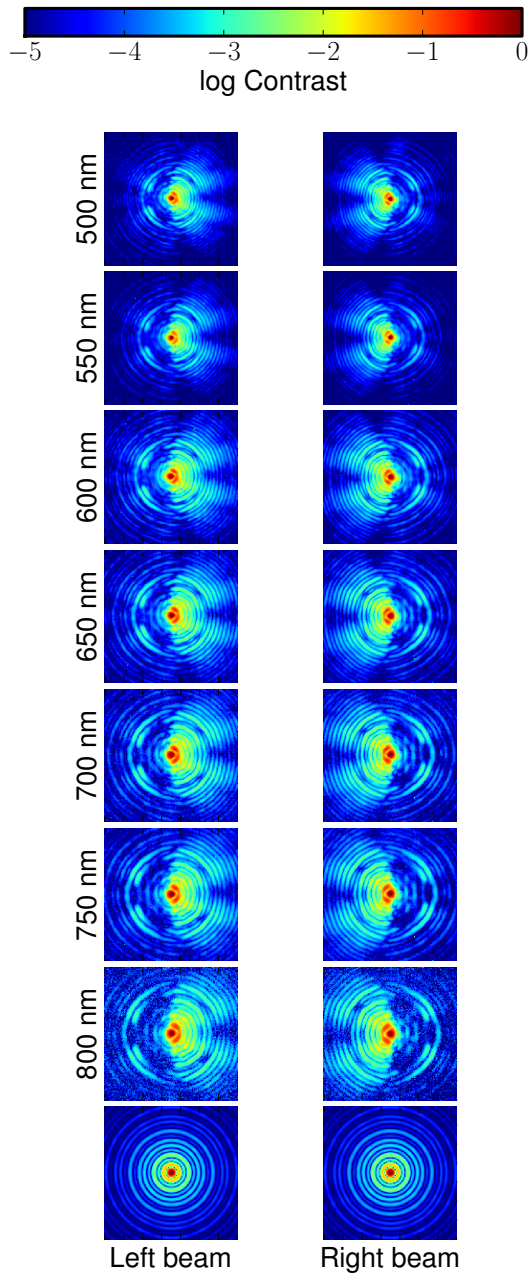


Figure 3.10: Laboratory measurements of PSFs ranging from 500 to 800 nm showing the PSFs of the Left and Right beam. For comparison, the bottom two panels show the unaberrated PSFs at 800 nm. All PSFs are normalized to the peak of the PSF and scaled logarithmically.

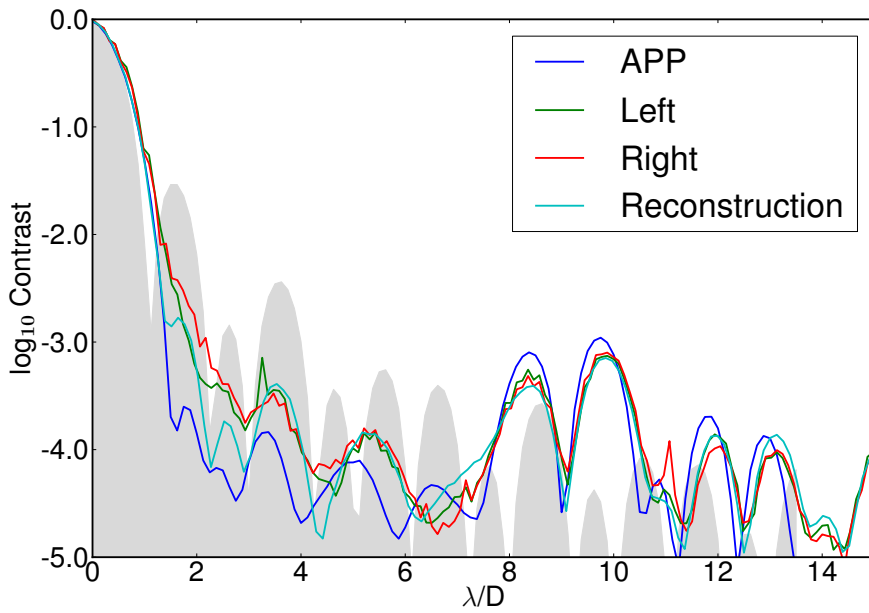


Figure 3.11: Normalized intensity ('contrast') curves for the two PSFs of the vAPP as measured in the lab at 750 nm compared to the ideal case, and compared to a reconstruction that used the pupil measurements as input. The lab measurements are shown in green and red for respectively the Left and Right PSFs. The theoretical contrast is shown in dark blue, and the contrast of the model PSF using the reconstructed transmission, fast axis and retardance is plotted in light blue. The gray shaded area shows the contrast for an unaberrated PSF.

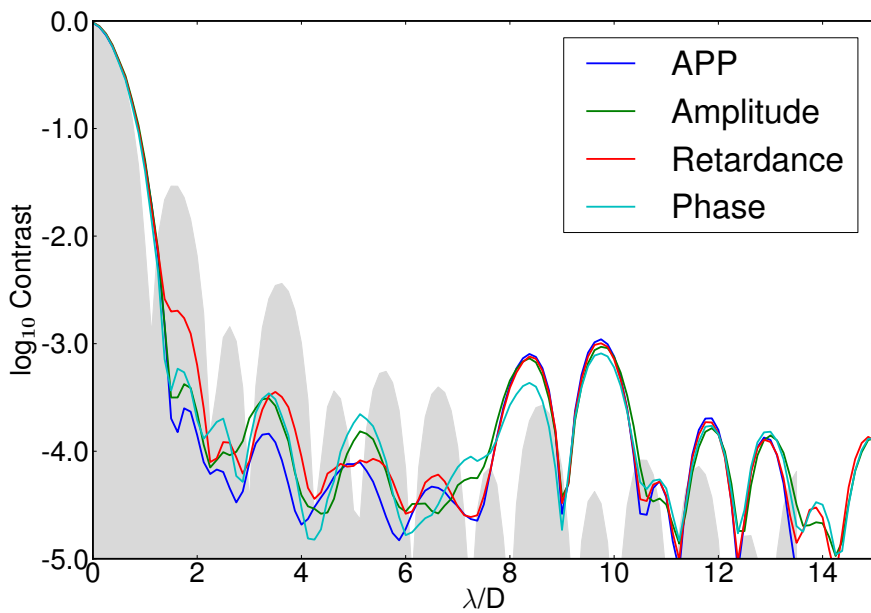


Figure 3.12: Theoretical normalized intensity ('contrast') curves of the most important influences on the vAPP's contrast degradation. Using the model described in Section 3.3 the theoretical PSF was created using measured offsets to only one of the three properties (i.e., transmission, fast axis or retardance) while keeping the other two properties at their ideal values. The theoretical APP curve is shown in blue. The gray shaded area shows the contrast for an unaberrated PSF.

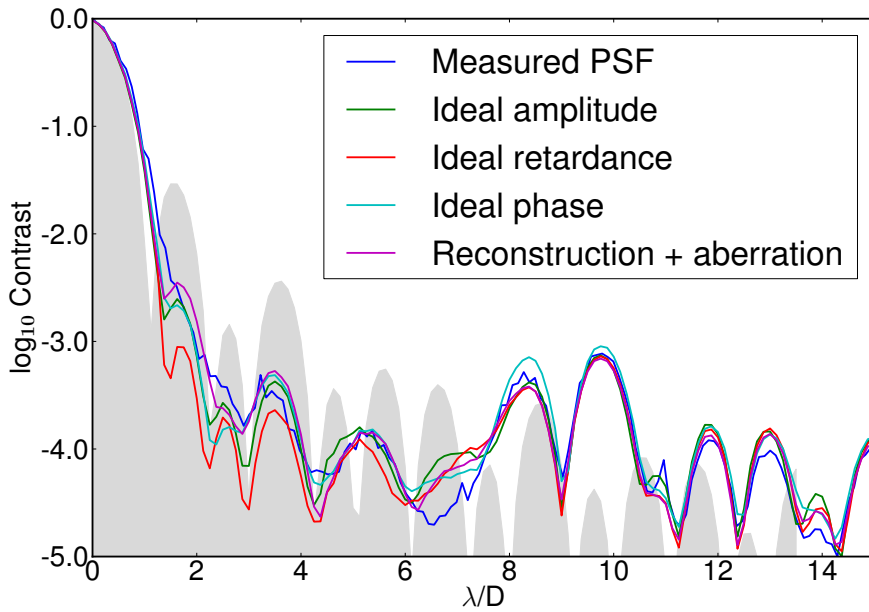


Figure 3.13: Theoretical normalized intensity ('contrast') curves of the most important combination of influences on the vAPP's contrast. Using the model described in Section 3.3 the theoretical PSF is created using two of the three measured properties (i.e., transmission, fast axis or retardance) while keeping the other property at its ideal value. The dark blue line shows the average of the two measured PSFs. The purple line shows the reconstruction using all three measured quantities together with the QWP performance and 0.15 radians of spherical aberration. The shaded gray area shows the contrast for an unaberrated PSF.

3.5 Conclusions & Outlook

In this paper we present the characterization of a prototype of the vector Apodizing Phase Plate Coronagraph. Owing to the application of the vector phase applied by patterned Multi-Twist Retarder liquid crystals, the coronagraphic performance is achieved over an unprecedented wavelength range of 500–900 nm in two complementary PSFs. With lab measurements we characterize the phase pattern, the retardance and the transmission of the constructed vAPP prototype, and measured and modeled the resultant PSFs. We compared the measured PSFs with the modeled PSFs and find excellent agreement at all wavelengths and angular separations when all known non-ideal effects are included. The vAPP provides up to two decades of suppression at $2 \lambda/D$ and keeps the diffraction halo at a level of $10^{-3.8}$ of the peak intensity out to $7 \lambda/D$ as measured in a 135 degree wedge. The retardance measurements show a wavelength behavior that is consistent with a 3-layer MTR, which provides coronagraphic performance over almost an order of magnitude wider in spectral bandwidth than the previous APP coronagraph. Still, the most significant degradation from the ideal APP PSF is due to offsets from half-wave retardance. Subsequent iterations of vAPP coronagraphs should therefore focus on improving the manufacturing technique with respect to the retardance and/or filter the leakage terms.

The retardance as a function of wavelength could still be further improved by adding more liquid crystal layers. For instance, a 4-layer device has significantly better performance than the 3-layer design that was used in this research. The improvement to the theoretical retardance and contrast are shown in Fig. 3.14 and Fig. 3.15 respectively.

The contrast in Fig. 3.15 bottoms out as it reaches the limit of the adopted APP phase pattern. Owing to the direct-write technique, the vAPP permits the adoption of more extreme phase patterns that reach much deeper (theoretical) contrasts (e.g. Carlotti et al. (2013); Otten et al. (2014)). Using the 200 by 200 pixels of this prototype it can be calculated that the outer working angle can theoretically go up to $100 \lambda/D$. The production of such an upgraded vAPP coronagraph will be subject to more demanding production tolerances. Particularly the retardance offsets will need to be much smaller than for the current prototype, or the spectral bandwidth will need to be decreased. However, the leakage terms can also be avoided by applying circular polarization filtering on either side of the vAPP (Snik et al., 2014). An alternative solution is found by integration of the circular polarization beam-splitting in the vAPP, by using a polarization grating (Otten et al., 2014). In this case, all leakage terms end up in a third, unaberrated PSF.

More extreme vAPP devices will also be more demanding in terms of the phase pattern itself. The accuracy of the fast axis orientation (and hence the vector phase) pattern depends on the accuracy of the angle of linear polarization of the UV laser that is used for the photo-alignment layer. The latest manufacturing setup has a Pockels cell to better control this angle and dramatically increases the speed at which the phase patterns are realized. Furthermore, the instrumental polarization issues due to the fold mirror should be avoided.

The measurement setup that we use for the reconstruction of the vAPP device properties is relatively easy to implement and use, but it has several limitations. The accuracy of the reconstruction is dominated by the photon noise on the input images. Unfortunately, the small fiber and narrowband filters attenuate light and therefore require long exposure times. The light source exhibits fluctuations especially within the first few hours after being switched on, which influence the accuracy of the reconstruction. The reconstruction method removes first order fluctuations of the light but is sensitive to fluctuations between measurements at orthogonal angles of the

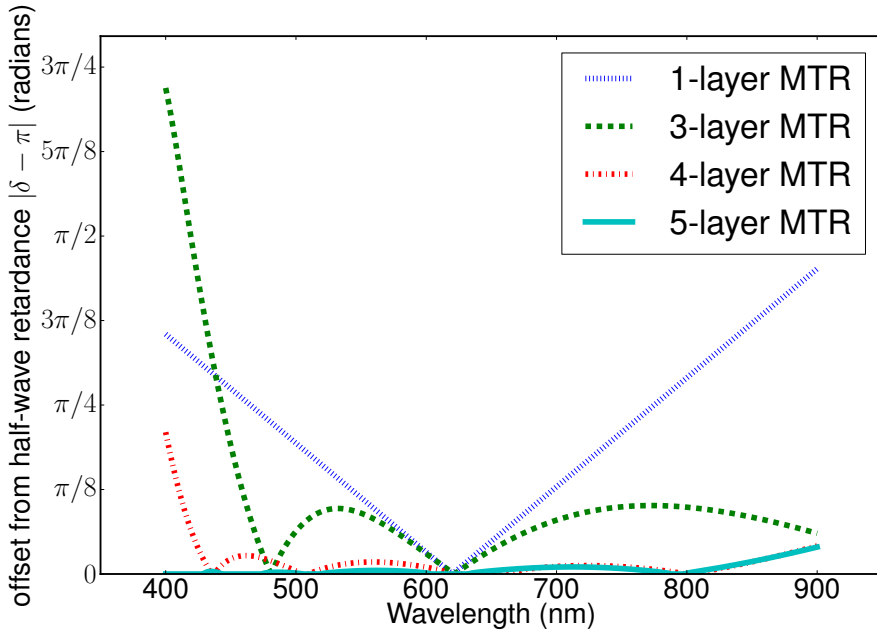


Figure 3.14: Theoretical retardance curves as a function of wavelength for different layered MTR designs. This paper describes the performance of a 3-layer MTR device. Increasing the number of twisting layers in the MTR improves the retardance performance across the wavelength range.

polarizer. By using a brighter light source, a larger diameter fiber, and/or a camera with better quantum efficiency we can minimize these effects by reducing measurement noise and taking the orthogonal exposures with shorter time intervals. Another solution for the fluctuations would be to independently monitor the light flux out of the fiber to allow for normalization in data reduction.

While the coronagraph in this paper is designed to work at visible wavelengths, most high-contrast imaging instruments typically work at near-infrared wavelengths. Fortunately the wavelength range at which the plate optimally works can be optimized by a judicious choice of different liquid crystals and substrates for the vAPP. Using these methods (Packham et al., 2010) have demonstrated a polarization grating system that works from 3 to 20 microns, and showed that the retardance is only marginally impacted (3%) at cryogenic temperatures. If necessary, such a change in retardance can be pre-compensated during manufacturing.

Instruments that would be suitable for a vAPP coronagraph are adaptive optics-fed high-contrast cameras such as SPHERE-ZIMPOL (Roelfsema et al., 2010) on the Very Large Telescope, GPI on Gemini South (Macintosh et al., 2014), ExPo on the William Herschel Telescope (Rodenhuis et al., 2012), and MMT-Pol (Packham et al., 2012). These polarimetric instruments already contain the required Wollaston prism (or other polarizing beam-splitter) to split the PSFs. Note that even in cases of moderate ($\sim 50\%$) Strehl ratio, the vAPP still delivers a average raw contrast of $10^{-3.9}$ at $4\text{--}6 \lambda/D$. The second vAPP prototype (cf. the design presented by Ot-

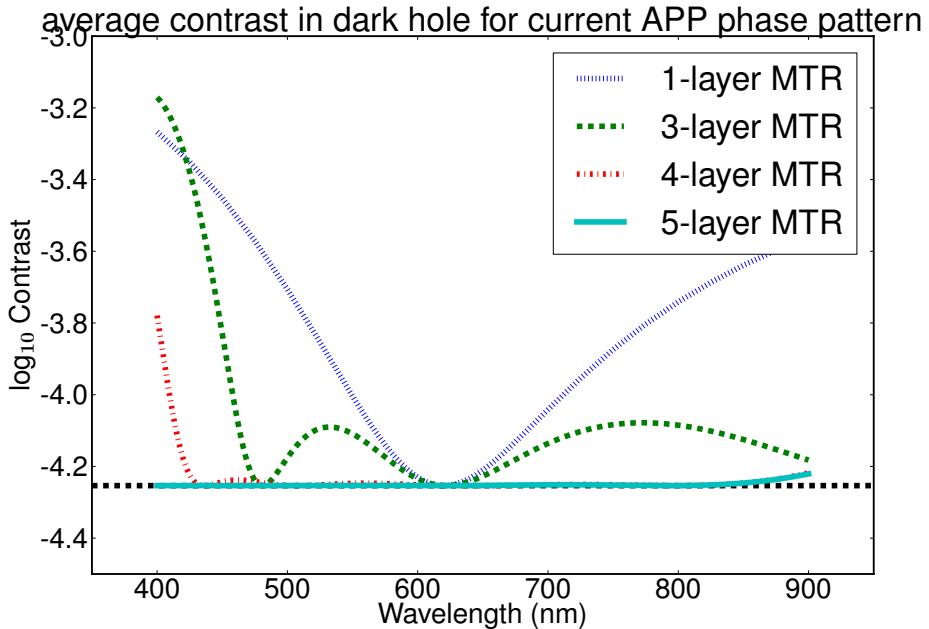


Figure 3.15: Theoretical contrast curves as a function of wavelength for different layered MTRs and the current vAPP phase pattern design. The contrast was derived from Fig. 3.14 by creating PSF models and measuring the depth of the dark hole between 2 and $7 \lambda/D$ in a 135 degree wedge. This paper describes the performance of a 3-layer vAPP device. The black dashed line shows the theoretical perfect contrast given the adopted phase pattern for a perfect half-wave retarder across all wavelengths. Even though the contrast seems to bottom out for device with more than three layers, the contrast could be improved by adopting a more extreme phase pattern with higher contrast.

ten et al. (2014)) has recently been integrated in LMIRCam on the Large Binocular Telescope (Skrutskie et al., 2010).

Moreover, as the vAPP coronagraph naturally pairs with polarimetry it is possible to reach an even deeper contrast for scattered planet light by combining the two techniques (Snik et al., 2014). The two complementary images may also furnish focal-plane wavefront sensing (cf. Riaud, P. et al. (2012)) to provide information for real-time or post-factor correction of (instrumental) wavefront aberrations. Finally, we must emphasize that the use of the achromatic patterning technique is not limited to phase manipulation in pupil-plane coronagraphs, but can also be used for focal-plane coronagraphs or a combination of both.

Acknowledgments

The authors would like to thank Remko Stuik and Gerard van Harten for their helpful suggestions on the laboratory measurements. Furthermore, we thank the anonymous referees for their helpful suggestions which improved this manuscript. This work is part of the research programme Instrumentation for the E-ELT, which is partly financed by the Netherlands Organisation for Scientific

Research (NWO).

3.A Pupil measurement theory and setup

3.A.1 Pupil reconstruction

This subsection provides the conventions and theory to describe the measurements of the vAPP properties with the setup presented in Fig. 3.5, and the subsequent data reduction.

The partial polarization of beam of light can be described by a 4-element Stokes vector. The four elements are I , Q , U and V where I denotes intensity, Q and U denote linear polarization at $0/90$ degrees and ± 45 degrees, respectively, and V denotes circular polarization. A 4×4 Mueller matrix describes polarization-changing optical components or media that convert an input Stokes vector into a new Stokes vector. Mathematically, the output Stokes vector can be calculated by multiplying the Mueller matrix against the Stokes input vector as seen in Eq. (3.8).

$$\mathbf{S}_{\text{out}} = \mathbf{M} \mathbf{S}_{\text{in}} = \begin{pmatrix} m_{00} & m_{01} & m_{02} & m_{03} \\ m_{10} & m_{11} & m_{12} & m_{13} \\ m_{20} & m_{21} & m_{22} & m_{23} \\ m_{30} & m_{31} & m_{32} & m_{33} \end{pmatrix} \begin{pmatrix} I_{\text{in}} \\ Q_{\text{in}} \\ U_{\text{in}} \\ V_{\text{in}} \end{pmatrix} \quad (3.8)$$

An ideal retarder with a certain retardance δ and a fast axis of $\theta = 0$ radians has the following Mueller matrix:

$$\mathbf{M}_{\text{HWP},0}(\delta) = \begin{pmatrix} 1 & 0 & 0 & 0 \\ 0 & 1 & 0 & 0 \\ 0 & 0 & \cos \delta & \sin \delta \\ 0 & 0 & -\sin \delta & \cos \delta \end{pmatrix}. \quad (3.9)$$

As the vAPP locally has a certain fast axis $\theta = \frac{\phi_{\text{APP}}}{2}$ we rotate this Mueller matrix with the rotation matrix $\mathbf{T}_{\text{M}}(\theta)$:

$$\mathbf{T}_{\text{M}}(\theta) = \begin{pmatrix} 1 & 0 & 0 & 0 \\ 0 & \cos 2\theta & \sin 2\theta & 0 \\ 0 & -\sin 2\theta & \cos 2\theta & 0 \\ 0 & 0 & 0 & 1 \end{pmatrix} \quad (3.10)$$

creating the equation

$$\mathbf{M}_{\text{HWP},\theta}(\delta) = \mathbf{T}_{\text{M}}(-\theta) \mathbf{M}_{\text{HWP},0}(\delta) \mathbf{T}_{\text{M}}(\theta). \quad (3.11)$$

Since this retarder is positioned between 2 polarizers with a certain position angle α with respect to the anti-symmetry axis we describe each polarizer with the following Mueller matrix

$$\mathbf{M}_{\text{pol},\alpha} = \mathbf{T}_{\text{M}}(-\alpha) \frac{1}{2} \begin{pmatrix} 1 & 1 & 0 & 0 \\ 1 & 1 & 0 & 0 \\ 0 & 0 & 0 & 0 \\ 0 & 0 & 0 & 0 \end{pmatrix} \mathbf{T}_{\text{M}}(\alpha). \quad (3.12)$$

In the case of parallel polarizers we obtain the equation

$$\mathbf{M}_{\text{setup},\parallel}(\alpha, \delta, \theta) = \mathbf{M}_{\text{pol},\alpha} \mathbf{M}_{\text{HWP},\theta}(\delta) \mathbf{M}_{\text{pol},\alpha}. \quad (3.13)$$

With crossed polarizers the Mueller matrix for the whole setup becomes

$$\mathbf{M}_{\text{setup},\perp}(\alpha, \delta, \theta) = \mathbf{M}_{\text{pol},\alpha+\pi/2} \mathbf{M}_{\text{HWP},\theta}(\delta) \mathbf{M}_{\text{pol},\alpha}. \quad (3.14)$$

The input light can be polarized or unpolarized with an intensity I_{in} and is represented by the Stokes vector

$$\mathbf{S}_{\text{in}} = \begin{pmatrix} I_{\text{in}} \\ Q_{\text{in}} \\ U_{\text{in}} \\ V_{\text{in}} \end{pmatrix}. \quad (3.15)$$

The output vector then becomes

$$\mathbf{S}_{\text{out}} = \mathbf{M}_{\text{setup},\parallel/\perp}(\alpha, \delta, \theta) \mathbf{S}_{\text{in}}. \quad (3.16)$$

Since we only measure the intensity of the vAPP plate in between polarizers we only look at the first element of the output Stokes vector S_{out} . This element will be referred to as $I_{\alpha,\parallel/\perp}(\delta, \theta)$. As an example; for the intensity of the plate between crossed polarizers with a position angle of 45 degrees the intensity is $I_{45^\circ,\perp}(\delta, \theta)$. A combination of intensity ratios gives us an equation with no dependency on the fast axis, input intensity or polarization, or the transmission:

$$\frac{I_{0^\circ,\parallel} - I_{0^\circ,\perp}}{I_{0^\circ,\parallel} + I_{0^\circ,\perp}} + \frac{I_{45^\circ,\parallel} - I_{45^\circ,\perp}}{I_{45^\circ,\parallel} + I_{45^\circ,\perp}} = 1 + \cos(\delta). \quad (3.17)$$

Similarly, the equation

$$\frac{I_{0^\circ,\parallel} - I_{0^\circ,\perp}}{I_{0^\circ,\parallel} + I_{0^\circ,\perp}} - \frac{I_{45^\circ,\parallel} - I_{45^\circ,\perp}}{I_{45^\circ,\parallel} + I_{45^\circ,\perp}} = 2 \cos(4\theta) \sin(\delta/2)^2 \quad (3.18)$$

gives us an expression that yields the retarder orientation (i.e. half the vector phase) that is insensitive to the input intensity and polarization as long as they are constant during the exposures.

The unknown retardance δ can be reconstructed with the equation

$$\delta = \arccos \left(\frac{I_{0^\circ,\parallel} - I_{0^\circ,\perp}}{I_{0^\circ,\parallel} + I_{0^\circ,\perp}} + \frac{I_{45^\circ,\parallel} - I_{45^\circ,\perp}}{I_{45^\circ,\parallel} + I_{45^\circ,\perp}} - 1 \right) \quad (3.19)$$

which is the inverse of Eq. (3.17). Using this retardance, the fast axis θ can be calculated using a rewritten version of Eq. (3.18)

$$\theta = \frac{1}{4} \arccos \left(\frac{1}{2} \frac{I_{0^\circ,\parallel} - I_{0^\circ,\perp} - I_{45^\circ,\parallel} + I_{45^\circ,\perp}}{I_{0^\circ,\parallel} + I_{0^\circ,\perp} + I_{45^\circ,\parallel} + I_{45^\circ,\perp}} \frac{1}{\sin(\delta/2)^2} \right) \quad (3.20)$$

Note that this equation will produce fast axis values that fold at $\pi/4$, because of the properties of the arccosine function. This problem will be resolved at the end of the following Subsection.

As a consistency check, the retardance was also estimated by looking at the flux ratio

$$\frac{I_{45^\circ, \parallel}}{I_{45^\circ, \perp} + I_{45^\circ, \parallel}} \quad (3.21)$$

in the anti-symmetry axis of the vAPP pattern, and assuming that the polarizers are at 45° with respect to the fast axis at that location. If the plate is exactly half-wave, the second polarizer will block the incoming light. A non-zero flux ratio indicates an offset from half-wave.

$$\delta = \arccos \left(2 (I_{45^\circ, \parallel} / (I_{45^\circ, \perp} + I_{45^\circ, \parallel})) - 1 \right). \quad (3.22)$$

relates this flux ratio to a retardance estimate.

We call reconstructing the retardance using Eq. (3.20) Method A and reconstructing using Eq. (3.22) Method B. To record these intensity measurements we construct a laboratory setup to measure the intensity across the vAPP clear aperture as seen through polarizers pairs. In total we need eight different polarizer pair positions and corresponding intensity measurements. The list is seen in Tab. 3.1 and Fig. 3.16.

Table 3.1: List of used polarizer positions. An example of the corresponding measured intensities can be seen in Fig. 3.16.

Polarizer 1	Polarizer 2	Intensity
0°	0°	$I_{0^\circ, \parallel}$
0°	90°	$I_{0^\circ, \perp}$
45°	45°	$I_{45^\circ, \parallel}$
45°	135°	$I_{45^\circ, \perp}$
22.5°	22.5°	$I_{22.5^\circ, \parallel}$
22.5°	112.5°	$I_{22.5^\circ, \perp}$
67.5°	67.5°	$I_{67.5^\circ, \parallel}$
67.5°	157.5°	$I_{67.5^\circ, \perp}$

3.A.2 Pupil measurement setup & data reduction

The pupil measurement setup consists of two polarizers and optics that re-image the vAPP pupil onto the SBIG ST2000XM CCD. A schematic overview of the layout is presented in Fig. 3.5. A Xenon arc lamp source from Cairn Research is focused into a single-mode SM600 fiber specified to be single mode between 550 and 800 nanometers. The fiber has a mode field diameter of $4.3 \mu\text{m}$ at 633 nm which is substantially smaller than the optical resolution of our setup. Thorlabs FKB-VIS-10 10 nm narrowband interference filters are placed between the Xenon source and the fiber to select quasi-monochromatic light (i.e., 500-800 nanometers at 50 nm steps). A $f = 250$ mm lens re-images the fiber to form a pupil on the APP. This 5.5 mm pupil of the vAPP is then re-imaged onto the 1600 by 1200 pixel detector with 7.4 micron pixel size. A combination of a $f = 250$ mm and $f = 300$ mm lens form a re-imaged pupil size of 6.6 mm on the 11.8 by 8.9 mm chip.

The measurements are recorded at the defined polarizer angles and at wavelengths from 400 to 800 nanometers at 50 nm intervals. The different angles used for the reconstruction are listed in Table 3.1 and shown in Fig. 3.16 together with the measured intensity images. The values in Fig. 3.3 are used to offset the angles of the polarizer pair between wavelengths. The offsets are fine-tuned by looking at the intensity image $I_{0^\circ, \parallel}$ and optimizing the symmetry of this image.

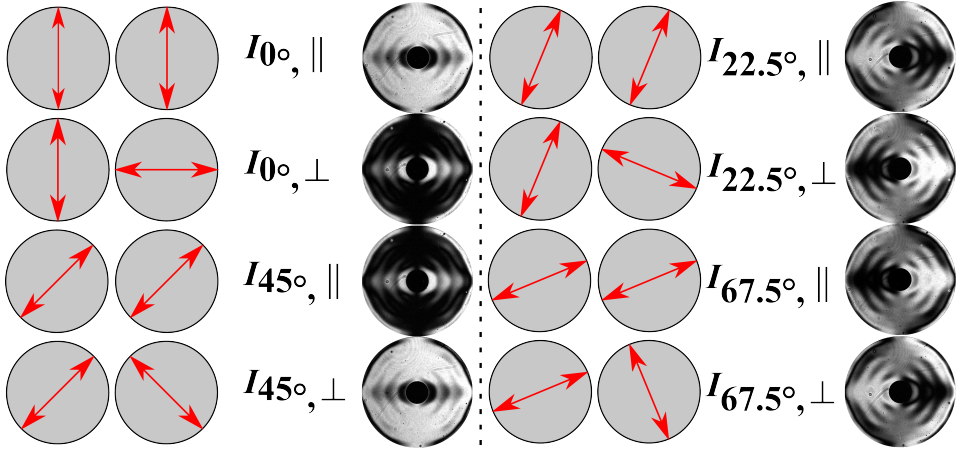


Figure 3.16: Polarizer orientation angles and resultant measured intensity map for each set of polarizer orientations. Using these 8 measurements we can reconstruct the transmission, fast axis and retardance of the optic.

The exposure time of the individual frames for these pupil measurements is 100 seconds because of the narrow spectral band and single-mode fiber. At each polarizer pair orientation, one exposure followed by one bias frame is repeated 10 times to form a total integration time of 1000 seconds. Additionally we also take 20 dark frames at 100 seconds each to form a master dark. The bias frames are median combined to create a master bias and similarly after subtracting the master bias from each individual frame the dark frames are median combined into a master dark. After removing the bias and dark from all the frames, they are stacked to form a final image. This is repeated for each wavelength and polarizer pair image.

To estimate the background in scattered light along with low spatial frequency structure, we use the region of the CCD that corresponds to a region that is blocked by the amplitude mask of the vAPP. After masking out the APP pupil image and determining the center of the pupil image, we fit a function of the form $f(x, y) = ax + by + c + d(x^2 + y^2)$ and we solve for a, b, c and d using a least-square approach, and subtract it off the image.

Using Eq. (3.19) we reconstruct the retardance from two sets of four corrected images. The arccosine in the equation is only defined for values between -1 and 1, and therefore the factor $\frac{I_{0^\circ, \parallel} - I_{0^\circ, \perp}}{I_{0^\circ, \parallel} + I_{0^\circ, \perp}} + \frac{I_{45^\circ, \parallel} - I_{45^\circ, \perp}}{I_{45^\circ, \parallel} + I_{45^\circ, \perp}} - 1$ is susceptible to noise. The factors that are outside of these limits are truncated to the nearest defined value of either -1 or 1 before taking the arccosine. Similarly, when computing the fast axis using Eq. (3.20) this procedure is used to ensure that all values are real.

The reconstructed fast axis values reflect at $\pi/2$ due to the invariance of the polarizer under rotations of 180 degrees. If the fast axis orientation is larger than $\pi/2$ radians the intensity decreases

again creating a non-unique relation between the intensity ratio and phase. To overcome this we obtain additional constraints by repeating these measurements with an offset of 22.5 degrees. The intensity and corresponding reconstructed phases fold back at different locations in the images while the retardance remains the same as before. The input phase pattern is used together with the two reconstructed fast axis maps in order to determine the fast axis orientation. With more signal to noise per pixel it would be possible to directly unfold the reconstructed fast axis using the input phase map by snapping to the phase solution that matches the input most closely. In our case the individual images have too much noise to directly convert using the known phase pattern. Each of the image pairs that are taken have areas where the fast axis is linear as a function of the input phase and does not fold backwards. The linear areas of the images are stitched together. At locations where $|\phi| > \pi/2$ radians a degeneracy still exists. This is solved by applying the appropriate sign and offset to this area of the reconstructed fast axis.

3.A.3 Error propagation

To determine the effect of misaligned polarizers and measurement noise on the reconstructed retardance and fast axis, we simulate intensity patterns using Eq. (3.16) and introduce small offsets to the polarizers (< 2 degrees) and simulated photon shot noise by injecting Poisson noise into these images. We then reconstruct unwrapped fast axis and retardance maps using the aforementioned method. From these simulations we see that identical angular offsets to the polarizer pair positions have no significant effect on the retardance reconstruction. Offsetting the polarizer pairs does change the reconstruction of the fast axis pattern. This polarizer offset slightly shifts the position at which the phase folds in individual images. This influences the reconstructed (un-folded) phase maps that joins these individual images although its impact depends how far the polarizers are offset. The relative positions between the polarizers can be determined to within 5 arcminutes, but there is an unknown but fixed offset (on the order of 1 degree) between the polarizer mount position and the fast axis orientation of the APP. The simulations show that offsetting the polarizers by 1 degree does not significantly affect the reconstruction of the phase apart from a piston term.

Figure 3.17 shows the reconstructed phase versus the input phase for the dataset taken at 750 nm. This image shows that the reconstructed phase matches the input phase to within 0.1 radians. At an input phase of $\phi = 0$ and $\phi = \pm\pi/2$ radians the reconstructed phase shows higher dispersion. This can be seen by the slightly flaring datapoints at those locations and is expected from simulations made with an equal amount of noise for the individual images. The measurement noise on the unbinned raw images at 750 nm propagates to an error on the phase per pixel of 0.07 radians.

Adding Poisson noise systematically offsets the reconstructed retardance values. To investigate how much this influences our reconstruction, we generate images with $\delta = \pi$ radians, rescale the intensity images with the measured flux of the images in the lab, and inject a similar amount of Gaussian noise. We obtain a systematically different average value across the pupil instead of the input half-wave retardance. This systematic offset becomes more significant as the noise is increased, and is an indicator of the noise limit on the retardance, as plotted in Fig. 3.8.

Our images highly oversample (approximately by a factor of 4) the spatial scales in the vAPP. To mitigate the Poisson noise, we bin the data before performing the reconstruction without loss of spatial information. If there is no significant change of reconstructed retardance as a function

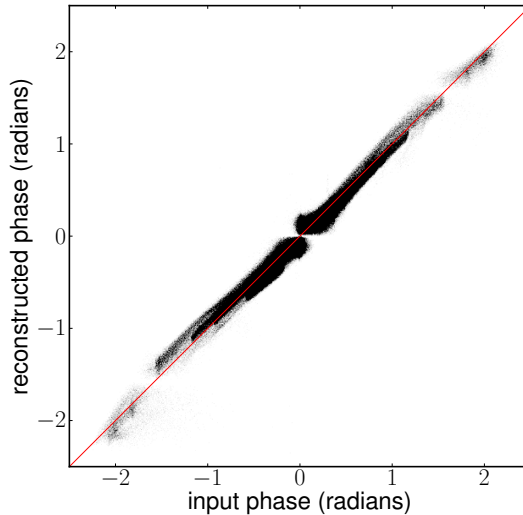


Figure 3.17: Plot of unwrapped reconstructed phase versus the input phase. The red line shows a perfect reconstruction.

of binning, then we conclude that the results are not limited by Poisson noise. Using 4×4 binned simulated data we derive a measurement noise per pixel of 0.02 radians on the phase and 0.08 radians on the retardance using the measurement noise at 750 nm. At shorter wavelengths the noise level per pixel improves.

3.B PSF modeling theory

To model the coronagraphic PSFs, we need to compute the Jones vector for both fully polarized beams, as it retains the complete phase information that determines the destructive interference inside the dark hole. The vAPP itself is modeled with a Jones matrix of an ideal retarder with a retardance δ_{HWP} and fast axis θ_{HWP} . Ideally the retardance of the half-wave plate $\delta_{\text{HWP}} = \pi$ radians and the fast axis $\theta_{\text{HWP}} = \phi_{\text{APP}}/2$, where ϕ_{APP} is the true phase pattern in the pupil. The Jones matrix of the HWP with fast axis $\theta_{\text{HWP}} = 0$ radians therefore is

$$\mathbf{J}_{\text{HWP},0} = \begin{pmatrix} \exp(-i\delta_{\text{HWP}}/2) & 0 \\ 0 & \exp(i\delta_{\text{HWP}}/2) \end{pmatrix}. \quad (3.23)$$

This matrix is rotated to the correct fast axis using

$$\mathbf{J}_{\text{HWP},\theta} = \mathbf{T}(-\theta) \mathbf{J}_{\text{HWP},0} \mathbf{T}(\theta) \quad (3.24)$$

for every pixel of the half-wave plate, where

$$\mathbf{T}(\theta) = \begin{pmatrix} \cos \theta & \sin \theta \\ -\sin \theta & \cos \theta \end{pmatrix} \quad (3.25)$$

is the rotation matrix with angle of rotation θ .

The second optical component in our setup is a quarter-wave plate that converts the two circular polarizations into orthogonal linear polarization states. The final contrast also depends on the quality and alignment of this optic. The QWP can be described in a similar fashion as the HWP:

$$\mathbf{J}_{\text{QWP},0} = \begin{pmatrix} \exp(-i\delta_{\text{QWP}}/2) & 0 \\ 0 & \exp(i\delta_{\text{QWP}}/2) \end{pmatrix}. \quad (3.26)$$

The value of δ_{QWP} should be $\pi/2$ in the ideal case. This matrix is rotated by a value θ_{QWP} which ideally is $\pi/4$ to fully convert circular into linear polarization at $0,90^\circ$ yielding

$$\mathbf{J}_{\text{QWP},\theta} = \mathbf{T}(-\theta)\mathbf{J}_{\text{QWP},0}\mathbf{T}(\theta). \quad (3.27)$$

The final element in our Jones model is the Wollaston prism which can be described by a linear polarizer with an efficiency ϵ_{pol} . The corresponding Jones matrix for one beam of the Wollaston is

$$\mathbf{J}_{\text{pol},\perp} = \begin{pmatrix} \epsilon_{\text{pol}} & 0 \\ 0 & 1 - \epsilon_{\text{pol}} \end{pmatrix}. \quad (3.28)$$

The other beam can be described in a similar way with

$$\mathbf{J}_{\text{pol},\parallel} = \begin{pmatrix} 1 - \epsilon_{\text{pol}} & 0 \\ 0 & \epsilon_{\text{pol}} \end{pmatrix}. \quad (3.29)$$

A rotation offset of the Wollaston also introduces leakage terms, and therefore these Jones matrices are also rotated with a rotation matrix. The angle of rotation $\theta_{\text{pol}} = 0$ radians if placed perfectly but in practice can vary by a few degrees.

After defining these three optical components we study the effect of the optical setup on circular polarization input states as defined in Eq. (3.5). The different components are combined in matrix form using

$$\mathbf{E}_{\text{out}} = \mathbf{J}_{\text{pol}}\mathbf{J}_{\text{QWP},\frac{\pi}{4}}\mathbf{J}_{\text{HWP},\theta_{\text{APP}}}\mathbf{E}_{\text{input}}. \quad (3.30)$$

With no vAPP in the laboratory setup, Left circularly (LHC) polarized light will form an Airy PSF in only one of the two Wollaston beams, which we label as the Left beam and the Right beam. In our definition, the LHC polarized light will form an Airy pattern in the Right beam. Inserting an ideal vAPP will then remove the Airy PSF from the Right beam and form the vAPP PSF in the Left beam. Introducing right circularly (RHC) polarized light will produce the complementary vAPP PSF in the Right beam. Recall that the vAPP is a patterned half-wave plate. If the optic is not exactly half-wave, then part of the flux from the vAPP appears as a leakage of the original Airy PSF in the other Wollaston beam. This effect is shown for a retardance offset of 0.1π radians in Fig. 3.18. The strength of the leakage increases with the offset from half-wave.

Another leakage term appears when the QWP departs from quarter-wave retardance. If the vAPP is illuminated with LHC polarized light, the leakage term appears as an attenuated APP PSF in the Right beam. For a retardance offset of 0.05π radians this is shown in Fig. 3.19.

The other error contributions in the system include offsets from the desired phase pattern, misalignments in the QWP and Wollaston, and additional aberrations of the wavefront, which modify the phase pattern and the resultant PSFs, in a different way. Also transmission variations in the vAPP and in the other optics change the PSF. We model all these effects with the Jones formalism and Fourier transform the resultant complex phase to model the PSF.

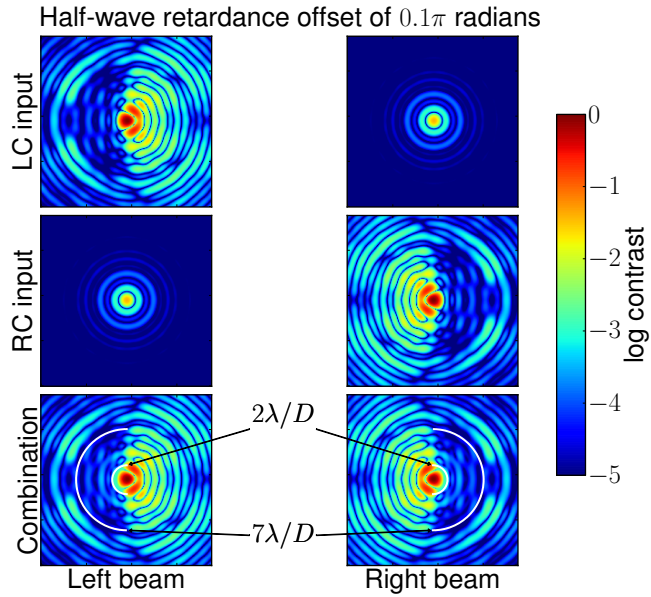


Figure 3.18: Effect of retardance offset of the HWP on the PSFs. Any offsets of the half-wave retardance of the vAPP fill the dark hole with an attenuated copy of the original PSF.

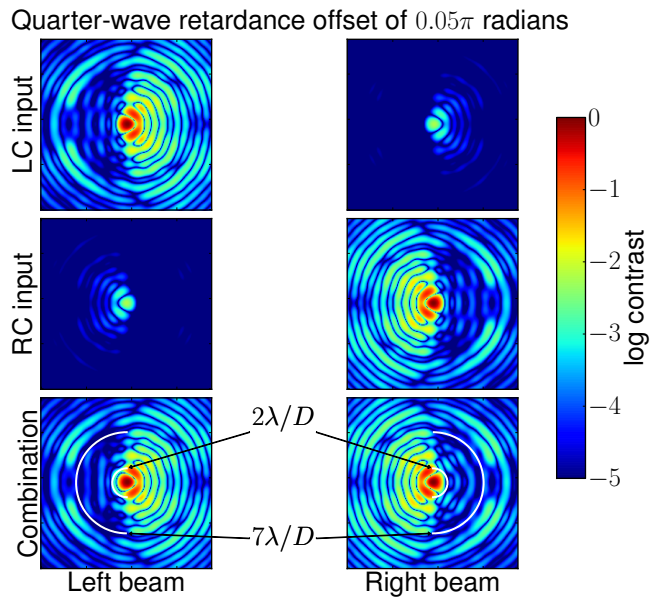


Figure 3.19: Effect of retardance offset of the QWP on the PSFs. Retardance offsets of the QWP fill the dark hole with the opposite handed PSF. Note that the leakage is normalized to the non-leaking term contribution to the PSF.

References

- Amara, A. and Quanz, S. P. (2012). PYNPOINT: an image processing package for finding exoplanets. *MNRAS*, 427:948–955.
- Avenhaus, H., Quanz, S. P., Meyer, M. R., Brittain, S. D., Carr, J. S., and Najita, J. R. (2014). HD100546 multi-epoch scattered light observations. *ApJ*, 790(1):56.
- Batalha, N. M., Rowe, J. F., Bryson, S. T., Barclay, T., Burke, C. J., Caldwell, D. A., Christiansen, J. L., Mullally, F., Thompson, S. E., Brown, T. M., Dupree, A. K., Fabrycky, D. C., Ford, E. B., Fortney, J. J., Gilliland, R. L., Isaacson, H., Latham, D. W., Marcy, G. W., Quinn, S. N., Ragozzine, D., Shporer, A., Borucki, W. J., Ciardi, D. R., Gautier, III, T. N., Haas, M. R., Jenkins, J. M., Koch, D. G., Lissauer, J. J., Rapin, W., Basri, G. S., Boss, A. P., Buchhave, L. A., Carter, J. A., Charbonneau, D., Christensen-Dalsgaard, J., Clarke, B. D., Cochran, W. D., Demory, B.-O., Desert, J.-M., Devore, E., Doyle, L. R., Esquerdo, G. A., Everett, M., Fressin, F., Geary, J. C., Girouard, F. R., Gould, A., Hall, J. R., Holman, M. J., Howard, A. W., Howell, S. B., Ibrahim, K. A., Kinemuchi, K., Kjeldsen, H., Klaus, T. C., Li, J., Lucas, P. W., Meibom, S., Morris, R. L., Prša, A., Quintana, E., Sanderfer, D. T., Sasselov, D., Seader, S. E., Smith, J. C., Steffen, J. H., Still, M., Stumpe, M. C., Tarter, J. C., Tenenbaum, P., Torres, G., Twicken, J. D., Uddin, K., Van Cleve, J., Walkowicz, L., and Welsh, W. F. (2013). Planetary Candidates Observed by Kepler. III. Analysis of the First 16 Months of Data. *ApJS*, 204:24.
- Berry, M. (1987). The adiabatic phase and pancharatnam's phase for polarized light. *J. Mod. Opt.*, 34(11):1401–1407.
- Bloemhof, E. E. (2003). Suppression of speckle noise by speckle pinning in adaptive optics. *The Astrophysical Journal Letters*, 582(1):L59.
- Borucki, W., Koch, D., Batalha, N., Caldwell, D., Christensen-Dalsgaard, J., Cochran, W. D., Dunham, E., Gautier, T. N., Geary, J., Gilliland, R., Jenkins, J., Kjeldsen, H., Lissauer, J. J., and Rowe, J. (2009). KEPLER: Search for Earth-Size Planets in the Habitable Zone. In Pont, F., Sasselov, D., and Holman, M. J., editors, *IAU Symposium*, volume 253 of *IAU Symposium*, pages 289–299.
- Carlotti, A. (2013). Apodized phase mask coronagraphs for arbitrary apertures. *A&A*, 551:A10.
- Carlotti, A., Kasdin, N. J., Vanderbei, R. J., and Riggs, A. J. E. (2013). Hybrid coronagraphic design: optimization of complex apodizers. In *Society of Photo-Optical Instrumentation Engineers (SPIE) Conference Series*, volume 8864 of *Society of Photo-Optical Instrumentation Engineers (SPIE) Conference Series*.
- Charbonneau, D., Brown, T. M., Latham, D. W., and Mayor, M. (2000). Detection of Planetary Transits Across a Sun-like Star. *ApJ*, 529:L45–L48.

- Codona, J. L. and Angel, R. (2004). Imaging Extrasolar Planets by Stellar Halo Suppression in Separately Corrected Color Bands. *ApJ*, 604:L117–L120.
- Codona, J. L., Kenworthy, M. A., Hinz, P. M., Angel, J. R. P., and Woolf, N. J. (2006). A high-contrast coronagraph for the MMT using phase apodization: design and observations at 5 microns and $2 \lambda/D$ radius. In *Society of Photo-Optical Instrumentation Engineers (SPIE) Conference Series*, volume 6269 of *Society of Photo-Optical Instrumentation Engineers (SPIE) Conference Series*.
- Guyon, O. (2005). Limits of Adaptive Optics for High-Contrast Imaging. *ApJ*, 629:592–614.
- Guyon, O., Pluzhnik, E. A., Galicher, R., Martinache, F., Ridgway, S. T., and Woodruff, R. A. (2005). Exoplanet imaging with a phase-induced amplitude apodization coronagraph. i. principle. *The Astrophysical Journal*, 622(1):744.
- Kasdin, N. J., Vanderbei, R. J., Littman, M. G., Carr, M., and Spergel, D. N. (2004). The shaped pupil coronagraph for planet finding coronagraphy: optimization, sensitivity, and laboratory testing. In *Society of Photo-Optical Instrumentation Engineers (SPIE) Conference Series*, volume 5487 of *Society of Photo-Optical Instrumentation Engineers (SPIE) Conference Series*.
- Kenworthy, M. A., Codona, J. L., Hinz, P. M., Angel, J. R. P., Heinze, A., and Sivanandam, S. (2007). First On-Sky High-Contrast Imaging with an Apodizing Phase Plate. *ApJ*, 660:762–769.
- Komanduri, R. K., Lawler, K. F., and Escuti, M. J. (2013). Multi-twist retarders: broadband retardation control using self-aligning reactive liquid crystal layers. *Opt. Express*, 21(1):404–420.
- Konopacky, Q. M., Barman, T. S., Macintosh, B., and Marois, C. (2013). Carbon and Oxygen in the Spectrum of HR 8799c. In *American Astronomical Society Meeting Abstracts #221*, volume 221 of *American Astronomical Society Meeting Abstracts*, page 126.03.
- Kostinski, A. B. and Yang, W. (2005). Pupil phase apodization for imaging of faint companions in prescribed regions. *Journal of Modern Optics*, 52:2467–2474.
- Lafrenière, D., Marois, C., Doyon, R., Nadeau, D., and Artigau, É. (2007). A New Algorithm for Point-Spread Function Subtraction in High-Contrast Imaging: A Demonstration with Angular Differential Imaging. *ApJ*, 660:770–780.
- Lyt, B. (1939). The study of the solar corona and prominences without eclipses (George Darwin Lecture, 1939). *MNRAS*, 99:580.
- Macintosh, B., Graham, J. R., Ingraham, P., Konopacky, Q., Marois, C., Perrin, M., Poyneer, L., Bauman, B., Barman, T., Burrows, A. S., Cardwell, A., Chilcote, J., De Rosa, R. J., Dillon, D., Doyon, R., Dunn, J., Erikson, D., Fitzgerald, M. P., Gavel, D., Goodsell, S., Hartung, M., Hibon, P., Kalas, P., Larkin, J., Maire, J., Marchis, F., Marley, M. S., McBride, J., Millar-Blanchaer, M., Morzinski, K., Norton, A., Oppenheimer, B. R., Palmer, D., Patience, J., Pueyo, L., Rantakyro, F., Sadakuni, N., Saddlemyer, L., Savransky, D., Serio, A., Soummer, R., Sivaramakrishnan, A., Song, I., Thomas, S., Wallace, J. K., Wiktorowicz, S., and Wolff, S. (2014). First light of the gemini planet imager. *Proceedings of the National Academy of Sciences*.

- Marois, C., Lafrenière, D., Doyon, R., Macintosh, B., and Nadeau, D. (2006). Angular Differential Imaging: A Powerful High-Contrast Imaging Technique. *ApJ*, 641:556–564.
- Marois, C., Macintosh, B., Barman, T., Zuckerman, B., Song, I., Patience, J., Lafrenière, D., and Doyon, R. (2008). Direct imaging of multiple planets orbiting the star hr 8799. *Science*, 322(5906):1348–1352.
- Marois, C., Zuckerman, B., Konopacky, Q. M., Macintosh, B., and Barman, T. (2010). Images of a fourth planet orbiting HR 8799. *Nature*, 468:1080–1083.
- Mawet, D., Absil, O., Delacroix, C., Girard, J. H., Milli, J., O’Neal, J., Baudoz, P., Boccaletti, A., Bourget, P., Christiaens, V., Forsberg, P., Gonté, F., Habraken, S., Hanot, C., Karlsson, M., Kasper, M., Lizon, J.-L., Muzic, K., Olivier, R., Peña, E., Slusarenko, N., Tacconi-Garman, L. E., and Surdej, J. (2013). L-band AGPM vector vortex coronagraph’s first light on VLT/NACO. Discovery of a late-type companion at two beamwidths from an F0V star. *A&A*, 552:L13.
- Mawet, D., Pueyo, L., Lawson, P., Mugnier, L., Traub, W., Boccaletti, A., Trauger, J. T., Gladysz, S., Serabyn, E., Milli, J., Belikov, R., Kasper, M., Baudoz, P., Macintosh, B., Marois, C., Oppenheimer, B., Barrett, H., Beuzit, J.-L., Devaney, N., Girard, J., Guyon, O., Krist, J., Mennesson, B., Mouillet, D., Murakami, N., Poyneer, L., Savransky, D., Vérinaud, C., and Wallace, J. K. (2012). Review of small-angle coronagraphic techniques in the wake of ground-based second-generation adaptive optics systems. In *Society of Photo-Optical Instrumentation Engineers (SPIE) Conference Series*, volume 8442 of *Society of Photo-Optical Instrumentation Engineers (SPIE) Conference Series*.
- Mawet, D., Riaud, P., Baudrand, J., Baudoz, P., Boccaletti, A., Dupuis, O., and Rouan, D. (2006). The four-quadrant phase-mask coronagraph: white light laboratory results with an achromatic device. *A&A*, 448:801–808.
- Mawet, D., Serabyn, E., Liewer, K., Hanot, C., McEldowney, S., Shemo, D., and O’Brien, N. (2009). Optical Vectorial Vortex Coronagraphs using Liquid Crystal Polymers: theory, manufacturing and laboratory demonstration. *Opt. Express*, 17:1902–1918.
- Mayor, M. and Queloz, D. (1995). A Jupiter-mass companion to a solar-type star. *Nature*, 378:355–359.
- Meshkat, T., Kenworthy, M. A., Quanz, S. P., and Amara, A. (2014). Optimized Principal Component Analysis on Coronagraphic Images of the Fomalhaut System. *ApJ*, 780:17.
- Miskiewicz, M. N. and Escuti, M. J. (2014). Direct-writing of complex liquid crystal patterns. *Opt. Express*, 22(10):12691–12706.
- Murakami, N., Nishikawa, J., Yokochi, K., Tamura, M., Baba, N., and Abe, L. (2010). Achromatic eight-octant phase-mask coronagraph using photonic crystal. *ApJ*, 714(1):772.
- Oppenheimer, B. R., Baranec, C., Beichman, C., Brenner, D., Burruss, R., Cady, E., Crepp, J. R., Dekany, R., Fergus, R., Hale, D., Hillenbrand, L., Hinkley, S., Hogg, D. W., King, D., Ligon, E. R., Lockhart, T., Nilsson, R., Parry, I. R., Pueyo, L., Rice, E., Roberts, J. E., Roberts,

- Jr., L. C., Shao, M., Sivaramakrishnan, A., Soummer, R., Truong, T., Vasisht, G., Veicht, A., Vescelus, F., Wallace, J. K., Zhai, C., and Zimmerman, N. (2013). Reconnaissance of the HR 8799 Exosolar System. I. Near-infrared Spectroscopy. *ApJ*, 768:24.
- Otten, G., Snik, F., Kenworthy, M., Codona, J., Escuti, M., and Miskiewicz, M. (2014). Vector apodizing phase plate coronagraph: prototyping, characterization and outlook. In *Society of Photo-Optical Instrumentation Engineers (SPIE) Conference Series*, volume 9151.
- Packham, C., Escuti, M., Ginn, J., Oh, C., Quijano, I., and Boreman, G. (2010). Polarization gratings: A novel polarimetric component for astronomical instruments. *Publications of the Astronomical Society of the Pacific*, 122(898):pp. 1471–1482.
- Packham, C., Jones, T. J., Warner, C., Krejny, M., Shenoy, D., Vonderharr, T., Lopez-Rodriguez, E., and DeWahl, K. (2012). Commissioning results of mmt-pol: the 1-5 μ m imaging polarimeter leveraged from the ao secondary of the 6.5m mmt. In *Society of Photo-Optical Instrumentation Engineers (SPIE) Conference Series*, volume 8446 of *Society of Photo-Optical Instrumentation Engineers (SPIE) Conference Series*.
- Pancharatnam, S. (1956). Generalized theory of interference, and its applications. part i. coherent pencils. In *Proceedings of the Indian Academy of Sciences, Section A*, volume 44, 5, pages 247–262. Indian Academy of Sciences.
- Quanz, S. P., Meyer, M. R., Kenworthy, M. A., Girard, J. H. V., Kasper, M., Lagrange, A.-M., Apai, D., Boccaletti, A., Bonnefoy, M., Chauvin, G., Hinz, P. M., and Lenzen, R. (2010). First results from very large telescope naco apodizing phase plate: 4 μ m images of the exoplanet beta pictoris b. *The Astrophysical Journal Letters*, 722(1):L49.
- Riaud, P., Mawet, D., and Magette, A. (2012). Instantaneous phase retrieval with the vector vortex coronagraph. *A&A*, 545:A151.
- Rodenhuis, M., Canovas, H., Jeffers, S. V., de Juan Ovelar, M., Min, M., Homs, L., and Keller, C. U. (2012). The extreme polarimeter: design, performance, first results and upgrades. In *Society of Photo-Optical Instrumentation Engineers (SPIE) Conference Series*, volume 8446 of *Society of Photo-Optical Instrumentation Engineers (SPIE) Conference Series*.
- Roelfsema, R., Schmid, H. M., Pragt, J., Gisler, D., Waters, R., Bazzon, A., Baruffolo, A., Beuzit, J.-L., Boccaletti, A., Charton, J., et al. (2010). The zimpol high-contrast imaging polarimeter for sphere: design, manufacturing, and testing. In *SPIE Astronomical Telescopes+ Instrumentation*, pages 77354B–77354B. International Society for Optics and Photonics.
- Skrutskie, M. F., Jones, T., Hinz, P., Garnavich, P., Wilson, J., Nelson, M., Solheid, E., Durney, O., Hoffmann, W., Vaitheeswaran, V., McMahon, T., Leisenring, J., and Wong, A. (2010). The Large Binocular Telescope mid-infrared camera (LMIRcam): final design and status. In *Society of Photo-Optical Instrumentation Engineers (SPIE) Conference Series*, volume 7735 of *Society of Photo-Optical Instrumentation Engineers (SPIE) Conference Series*.
- Snik, F., Otten, G., Kenworthy, M., Mawet, D., and Escuti, M. (2014). Combining vector-phase coronagraphy with dual-beam polarimetry. In *Society of Photo-Optical Instrumentation Engineers (SPIE) Conference Series*, volume 9147.

- Snik, F., Otten, G., Kenworthy, M., Miskiewicz, M., Escuti, M., Packham, C., and Codona, J. (2012). The vector-APP: a broadband apodizing phase plate that yields complementary PSFs. In *Society of Photo-Optical Instrumentation Engineers (SPIE) Conference Series*, volume 8450 of *Society of Photo-Optical Instrumentation Engineers (SPIE) Conference Series*.
- Sparks, W. B. and Ford, H. C. (2002). Imaging Spectroscopy for Extrasolar Planet Detection. *ApJ*, 578:543–564.
- Vigan, A., Moutou, C., Langlois, M., Mouillet, D., Dohlen, K., Boccaletti, A., Carillet, M., Smith, I., Ferrari, A., Mugnier, L., and Thalmann, C. (2010). Comparison of methods for detection and characterization of exoplanets with sphere/iridis. In *Society of Photo-Optical Instrumentation Engineers (SPIE) Conference Series*, volume 7735 of *Society of Photo-Optical Instrumentation Engineers (SPIE) Conference Series*.
- Wolszczan, A. and Frail, D. A. (1992). A planetary system around the millisecond pulsar PSR1257 + 12. *Nature*, 355:145–147.
- Yang, W. and Kostinski, A. B. (2003). Phase-modulated pupil for achromatic imaging of faint companions. *Physics Letters A*, 320(1):5 – 8.
- Yang, W. and Kostinski, A. B. (2004). One-sided achromatic phase apodization for imaging of extrasolar planets. *The Astrophysical Journal*, 605(2):892.
- Yaroshchuk, O. and Reznikov, Y. (2012). Photoalignment of liquid crystals: basics and current trends. *J. Mater. Chem.*, 22:286–300.

4 | Vector Apodizing Phase Plate coronagraph: prototyping, characterization and outlook

Abstract

The Apodizing Phase Plate (APP) is a phase-only pupil-plane coronagraph that suppresses starlight in a D-shaped region from 2 to $7 \lambda/D$ around a target star. Its performance is insensitive to residual tip-tilt variations from the AO system and telescope structure. Using liquid crystal technology we develop a novel and improved version of the APP: the broadband vector Apodizing Phase Plate (vAPP). The vAPP prototype consists of an achromatic half-wave retarder pattern with a varying fast axis encoding phase structure down to 25 microns. The fast axis encodes the required phase pattern through the vector phase, while multiple twisting liquid crystal layers produce a nearly constant half-wave retardance over a broad bandwidth. Since pupil phase patterns are commonly designed to be antisymmetric, two complementary PSFs are produced with dark holes on opposite sides.

We summarize results of the characterization of our latest vAPP prototype in terms of pupil phase reconstruction and PSF contrast performance. The liquid crystal patterning technique allows us to manufacture more extreme phase patterns than was possible before. We consider phase-only patterns that yield higher contrasts and better inner working angles than previous APPs, and patterns that produce dark regions 360 degrees around the PSF core. The possibility of including a phase ramp into the coronagraph is demonstrated, which simplifies the vAPP into a single optic. This additional phase ramp removes the need for a quarter-wave plate and a Wollaston prism, and enables the simplified implementation of a vAPP in a filter wheel at a pupil-plane location. Since the phase ramp is analogous to a polarization grating, it generates a (polarized) spectrum of a planet inside the dark hole, and thus allows for instantaneous characterization of the planet.

4.1 Introduction

The conceptually easiest way of suppressing light of a star is by physically blocking it at the focal plane, as is done with Lyot-type focal-plane coronagraphs. Light that diffracts around this blocking element is subsequently removed by a Lyot stop in the pupil plane. More exotic designs of Lyot-type coronagraphs using amplitude and/or phase techniques have been made that show excellent contrasts, but focal-plane devices are susceptible to pointing errors and vibrations in the optical system. Therefore, additional telescope vibrations cause starlight to leak from behind the coronagraph.

A class of coronagraphs exist which are insensitive to tip-tilt variations by being located in the pupil plane. The Apodizing Phase Plate (APP) coronagraph is a pupil plane coronagraph that only uses phase to suppress the diffraction pattern on one side of the star (Codona et al., 2006; Kenworthy et al., 2007). The power of the APP was most dramatically demonstrated in the case of VLT/NACO before 2011 when the star drifted in a circle during observations when pupil tracking was enabled, reducing the efficiency of Lyot-type coronagraphs until a fix was implemented (Girard et al., 2012). The APP coronagraph was not susceptible to this drifting. Residual tip-tilt variations remain an important limiting factor in coronagraphs installed in the latest generation of planet-finding instruments (e.g., GPI (Macintosh et al., 2014), SPHERE, SCEAO (Singh et al., 2014)). Substantial investments have to be made in order to create a system that keeps these variations at an acceptable level.

Despite the successes of the APP coronagraph (Kenworthy et al., 2007; Quanz et al., 2010; Quanz et al., 2013) and its ease of implementation, it has some limitations that are partly due to the manufacturing method. The commonly stated limitations of the APP coronagraph are the suppression of only one side of the PSF, the dependence of the phase delay on the wavelength, and limited contrast. We can overcome all these problems in by using a different manufacturing technique based on patterned liquid crystal retarders. The so-called vector APP (Snik et al., 2012; Otten et al., 2014) produces two complementary PSFs with broadband suppression $\frac{\delta\lambda}{\lambda} \approx 100\%$. Moreover this manufacturing technique allows for phase patterns that deliver higher raw contrast.

4.2 Vector Apodizing Phase Plate prototype

The classical Apodizing Phase Plate uses optical path difference to induce a phase as a function of pupil position. The phase delay arises from a varying optical path difference. This phase is highly dependent on the wavelength and any deviation from the design wavelength will create a phase pattern that is not optimal for suppression of starlight.

Instead of using optical path differences to create a phase delay across the pupil, the vAPP works with the vector phase, also known as Pancharatnam-Berry phase (Pancharatnam, 1956; Berry, 1984; Mawet et al., 2009), which arises when a beam of light hits a half-wave plate (HWP). This beam is decomposed into the two different circular polarization states. The HWP flips the handedness and imposes a phase delay depending on the orientation of the fast axis of the HWP. The vector phase $\Delta\phi$ of a birefringent retarder is given by

$$\Delta\phi = \pm 2 \cdot \theta \tag{4.1}$$

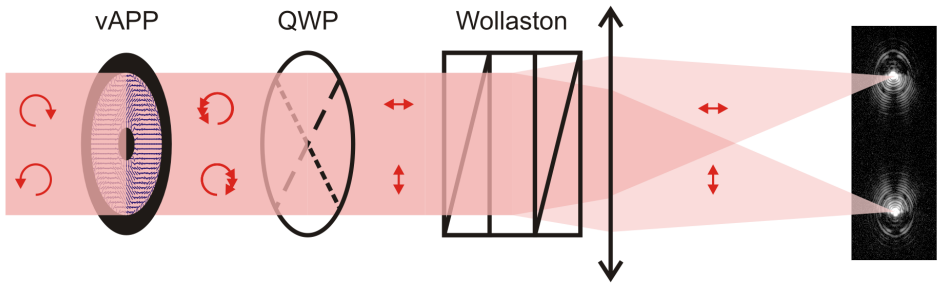


Figure 4.1: Working principle of the vAPP. Circular polarized light passing through the vAPP flips handedness and picks up a phase. The combination of quarter-wave plate and Wollaston prism splits the light based on circular polarization forming two PSFs on the focal plane. The focal plane image on the right was taken with the lab setup.

where θ is the local fast axis and the sign depends on the handedness of circular polarization. A beam-splitting step is required to separate the two circular polarization states with opposite phase patterns. This is implemented in Figure 4.1 with a quarter-wave plate and a Wollaston prism.

The phase delay of Equation 4.1 does not depend on the wavelength of the light and therefore is achromatic. When the HWP is not completely half-wave, a fraction of light will leak through unaberrated and contaminates the suppressed beam with the original PSF. Therefore, in order to be truly achromatic this HWP needs to be half-wave across the required wavelength range. Using liquid crystal technology it is possible to create patterned vector phase elements which retardance can be made achromatic over a large wavelength range. The patterning is enabled by a direct-write technique (Miskiewicz and Escuti, 2014) and the achromatization is accomplished with Multi-Twist Retarders (MTRs) (Komanduri et al., 2013). The vAPP consists of a substrate and a photoalignment polymer that aligns itself to the linear polarization direction of a UV laser that writes the desired pattern. Additional layers of chromatic birefringent liquid crystal align themselves with the layer underneath. By combining several layers together in a predetermined way, an increasingly achromatic retarder is built (Komanduri et al., 2013).

A prototype vector APP was constructed using these two manufacturing methods. It was specified to be within 11 degrees from half-wave retardance over the wavelength range of 500 to 900 nm. The active surface with the APP phase pattern has a 5.5 mm diameter with a 20% secondary obscuration. An opaque mask of the same dimensions was made, aligned to the HWP under a microscope and bonded with optical glue (Otten et al., 2014).

The properties of the prototype were verified using a polarimetric imaging method (Otten et al., 2014) and uses 8 images of the optic in between two polarizers at varying position angles. To assess the coronagraphic performance, the prototype was placed in an optical setup following the layout of Figure 4.1. The point spread function (PSF) was measured by looking at a white fiber-fed light source using narrowband filters from 500 to 800 nm. The corresponding PSFs for different wavelengths can be seen in Figure 4.2. To demonstrate the raw contrast that can be reached with this plate, the PSFs at 750 nm were converted to contrast curves by azimuthally averaging the flux in the dark hole and dividing it by the peak flux of the PSF. Both measured PSFs match each other well. The model of the contrast curve includes the non-ideal properties of

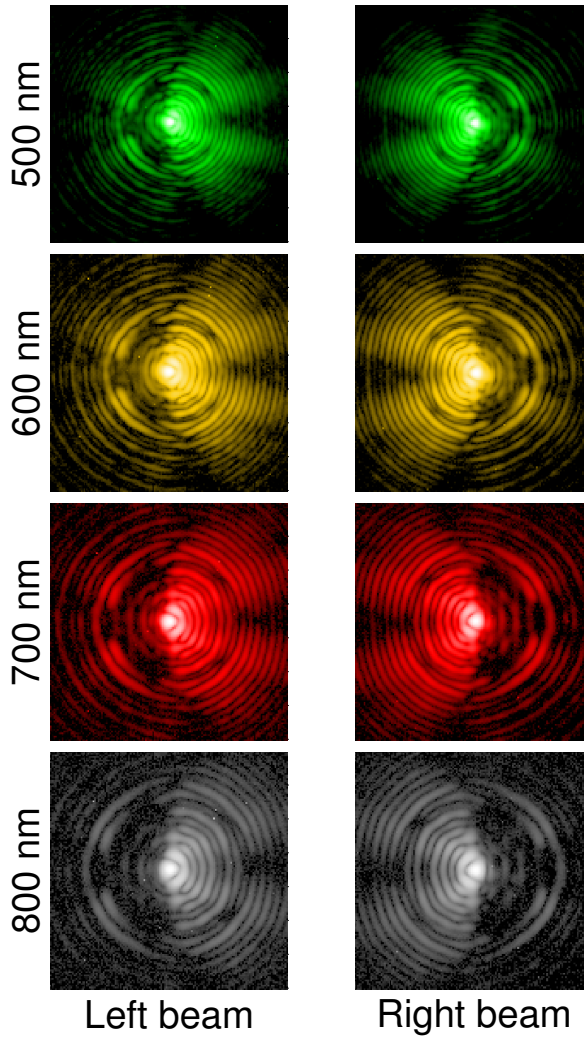


Figure 4.2: Simultaneously taken images of Left and Right PSFs from 500 to 800 nanometers showing a dark hole at all wavelengths on both sides of the star.

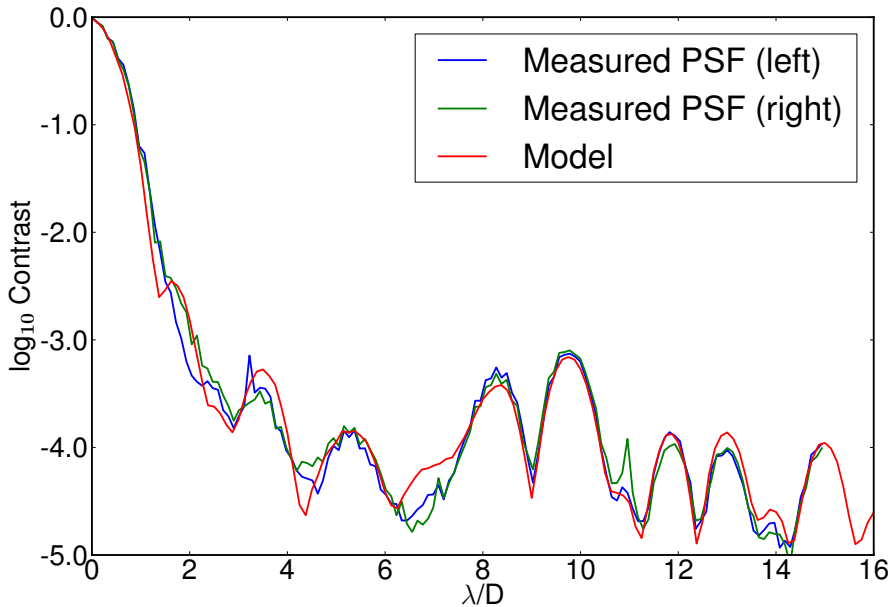


Figure 4.3: Contrast of Left and Right PSFs measured in a wedge centered on the dark hole compared to a forward model that is based on the measured properties of the coronagraph.

the vAPP as measured in the lab. This model matches the measured PSF data (as seen in Fig. 4.3) and confirms the validity of our model.

The one factor that limits the contrast most is the retardance offset from half-wave as presented in Figure 4.4. The same figure also presents designs with more layers that yield superior retardance performance. Future revisions should therefore focus on improving the retardance or mitigating the effect it has on the contrast.

4.3 New opportunities

The liquid crystal patterning technique gives high control over the phase of the optic, especially in terms of spatial frequencies that were not offered by the traditional diamond turning technique. It also allows for a natural match with polarization tricks and polarimetric techniques (Snik et al., 2014). This gives a lot of options to improve the coronagraph.

4.3.1 Integration of beam splitting

The vector Apodizing Phase Plate requires a combination of a quarter-wave plate and a Wollaston prism in order to split based on the circular polarization (Figure 4.1). This adds two extra optical elements in the path that have to be both broad-band and properly aligned. Therefore, despite

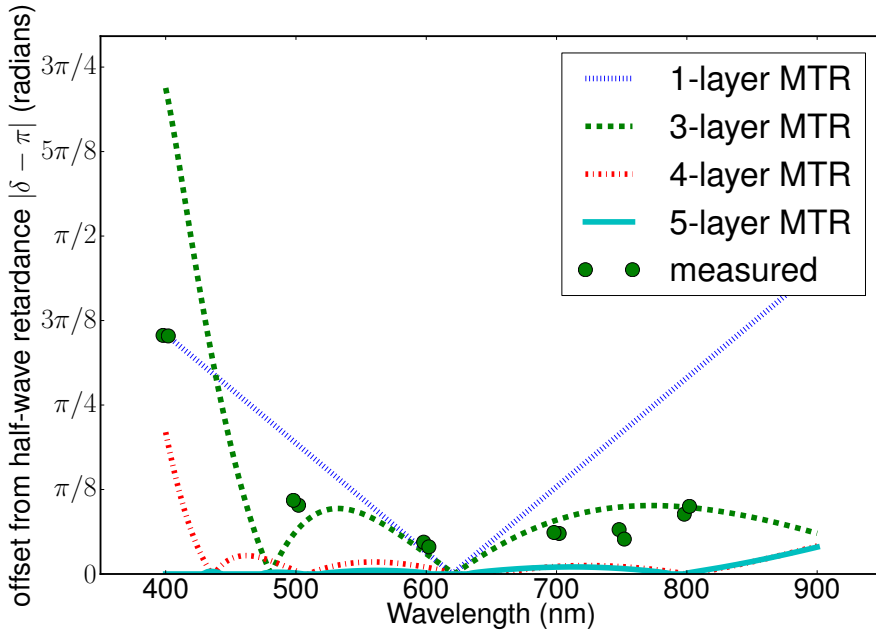


Figure 4.4: Offset from half-wave retardance of the plate as theoretically expected for several layered designs and measured in the lab. The three-layer recipe denoted with the green line was used for the optic that was tested. The corresponding measurements are shown in green circles.

being an improved version of the APP it complicates the installation at telescopes.

Another way of splitting the PSFs is by applying a tip-tilt phase ramp to the APP phase pattern itself, as is shown in Figure 4.5. Depending on the circular polarization of the beam it will either deflect in one direction or the other while still maintaining the APP phase pattern. Since the splitting is now done by the tip-tilt phase, the QWP and Wollaston are no longer needed. The errors associated with them are consequently absent. The coronagraph is again reduced to a single optic in the pupil plane.

Any leakage term is not deflected and passes straight through, forming an image between the two APP PSFs, and avoiding contrast loss in the APP PSFs. It is possible to observe outside of the designed wavelength range in exchange for greater leakage losses. The phase ramp is a polarization grating (Packham et al., 2010; Oh and Escuti, 2008) and therefore disperses the split PSFs as a function of wavelength. This limits the spectral bandwidth that can be used for observing due to wavelength smearing, although a single optic can still be used with multiple narrow/intermediate band filters.

In Figure 4.6 we simulate the effect of a 10% bandwidth beam of light through this optic with a retardance of 0.45 waves. The leakage term of the half-wave plate ends up between the two APP PSFs and does not impact the contrast. It is also possible to exploit this splitting effect to obtain low resolution spectra of the planet.

For the three layer device, the leakage term contains a few percent of the total light through the

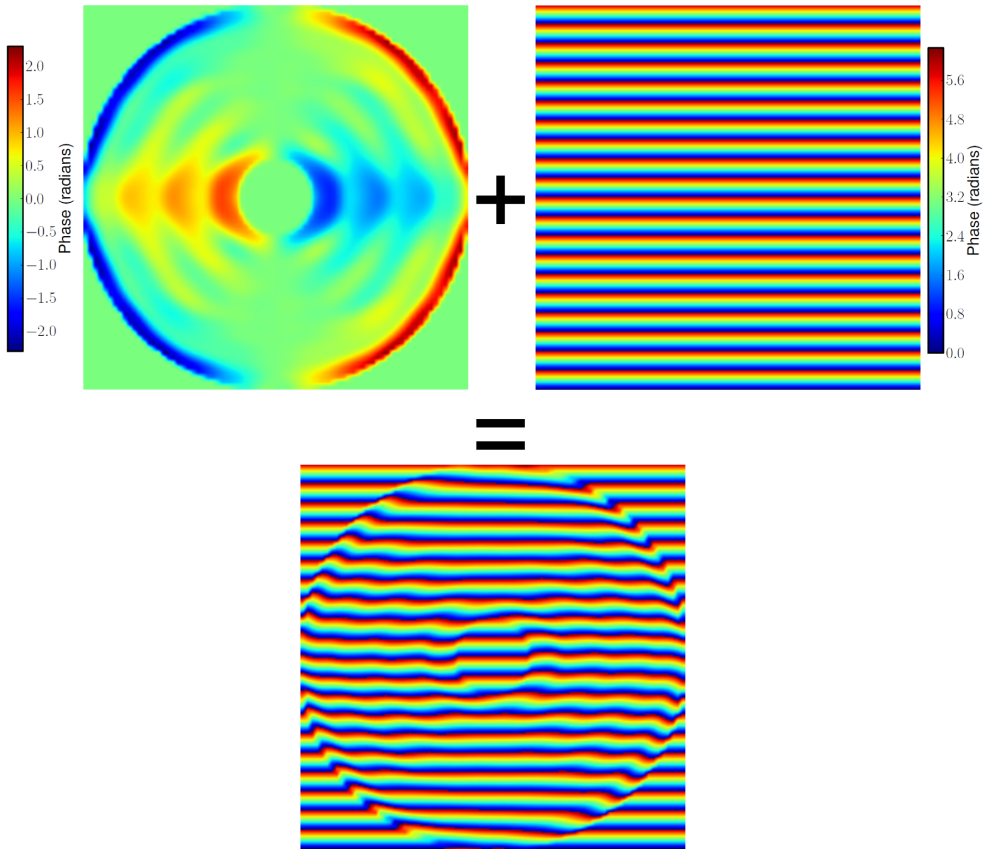


Figure 4.5: The two top images show a phase pattern for creating a dark hole on one side of the star and a tip-tilt phase pattern that moves the star to one side. The combined phase pattern in the bottom panel therefore suppresses the starlight in complementary sides of the PSF and simultaneously splits the beams.

coronagraph. This third unaberrated PSF can be used as a photometric and astrometric reference source, as it is not saturated and remains unaltered by the phase pattern on the plate. Furthermore, it opens up the possibility of using phase diversity wavefront estimation methods to measure the wavefront in the focal plane. (Gonsalves, 1982; Blanc et al., 2003; Riaud, P. et al., 2012)

4.3.2 Aggressive phase patterns

The direct-write method offers control over the phase with a spatial resolution of at least 10 microns (Miskiewicz and Escuti, 2014). In contrast to diamond-turning methods, the phase pattern can be made with rapidly changing phases over very small spatial scales. It is therefore possible to realize phase patterns that have higher contrast than the diamond-turning optimized patterns of the previous APP. Many phase pattern solutions with theoretically high contrasts have been obtained (Carlotti, 2013; Codona and Angel, 2004). All of these are anti-symmetric and therefore produce two PSFs with complementary dark holes in a vector APP configuration.

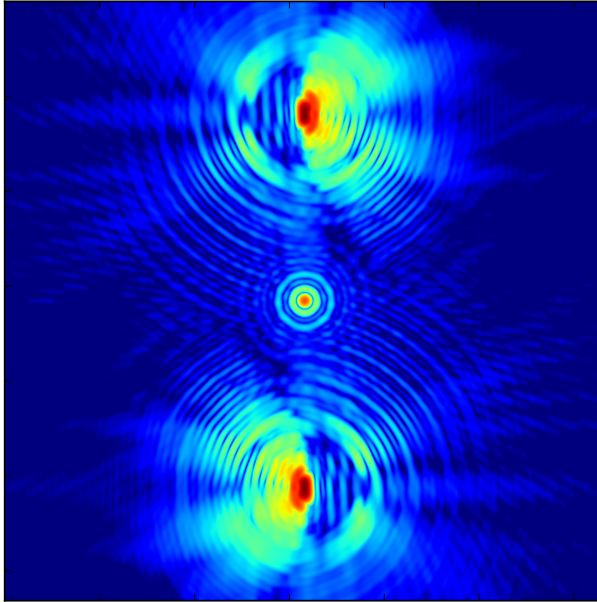


Figure 4.6: Simulated PSF of the APP pattern with a ramp of phase added. The bandwidth was set to 10% and the retardance of the HWP was set to 0.45 waves. The leakage term ends up between the two PSFs and consequently does not impact the contrast.

4.3.3 360 degree suppression

In the process of looking for APP solutions, phase-only solutions that are not anti-symmetric were found (Codona, private communications). One specific phase design that was encountered produces a 360 degree dark ring around the PSF core. A vAPP prototype with this 360 degree pattern was made using the aforementioned manufacturing method and is shown in Figure 4.7.

The theoretical PSF for this phase pattern is shown in Figure 4.8. Note that for a vAPP implementation this PSF is only obtained for one circular polarization. The Strehl ratio of this design is 0.176 and has a contrast of $\approx 10^{-5}$ in a 360 degree region between 2 and $8 \lambda/D$. To verify the reality of this solution we implemented this phase pattern with a spatial light modulator (Korkiakoski et al., 2013) with the preliminary result for the PSF shown in Figure 4.9. Further research with the 360 degree vAPP is ongoing.

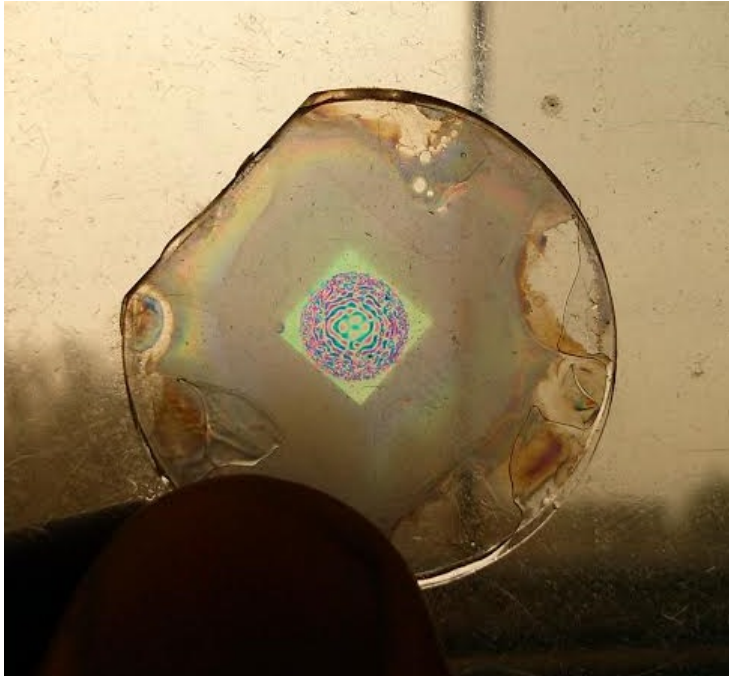


Figure 4.7: Image of 360 degree suppressing phase pattern made using the liquid crystal patterning technique. It can be seen that the pattern at the edge of the phase pattern is very aggressive and could not have been manufactured without the direct-write method.

4.4 Conclusion

In this paper we describe the prototyping of the first achromatic vector APP and its characterization. We demonstrate that the coronagraph meets its design specifications between 500 and 800 nanometers and provides $10^{-3.8}$ contrast in complementary dark holes between 2 and $7 \lambda/D$. After successful prototyping we further develop the vAPP concept. By adding a phase ramp to the APP pattern, it is possible to make a simplified version of the vAPP that can be easily implemented into existing telescopes at the cost of limited spectral bandwidth. This version is extremely robust against offsets from half-wave retardance. The manufacturing technique allows us to locally encode a certain phase with a very high spatial resolution which allows us to create phase patterns that have a better contrast than the previous versions and it is now possible to create phase patterns with 360 degree suppression around the PSF core.

The use of the MTR class of half-wave plates is not limited to the visible band but by choosing a different substrate and liquid crystal compounds devices can also be made to work at the NIR/Thermal IR. We are currently implementing vector APP coronagraphs at large telescopes such as the LBT and Magellan to directly image extrasolar planets at infrared wavelengths.

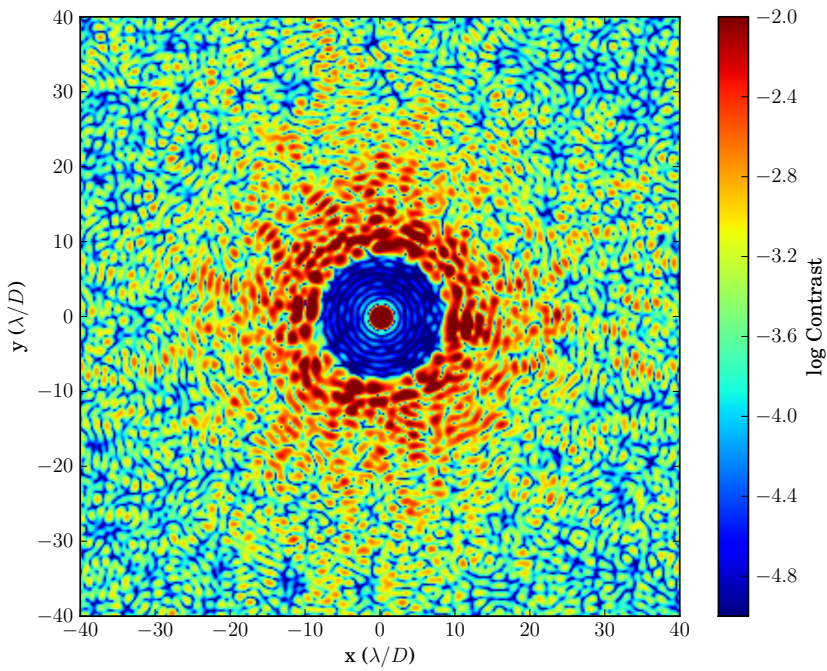


Figure 4.8: Theoretical PSF of a 360 degree suppressing APP pattern. Between 2 and 7 λ/D the contrast is about 10^{-5} .

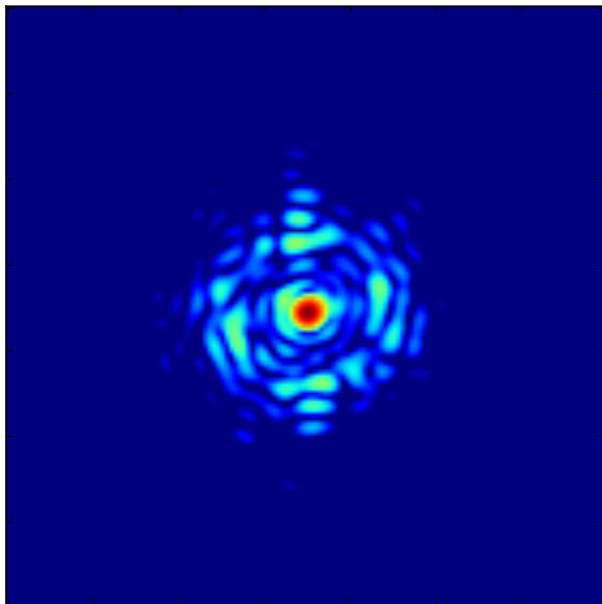


Figure 4.9: Measured laboratory PSF of a 360 degree suppressing APP pattern simulated with a spatial light modulator. It is seen that the light is suppressed in a circular region and moved outward.

Acknowledgments

The authors would like to thank Alex Pietrow and Visa Korhikoski for their support with the laboratory setup. This work is part of the research programme Instrumentation for the E-ELT, which is partly financed by the Netherlands Organisation for Scientific Research (NWO).

References

- Berry, M. V. (1984). Quantal Phase Factors Accompanying Adiabatic Changes. *Royal Society of London Proceedings Series A*, 392:45–57.
- Blanc, A., Fusco, T., Hartung, M., Mugnier, L., and Rousset, G. (2003). Calibration of naos and conica static aberrations. *Astronomy and Astrophysics*, 399(1):373–383.
- Carlotti, A. (2013). Apodized phase mask coronagraphs for arbitrary apertures. *A&A*, 551:A10.
- Codona, J. L. and Angel, R. (2004). Imaging Extrasolar Planets by Stellar Halo Suppression in Separately Corrected Color Bands. *ApJ*, 604:L117–L120.
- Codona, J. L., Kenworthy, M. A., Hinz, P. M., Angel, J. R. P., and Woolf, N. J. (2006). A high-contrast coronagraph for the MMT using phase apodization: design and observations at 5 microns and 2 λ/D radius. In *Society of Photo-Optical Instrumentation Engineers (SPIE) Conference Series*, volume 6269 of *Society of Photo-Optical Instrumentation Engineers (SPIE) Conference Series*.
- Girard, J. H. V., O’Neal, J., Mawet, D., Kasper, M., Zins, G., Neichel, B., Kolb, J., Christiaens, V., and Tourneboeuf, M. (2012). Image quality and high contrast improvements on vlt/naco. In *Proc. SPIE*, volume 8447, pages 84470L–84470L–14.
- Gonsalves, R. A. (1982). Phase retrieval and diversity in adaptive optics. *Optical Engineering*, 21(5):215829–215829–.
- Kenworthy, M. A., Codona, J. L., Hinz, P. M., Angel, J. R. P., Heinze, A., and Sivanandam, S. (2007). First On-Sky High-Contrast Imaging with an Apodizing Phase Plate. *ApJ*, 660:762–769.
- Komanduri, R. K., Lawler, K. F., and Escuti, M. J. (2013). Multi-twist retarders: broadband retardation control using self-aligning reactive liquid crystal layers. *Opt. Express*, 21(1):404–420.
- Korkiakoski, V., Doelman, N., Codona, J., Kenworthy, M., Otten, G., and Keller, C. U. (2013). Calibrating a high-resolution wavefront corrector with a static focal-plane camera. *Appl. Opt.*, 52:7554.
- Macintosh, B., Graham, J. R., Ingraham, P., Konopacky, Q., Marois, C., Perrin, M., Poyneer, L., Bauman, B., Barman, T., Burrows, A. S., Cardwell, A., Chilcote, J., De Rosa, R. J., Dillon, D., Doyon, R., Dunn, J., Erikson, D., Fitzgerald, M. P., Gavel, D., Goodsell, S., Hartung, M., Hibon, P., Kalas, P., Larkin, J., Maire, J., Marchis, F., Marley, M. S., McBride, J., Millar-Blanchaer, M., Morzinski, K., Norton, A., Oppenheimer, B. R., Palmer, D., Patience,

- J., Pueyo, L., Rantakyro, F., Sadakuni, N., Saddlemyer, L., Savransky, D., Serio, A., Soummer, R., Sivaramakrishnan, A., Song, I., Thomas, S., Wallace, J. K., Wiktorowicz, S., and Wolff, S. (2014). First light of the gemini planet imager. *Proceedings of the National Academy of Sciences*, 111(35):12661–12666.
- Mawet, D., Serabyn, E., Liewer, K., Hanot, C., McEldowney, S., Shemo, D., and O'Brien, N. (2009). Optical Vectorial Vortex Coronagraphs using Liquid Crystal Polymers: theory, manufacturing and laboratory demonstration. *Optics Express*, 17:1902–1918.
- Miskiewicz, M. N. and Escuti, M. J. (2014). Direct-writing of complex liquid crystal patterns. *Opt. Express*, 22(10):12691–12706.
- Oh, C. and Escuti, M. J. (2008). Achromatic diffraction from polarization gratings with high efficiency. *Opt. Lett.*, 33(20):2287–2289.
- Otten, G. P. P. L., Snik, F., Kenworthy, M. A., Miskiewicz, M. N., and Escuti, M. J. (2014). Performance characterization of a broadband vector apodizing phase plate coronagraph. *Opt. Express*, 22(24):30287–30314.
- Packham, C., Escuti, M., Ginn, J., Oh, C., Quijano, I., and Boreman, G. (2010). Polarization gratings: A novel polarimetric component for astronomical instruments. *Publications of the Astronomical Society of the Pacific*, 122(898):pp. 1471–1482.
- Pancharatnam, S. (1956). Generalized theory of interference, and its applications. part i. coherent pencils. In *Proceedings of the Indian Academy of Sciences, Section A*, volume 44,5, pages 247–262. Indian Academy of Sciences.
- Quanz, S. P., Amara, A., Meyer, M. R., Kenworthy, M. A., Kasper, M., and Girard, J. H. (2013). A Young Protoplanet Candidate Embedded in the Circumstellar Disk of HD 100546. *ApJ*, 766:L1.
- Quanz, S. P., Meyer, M. R., Kenworthy, M. A., Girard, J. H. V., Kasper, M., Lagrange, A.-M., Apai, D., Boccaletti, A., Bonnefoy, M., Chauvin, G., Hinz, P. M., and Lenzen, R. (2010). First results from very large telescope naco apodizing phase plate: 4 um images of the exoplanet beta pictoris b. *The Astrophysical Journal Letters*, 722(1):L49.
- Riaud, P., Mawet, D., and Margette, A. (2012). Instantaneous phase retrieval with the vector vortex coronagraph. *A&A*, 545:A151.
- Singh, G., Guyon, O., Baudoz, P., Jovanovich, N., Martinache, F., Kudo, T., Serabyn, E., and Kuhn, J. G. (2014). Lyot-based low order wavefront sensor: implementation on the subaru coronagraphic extreme adaptive optics system and its laboratory performance. In *Proc. SPIE*, volume 9148, pages 914848–914848–9.
- Snik, F., Otten, G., Kenworthy, M., Mawet, D., and Escuti, M. (2014). Combining vector-phase coronagraphy with dual-beam polarimetry. In *Proc. SPIE*, volume 9147, pages 91477U–91477U–12.
- Snik, F., Otten, G., Kenworthy, M., Miskiewicz, M., Escuti, M., Packham, C., and Codona, J. (2012). The vector-APP: a broadband apodizing phase plate that yields complementary PSFs. In *Proc. SPIE*, volume 8450.

5 | First on-sky demonstration of the vector Apodizing Phase Plate on LBT/LMIRCam

Abstract

We present the first on-sky observations of the grating vector Apodizing Phase Plate coronagraph that can suppress both sides of a star using a single pupil-plane optic. A linear phase ramp is added to the APP phase pattern and both are encoded in the fast axis of a single layer of liquid crystals. The linear ramp makes the coronagraph robust against half-wave retardance offsets by creating a third PSF between the two coronagraphic PSFs. An optic was produced for LBT/LMIRCam, optimized for 4 microns and was used to expose on Regulus for 220 seconds in the narrow-band Brackett Alpha filter. The performance of the coronagraph in this initial test is shown through simulations to be affected by pupil misalignment and a wavefront error in the optics. The pupil misalignment is measured to be 15% in X and 2% in Y. To match the shape of the leakage term PSF our simulation requires 0.7 radians RMS of common wavefront error in the form of astigmatism. Using a more advanced turbulence model we predict that after correction of these two factors, the coronagraph can reach a 5σ sensitivity of approximately 11 magnitudes at $2.5 \lambda/D$ around bright stars in one hour of observing time.

G. P. P. L. Otten, F. Snik, M. A. Kenworthy, A. Skemer, J. L. Codona, M. Montoya, P. Hinz, M. N. Miskiewicz, L. Brickson, M. J. Escuti, C. U. Keller, V. Bailey, M. Skrutskie, J. Leisenring, A. Vaz, D. Defrere.

5.1 Introduction

The Apodizing Phase Plate coronagraph is a pupil plane phase-only coronagraph. It is located in the pupil plane and is therefore insensitive to tip-tilt variations. The coronagraph works by using an optical path difference to delay the phase of a beam of light across the pupil (Codona and Angel, 2004; Codona et al., 2006). This optical path difference is typically carved out of a high refractive index substrate using a diamond turning method. The biggest limitation of this method is that the optical path difference is inherently chromatic. Nonetheless, this tip-tilt insensitive coronagraph has been used to detect and characterize exoplanets in the near-infrared with great success (Kenworthy et al., 2007; Quanz et al., 2010; Quanz et al., 2013).

The vector Apodizing Phase Plate coronagraph (vAPP) is a modified version of the APP coronagraph that uses birefringent liquid crystals to create a phase pattern that is achromatic across a broad wavelength range (Snik et al., 2012). This vAPP has been tested in the lab in Chapter 3, has proven to be broad-band, and suppresses two sides of the star simultaneously. Unfortunately the original design requires two extra optical components for circular polarization splitting of the beam into two PSFs, which complicates installation into telescopes. Furthermore it is sensitive to the offset from half-wave retardance which creates a leaked copy of the original PSF. Depending on the amount of offset from half-wave retardance, this leakage term can destroy the contrast in the dark hole. In Chapter 4 the grating-vAPP was presented that can be implemented using a single pupil plane optic and is substantially less impacted by the leakage. A side-effect of the grating is that it disperses the light in one dimension so, to keep the lateral smearing small, the filter full width half maximum bandwidths are limited to about $\Delta\lambda/\lambda = 5\%$ unless the dispersion is taken into account during reduction. In this paper we present first on-sky results of this robust grating-vAPP (gvAPP) at thermal infrared wavelengths with LBT/LMIRCam.

5.2 Principle of the grating-vAPP optic

The grating-vAPP works by adding a phase ramp to the normal APP phase pattern (see Fig. 5.1). Depending on the input polarization, the PSF will deflect to one side or the other and pick up the APP phase necessary to suppress one side of the star. Both sides of the star are thereby covered in one shot. The splitting angle becomes dependent on λ/D and the linear phase ramp therefore acts as a grating.

The plate is optimized for a central wavelength of 4 microns and uses a single layer of liquid crystals that is tuned to be half-wave at that wavelength. The working angle of the phase design is from 2 to 7 λ/D with an average normalized intensity structure in the dark hole of 10^{-4} . The separation between both PSFs was chosen to be 40 λ/D so the wings of one PSF do not significantly alter the contrast of the other PSF, yet are still small enough to fit on the $\sim 100 \times 100 \lambda/D$ field of view of the IR detector. The main substrate consists out of a 1.1 mm thick piece of CaF₂ (see Fig. 5.2). On this substrate a pixelated aluminum aperture mask with an undersized LBT aperture shape is deposited. A second 0.2 mm thin substrate of borosilicate glass¹ is used to deposit a patterned alignment layer and liquid crystal layer to produce a near half-wave retardance at 4.05 microns. Both substrates are bonded together with optical glue (NOA-61). The plate does

¹ the originally planned AR-coated CaF₂ substrate was (by error) coated like a mirror

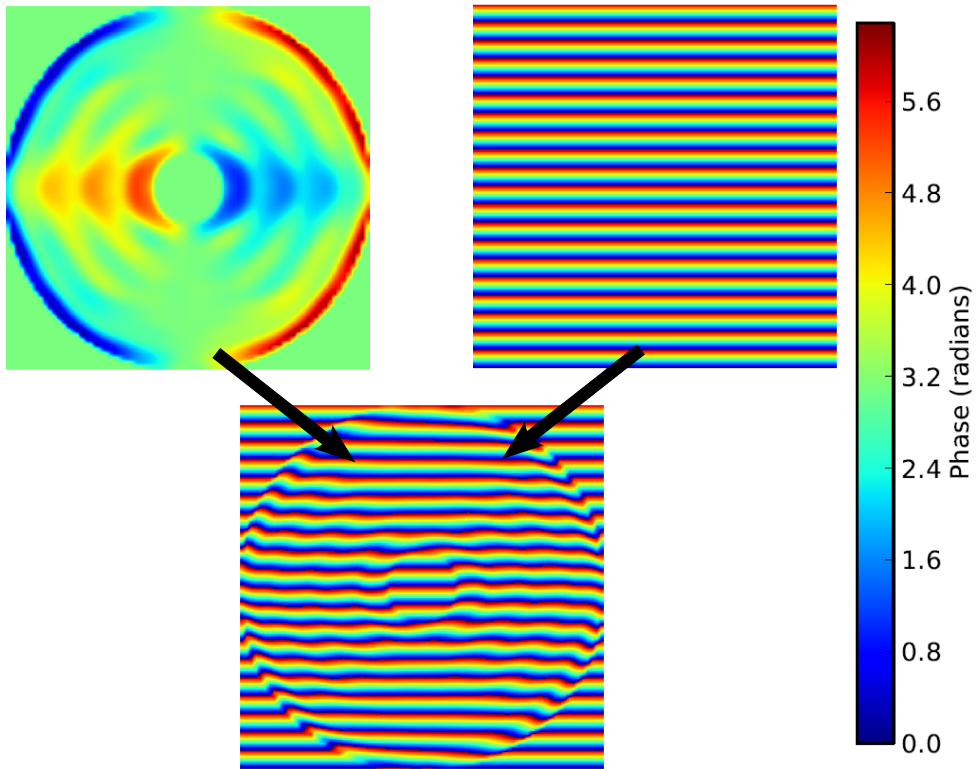


Figure 5.1: Combination of APP phase pattern and phase ramp creates new pattern that splits and suppresses PSF in one layer.

not have an anti-reflection coating, so ghosts are moved away from the science PSFs by putting the coronagraph at a tilt of about 1.5 degrees in the pupil wheel holder. The expected throughput of the plate is summed up in Table 5.1 and broken down into separate layers. Both the borosilicate cover slip and the bonding glue are shown to be poor transmitters and alternatives should be used to improve the transmission. The best alternative for the cover slip is the originally planned CaF_2 substrate.

The grating-vAPP creates three PSFs of the same target. Two of the PSFs will have oppositely suppressed D-shaped regions while the center PSF will have a regular PSF. The brightness of the central PSF with respect to the coronagraphic PSFs depends on the retardance of the plate. A perfect half-wave plate will have no central leakage, while a N -wave retarder will have no coronagraphic PSFs. The advantages of the grating-vAPP are therefore that it is a single pupil plane optic; that it separates the leakage term from the science PSFs, and that it is insensitive to tip-tilt variations. This enables the use of nodding for background subtraction at thermal infrared wavelengths. The disadvantage is that the plate smears the PSF in one dimension when using broad-band filters, as it acts as a grating. This plate is therefore ideal for observations close to the star and provides a 360 degree field of view around the star in a single shot. A single vAPP can

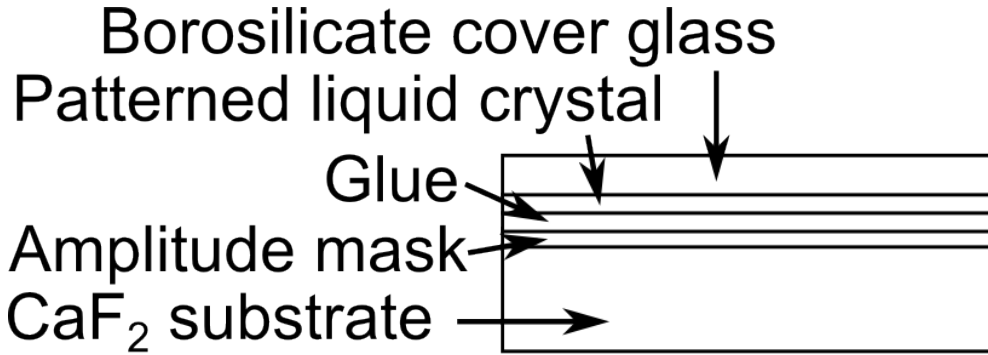


Figure 5.2: Schematic overview of the different layers in the coronagraph.

Table 5.1: Table describing the thickness and transmission properties of the different layers.

layers	material	thickness	3.2 micron	4.0 micron
vacuum-CaF ₂ boundary	-	-	0.970	0.971
substrate	CaF ₂	1.23 mm	0.944	0.940
amplitude mask	evaporated aluminum	180 nm	-	-
bonding glue	NOA-61 epoxy	0.01 mm	0.752	0.959
retarder layer	Merck RMS09-025	0.0075 mm	0.943	0.920
alignment layer	polymer LIA-C001	50 nm	-	-
cover slip	borosilicate 12-540-C	0.21 mm	0.876	0.619
vacuum-boro boundary	-	-	~ 0.97	~ 0.97
theoretical throughput	-	-	0.569	0.498
measured throughput	-	-	0.55	not measured

span a broad wavelength range when a multi-layer liquid crystal design is used to achromatize the half-wave performance.

5.3 Observations

The vector Apodizing Phase Plate saw first light with the LMIRCam instrument at the Large Binocular Telescope on November 4th 2014 at 13:02:02 UT. The dataset was taken of Regulus (B7V, $L = 1.66$; van Belle and von Braun (2009); Koornneef (1983)) using the Brackett Alpha filter (4.02 – 4.09 microns). The telescope is moved between alternating beam positions to enable background subtraction using beam-switching. Each beam position consists of 50 exposures of 0.7860 seconds in duration. The telescope is then moved to the second beam position 10 arcseconds away. Fourteen sequences of 50 exposures are taken alternating between the two beam positions. The total exposure time on target is 275.09 seconds. The start of the sequence is at 13:02:02 UT and ends at 13:16:42 UT on November 4th, 2014. The cores of the PSFs are saturated, and so a second set of 50 images with a exposure time of 0.611 seconds (each a coadd

of three 0.204 second images) provide photometric calibration. The DIMM seeing was approximately 1.2 arcseconds, air temperature of -5.5 degrees Centigrade and a local wind speed of 1.2 m/s coming from 150 degrees east from north.

5.3.1 Data reduction

The dataset is reduced by taking the median of each 'off' nod stack of images and subtracting it from every image of the preceding 'on' nod. The centroid of the leakage term is determined for every reduced frame on target using a Gaussian fit to the intensity of the Airy core. The images are shifted to a sub-pixel level with these coordinates. A subset of images is selected by taking only the images where the AO system has a stable lock on the turbulence. This selection is done by subtracting every image by the mean and taking the standard deviation in a 38 by 38 pixel box in the dark hole. After sorting based on the standard deviation, 80% of the images with lowest noise are selected. This is the tipping point where adding increasingly turbulent images decreases the signal to noise. This reduces the total amount of total images in the stack from 350 to 280. After shifting, the images are stacked by taking the average across the 280 'on' images. After this selection the on-target exposure time totals 220.07 seconds.

5.4 On-sky performance of gvAPP

5.4.1 PSF modeling

After visually inspecting the stacked image we immediately notice that the vAPP PSF deviates from the ideal PSF. We use the PSF model from Chapter 3 to simulate the PSF by introducing estimates for the pupil misalignment, retardance, wavefront errors and residual AO halo. In this way we can model the impact of contrast degrading effects.

In Chapter 3 we show that the vector-APPs are primarily limited by the offset from half-wave retardance. The variant of the vAPP described in this Chapter is designed to be less susceptible to these offsets. By comparing the flux ratio between the two vAPP PSFs and the leakage term, we can adjust the offset from half-wave retardance of the model to fit this ratio. A modeled retardance of 2.75 radians is consistent with the measured ratio between the leakage term and coronagraphic PSFs.

Using pupil images of the telescope, both with and without the vAPP coronagraph in the beam, we see how well aligned the telescope pupil is with respect to the coronagraph. We detect that the telescope pupil position is misaligned by 15% in the X-direction and 2% in the Y-direction with respect to the diameter of the coronagraph mask. Using this amount of misalignment we model the pupil transmission by overlaying the two pupil shapes of both the coronagraphic mask and the telescope. The misaligned pupil is inserted into the model.

By looking at the shape of the leakage term PSF, it is apparent that there is a significant amount of astigmatism present in the optical system. The leakage term is unaffected by the geometric phase and should therefore be identical to the regular LBT PSF. We add a common wavefront aberration to both beams to model the PSF shape. After adding 0.7 radians RMS of astigmatism, with a ratio of 5:1 between orthogonal modes, the ratio between the peak of the leakage term and its sidelobes match the observations. The ratio between orthogonal states of astigmatism effectively

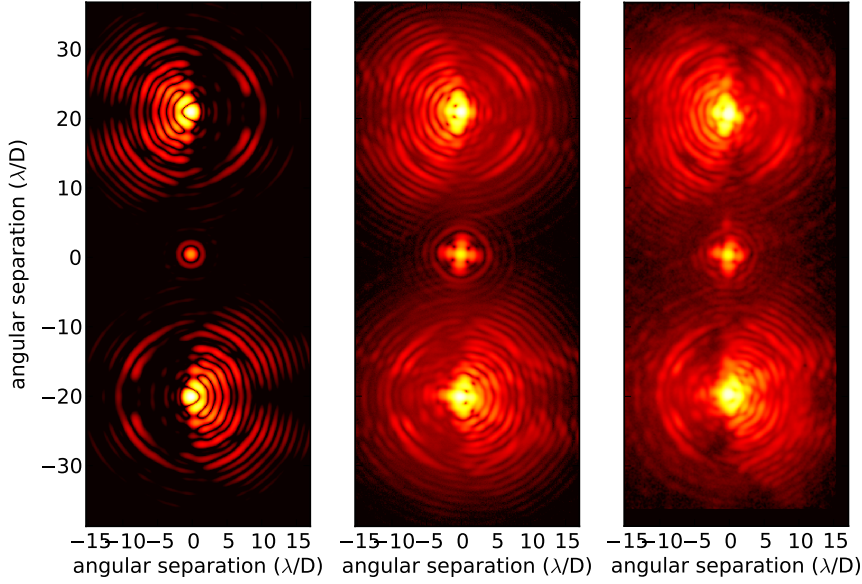


Figure 5.3: Theory, simulation and observation of the first light dataset taken with the narrow-band Brackett Alpha filter. The leakage term can be seen between the two PSFs.

rotates the aberrated PSF. All four lobes have roughly the same intensity, showing that defocus is not a significant component of the wavefront error. The presence of defocus would relatively intensify the lobes along one dimension with respect to the other. The source of this astigmatism is suspected to be a thermal expansion coefficient mismatch in two bonded substrates that warp when cooled. This substrate mismatch is easily resolved in a next vAPP design.

To model the residual AO halo we add a Gaussian centered on every APP PSF with a σ of 65 pixels (equivalent to 0.66 arcseconds) and a peak value of $9 \cdot 10^{-4}$ in normalized intensity. A third Gaussian is added to the central leakage term by another scaling with the ratio between the leakage terms and the APP PSFs. This halo creates a good match between the model and the observations in the radial intensity profile at large angular separations, as is seen in Fig. 5.3.

Figure 5.3 shows (from left to right) the typically expected PSFs assuming no errors apart from retardance offsets; the performance including telescope errors, residual AO halo and half-wave offset tuned to match dataset; and finally the observed image.

To show that the model matches the data we plot the normalized intensity profiles in Figure 5.4. The normalized intensity is calculated by taking azimuthal averages of the flux in annular rings in a 140 degree wedge and dividing it by the peak flux of the unsaturated dataset (scaled to the saturated images). The saturation of the core is the reason why the curve does not go through the coordinate (0,1). The profiles of the model and the data are consistent with each other.

To get an estimate of the Strehl ratio supplied by the AO system we plot the encircled energy (EE) of the previous PSF model, with and without the Gaussian halo contribution. The encircled energy is calculated by summing all the flux within a radius of r and afterwards normalizing with the highest value (at highest r). In Figure 5.5, we plot EE curves for both cases. The ratio of the EE at $1 \lambda/D$ shows that the Strehl ratio of the AO system is 85%. This Strehl ratio is typical for LBT/LMIRCam and the AO performance at 4 microns.

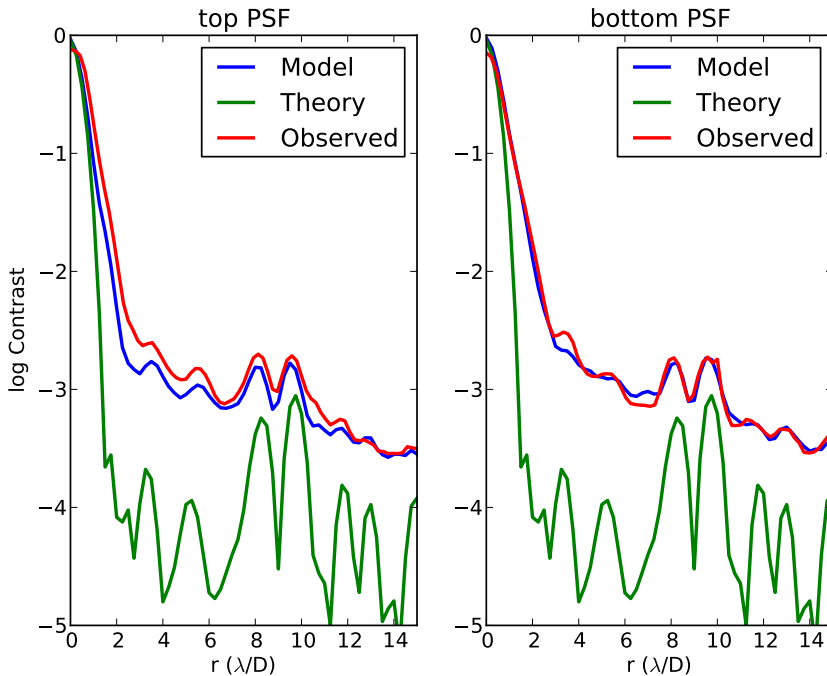


Figure 5.4: Radial intensity profiles for both the top and bottom PSFs with simple PSF model estimate. The model estimate includes the pupil misalignment, retardance offset, wavefront error and Gaussian AO halo. The theoretical contrast without any aberrations and without atmosphere can be seen in green.

5.4.2 Sensitivity maps & contrast curves

The ultimate limit of the coronagraph is defined by its time stability and how well the PSF subtraction techniques work. For this fundamental limit we look at the 5σ point source sensitivity. The individual images are convolved with a Gaussian with a full width half maximum of 10.11 pixels, corresponding to the full width of a diffraction limited PSF at 4.05 microns. We take the standard deviation of the stack of images of the data set and divide by the square root of the number of images to get the standard error on the average as was done by Kenworthy et al. (2010). We make a 5σ sensitivity map by multiplying this value by 5 and dividing by the peak flux of the exposure-time-corrected convolved unsaturated PSF. These values are converted into magnitudes

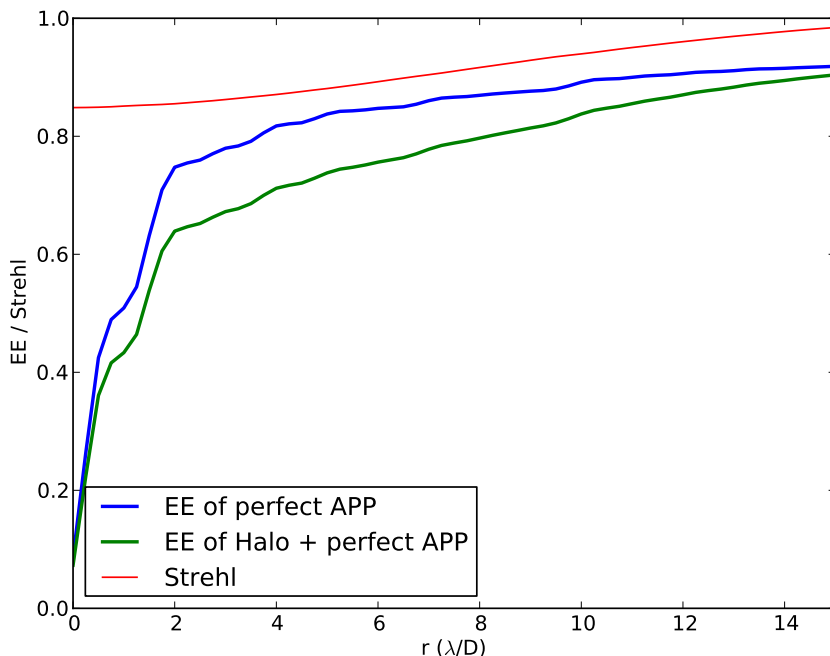


Figure 5.5: Encircled energy plot for both the theoretically perfect model and a model with a Gaussian AO halo added to it. The ratio of the encircled energies is plotted in red as an approximation of the Strehl ratio. This ratio equals 0.85 at $1 \lambda/D$ which is comparable to the typical post-AO Strehl ratio at 4 microns.

using the standard relation $-2.5 \cdot \log_{10}(F)$. Azimuthal averages are taken of this sensitivity in a wedge spanning 140 degrees and later compared with the models.

5.4.3 Detailed turbulence model

The raw contrast of the coronagraph is partly limited by the previously mentioned misalignments. We simulate the performance of the coronagraph in more detail for the case that everything is properly aligned. This is compared to simulations that include the aberrations. We make an AO simulation using the two main misalignments (the common wavefront error and pupil misalignment). The code that is used is the AOSim2 MATLAB code by Codona². The detailed simulations use a Kolmogorov spectrum with an outer scale of 30 meters generated using the FFT-method (Lane et al., 1992). This works by injecting random complex Gaussian noise into an image, FFT-ing and scaling with powerlaws in order to produce turbulence maps. An AO correction with a time lag is simulated by smoothing the turbulence with a Gaussian kernel and subtracting it with a lateral shift from the original turbulence map. The size of the Gaussian kernel is taken to be the full diameter of the mirror divided by the square root of 336. This is based on the 336 modes

²<https://github.com/jlcodona/AOSim2>

that the 672 actuator deformable secondary mirror can theoretically generate. The spatial resolution of the turbulence map is 4 centimeters. Out of the larger turbulence map pupil-sized phase maps are extracted every 20 cm for PSF calculations. The phase extractions are done by shifting along the same dimension as the AO-lag, in order to keep a consistent wind direction. The AO-corrected turbulence map is used to aberrate a simple PSF model where the pupil and phase can be adjusted. PSFs are generated by taking the modulus squared of the FFT of the complex pupil. When scrolling through the PSF images, speckles close to the star are seen to be evolving smoothly. We calculate the wind speed and the number of frames covered during one exposure from the previously mentioned lateral shift together with the AO time lag constraint. Frames are then summed together to be equivalent to the exposure time of 0.785959 seconds. The image cube is normalized to the flux level of the observations. Gaussian noise is injected into each image with the same standard deviation as the observed images. Every single image is convolved with a Gaussian PSF in order to calculate the S/N over a PSF-sized region. The standard deviation is taken across the time axis in the image cube and divided by the peak flux and the square root of the number of frames used for the real observations. This value is multiplied by 5 to get the 5σ sensitivity that can be obtained in 220 seconds. Afterwards, a radial profile using azimuthal averages is calculated for this image cube. The two parameters that are varied are the Fried parameter r_0 and the wind shift distance. The wind shift distance is the distance covered by the turbulent layer before the AO system can apply the correction and is combination of the AO lag and the wind speed. An image cube is generated with misalignments for different combinations of r_0 and wind shift distances. The same AO halo parameters are used with no misalignments and a perfect coronagraph to produce a second image cube. The expected sensitivity curve of the AO models with misalignments are plotted with varying AO parameters. These curves are shown in 5.6. In Figure 5.7 we compare the one hour 5σ sensitivity with and without an APP coronagraph, and models with varying windspeed and r_0 . We failed to find a model that best matches our observations. The figure also shows that at angular separations between 2 and 7 λ/D the APP coronagraph boosts the contrast compared to not using a coronagraph up to one magnitude. Outside of the dark hole the sensitivity is higher without a coronagraph. The amount of contrast improvement in the dark hole is dependent on the wind speed and seeing conditions but if we apply the same improvement of 1 magnitude on our observed contrast we can predict a 5σ sensitivity of approximately 11 magnitudes at 2.5 λ/D in one hour of observing time. Interesting to see is that the APP with aberrations has similar performance to the case where there is no coronagraph and no aberrations. The advantage of adding coronagraphs clearly shows.

5.5 Conclusions

In this paper we present the grating vector Apodizing Phase Plate coronagraph at thermal infrared wavelengths. The vAPP coronagraph produces two PSFs with a combined 360 degree zone of suppression. By using a linear ramp of phase embedded in the fast axis pattern, a grating is produced that splits orthogonal polarization directions with opposite APP PSFs. The grating-vAPP is demonstrated to be far less susceptible to offsets from half-wave retardance than the normal vAPP due to the fact that the leakage term does not see the phase ramp. Furthermore the coronagraph consists out of only one optic which greatly facilitates the installation into existing instruments. The data used in this paper shows that the coronagraph is affected by a misalignment of the tele-

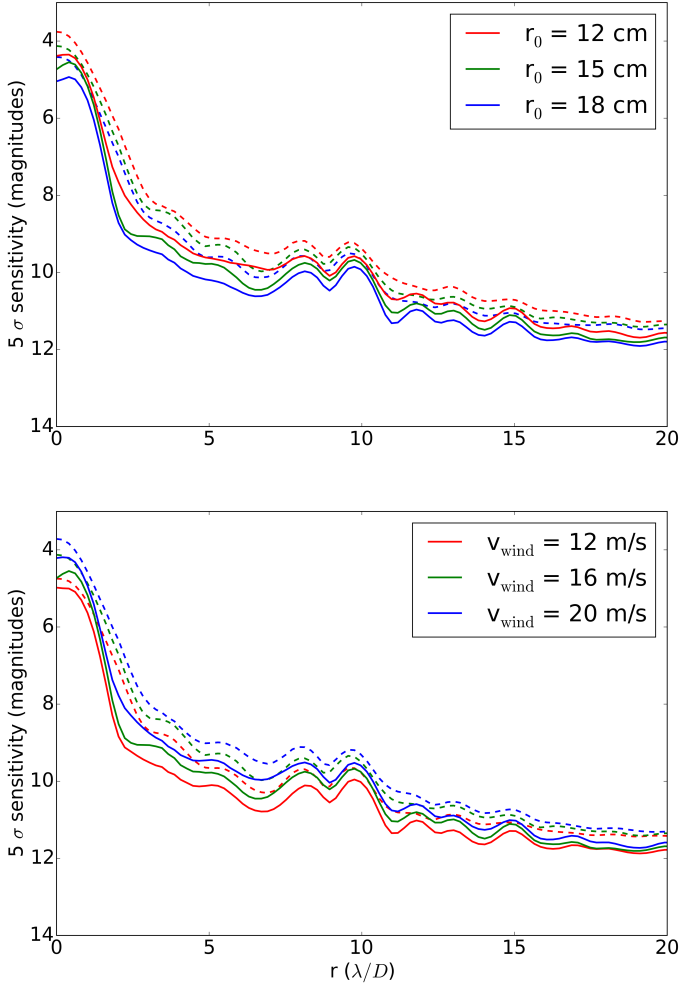


Figure 5.6: 5σ sensitivity curves in 220 seconds. Top panel: effect of changing Fried parameter. Bottom panel: effect of changing windspeed. Dashed line shows the sensitivity including aberrations and the solid line shows the sensitivity without the aberrations.

scope pupil with the coronagraph by resp. 15% and 2% for the X and Y directions and that a common path wavefront error in the form of astigmatism is present with an RMS of 0.7 radians. Both problems can be easily resolved; firstly by realigning the telescope pupil onto the coron-

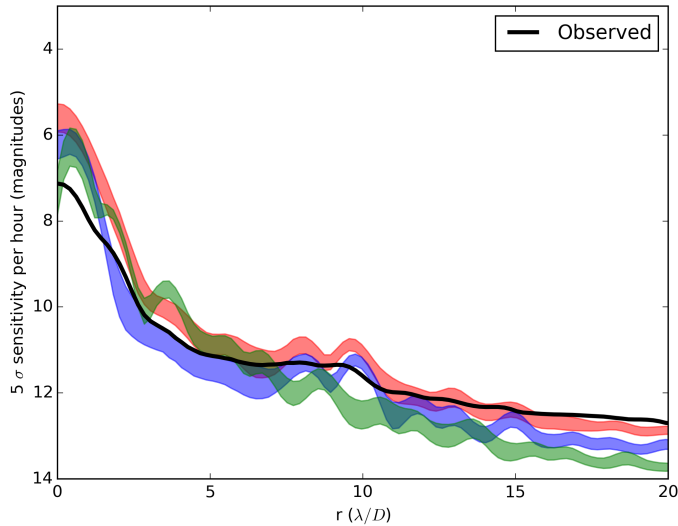


Figure 5.7: 5σ sensitivity curves in one hour of best fitting AO model with and without vAPP coronagraph. In this dataset the observed wind direction was predominantly in the X-direction. The thick black line shows the observed data. The shaded red region shows the simulated performance with the aberrations included and slightly varying r_0 and windspeed values. This area shifts to the blue shaded region after removing the aberrations. The green shaded region is the same simulation without aberrations for the case without APP coronagraph.

agraph and secondly by preshaping the deformable mirror of the telescope with the inverse of the astigmatism. Alternatively, in an updated coronagraph the thermal expansion coefficient of the substrates needs to be matched. After correction of the two factors we predict, based on advanced turbulence models, that the coronagraph can reach a 5σ sensitivity of approximately 11 magnitudes at $2.5 \lambda/D$ around bright stars in one hour of observing time.

Acknowledgements

This work is part of the research programme Instrumentation for the E-ELT, which is partly financed by the Netherlands Organisation for Scientific Research (NWO). This research has made use of the SIMBAD database, operated at CDS, Strasbourg, France.

References

- Codona, J. L. and Angel, R. (2004). Imaging Extrasolar Planets by Stellar Halo Suppression in Separately Corrected Color Bands. *ApJ*, 604:L117–L120.
- Codona, J. L., Kenworthy, M. A., Hinz, P. M., Angel, J. R. P., and Woolf, N. J. (2006). A high-contrast coronagraph for the MMT using phase apodization: design and observations at 5 microns and 2 λ/D radius. In *Society of Photo-Optical Instrumentation Engineers (SPIE) Conference Series*, volume 6269 of *Society of Photo-Optical Instrumentation Engineers (SPIE) Conference Series*.
- Kenworthy, M. A., Codona, J. L., Hinz, P. M., Angel, J. R. P., Heinze, A., and Sivanandam, S. (2007). First On-Sky High-Contrast Imaging with an Apodizing Phase Plate. *ApJ*, 660:762–769.
- Kenworthy, M. A., Quanz, S. P., Meyer, M. R., Kasper, M. E., Lenzen, R., Codona, J. L., Girard, J. H., and Hinz, P. M. (2010). An apodizing phase plate coronagraph for VLT/NACO. In *Ground-based and Airborne Instrumentation for Astronomy III*, volume 7735 of *Proc. SPIE*, page 773532.
- Koornneef, J. (1983). Near-infrared photometry. II - Intrinsic colours and the absolute calibration from one to five micron. *A&A*, 128:84–93.
- Lane, R. G., Glindemann, A., and Dainty, J. C. (1992). Simulation of a kolmogorov phase screen. *Waves in Random Media*, 2(3):209–224.
- Quanz, S. P., Amara, A., Meyer, M. R., Kenworthy, M. A., Kasper, M., and Girard, J. H. (2013). A Young Protoplanet Candidate Embedded in the Circumstellar Disk of HD 100546. *ApJ*, 766:L1.
- Quanz, S. P., Meyer, M. R., Kenworthy, M. A., Girard, J. H. V., Kasper, M., Lagrange, A.-M., Apai, D., Boccaletti, A., Bonnefoy, M., Chauvin, G., Hinz, P. M., and Lenzen, R. (2010). First results from very large telescope naco apodizing phase plate: 4 um images of the exoplanet beta pictoris b. *The Astrophysical Journal Letters*, 722(1):L49.
- Snik, F., Otten, G., Kenworthy, M., Miskiewicz, M., Escuti, M., Packham, C., and Codona, J. (2012). The vector-APP: a broadband apodizing phase plate that yields complementary PSFs. In *Society of Photo-Optical Instrumentation Engineers (SPIE) Conference Series*, volume 8450 of *Society of Photo-Optical Instrumentation Engineers (SPIE) Conference Series*.
- van Belle, G. T. and von Braun, K. (2009). Directly Determined Linear Radii and Effective Temperatures of Exoplanet Host Stars. *ApJ*, 694:1085–1098.

6 | On-sky performance analysis of the vector Apodizing Phase Plate coronagraph on MagAO/Clio2

Abstract

We report on the performance of a vector Apodizing Phase Plate coronagraph that operates over a wavelength range of $2 - 5 \mu\text{m}$, and is installed in MagAO/Clio2 at the 6.5-m Magellan Clay telescope at Las Campanas Observatory, Chile. The coronagraph manipulates the phase in the pupil to produce three beams yielding two coronagraphic PSFs and one faint leakage PSF. The phase pattern is imposed through the inherently achromatic geometric phase, enabled by liquid crystal technology and polarization techniques. The coronagraphic optic is manufactured using a direct-write technique for precise control of the liquid crystal pattern, and multi-twist retarders for achromatization. By integrating a linear phase ramp to the coronagraphic phase pattern, two separated coronagraphic PSFs are created with a single pupil-plane optic, which makes it robust and easy to install in existing telescopes. The two coronagraphic PSFs contain a 180° dark hole on each side of a star, and these complementary copies of the star are used to correct the seeing halo close to the star. To characterize the coronagraph we collected a dataset of a bright ($L = 0 - 1$) nearby star with ~ 1.5 hours of observing time. By rotating and optimally scaling one PSF, and subtracting it from the other PSF we see a contrast improvement by 1.46 magnitudes at $3.5 \lambda/D$. With regular Angular Differential Imaging at $3.9 \mu\text{m}$, the MagAO vAPP coronagraph delivers a 5σ Δmag contrast of 8.3 ($= 10^{-3.3}$) at $2 \lambda/D$, 10.8 ($= 10^{-4.3}$) at $2.5 \lambda/D$, 12.2 ($= 10^{-4.8}$) at $3.5 \lambda/D$, and 12.5 ($= 10^{-5}$) at $4.5 \lambda/D$.

G. P. P. L. Otten, F. Snik, M. A. Kenworthy, C. U. Keller, J. R. Males, K. M. Morzinski, L. M. Close, J. L. Codona, M. Montoya, P. M. Hinz, K. J. Hornburg, L. L. Brickson, M. J. Escuti
Submitted to ApJ

6.1 Introduction

In direct imaging, the sensitivity for detecting companions close to the star is primarily limited by residual atmospheric (Racine et al., 1999) and quasi-static wavefront variations (Marois et al., 2005; Hinkley et al., 2007). These time-varying wavefront errors manifest themselves as irregularities in the diffraction halo around the star (speckles). Coronagraphs reduce the diffraction halo of the star at specific angular scales and since errors are modulated by diffraction rings the S/N is thereby increased. This means that a coronagraph can significantly improve the contrast performance by suppressing the diffraction structure around the star. Both pupil and focal plane coronagraphs exist and are used on-sky with success (Guyon et al., 2006; Mawet et al., 2012). Many of the latest generation of instruments optimized for high contrast imaging contain focal-plane coronagraphs, which are typically limited to a raw contrast of $\sim 10^{-4}$ at small angular separations from the star (a few λ/D), mostly because of tip/tilt instabilities of the PSF due to, e.g., telescope vibrations and residual seeing effects (Macintosh et al., 2014; Fusco et al., 2014; Jovanovic et al., 2014). Pupil-plane coronagraphs are inherently impervious to such effects, as their performance is independent of the position of the star on the science detector, and can be amplitude (Carlotti et al., 2011) or phase-based (Codona and Angel, 2004). One type of pupil plane coronagraph, called the Apodizing Phase Plate (APP) coronagraph, sits in the pupil plane and modifies the complex field of the incoming wavefront by adjusting only the phase (Codona et al., 2006; Kenworthy et al., 2007). The flux within the point spread function (PSF) of the telescope is redistributed, resulting in a D-shaped dark region close to the star. Since the apodization is with phase only, the throughput of the APP is higher compared to traditional amplitude apodizers, and the PSF core remains roughly the same angular size. Because the Apodizing Phase Plate is located in the pupil plane it is not only insensitive to residual tip-tilt variations, but also nodding, chopping and dithering motions of the telescope. The PSFs of all stars in the image remain suppressed in the dark hole regardless of the motions of the telescope. In the infrared, the APP can be combined with conventional nodding motions as a background subtraction technique. Early versions of the APP were realized by varying the thickness of a piece of Zinc Selenide substrate (Kenworthy et al., 2007). The phase pattern corresponded to a variation in height of the substrate as a function of position in the telescope pupil. As a result of this, the APP was chromatic, suppressed only one side of the star at a time, and the diamond turning was limited to phase solutions with low spatial frequencies.

The vector Apodizing Phase Plate (vAPP, Snik et al., 2012) is an improved version of the APP coronagraph and is designed to yield high contrast performance across a large wavelength range, typically up to $\frac{\lambda}{\Delta\lambda} = 1$. The phase pattern of the vAPP is encoded in an orientation pattern of the fast axis of a half-wave retarder. Such a device imposes a positive phase pattern upon right-handed circular polarization, and a negative phase pattern upon left-circular polarization, through the geometric (or Pancharatnam-Berry) phase. (Pancharatnam, 1956; Berry, 1984; Mawet et al., 2009). This orientation pattern, as well as any other arbitrary pattern, can be embodied by a liquid crystal layer, that locally aligns its fast axis to a photo-alignment layer. The geometric phase is inherently achromatic, but leakage terms can emerge if the retardance is not exactly half-wave (Mawet et al., 2009; Kim et al., 2015). A typical APP phase design is antisymmetric in the pupil function that results in a D-shaped dark hole next to the star. By splitting circular polarization states with inverse geometric phase signs in the pupil, the vAPP creates two PSFs with dark holes on either side. By combining multiple self-aligning layers of twisting liquid crystals, it is possible

to create retarder structures that are close to half-wave across a broad wavelength range (up to even more than one octave, (Komanduri et al., 2013)). This class of retarders is called Multi-Twist Retarders (MTRs). The direct-write manufacturing technique of the alignment layer and hence the liquid crystal orientation pattern (Miskiewicz and Escuti, 2014) gives high control of the phase of the optic and allows the manufacturing of complex phase designs with typically ~ 10 microns spatial resolution, that were not manufacturable using the diamond turning techniques of earlier APPs. A vAPP prototype that was optimized for 500 – 900 nm was built using both these techniques and characterized in Otten et al. (2014a).

In this paper we present the first on-sky results of the vector Apodizing Phase Plate installed inside the MagAO/Clio2 (Close et al., 2010; Sivanandam et al., 2006; Close et al., 2013; Morzinski et al., 2014) instrument on the 6.5-m Magellan/Clay telescope at Las Campanas Observatory. We demonstrate the contrast performance at small angular separations from a bright star, and show how the two PSFs of the vAPP can be combined to suppress speckle noise inside the dark holes.

6.2 The vAPP coronagraph for MagAO/Clio2

6.2.1 The grating-vAPP principle

The vAPP coronagraph designed for MagAO/Clio2 has a phase pattern that is composed of two separate patterns - the first is the APP phase pattern, which produces the dark D-shaped hole, and the second is a polarization grating (i.e., a linear phase ramp that is opposite for the two circular polarization states). This polarization grating splits the two PSFs without the need for a quarter-wave plate and Wollaston prism, as introduced in Chapter 4 (Otten et al., 2014b), which greatly improves the ease of installation. As both the modification of the PSF and the splitting direction depends on the handedness of circular polarization cf. the geometric phase, the grating-vAPP produces two separate coronagraphic PSFs with dark holes on opposite sides, providing continuous coverage around the star. The inclusion of the linear phase also means that any leakage term due to the plate not being perfectly half-wave ends up between the two coronagraphic PSFs as a third PSF. The positioning of the leakage term PSF in between the coronagraphic PSFs minimizes the impact of any residual non-half-wave behavior of the retarder to the contrast inside the dark holes (Chapter 3). This PSF can be used as a photometric and astrometric reference, and as an image quality indicator. Both the coronagraphic PSFs and the splitting angle are not dependent on the value of the average retardance of the plate. Only the brightness ratio of the leakage PSF with respect to the coronagraphic PSFs changes with varying retardance. As the splitting between the PSFs is imposed by a diffractive grating pattern, their separation is a linear function of wavelength. Hence, while the vAPP optic offers high-contrast coronagraphic performance over a broad wavelength range, we apply narrowband filters throughout this wavelength range to produce sharp PSFs without radial smearing. By orienting the dark holes left/right with respect to the up/down splitting, this grating effect furnishes low-resolution spectroscopy of point sources inside either of the dark holes.

6.2.2 Phase pattern design

The phase pattern is determined with a simple, iterative algorithm akin to a Gerchberg-Saxton iteration (Gerchberg and Saxton, 1972; Fienup, 1980). We switch between electric fields in the pupil plane and the focal plane with Fourier transformations and enforce constraints in the corresponding planes. In the pupil plane, the amplitude field amplitude is set to unity inside the telescope aperture and zero everywhere else. In the focal plane, we set the electric field amplitude to zero in the dark hole. This process is repeated hundreds of times until we obtain a phase pattern that achieves the desired contrast. This approach does not guarantee the highest Strehl ratio for a desired contrast, but we found it to perform better than any other design approach that we are aware of.

Since this particular APP design only has a dark hole on one side of the focal plane, the phase pattern in the pupil will be antisymmetric. We use this symmetry to improve the performance of the algorithm. Instead of setting the electric field to zero in the dark hole, we add a scaled and mirrored version to the electric field on the other side of the dark hole. This is motivated by the fact that a one-sided dark hole created by an antisymmetric phase pattern is achieved in the focal plane by symmetric and anti-symmetric parts of the electrical field canceling each other in the dark hole and adding to each other on the other side. The scaling enforces energy conservation in the focal plane. A comprehensive description of our design algorithm including applications to symmetric dark holes will be provided in a forthcoming publication by Keller (in prep). For the optimization in this paper we define a dark hole from 2 to 7 λ/D and with a 180° opening angle and a desired normalized intensity of 10^{-5} . The final design has a peak intensity of 40.3% with respect to an unaberrated PSF.

6.2.3 Coronagraph optic specifications

The optic has a diameter of 1 inch and a thickness of approximately 3.3 mm, and is designed to work with the Clio2 camera with a nominal size of 3.32 mm of the MagAO telescope pupil image. The diameter of the vAPP was undersized by 100 microns (from a diameter of 3.32 mm to 3.22 mm) to create a tolerance against pupil misalignments in the instrument. A 1° wedge is added on one side of the coronagraph in order to deflect reflection ghosts. To further suppress ghost reflections, both sides of the optic are broad-band anti-reflection coated with an average transmission between 2 and 5 micron of 98.5%. An aluminum aperture mask, matching the Magellan pupil, with a pixelated edge (with a pixel size of 11.54 microns) is deposited on one of the substrates and is sandwiched directly against the retarder layers, manually aligned using a high power microscope, and fixed in place with an optical adhesive. The phase pattern (the coronagraphic pupil phase pattern plus the grating pattern) is written as an orientation pattern of an alignment layer of "DIC LIA-CO01" by a UV-laser with polarization-angle control (Miskiewicz and Escuti, 2014). The pixel size is 11.54 microns for both the phase and amplitude pattern. During fabrication the writing accuracy of the fast axis is calibrated to approximately 2° , corresponding to a maximum phase error of 4° , i.e. $\sim \lambda/100$. The patterned retarding layer consists of three MTR layers (Merck RMS09-025, see also Table 6.1) and is optimized to produce a retardance δ that is half-wave to within 0.38 radians for wavelengths between 2 and 5 microns, corresponding to a maximum flux leakage from the coronagraphic PSFs to the leakage term PSF of 3.5%. The design recipe of the MTR is [$\phi_1 = 78^\circ$, $d_1 = 3.5 \mu\text{m}$, $\phi_2 = 0^\circ$, $d_2 = 7.3 \mu\text{m}$, $\phi_3 = -78^\circ$, $d_3 = 3.5 \mu\text{m}$] where d_i

stands for layer thickness, ϕ_i for the twist of a layer and i for the layer number. This recipe is used to build our coronagraph with our custom fast axis pattern and also a test article with the same parameters but a fixed fast axis. The transmission of this test article is measured between crossed linear polarizers with a VIS-NIR spectrometer up to 2800 nm. A model of the MTR is fitted to the observed transmission between crossed polarizers with 5 free parameters (3 thicknesses and 2 relative twists with respect to the middle layer). The best fit parameters are [$\phi_1 = 81^\circ$, $d_1 = 3.5 \mu\text{m}$, $\phi_2 = 0^\circ$, $d_2 = 7.3 \mu\text{m}$, $\phi_3 = -77^\circ$, $d_3 = 3.9 \mu\text{m}$] and used afterwards to predict the transmission, retardance and leakage at wavelengths out to 5000 nm, which is shown in Fig. 6.1, 6.2 and 6.3.

The leakage PSF intensity is derived by measuring the peak ratio of the coronagraphic to leakage term PSF in a sequence of unsaturated images. The mean and standard deviation of the ratio in this sequence is 31.47 ± 1.07 . This ratio is divided by the theoretical strehl ratio 0.403 to yield the ratio as if the coronagraph was not present. This means that the intensity of the leakage term is $1/78.1 \cdot I_{\text{CORON}}$, where I_{CORON} is intensity of the coronagraphic PSF. This value is normalized by the total intensity $(2 + 1/78.1) \cdot I_{\text{CORON}}$ to yield the fractional leakage intensity (the amount of light that goes into the leakage term). In the completed coronagraph we measure a leakage term intensity of 0.636% at 3.94 microns, which corresponds to $\delta = 2.98$ rad, using this method which is within the previously defined specifications. While this leakage is larger than the theoretical expectation at that wavelength (0.16%) it is comparable in magnitude to the maximum retardance offset of the curve.

The polarization grating spans 17.5 waves in terms of phase. Corresponding to a displacement of $35 \lambda/D$ between the two coronagraphic PSFs, and so that both of the PSFs fit on the chip at the longest wavelengths (M' -band) while minimizing the contribution of the leakage term diffraction pattern into the dark holes. The grating creates a splitting angle that is dependent on the wavelength in terms of pixels of separation, and so the PSFs are laterally smeared. For optimal image quality, where the smearing is at most $1 \lambda/D$, the filter full width half maximum needs to be $\frac{\Delta\lambda}{\lambda} \leq 0.06$. Due to the optic's efficiency, narrowband filters can be used anywhere between 2 and 5 microns to produce coronagraphic suppression, leading to a natural use of vAPPs with integral field spectrographic units. Note that even outside the specified wavelength range, the coronagraphic performance is never deteriorated by leakage terms, but the coronagraphic PSFs are less efficient as they lose light to the leakage term PSF.

We collected pupil image measurements with and without the coronagraph at several IR bands during good sky conditions and with AO to obtain accurate on-sky pupil transmission measurements. We determine the transmission of the optic from the ratio of the pupil intensity with and without the coronagraph. The theoretical transmission values are detailed in Table 6.1 per layer and compared to the measured transmission. Since the measured retardance is close to half-wave (as expected from the theory), the thickness of the liquid crystal layers must not deviate significantly from the theoretical value. We therefore set the thickness to the fitted value for the MTR recipe which is 14.7 microns. The absorption properties of the retarder layer were measured in a 900 nanometer thick sample at a wavelength of 4 microns and extrapolated to the 14.7 micron thick layer. The absorption coefficient derived from this measurement falls on the high end of the range seen in Fig. 3 of Packham et al. (2010), who used a similar family of liquid crystals. The absorption coefficient of the glue layer is derived from the spectral transmission graph on

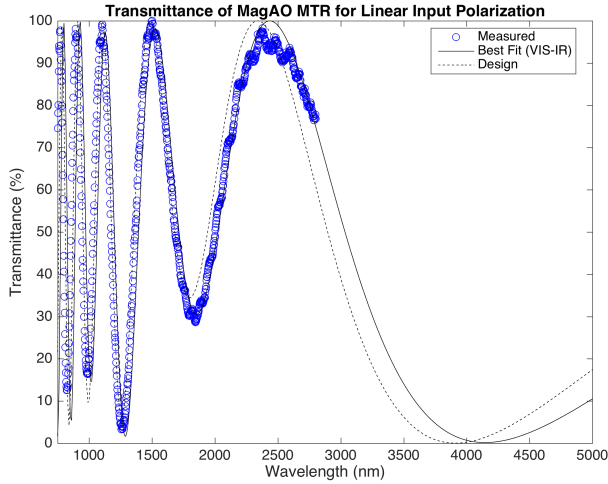


Figure 6.1: Transmission of optic between crossed polarizers against wavelength for the theoretical design and a test article with linear fast axis made according to the same recipe. A model of the MTR is fitted to the test article and used for Fig. 6.2 and 6.3.

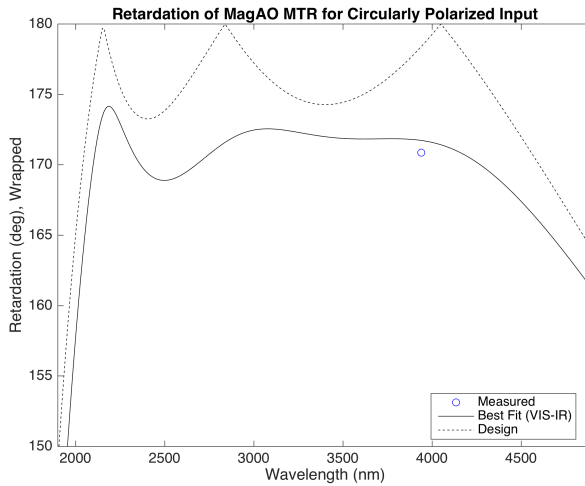


Figure 6.2: Plot of retardance versus wavelength based on design and best fit of MTR model to the crossed polarizer transmission. The retardation requirement corresponds to a maximum leakage of 3.5% and a retardance offset of 0.38 radians or 21.6 degrees. The on-sky measured datapoint of the leakage is converted into retardance and shown with a blue circle. The measurement error on the datapoint is 0.15 degrees (estimated by propagating the standard deviation of the leakage to retardance) and smaller than the blue circle that was used.

the Norland Products website¹ and the known thickness of their sample. The thickness of the

¹<https://www.norlandprod.com/adhesives/NOA%2061.html>

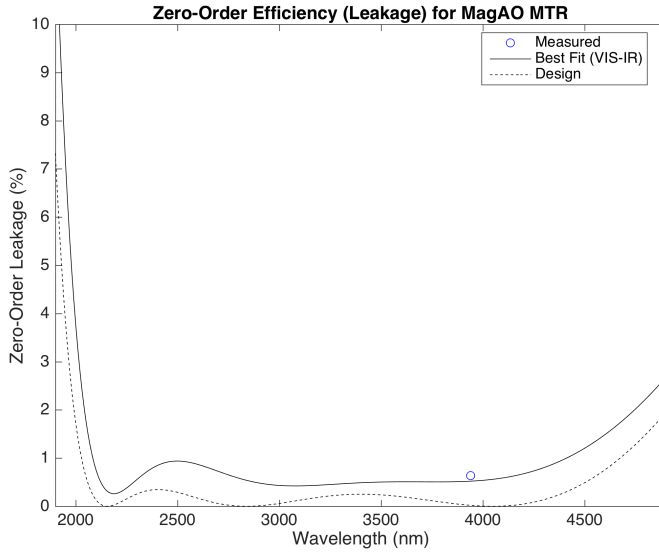


Figure 6.3: Percentage of leakage corresponding to the retardance in Fig. 6.2 against wavelength for both the theoretical design and the best fitting model of the test article. The on-sky measured datapoint of the leakage is shown with a blue circle.

glue layer is the biggest uncertainty as it was not measured during the manufacturing process. Because the other transmission values are well constrained, we let the thickness of the glue layer vary as a free parameter to match the observed transmission. Our derived glue layer thickness of 50 microns is not unexpected for glass-glass interface bonding. The breakdown shows that the throughput is primarily limited by the optical adhesive NOA-61. The absorption features of both the optical adhesive and the retarding layer are related to vibrational modes of chemical bonds with Carbon, such as C-C, C-O, C-N and C-H. The optical adhesive is based on urethane-related compounds².

The coronagraph is located in the pupil stop wheel of Clio2 and orientated with the grating splitting angle perpendicular to the arc traveled by the pupil in the pupil wheel. The wedge splitting angle was orientated parallel to the motion of the pupil. This orientation of the splitting angle corresponds in theory with splitting the PSFs along the short axis of the chip. This leaves a large amount of space along the long axis to nod the PSFs along for background subtraction. From our PSF measurements we see that the orientation of the PSFs on the chip is approximately 26 degrees rotated away from the short axis. This rotation does not interfere with the background subtraction.

²<https://www.norlandprod.com/msds/noa%2061msd.html>

Table 6.1: Table describing the thickness and transmission properties of the different layers.

layers	material	thickness	3.9 micron	4.7 micron (M')
AR-coating	-	-	0.98	0.99
substrate with 1° wedge	CaF ₂	0.8 mm	0.99	0.99
amplitude mask	evaporated aluminum	250 nm	-	-
bonding glue	NOA-61 epoxy	50 μm	0.81	0.81
substrate	CaF ₂	1 mm	0.99	0.99
retarder layers	Merck RMS09-025	14.7 μm	0.85	~ 0.85
alignment layer	DIC LIA-CO01	50 nm	-	-
bonding glue	NOA-61 epoxy	50 μm	0.81	0.81
substrate	CaF ₂	1 mm	0.99	0.99
AR-coating	-	-	0.98	0.99
theoretical throughput	-	-	0.53	0.54
measured throughput	-	-	0.51	0.54

6.3 Observations

The observations with the vAPP coronagraph at MagAO/Clio2 were taken during 2015 June 6, 07:38:40 - 10:07:34 UT during excellent conditions (with only high cirrus). The filter used for these observations is the 3.9 micron narrowband filter with a width of 90 nm and a central wavelength of 3.94 microns. The plate scale of the detector is 15.85 arcseconds/pixel³. The target discussed in this paper to assess the vAPP's contrast performance is an single A-type star with an L' -band magnitude between 0 and 1. The star was picked to be bright and without a known companion to reach the limits of the coronagraph's performance. 287 data-cubes were taken on-sky, each with 20 subframes and an exposure time of 1 second each. The dataset has a total on-target exposure time of 5 740 seconds. The derotator was off during the observations and spans a total of 39.45° of field rotation. To perform background subtraction, data-cubes were recorded with the PSF centered approximately 10 arcseconds to the left from the nominal center of the science camera array, so that no sources and ghosts are seen on the same part of the chip. Our target was therefore located off the chip. This background estimation was repeated 4 times during the sequence. No flats have been applied to the data and a sky correction was made using the off-target nods.

Fig. 6.4 shows a comparison between the theoretical and observed PSFs using a median combination of the top 50% best frames in terms of the fitted radius ($1.22 \lambda/D$) of the leakage term PSF, acting as a proxy for subframe quality as it expands to match increased turbulence. The observed coronagraphic PSFs are saturated in the core and the first diffraction ring but are corrected to the peak flux consistent with the unsaturated calibration images. While the two PSFs have approximately the same brightness, the two PSF halos inside the dark holes have a slight difference. A potential source of the difference is discussed in Section 6.3.2.

³<https://visao.as.arizona.edu/observers/>

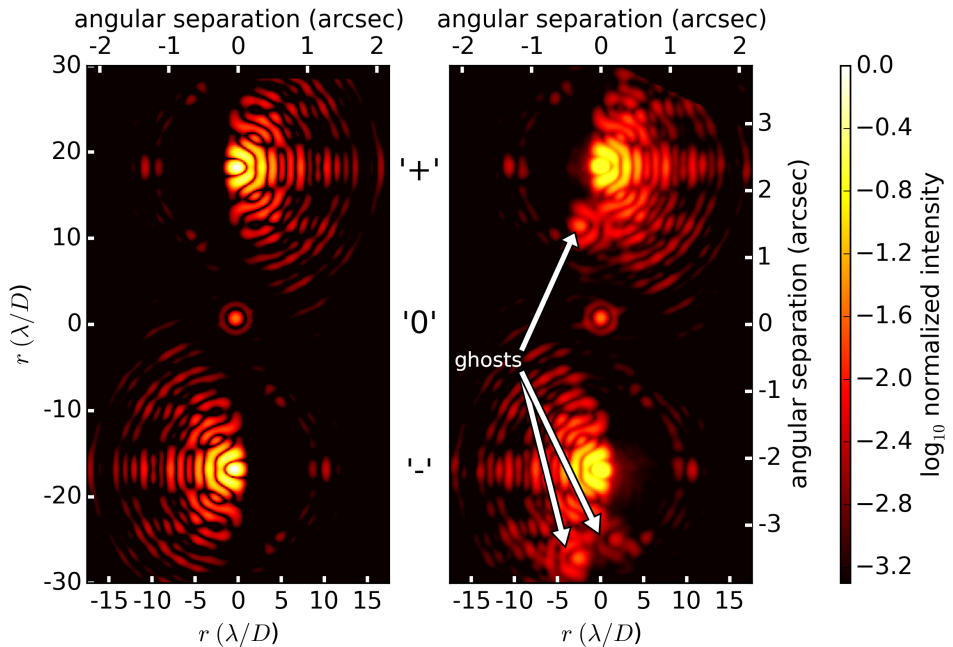


Figure 6.4: Comparison of theoretical (left) with observed PSFs (right). Both images are at the same logarithmic scale with a lower threshold of $10^{-3.3}$. The theoretical PSF is calculated for the central monochromatic wavelength of 3.94 microns. The retardance in the simulation was set to $\delta = 2.98$ radians, thereby creating the leakage PSF “0”. The observed image is saturated on the first diffraction ring and the central core but is corrected to the unsaturated flux level. A small asymmetry of the intensities of the wind-driven halos of the star is seen between the two PSFs at the location of the first diffraction ring. Instrumental ghosts are indicated with arrows and not related to coronagraphic optic. Further investigation showed that these ghosts can be removed from the dark hole by setting the rotator to an angle of 30° . As a reference to the text we indicate the “+”, “0” and “-” PSFs.

6.3.1 Data reduction

To remove hot, dead or flaky pixels in each image, a median filtered image with a 3×5 pixel box is subtracted from the cleaned and centroided image cube to generate an image where the outliers clearly stand out. The 3×5 box is chosen because the outlying pixels tend to have structure in the direction of the readout and not perpendicular to it. The data points that deviate more than 1 000 counts are replaced by the local value of the 3×5 median. Four sets of sky reference frames are taken between on-target observations. The sky frames were median combined for every one of the 4 sets. Each of the previously taken frames on target were subtracted by the first consecutive median-combined master sky frame. After the background subtraction, the median of a cosmetically clean part of the chip is subtracted in order to remove any residual background offset. A theoretical diffraction pattern consistent with the geometry of the telescope and wavelength of observation is used as a fiducial. This theoretical PSF is then fit to the central leakage PSF by

minimizing the chi-squared residuals between the theoretical PSF and the leakage PSF, with x , y , radius ($1.22 \lambda/D$) and intensity as the free parameters of the fit. All images of the data-cubes are co-registered by shifting the images to the central pixel of the frame with the previously fitted x and y values using a bi-linear interpolator. The radius of the leakage PSF fit is used as a sub-frame quality indicator. The few images that have fitted radii significantly smaller (< 9 pixels) or larger (> 12 pixels) than the diffraction limit are excluded. The best 91% (5 200) of images are selected after sorting the frames by radius from smallest to largest. This selection removes the frames where the seeing conditions temporarily worsened or where the AO-system lost its lock. After this selection, the images are reordered to original chronological order and binned by 4 frames, corresponding to 4 seconds integration time per binned frame to reduce memory consumption and computational time. Instrumental ghosts due to internal reflection of the refractive optics are present in the image, see Fig. 6.4. Several of these ghosts are typically 10^{-2} to 10^{-3} in intensity, and their position relative to the central PSF changes as a function of position on the chip. To reduce their influence, the regions of identified ghosts are masked off from any subsequent fitting and/or stacking process. These ghosts can be removed from the dark hole by setting the rotator to an angle of 30° .

6.3.2 Rotation, scaling & subtraction

Each on-target image consists of three PSFs which we label “+” for the upper coronagraphic APP PSF, “-” for the lower coronagraphic PSF with the dark region on the opposite side of the star, and “0”, the leakage PSF which is consistent with the PSF obtained with no coronagraph in the optical path, and with a flux typically 10^{-2} of the other two PSF cores. To suppress the noise contribution of the seeing-driven halo inside the dark holes, we use one coronagraphic PSF as a reference for the other coronagraphic PSF of the same star, and subtract “-” from “+”. This reduces self-subtraction of the flux of a potential companion as it is very unlikely to have another companion at the same separation and brightness on the opposite side of the star. A similar approach is taken by Marois (2007); Dou et al. (2015) who use the (non-coronagraphic) PSF (itself) under rotation as a reference and measure an order of magnitude improvement compared to normal LOCI (Lafrenière et al., 2007) without rotation. Our approach works by rotating, scaling and subtracting PSF “-” from PSF “+” in a three-step process. First, the image is flipped in both dimensions so that “-” has the same orientation as “+”. We align each “+” and “-” PSF with the median of all “+” PSFs, by performing a cross-correlation on a bright, isolated feature at $10 \lambda/D$ on the bright side of the PSF. With the obtained centroids, the “+” and “-” PSFs are sub-pixel shifted to the frame center with the python routine `scipy.ndimage.interpolation.shift` set to first-order spline interpolation. The “-” cube is then multiplied by a fixed amplitude ratio and subtracted from the “+” cube. An example of the PSFs before and after subtraction can be seen in Fig. 6.5 for three different scaling factors (resp., 0, 1.04 and 0.71). The diffraction structures on the bright side of the PSFs are optimally canceled using an amplitude scaling ratio of 1.04. This is consistent with the ratio of the encircled energies of both PSFs. However, with this ratio the seeing-driven halo in “-” is oversubtracting the halo in “+”, resulting in larger amounts of noise in the final combined image. A likely cause for this is that aberrations create pinned speckles upon the diffraction structure in the dark holes, but the intensities may be different in the left and right dark holes. Although this diffraction structure ideally has an intensity of $< 10^{-5}$ with respect to the PSF core (and therefore not visible in the left panel of Fig. 6.4), it becomes brighter due to

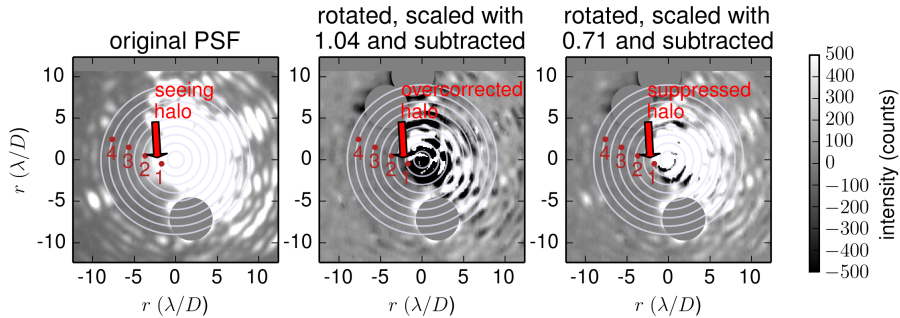


Figure 6.5: Comparison between subtractions of “+” and “-” PSFs for different scaling factors. The purple circles indicate distances from the center in λ/D . The dark red points and numbers show probe locations as a reference. The factor of 1.04 minimizes the residual diffraction structure while the factor of 0.71 minimizes the standard deviation across time close to the star. Note that a companion inside the dark hole in the top PSF would show up as a positive signal, while a detection in the other PSF’s dark hole would yield a negative signal. An instrumental ghost was masked off on both sides of the PSF.

residual seeing and/or optical aberrations of the telescope and instrument. Because this diffraction structure is fully symmetric between the two PSFs, a rotation-subtraction approach with a variable scaling factor always reduces the intensity in the halo. A simple simulation shows that with the realistic seeing and AO performance the intensity of this halo is practically balanced, even when a AO loop time lag (3 ms) and wind speed (10 m/s) are taken into account. As for (quasi-)static optical aberrations, only odd modes (like trefoil aberration) cause an intensity asymmetry between the holes in the two dark holes. Assuming trefoil is the dominant aberration we simulate how much trefoil is at most allowed to create a PSF that is still consistent with the observed in terms of the asymmetry between the dark holes. Based on this simulation we conclude that the RMS error of the trefoil aberration needs to be at least 0.04 radians (25 nm at 3.94 microns) of trefoil to match the observations.

Another option for scaling the two PSFs is to take the amplitude ratio that minimizes the halo noise in time and applying that to all frames (c.f. Marois et al. (2006)). To determine this ratio we calculate the standard deviation for the temporal intensity variation in many randomly selected 3×3 pixel patches across the dark hole. Figure 6.6 shows the standard deviation for various 3×3 patches as a function of the amplitude ratio. The vertical lines indicate the ratio at which the noise is minimal on average for a series of radial λ/D bins. As reducing the noise closest to the star is the most important, the value 0.71 that on average minimizes the noise in the bin from $2 - 3 \lambda/D$ is used to scale the amplitude of the bottom PSF cube before subtracting it from the top PSF. As mentioned before, to minimize the intensity of the brightest parts of the PSF and not the noise an amplitude scaling ratio of 1.04 is required. Fig. 6.7 shows the same optimal scaling factor for each pixel inside the combination of dark holes. It is apparent that rotation-subtracting PSFs is only effective close to the star, at the location of the seeing-driven halo. Further away from the star it is preferred to not perform any subtraction at all, as at the outer parts of the dark holes the noise is uncorrelated (e.g., photon shot noise from the thermal background, and read-noise) and

therefore subtracting the two images will actually inject noise and consequently increase it with a factor $\approx \sqrt{2}$. This effect can be reduced by optimizing the ratio in radial bins as is commonly done with LOCI (Lafrenière et al., 2007) and Principal Component Analysis (Amara and Quanz, 2012; Soummer et al., 2012).

For a scaling ratio of 0.71 we plot in Fig. 6.8 time series and histograms for three 3×3 pixel patches at locations inside the dark holes as indicated in Fig. 6.5 before and after the subtraction to see how the rotation-subtraction technique improves the intensity variability. At the location closest to the PSF core ($1.8 \lambda/D$) both the average value and the standard deviation of the intensity is significantly reduced. This effect is seen in both the time series and the histograms. This is particularly evident in cases of worse AO performance (for instance, around the $\# = 750$ mark). Moreover, the rotation-subtraction technique produces histograms that are much more Gaussian than before. As discussed already, pixels further away from the central star actually obtain a $\sim \sqrt{2}$ increase in the noise.

6.4 Results: contrast curve

The combination of the intrinsic coronagraphic performance of the vAPP coronagraph inside the dark holes, and the optimal rotation-subtraction of its two complementary PSFs to subtract the residual seeing-driven halo delivers essential suppression at very small angular separations from the central star to detect and characterize planetary companions. We apply median-filtering and classical Angular Differential Imaging (Marois et al., 2006) (without excluding frames based on the angular distance) to further suppress static and quasi-static speckles inside the combined dark holes to reach the ultimate contrast. After rotation-subtracting the two PSFs with the optimal ratio, the median value inside a wedge from $5 - 7 \lambda/D$ in the dark hole is subtracted from every pixel in every frame of the data cube. This process is repeated for every frame to remove any residual intensity offsets. The median across the time dimension per pixel is removed from the whole cube to remove any residual static PSF structures. After these steps the frames are derotated and co-added by taking the mean across the time dimension.

Artificial companions are injected in the original datacube at steps of $0.5 \lambda/D$ and with steps in magnitude of 1 with the expected amount of sky rotation. The injected sources are a rescaled and translated version of the unsaturated calibration dataset. Note that a companion in the top (“+”) PSF emerges as a positive signal detection, while a companion on the other side of the star (i.e. in the dark hole of the lower “-” PSF) is seen as a negative signal. The previously described pipeline of optimal rotation-subtraction, median-filtering and ADI is applied to these data-cubes with injected sources of varying contrast ratio. The signal to noise of these planets is calculated by calculating both the sum of the flux in an aperture with a width of $1 \lambda/D$, and the noise in the same aperture without the planet added. The noise in this aperture is multiplied by the square root of the number of pixels in the sub-aperture to obtain the measurement noise on the planet flux, assuming that this noise is Gaussian. The magnitude of the injected point source is rescaled to obtain a $S/N = 5$ and these values are plotted as a contrast curve for 5σ point source detection sensitivity versus angular separation in Fig. 6.9.

In Fig. 6.9 we note that within $4.5 \lambda/D$ the contrast of a single PSF (ratio = 0) is improved by subtracting the other PSF with a fixed amplitude scaling factor of 0.71. This is most evident at a angular separation of $3.5 \lambda/D$ where the improvement is 1.46 magnitudes (4-fold improvement)

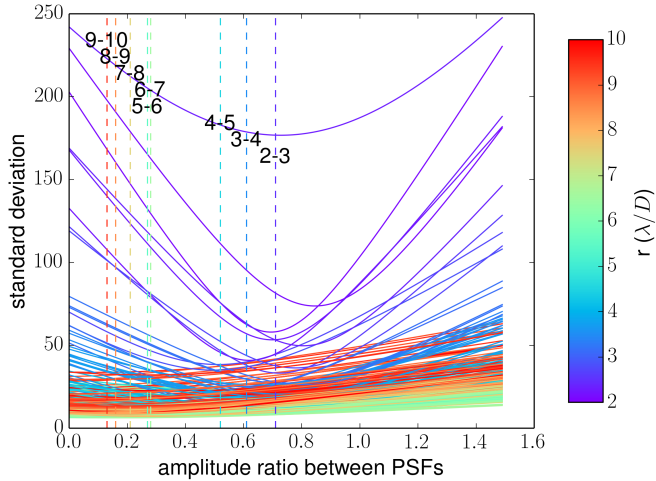


Figure 6.6: Standard deviation of many randomly selected pixel patches inside the combined dark holes as a function of the scaling factor between the two PSFs. The lines are color-coded according to their distance from the star. For different radial bins the average scaling ratio that creates the minimal noise value is shown with the vertical lines and labeled with the inner and outer angle of that bin.

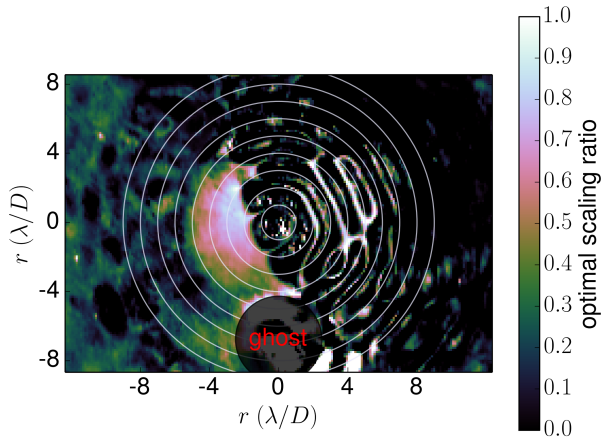


Figure 6.7: Map showing the optimal scaling factor for every pixel in the data-cube. Far away from the star the optimal ratio is close to zero, as the noise is fully random and uncorrelated between the two PSFs. Close to the star in the seeing halo a ratio of about 0.7 is required for optimal noise reduction. The ghost is seen as a clear outlier at the bottom. While we used a fixed scaling factor in this work, it can also be varied in radial bins to optimally minimize the noise as a function of distance from the star.

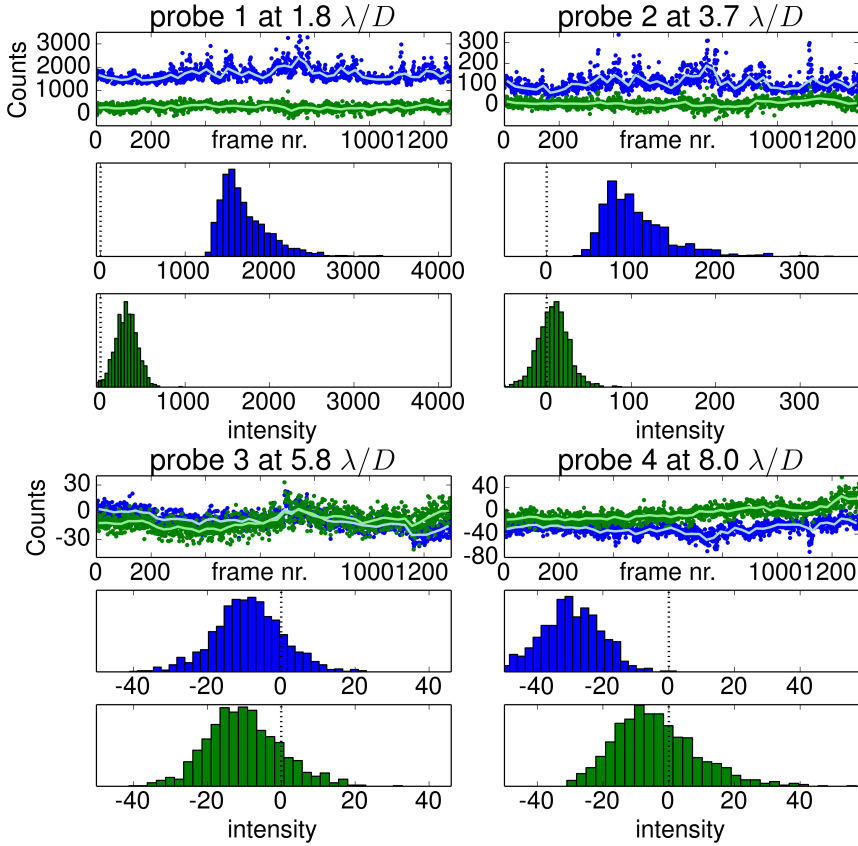


Figure 6.8: Time series and histograms before and after PSF subtraction for each of the 4 pixel patches shown in Fig. 6.5. A boxcar-averaged line is overlotted for both cases. The range of the x-axes of the histograms is adjusted to be identical in length before and after PSF subtraction. Within $4.5 \lambda/D$ the histograms after subtraction have an average closer to 0, become more Gaussian, and their width decreases.

to a Δmag of 12.2, which corresponds to a contrast of $10^{-4.8}$. Beyond $4.5 \lambda/D$ the contrast performance for the rotation-subtraction technique is degraded, as here the noise is random and uncorrelated, and therefore aggravated after the combination with the second PSF. As previously commented, we expect to be able to reduce this effect by optimizing the scaling factor in radial bins, although this also increased the degrees of freedom. This turnover point at $4.5 \lambda/D$ is dependent on the brightness of the target and moves inward with fainter targets as the background noise contribution becomes more dominant. For this dataset this turnover point at $4.5 \lambda/D$ has a Δmag of 12.5, corresponding to a contrast of 10^{-5} . Like many other reduction methods our classical ADI approach also removes part of the planet flux in addition to residual speckles in the stellar PSF. To quantify this effect we retrieve the planet flux after applying the whole data reduction pipeline to the data and compare it to the injected planets. The efficiency of the ADI

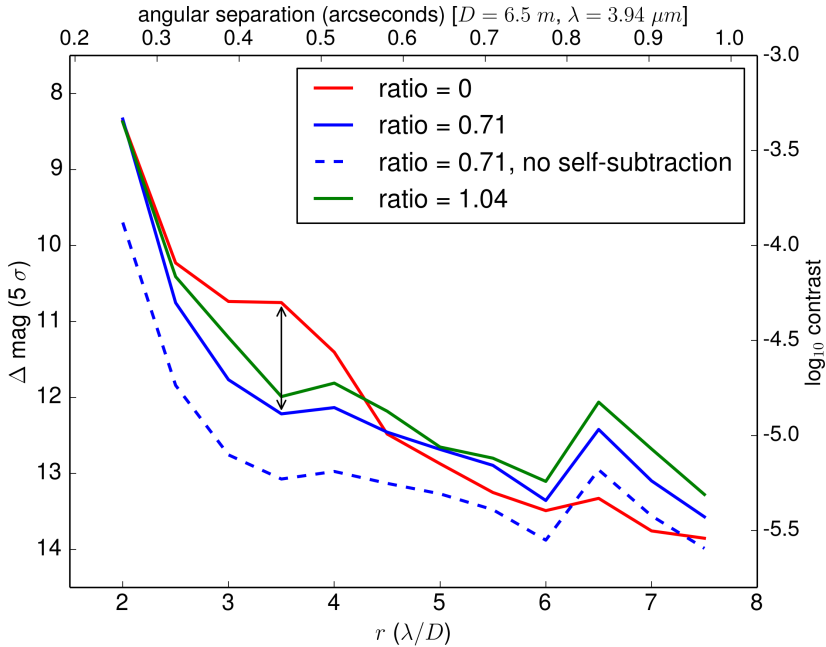


Figure 6.9: 5σ Contrast curve as a function of angular separation from the central star for different scaling factors. The contrast is calculated after ADI and a mean combination of the derotated images. The PSF subtraction improves the contrast within $4.5 \lambda/D$ up to 1.46 magnitudes compared to only using ADI. The dashed line shows the contrast if there is no self-subtraction of planet flux due to the data reduction.

algorithm is as low as 29% at $2 \lambda/D$ and reaches 68% at $7.5 \lambda/D$. This lower efficiency close to the star is expected as there is less displacement of the planet in terms of λ/D which leads to more self-subtraction. Overplotted with a dashed curve in Fig. 6.9 this efficiency factor shows the contrast excluding self-subtraction. This limiting case may be reached by applying more advanced PSF subtraction techniques, like Principal Component Analysis (Amara and Quanz, 2012; Soummer et al., 2012).

6.5 Discussion and conclusions

To put this contrast performance of the vAPP coronagraph at MagAO/Clio2 in context, we compare our results to published on-sky contrast curves for different coronagraphic instruments. Such an analysis uses heterogeneous data sets due to variations in the brightness of the star, the wavelength, the size of the telescope and applied data reduction techniques. Nonetheless we attempt to make a comparison to existing coronagraphs. To begin with a related coronagraph; in comparison to the performance of the regular APP at VLT/NACO (Quanz et al., 2010; Kenworthy et al., 2013; Meshkat et al., 2014), the vAPP PSFs do not exhibit any clear diffraction structure close to the star, whereas the VLT APP PSF clearly does. The much-improved manufacturing accuracy of phase patterns now permits the creation of dark holes that are devoid of diffraction structure down

to 10^{-5} . Moreover, the coronagraphic PSFs of the grating-vAPP are not deteriorated by leakage PSFs, as they form a separate PSF, that actually can be used to one's advantage as a photometric and/or astrometric reference.

The contrast performance is compared in Fig. 6.10 with the following contrast curves: Annular Groove Phase Mask (AGPM) at LBT (Defrère et al., 2014), the Vector-Vortex Coronagraph (VVC) at the 1.5 m well-corrected aperture at Palomar (Serabyn et al., 2010), the GPI first light results (Macintosh et al., 2014), SPHERE with the Apodized Lyot Coronagraph (ALC) (Vigan et al., 2015), and the APP at the VLT (Meshkat et al., 2014). We compare all the contrast curves in terms of λ/D to account for differences in telescope diameter and observed wavelength. All the contrast curves are corrected from a $N\sigma$ to 5σ detection limit. We assume the contrast is limited by speckle noise in all cases and therefore do not correct the curves for differences in exposure time and telescope diameter. The SPHERE P95 User manual comments that while they have several types of coronagraphs to first order they all have the same contrast performance⁴. In terms of λ/D , both the GPI and SPHERE contrast curves tend to reach high contrasts farther away from the star. The inner working angle (IWA) of the SPHERE ALC is restricted by the design of the K-band ALC coronagraph which can be used from 120 mas outwards. The VVC result at Palomar 1.5-m well-corrected aperture is a bit of an outlier because of the significantly different D/r_0 ratio compared with the other telescopes, but is included because of its high performance at a λ/D -sized inner working angle. The assumption of being speckle limited likely does not hold here as the VVC results were within a factor of two from the photon noise on the background. We see that the vAPP outperforms the other coronagraphs within $5 \lambda/D$ with an improvement up to 2 magnitudes from $2.5 - 3.5 \lambda/D$.

The exceptional contrast performance of the vAPP coronagraph is owing to the unique combination of the following properties:

1. Insensitivity to tip-tilt errors that plague focal-plane coronagraphs but not pupil-plane coronagraphs like the vAPP.
2. Deep suppression of the PSF diffraction structure with an accurately manufactured (geometric) phase pattern already at the first diffraction ring down below the seeing-driven halo.
3. Subtraction of the halo in the dark holes by combining both PSFs with a rotation-subtraction technique.

We see that using the second coronagraphic PSF as a PSF reference gives an improvement of 1 – 1.5 magnitudes (factor 2.5-4 in terms of S/N) at $3 - 3.5 \lambda/D$. The PSF subtraction is shown to improve the contrast within $4.5 \lambda/D$. With a radially optimized subtraction the degradation of the contrast outside of this distance can be reduced. Given a fixed ratio based on optimal contrast close to the star, we obtain a $5\sigma \Delta \text{mag}$ contrast of 10.8 ($= 10^{-4.3}$) at $2.5 \lambda/D$, 12.2 ($= 10^{-4.8}$) at $3.5 \lambda/D$, and 12.5 ($= 10^{-5.0}$) at $4.5 \lambda/D$. With a PCA-based algorithm we expect that our performance will be less impacted by self-subtraction and will improve towards the dashed line of Fig. 6.9. This also makes it possible to make a correction based on the time dependence of the PSF in order to remove the longer scale variations, although it is expected that most of the correction power comes from the same frame. Using a contemporary reference PSF is explored by Dou et al.

⁴SPHERE Period 95, phase 2 User Manual

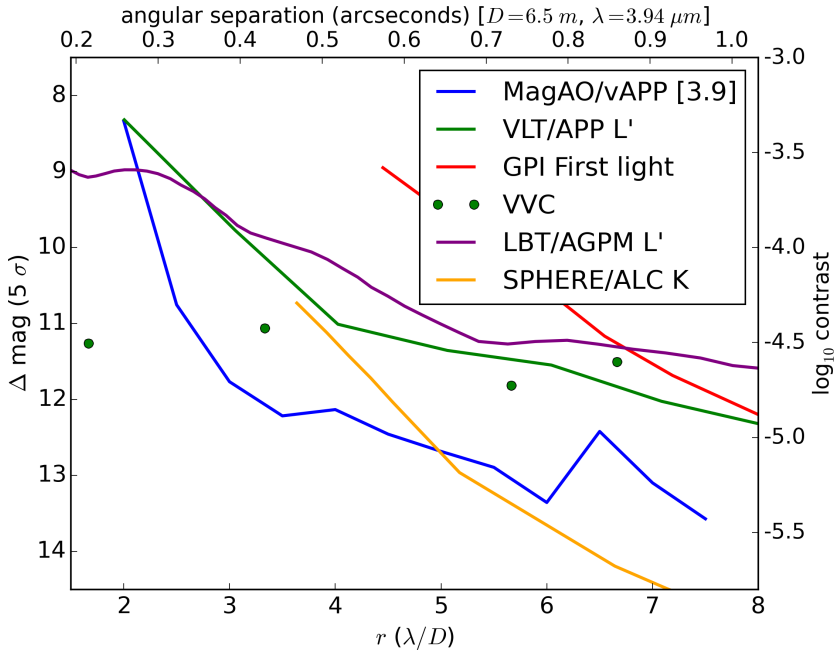


Figure 6.10: Comparison of 5σ contrast as a function of angular separation from the central star from literature. The curves of other studies have been overplotted at the same λ/D to correct for different telescope sizes. The vAPP outperforms many other coronagraphs close to bright stars where one expects to be speckle limited.

(2015), who used the roughly symmetric PSF itself under rotation to feed a PCA algorithm. Their approach gave an improvement of an order of magnitude in terms of contrast when compared to LOCI. Rodrigues et al. (2015) use a close binary star to build their reference PSF library. By having a simultaneous reference within the isoplanatic patch, and with roughly the same optical path through the telescope, a better sensitivity is expected than using the star as its own reference. In their study a 0.5 magnitude improvement within 1 arcsecond from the star was seen compared to normal ADI. Rodrigues et al. (2015) suggests combining their Binary Differential Imaging (BDI) technique with the vAPP coronagraph to reach better contrasts. We can extend this by noting that a double correction can be done by combining BDI and the second vAPP PSF as another reference. In both previous cases the methods are less impacted by self-subtraction because it is unlikely that a companion exists in the reference library with similar brightness, position angle, and radius. Both papers give us confidence that a PCA-based algorithm can be used to generate a better reference PSF and the contrast can be pushed down even more.

One substrate and consequently one adhesive layer can be removed by directly depositing the retarding layer on top of the AR coated substrate and bonding it directly with the substrate with the aluminum mask. This procedure increases the throughput by about 20% but makes manufacturing slightly more difficult and expensive.

6.5.1 Future work

We have shown a manufacturing technique, based on the geometric phase due to patterned liquid crystals, that allows precise control of the phase pattern and a broad-band coronagraphic response that can be optimized anywhere between the visible range and the mid-IR. The optic is relatively straightforward to manufacture and install at existing telescopes as it only uses one pupil plane. Using these capabilities we are looking into new phase patterns with different properties than normally expected from the classical APP theory. For instance, a dark hole spanning 360° per PSE, or integrated wavefront sensing solutions (Wilby et al., 2016) has been implemented and tested on-sky. Future work includes improving the 360° phase-only solutions to increase the working area of the coronagraph, and the potential development of hybrid coronagraphs as described by Ruane et al. (2015). Furthermore we will study the photometric and astrometric stability of the leakage term to assess how well this reference works. Another option that we intend to explore is using the three PSFs of the vAPP to retrieve the wavefront through phase diversity methods. If they are computationally fast to derive, the wavefront error estimates can be fed back to the telescope to correct quasi-static aberrations.

Following the work of Snik et al. (2014) we also intend to explore the dual-beam polarimetric capabilities of the vector APP in the optical lab and on-sky. For polarized sources an increased sensitivity is expected by simultaneously using the coronagraphic capabilities and polarimetric beam switching.

Acknowledgments

This work is part of the research programme Instrumentation for the E-ELT, which is partly financed by the Netherlands Organization for Scientific Research (NWO). The MagAO vAPPs were purchased with help from the Lucas Foundation and NASA Origins of Solar Systems program. This research has made use of the SIMBAD database, operated at CDS, Strasbourg, France.

References

- Amara, A. and Quanz, S. P. (2012). PYNPOINT: an image processing package for finding exoplanets. *MNRAS*, 427:948–955.
- Berry, M. V. (1984). Quantal Phase Factors Accompanying Adiabatic Changes. *Royal Society of London Proceedings Series A*, 392:45–57.
- Carlotti, A., Vanderbei, R., and Kasdin, N. J. (2011). Optimal pupil apodizations of arbitrary apertures for high-contrast imaging. *Opt. Express*, 19(27):26796–26809.
- Close, L. M., Gasho, V., Kopon, D., Males, J., Follette, K. B., Brutlag, K., Uomoto, A., and Hare, T. (2010). The Magellan Telescope Adaptive Secondary AO System: a visible and mid-IR AO facility. In *Society of Photo-Optical Instrumentation Engineers (SPIE) Conference Series*, volume 7736 of *Society of Photo-Optical Instrumentation Engineers (SPIE) Conference Series*, page 5.
- Close, L. M., Males, J. R., Morzinski, K., Kopon, D., Follette, K., Rodigas, T. J., Hinz, P., Wu, Y.-L., Puglisi, A., Esposito, S., Riccardi, A., Pinna, E., Xompero, M., Briguglio, R., Uomoto, A., and Hare, T. (2013). Diffraction-limited Visible Light Images of Orion Trapezium Cluster with the Magellan Adaptive Secondary Adaptive Optics System (MagAO). *ApJ*, 774:94.
- Codona, J. L. and Angel, R. (2004). Imaging Extrasolar Planets by Stellar Halo Suppression in Separately Corrected Color Bands. *ApJ*, 604:L117–L120.
- Codona, J. L., Kenworthy, M. A., Hinz, P. M., Angel, J. R. P., and Woolf, N. J. (2006). A high-contrast coronagraph for the MMT using phase apodization: design and observations at 5 microns and $2 \lambda/D$ radius. In *Society of Photo-Optical Instrumentation Engineers (SPIE) Conference Series*, volume 6269 of *Society of Photo-Optical Instrumentation Engineers (SPIE) Conference Series*.
- Defrère, D., Absil, O., Hinz, P., Kuhn, J., Mawet, D., Mennesson, B., Skemer, A., Wallace, K., Bailey, V., Downey, E., Delacroix, C., Durney, O., Forsberg, P., Gomez, C., Habraken, S., Hoffmann, W. F., Karlsson, M., Kenworthy, M., Leisenring, J., Montoya, M., Pueyo, L., Skrutskie, M., and Surdej, J. (2014). L-band AGPM vector vortex coronagraph's first light on LBTI/LMIRCam. In *Society of Photo-Optical Instrumentation Engineers (SPIE) Conference Series*, volume 9148 of *Society of Photo-Optical Instrumentation Engineers (SPIE) Conference Series*, page 3.
- Dou, J., Ren, D., Zhao, G., Zhang, X., Chen, R., and Zhu, Y. (2015). A High-contrast Imaging Algorithm: Optimized Image Rotation and Subtraction. *ApJ*, 802:12.
- Fienup, J. R. (1980). Iterative method applied to image reconstruction and to computer-generated holograms. *Optical Engineering*, 19:297–305.

- Fusco, T., Sauvage, J.-F., Petit, C., Costille, A., Dohlen, K., Mouillet, D., Beuzit, J.-L., Kasper, M., Suarez, M., Soenke, C., Fedrigo, E., Downing, M., Baudoz, P., Sevin, A., Perret, D., Barufolo, A., Salasnich, B., Puget, P., Feautrier, F., Rochat, S., Moulin, T., Deboulb e, A., Hugot, E., Vigan, A., Mawet, D., Girard, J., and Hubin, N. (2014). Final performance and lesson-learned of saxo, the vlt-sphere extreme ao: from early design to on-sky results. In *Proc. SPIE*, volume 9148 of *Society of Photo-Optical Instrumentation Engineers (SPIE) Conference Series*, pages 91481U–91481U–15.
- Gerchberg, R. and Saxton, W. (1972). A practical algorithm for the determination of the phase from image and diffraction plane pictures. *Optik*, 35:237–246.
- Guyon, O., Pluzhnik, E. A., Kuchner, M. J., Collins, B., and Ridgway, S. T. (2006). Theoretical Limits on Extrasolar Terrestrial Planet Detection with Coronagraphs. *ApJS*, 167:81–99.
- Hinkley, S., Oppenheimer, B. R., Soummer, R., Sivaramkrishnan, A., Roberts, Jr., L. C., Kuhn, J., Makidon, R. B., Perrin, M. D., Lloyd, J. P., Kratter, K., and Brenner, D. (2007). Temporal Evolution of Coronagraphic Dynamic Range and Constraints on Companions to Vega. *ApJ*, 654:633–640.
- Jovanovic, N., Guyon, O., Martinache, F., Clergeon, C., Singh, G., Kudo, T., Newman, K., Kuhn, J., Serabyn, E., Norris, B., Tuthill, P., Stewart, P., Huby, E., Perrin, G., Lacour, S., Vievard, S., Murakami, N., Fumika, O., Minowa, Y., Hayano, Y., White, J., Lai, O., Marchis, F., Duchene, G., Kotani, T., and Woillez, J. (2014). Development and recent results from the subaru coronagraphic extreme adaptive optics system. In *Proc. SPIE*, volume 9147 of *Society of Photo-Optical Instrumentation Engineers (SPIE) Conference Series*, pages 91471Q–91471Q–11.
- Kenworthy, M. A., Codona, J. L., Hinz, P. M., Angel, J. R. P., Heinze, A., and Sivanandam, S. (2007). First On-Sky High-Contrast Imaging with an Apodizing Phase Plate. *ApJ*, 660:762–769.
- Kenworthy, M. A., Meshkat, T., Quanz, S. P., Girard, J. H., Meyer, M. R., and Kasper, M. (2013). Coronagraphic Observations of Fomalhaut at Solar System Scales. *ApJ*, 764:7.
- Kim, J., Li, Y., Miskiewicz, M. N., Oh, C., Kudenov, M. W., and Escuti, M. J. (2015). Fabrication of ideal geometric-phase holograms with arbitrary wavefronts. *Optica*, 2(11):958–964.
- Komanduri, R. K., Lawler, K. F., and Escuti, M. J. (2013). Multi-twist retarders: broadband retardation control using self-aligning reactive liquid crystal layers. *Opt. Express*, 21(1):404–420.
- Lafreni re, D., Marois, C., Doyon, R., Nadeau, D., and Artigau,  . (2007). A New Algorithm for Point-Spread Function Subtraction in High-Contrast Imaging: A Demonstration with Angular Differential Imaging. *ApJ*, 660:770–780.
- Macintosh, B., Graham, J. R., Ingraham, P., Konopacky, Q., Marois, C., Perrin, M., Poyneer, L., Bauman, B., Barman, T., Burrows, A. S., Cardwell, A., Chilcote, J., De Rosa, R. J., Dillon, D., Doyon, R., Dunn, J., Erikson, D., Fitzgerald, M. P., Gavel, D., Goodsell, S., Hartung, M., Hibon, P., Kalas, P., Larkin, J., Maire, J., Marchis, F., Marley, M. S., McBride, J.,

- Millar-Blanchaer, M., Morzinski, K., Norton, A., Oppenheimer, B. R., Palmer, D., Patience, J., Pueyo, L., Rantakyro, F., Sadakuni, N., Saddlemyer, L., Savransky, D., Serio, A., Soummer, R., Sivaramakrishnan, A., Song, I., Thomas, S., Wallace, J. K., Wiktorowicz, S., and Wolff, S. (2014). First light of the gemini planet imager. *Proceedings of the National Academy of Sciences*, 111(35):12661–12666.
- Marois, C. (2007). Speckle Noise Attenuation in Coronagraphy and High-Contrast Imaging. In *In the Spirit of Bernard Lyot: The Direct Detection of Planets and Circumstellar Disks in the 21st Century*.
- Marois, C., Doyon, R., Racine, R., Nadeau, D., Lafreniere, D., Vallee, P., Riopel, M., and Macintosh, B. (2005). Direct Exoplanet Imaging around Sun-like Stars: Beating the Speckle Noise with Innovative Imaging Techniques. *JRASC*, 99:130.
- Marois, C., Lafrenière, D., Doyon, R., Macintosh, B., and Nadeau, D. (2006). Angular Differential Imaging: A Powerful High-Contrast Imaging Technique. *ApJ*, 641:556–564.
- Mawet, D., Pueyo, L., Lawson, P., Mugnier, L., Traub, W., Boccaletti, A., Trauger, J. T., Gladysz, S., Serabyn, E., Milli, J., Belikov, R., Kasper, M., Baudoz, P., Macintosh, B., Marois, C., Oppenheimer, B., Barrett, H., Beuzit, J.-L., Devaney, N., Girard, J., Guyon, O., Krist, J., Mennesson, B., Mouillet, D., Murakami, N., Poyneer, L., Savransky, D., Véraud, C., and Wallace, J. K. (2012). Review of small-angle coronagraphic techniques in the wake of ground-based second-generation adaptive optics systems. In *Society of Photo-Optical Instrumentation Engineers (SPIE) Conference Series*, volume 8442 of *Society of Photo-Optical Instrumentation Engineers (SPIE) Conference Series*.
- Mawet, D., Serabyn, E., Liewer, K., Hanot, C., McEldowney, S., Shemo, D., and O'Brien, N. (2009). Optical Vectorial Vortex Coronagraphs using Liquid Crystal Polymers: theory, manufacturing and laboratory demonstration. *Optics Express*, 17:1902–1918.
- Meshkat, T., Kenworthy, M. A., Quanz, S. P., and Amara, A. (2014). Optimized Principal Component Analysis on Coronagraphic Images of the Fomalhaut System. *ApJ*, 780:17.
- Miskiewicz, M. N. and Escuti, M. J. (2014). Direct-writing of complex liquid crystal patterns. *Opt. Express*, 22(10):12691–12706.
- Morzinski, K. M., Close, L. M., Males, J. R., Kopon, D., Hinz, P. M., Esposito, S., Riccardi, A., Puglisi, A., Pinna, E., Briguglio, R., Xompero, M., Quirós-Pacheco, F., Bailey, V., Follette, K. B., Rodigas, T. J., Wu, Y.-L., Arcidiacono, C., Argomedo, J., Busoni, L., Hare, T., Uomoto, A., and Weinberger, A. (2014). MagAO: Status and on-sky performance of the Magellan adaptive optics system. In *Society of Photo-Optical Instrumentation Engineers (SPIE) Conference Series*, volume 9148 of *Society of Photo-Optical Instrumentation Engineers (SPIE) Conference Series*, page 4.
- Otten, G. P. P. L., Snik, F., Kenworthy, M. A., Miskiewicz, M. N., and Escuti, M. J. (2014a). Performance characterization of a broadband vector apodizing phase plate coronagraph. *Opt. Express*, 22(24):30287–30314.

- Otten, G. P. P. L., Snik, F., Kenworthy, M. A., Miskiewicz, M. N., Escuti, M. J., and Codona, J. L. (2014b). The vector apodizing phase plate coronagraph: prototyping, characterization and outlook. In *Society of Photo-Optical Instrumentation Engineers (SPIE) Conference Series*, volume 9151, pages 91511R–91511R–10.
- Packham, C., Escuti, M., Ginn, J., Oh, C., Quijano, I., and Boreman, G. (2010). Polarization gratings: A novel polarimetric component for astronomical instruments. *Publications of the Astronomical Society of the Pacific*, 122(898):pp. 1471–1482.
- Pancharatnam, S. (1956). Generalized theory of interference, and its applications. part i. coherent pencils. *Proceedings of the Indian Academy of Sciences, Section A*, 44, 5:247–262.
- Quanz, S. P., Meyer, M. R., Kenworthy, M. A., Girard, J. H. V., Kasper, M., Lagrange, A.-M., Apai, D., Boccaletti, A., Bonnefoy, M., Chauvin, G., Hinz, P. M., and Lenzen, R. (2010). First results from very large telescope naco apodizing phase plate: 4 μm images of the exoplanet β pictoris b. *The Astrophysical Journal Letters*, 722(1):L49.
- Racine, R., Walker, G. A. H., Nadeau, D., Doyon, R., and Marois, C. (1999). Speckle Noise and the Detection of Faint Companions. *PASP*, 111:587–594.
- Rodigas, T. J., Weinberger, A., Mamajek, E. E., Males, J. R., Close, L. M., Morzinski, K., Hinz, P. M., and Kaib, N. (2015). Direct Exoplanet Detection with Binary Differential Imaging. *ArXiv e-prints*.
- Ruane, G. J., Huby, E., Absil, O., Mawet, D., Delacroix, C., Carlomagno, B., and Swartzlander, G. A. (2015). Lyot-plane phase masks for improved high-contrast imaging with a vortex coronagraph. *ArXiv e-prints*.
- Serabyn, E., Mawet, D., and Burruss, R. (2010). An image of an exoplanet separated by two diffraction beamwidths from a star. *Nature*, 464:1018–1020.
- Sivanandam, S., Hinz, P. M., Heinze, A. N., Freed, M., and Breuninger, A. H. (2006). Clio: a 3-5 micron AO planet-finding camera. In *Society of Photo-Optical Instrumentation Engineers (SPIE) Conference Series*, volume 6269 of *Society of Photo-Optical Instrumentation Engineers (SPIE) Conference Series*, page 0.
- Snik, F., Otten, G., Kenworthy, M., Mawet, D., and Escuti, M. (2014). Combining vector-phase coronagraphy with dual-beam polarimetry. In *Proc. SPIE*, volume 9147 of *Society of Photo-Optical Instrumentation Engineers (SPIE) Conference Series*, pages 91477U–91477U–12.
- Snik, F., Otten, G., Kenworthy, M., Miskiewicz, M., Escuti, M., Packham, C., and Codona, J. (2012). The vector-APP: a broadband apodizing phase plate that yields complementary PSFs. In *Society of Photo-Optical Instrumentation Engineers (SPIE) Conference Series*, volume 8450 of *Society of Photo-Optical Instrumentation Engineers (SPIE) Conference Series*.
- Soummer, R., Pueyo, L., and Larkin, J. (2012). Detection and characterization of exoplanets and disks using projections on karhunen-loève eigenimages. *The Astrophysical Journal Letters*, 755(2):L28.

- Vigan, A., Gry, C., Salter, G., Mesa, D., Homeier, D., Moutou, C., and Allard, F. (2015). High-contrast imaging of Sirius A with VLT/SPHERE: looking for giant planets down to one astronomical unit. *MNRAS*, 454:129–143.
- Wilby, M. J., Keller, C. U., Snik, F., Korkiakoski, V., and Pietrow, A. G. M. (2016). The coronagraphic Modal Wavefront Sensor: a hybrid focal-plane sensor for the high-contrast imaging of circumstellar environments. *ArXiv e-prints*.

7 | Outlook

This thesis focuses on the development of the vector Apodizing Phase Plate that overcomes the limitations of the original APP manufacture. The main selling points of the vAPP are its broad-band achromatic behavior from anywhere in the near-UV to mid-IR and the highly customizable phase patterns. In this Chapter we look at the current possibilities with the vAPP and future developments.

7.1 Science observations with vAPP

7.1.1 NIR observations

The first observations with the vAPP at MagAO show an unprecedented contrast close to the star. As presented in Chapter 6 the two vAPP images can be used under rotation, scaling and subtraction to improve the contrast close to the star. We measured a 5σ contrast of 8.3 ($= 10^{-3.3}$) magnitudes at $2 \lambda/D$, 10.8 ($= 10^{-4.3}$) at $2.5 \lambda/D$, 12.2 ($= 10^{-4.8}$) at $3.5 \lambda/D$, and 12.5 ($= 10^{-5}$) at $4.5 \lambda/D$, all derived at 3.9 microns narrow-band.

For a sample of bright nearby young stars (< 100 pc) these contrasts correspond with a detection sensitivity down to $4 M_{\text{Jup}}$ with separations of 4 AU within 3 hours of observations per target. Most of the mass for the formation of planets is available at these separations around stars. Just beyond the iceline around stars it is expected that most of the giant gas planets form. By measuring the occurrence rate of giant gas planets at these distances formation models can be constrained.

In the near future we intend to expand our observations of nearby (< 70 pc) young stars (in moving groups) and also explore the increased detection sensitivity (in terms of mass) at M -band with MagAO where even smaller planets can be detected. Based on a limit of $1 \lambda/D$ spectral smearing we expect that the following filters in MagAO are usable: $Br\gamma$, [3.1], [3.9], M' . The broader filters are usable but the spectral smearing is significant and needs to be taken into account while interpreting the data.

7.1.2 Broad-band observations

While the design of the vAPP with the included grating is incredibly simple and robust against retardance offsets, it does reduce the maximum width of the filter that can be used for observations. Some telescopes are already equipped with some of the optics necessary to perform achromatic handedness-based splitting and are therefore very suitable to quickly explore this option. MMTpol is a 1–5 micron diffraction limited polarimetric imager located at the AO-capable 6.5m MMT in Arizona (Packham and Jones, 2008). It has a Wollaston prism that we can use in combination with an achromatic quarter wave plate and a vAPP coronagraph. This is identical to the original optical

setup used for our laboratory measurements with the vAPP prototype in Chapter 3. MMTpol already has a rotatable half-wave plate as polarization modulator. This combination of optical components makes it possible to do broadband dual beam polarimetry in the NIR. Note that the retardance offset again becomes a problem in this setup but this effect can be reduced by developing a device with more liquid crystal layers to push the retardance closer to half-wave.

7.1.3 The push towards shorter wavelengths

The vAPP can be optimized for different wavelengths from the near-UV to the mid-Infrared with broad-band achromatic performance. A logical step after demonstrating the broad-band vAPP between $K - M$ band is to apply the coronagraph to shorter NIR wavelengths like J, H, K (resp., 1.25, 1.65, 2.2 microns) and the filters at the red edge of the visible range r, i, z, y . The transmission of the coronagraph is $\sim 90\%$ in the visible, even for the achromatic multilayer devices, which means that the coronagraph is almost twice as efficient in the visible than in the NIR. Logical contenders for a move to shorter wavelengths are VisAO at the Magellan Clay telescope and ZIMPOL ($V - I$), IFS ($Y - H$) and IRDIS ($Y - K_s$) in SPHERE. Both ZIMPOL and IRDIS are already equipped with polarizing beamsplitters, facilitating the installation of vAPP coronagraphs. For bright ($V < 8$) stars ZIMPOL produces Strehl ratios of 50-70% depending on the filter (Fusco et al., 2014). VisAO at Magellan currently has a Strehl ratio of $> 30\%$ (Close et al., 2014). With the expected upgrades of MagAO with a deformable mirror and increased correction speed (MagAO-X and MagAO-2K) the Strehl ratio in the visible will become even more favorable for direct imaging. Interesting scientific targets in the visible are planetary accretion around young stars in Hydrogen alpha (Close et al., 2014) and the reflected light of planets in the habitable zone around the closest stars, such as Alpha Centauri (Males et al., 2014).

7.1.4 Binary observations with vAPP

Many massive stars reside in roughly equal mass binary systems. These targets are often ignored in direct imaging studies as only select coronagraphs (like the APP) can cope with double stars. Binary Differential Imaging was used by Rodigas et al. (2015) on a wide (4 arcseconds) system to improve the contrast within 1 arcsecond by 0.5 magnitudes with respect to a normal ADI reduction. BDI requires that the PSF is approximately the same across the field of view. This only works without focal-plane coronagraphs and if the isoplanatic patch is large enough to cover both stars. This is easier to achieve in the NIR since the atmosphere has less impact. As it is located in the pupil-plane the vAPP is 100% compatible with this technique and is expected to boost the contrast even more. Further study is necessary to determine the magnitude of this improvement. Rodigas et al. (2015) mention that they are performing a survey of 140 nearby visual binaries with MagAO/Clio2 using the BDI technique. The current presence of the vAPP in Clio2 makes it trivial to confirm the improvement. A second correction step using the rotation, scaling and subtraction method presented in this thesis can be used to improve the contrast. Furthermore, we can design PSF structures such that the far rings of one star do not deteriorate the contrast in the dark hole next to the other star as was proposed by Thomas et al. (2015), and in the case of the 360 degree grating vAPP; applied by Christoph Keller to reduce cross contamination between the two coronagraphic PSFs.

7.1.5 Disk observations with 360 degree vAPP

A 180 degree suppressing coronagraph is not ideal for imaging disks as the complicated asymmetric PSF can disturb the apparent shape of the convolution. In Chapter 4 we also demonstrated that the extreme phase patterns that can be implemented can be leveraged to suppress the starlight in a 360 degree region around the star. This 360 degree dark hole can be used to observe disks around bright stars without significant impact to the shape of the disk, which would happen with the regular asymmetric APP PSF. A 360 degree suppressing coronagraph is currently located in pupil wheel of Clío2. The feasibility of this technique can therefore be easily tested.

7.2 Combining vAPP with complementary techniques

7.2.1 Focal plane wavefront sensing

Focal plane wavefront sensing and the subsequent wavefront correction is important to reduce the noise contribution of quasi-static speckles. The phase sorting-interferometry method by Codona et al. (2008); Codona and Kenworthy (2013) has been previously introduced as a promising solution for this (see also Chapter 2). Its main advantage is that it does not require hardware changes to the telescope. The reconstruction is purely software-based using the wavefront sensor telemetry and rapid science camera images. The reconstructed wavefronts can be applied on the deformable mirror to correct the images.

Several focal plane sensing methods could potentially be implemented in the vAPP coronagraph concept. It is known that wavefronts can be estimated from images with a known phase diversity (Roddier and Roddier, 1993). In the case of the grating-vAPP we have 3 PSFs with a known phase error which potentially can be used to do instantaneous phase diversity wavefront estimation similar to what was proposed for the Vector Vortex Coronagraph (Riaud, P. et al., 2012). The reconstructed wavefront includes the non-common path aberrations and can be sent to the deformable mirror to correct the distortion.

Another method that is being developed in Leiden is the holographic focal-plane wavefront sensing technique by Wilby et al. (2016). A binary phase mask is added to the vAPP phase that projects satellite PSFs around the coronagraphic PSF that are sensitive to certain basic wavefront modes. By measuring the intensity of these satellites the incoming wavefront can be estimated. This method has been demonstrated on-sky at the William Herschel Telescope in April 2015 and will be developed in the coming years.

7.2.2 Spectroscopy

We have already seen that the achromatic nature of the vector APP allows for spectrophotometry with narrow-band filters. The MagAO coronagraph covers 2 to 5 microns using a single optic which reduces the overhead with respect to the old situation where 2 APPs covered only a fraction of this wavelength range. The latter case also required a time-costly realignment of the pupil when switching wavelengths.

To use the full achromatic wavelength range the vAPP can be used in combination with an Integral Field Unit (IFU). The chromatic dependence of the splitting angle can be nullified using the wavelength channels of the IFU. The more conventional setup with an achromatic

quarter wave and Wollaston prism keeps all the planet light at the same position. The slit of the spectrograph can be placed exactly across the planet to perform spectroscopy.

A combination of the achromatic vAPP and a fiber-fed high spectral resolution spectrograph can be used to improve the detection of atmospheric signatures through the radial velocity technique as pioneered by Snellen et al. (2014). The contribution of the stellar light to the noise is reduced by the coronagraphic step. In Leiden a dedicated instrument (LEXI) is being developed to further explore this concept.

7.2.3 Polarimetry

Due to the polarization-based technology behind some coronagraphs they can be relatively easily adapted to perform polarimetry. Combining polarimetry and coronagraphs is expected to give an improvement for planets with a polarized signal over the contrast achieved by each method individually. Polarized signals can be expected from planets close to the star reflecting starlight at visible wavelengths.

In recent years several coronagraphs have been developed that use these retarding optics. The Vector Vortex Coronagraph (VVC) uses liquid crystals like the vAPP and was introduced by Mawet et al. (2009a,b, 2010). The Annular Groove Phase Mask (AGPM) (Mawet et al., 2005) is related to the VVC but uses sub-wavelength gratings as retarders. Murakami et al. (2012) performed a laboratory study of PDI and ADI with both the VVC and the Eight-Octant Phase Mask, in their case based on photonic crystals. Recently, Snik et al. (2014) presented dual beam polarimetric setups for both the VVC and the vAPP although they did not explore the vAPP with included phase grating. Adapting the grating vAPP for polarimetry only requires the addition of a polarization modulator like a rotatable half-wave plate or Ferroelectric liquid crystal (FLC) in front of the coronagraph. An achromatic quarter-wave plate has to be added between the modulator and the coronagraph to allow the modulation of linear states.

7.2.4 Instruments applying lessons learned

In the short term there are several instruments where we can explore some of the previously mentioned options. There are several logical instruments that can be named, namely: ExPo (Rodenhuis et al., 2012) and LEXI, both being developed in Leiden as on-sky technology testbeds to prepare for the next generation of telescopes.

Broad-band vAPP coronagraphs will go to the LBT to replace the current narrow-band version in LMIRCam. One of the coronagraphs will also be optimized for the field of view of the ALES IFU. The vAPP is also being considered for use with VLT/SPHERE and in the near future for the ERIS instrument (Kuntzschner et al., 2014); the successor of the very successful NACO instrument at the VLT.

7.3 The vAPP in the ELT-era

We expect that the capabilities of the vAPP will become even more relevant in the era of Extremely Large Telescopes that are planned with diameters of 24 – 40 meters. The increased sensitivity of

the telescopes requires better control of systematics. Vibrations will become an even larger problem with the increased spatial resolution and large mechanical structure, and like with any newly constructed large telescope startup difficulties are expected. A robust and simple coronagraph like the vAPP works under difficult and suboptimal conditions. Its simplicity of manufacturing facilitates a quick adaption to different pupil designs varying from the 7-mirror Giant Magellan Telescope (Johns et al., 2012; Codona, 2004) to the possible annular first phase of the segmented E-ELT. A third ELT that it can be adapted to is the segmented Thirty Meter Telescope (TMT). Adapting focal-plane coronagraphs to work with complicated / segmented pupil designs is not a trivial task and also requires phase and/or amplitude modifications in the pupil (Carlotti, 2013; Ruane et al., 2015). Future instruments behind the ELTs are designed with very broad wavelength ranges and are outfitted with spectrometers and IFUs to take full advantage of this. Current coronagraphs are generally optimized for specific narrow bands. The vAPP coronagraph's achromatic behavior is fundamental for the optimal usage of these instruments. With 100% bandwidth only several coronagraphs are required to span the full spectral range of an instrument. Furthermore, the coronagraph can be optimized from anywhere from NUV to the MIR. A common problem in segmented telescopes like the E-ELT and the TMT is that mirror segments are swapped out to be cleaned. It is expected for these ELTs that several mirror segments will not be in place at any time. Without complicated methods to circumvent the impact to the contrast all coronagraphs will be in theory limited to a contrast level of 10^{-5} ¹. To deal with this ever changing pupil requires flexible adaptive optics and/or adaptive or quickly manufacturable coronagraphs. In light of the expected start-up difficulties with ELTs, and the simplicity and broad-band efficiency of the vAPP, it may very well be the first small inner working angle coronagraph going on-sky in the next generation of telescopes.

7.3.1 European Extremely Large Telescope

The E-ELT has multiple planned instruments that can be used for direct imaging. MICADO will be a 0.8 – 2.4 micron diffraction limited imager and is a first light instrument (Davies et al., 2010). METIS is a 3 – 19 micron diffraction limited imager and spectrograph (Brandl et al., 2014). Quanz et al. (2015) simulated the direct imaging performance of METIS on the E-ELT and concluded that Earth-sized planets are in reach of direct detection. In Snellen et al. (2015) the prediction was made that the atmospheric signature of rocky Earth-like planets can be detected in the habitable zone of Alpha Centauri with the combination of high contrast imaging and high dispersion spectroscopy in only one night of observing with E-ELT/METIS. Even the HARMONI instrument (Thatte et al., 2014), while not optimized for high contrast imaging, can accept pupil-plane coronagraphs such as the vAPP. Focal-plane coronagraphs are unavailable in HARMONI due to the uncorrected atmospheric dispersion. MICADO, HARMONI and METIS are all three first-light instruments. The E-ELT instrument EPICS is an dedicated high-contrast imager and is expected to reach a contrast of 10^{-8} to 10^{-9} in the visible and NIR (600 – 1650 nm) (Kasper et al., 2010). This makes it possible to detect atmospheric signatures in reflected light from rocky planets. Most instruments planned for the E-ELT can therefore easily accept the simple, robust and achromatic vAPP coronagraph.

The techniques introduced in this thesis are robust and versatile, we will continue to use their

¹Carlotti during 'Combining Coronagraphs and Wavefront Control' workshop in Leiden

performance in the near future to discover and characterize exoplanets, and to contribute directly to the next generation of telescopes and direct imaging instruments.

References

- Brandl, B. R., Feldt, M., Glasse, A., Guedel, M., Heikamp, S., Kenworthy, M., Lenzen, R., Meyer, M. R., Molster, F., Paalvast, S., Pantin, E. J., Quanz, S. P., Schmalzl, E., Stuik, R., Venema, L., and Waelkens, C. (2014). METIS: the mid-infrared E-ELT imager and spectrograph. In *Ground-based and Airborne Instrumentation for Astronomy V*, volume 9147 of *Proc. SPIE*, page 914721.
- Carlotti, A. (2013). Apodized phase mask coronagraphs for arbitrary apertures. *A&A*, 551:A10.
- Close, L. M., Follette, K. B., Males, J. R., Puglisi, A., Xompero, M., Apai, D., Najita, J., Weinberger, A. J., Morzinski, K., Rodigas, T. J., Hinz, P., Bailey, V., and Briguglio, R. (2014). Discovery of H α Emission from the Close Companion inside the Gap of Transitional Disk HD 142527. *ApJ*, 781:L30.
- Close, L. M., Males, J. R., Follette, K. B., Hinz, P., Morzinski, K., Wu, Y.-L., Kopon, D., Riccardi, A., Esposito, S., Puglisi, A., Pinna, E., Xompero, M., Briguglio, R., and Quiros-Pacheco, F. (2014). Into the blue: Ao science with magao in the visible.
- Codona, J. L. (2004). Exoplanet imaging with the giant magellan telescope.
- Codona, J. L. and Kenworthy, M. (2013). Focal Plane Wavefront Sensing Using Residual Adaptive Optics Speckles. *ApJ*, 767:100.
- Codona, J. L., Kenworthy, M. A., and Lloyd-Hart, M. (2008). A novel WFS technique for high-contrast imaging: Phase Sorting Interferometry (PSI). In *Society of Photo-Optical Instrumentation Engineers (SPIE) Conference Series*, volume 7015 of *Society of Photo-Optical Instrumentation Engineers (SPIE) Conference Series*, page 5.
- Davies, R., Ageorges, N., Barl, L., Bedin, L. R., Bender, R., Bernardi, P., Chapron, F., Clenet, Y., Deep, A., Deul, E., Drost, M., Eisenhauer, F., Falomo, R., Fiorentino, G., Förster Schreiber, N. M., Gendron, E., Genzel, R., Gratadour, D., Greggio, L., Grupp, F., Held, E., Herbst, T., Hess, H.-J., Hubert, Z., Jahnke, K., Kuijken, K., Lutz, D., Magrin, D., Muschiello, B., Navarro, R., Noyola, E., Paumard, T., Piotto, G., Ragazzoni, R., Renzini, A., Rousset, G., Rix, H.-W., Saglia, R., Tacconi, L., Thiel, M., Tolstoy, E., Trippe, S., Tromp, N., Valentijn, E. A., Verdoes Kleijn, G., and Wegner, M. (2010). MICADO: the E-ELT adaptive optics imaging camera. In *Ground-based and Airborne Instrumentation for Astronomy III*, volume 7735 of *Proc. SPIE*, page 77352A.
- Fusco, T., Sauvage, J.-F., Petit, C., Costille, A., Dohlen, K., Mouillet, D., Beuzit, J.-L., Kasper, M., Suarez, M., Soenke, C., Fedrigo, E., Downing, M., Baudoz, P., Sevin, A., Perret, D., Barrufolo, A., Salasnich, B., Puget, P., Feautrier, F., Rochat, S., Moulin, T., Deboulb e, A., Hugot, E.,

- Vigan, A., Mawet, D., Girard, J., and Hubin, N. (2014). Final performance and lesson-learned of saxo, the vlt-sphere extreme ao: from early design to on-sky results.
- Johns, M., McCarthy, P., Raybould, K., Bouchez, A., Farahani, A., Filgueira, J., Jacoby, G., Shectman, S., and Sheehan, M. (2012). Giant magellan telescope: overview.
- Kasper, M., Beuzit, J.-L., Verinaud, C., Gratton, R. G., Kerber, F., Yaitskova, N., Boccaletti, A., Thatte, N., Schmid, H. M., Keller, C., Baudoz, P., Abe, L., Aller-Carpentier, E., Antichi, J., Bonavita, M., Dohlen, K., Fedrigo, E., Hanenburg, H., Hubin, N., Jager, R., Korkiakoski, V., Martinez, P., Mesa, D., Preis, O., Rabou, P., Roelfsema, R., Salter, G., Tecza, M., and Venema, L. (2010). Epics: direct imaging of exoplanets with the e-elt.
- Kuntschner, H., Jochum, L., Amico, P., Dekker, J. K., Kerber, F., Marchetti, E., Accardo, M., Brast, R., Brinkmann, M., Conzelmann, R. D., Delabre, B. A., Duchateau, M., Fedrigo, E., Finger, G., Frank, C., Rodriguez, F. G., Klein, B., Knudstrup, J., Le Louarn, M., Lundin, L., Modigliani, A., Müller, M., Neeser, M., Tordo, S., Valenti, E., Eisenhauer, F., Sturm, E., Feuchtgruber, H., George, E. M., Hartl, M., Hofmann, R., Huber, H., Plattner, M. P., Schubert, J., Tarantik, K., Wiezorrek, E., Meyer, M. R., Quanz, S. P., Glauser, A. M., Weisz, H., Esposito, S., Xompero, M., Agapito, G., Antichi, J., Biliotti, V., Bonaglia, M., Briguglio, R., Carbonaro, L., Cresci, G., Fini, L., Pinna, E., Puglisi, A. T., Quirós-Pacheco, F., Riccardi, A., Di Rico, G., Arcidiacono, C., and Dolci, M. (2014). Eris: preliminary design phase overview.
- Males, J. R., Close, L. M., Guyon, O., Morzinski, K., Puglisi, A., Hinz, P., Follette, K. B., Monnier, J. D., Tolls, V., Rodigas, T. J., Weinberger, A., Boss, A., Kopon, D., Wu, Y.-l., Esposito, S., Riccardi, A., Xompero, M., Briguglio, R., and Pinna, E. (2014). Direct imaging of exoplanets in the habitable zone with adaptive optics.
- Mawet, D., Pueyo, L., Moody, D., Krist, J., and Serabyn, E. (2010). The Vector Vortex Coronagraph: sensitivity to central obscuration, low-order aberrations, chromaticism, and polarization. In *Modern Technologies in Space- and Ground-based Telescopes and Instrumentation*, volume 7739 of *Proc. SPIE*, page 773914.
- Mawet, D., Riaud, P., Absil, O., and Surdej, J. (2005). Annular groove phase mask coronagraph. *The Astrophysical Journal*, 633(2):1191.
- Mawet, D., Serabyn, E., Liewer, K., Hanot, C., McEldowney, S., Shemo, D., and O'Brien, N. (2009a). Optical Vectorial Vortex Coronagraphs using Liquid Crystal Polymers: theory, manufacturing and laboratory demonstration. *Optics Express*, 17:1902–1918.
- Mawet, D., Trauger, J. T., Serabyn, E., Moody, Jr., D. C., Liewer, K. M., Krist, J. E., Shemo, D. M., and O'Brien, N. A. (2009b). Vector vortex coronagraph: first results in the visible. In *Techniques and Instrumentation for Detection of Exoplanets IV*, volume 7440 of *Proc. SPIE*, page 74400X.
- Murakami, N., Nishikawa, J., Traub, W. A., Mawet, D., Moody, D. C., Kern, B. D., Trauger, J. T., Serabyn, E., Hamaguchi, S., Oshiyama, F., Sakamoto, M., Ise, A., Oka, K., Baba, N., Murakami, H., and Tamura, M. (2012). Coronagraph focal-plane phase masks based on photonic crystal technology: recent progress and observational strategy.

- Packham, C. and Jones, T. J. (2008). Mmt-pol: an adaptive optics optimized 1-5 μ m polarimeter.
- Quanz, S. P., Crossfield, I., Meyer, M. R., Schmalzl, E., and Held, J. (2015). Direct detection of exoplanets in the 3-10 μ m range with E-ELT/METIS. *International Journal of Astrobiology*, 14:279–289.
- Riaud, P., Mawet, D., and Magette, A. (2012). Instantaneous phase retrieval with the vector vortex coronagraph. *A&A*, 545:A151.
- Roddier, C. and Roddier, F. (1993). Wave-front reconstruction from defocused images and the testing of ground-based optical telescopes. *Journal of the Optical Society of America A*, 10:2277–2287.
- Rodenhuis, M., Canovas, H., Jeffers, S. V., de Juan Ovelar, M., Min, M., Homs, L., and Keller, C. U. (2012). The extreme polarimeter: design, performance, first results and upgrades. In *Society of Photo-Optical Instrumentation Engineers (SPIE) Conference Series*, volume 8446 of *Society of Photo-Optical Instrumentation Engineers (SPIE) Conference Series*.
- Rodigas, T. J., Weinberger, A., Mamajek, E. E., Males, J. R., Close, L. M., Morzinski, K., Hinz, P. M., and Kaib, N. (2015). Direct Exoplanet Detection with Binary Differential Imaging. *AJ*, 811:157.
- Ruane, G. J., Huby, E., Absil, O., Mawet, D., Delacroix, C., Carlomagno, B., and Swartzlander, G. A. (2015). Lyot-plane phase masks for improved high-contrast imaging with a vortex coronagraph. *ArXiv e-prints*.
- Snellen, I., de Kok, R., Birkby, J. L., Brandl, B., Brogi, M., Keller, C., Kenworthy, M., Schwarz, H., and Stuik, R. (2015). Combining high-dispersion spectroscopy with high contrast imaging: Probing rocky planets around our nearest neighbors. *A&A*, 576:A59.
- Snellen, I. A. G., Brandl, B. R., de Kok, R. J., Brogi, M., Birkby, J., and Schwarz, H. (2014). Fast spin of the young extrasolar planet β Pictoris b. *Nature*, 509:63–65.
- Snik, F., Otten, G., Kenworthy, M., Mawet, D., and Escuti, M. (2014). Combining vector-phase coronagraphy with dual-beam polarimetry.
- Thatte, N. A., Clarke, F., Bryson, I., Schnetler, H., Tecza, M., Bacon, R. M., Remillieux, A., Mediavilla, E., Herreros Linares, J. M., Arribas, S., Evans, C. J., Lunney, D. W., Fusco, T., O'Brien, K., Tosh, I. A., Ives, D. J., Finger, G., Houghton, R., Davies, R. L., Lynn, J. D., Allen, J. R., Zieleniewski, S. D., Kendrew, S., Ferraro-Wood, V., Pécontal-Rousset, A., Kosmalski, J., Richard, J., Jarno, A., Gallie, A. M., Montgomery, D. M., Henry, D., Zins, G., Freeman, D., García-Lorenzo, B., Rodríguez-Ramos, L. F., Revuelta, J. S. C., Hernandez Suarez, E., Bueno-Bueno, A., Gigante-Ripoll, J. V., Garcia, A., Dohlen, K., and Neichel, B. (2014). HARMONI: the first light integral field spectrograph for the E-ELT. In *Ground-based and Airborne Instrumentation for Astronomy V*, volume 9147 of *Proc. SPIE*, page 914725.
- Thomas, S. J., Belikov, R., and Bendek, E. (2015). A method to directly image exoplanets in multi-star systems such as Alpha-Centauri. In *Techniques and Instrumentation for Detection of Exoplanets VII*, volume 9605 of *Proc. SPIE*, page 96052G.

Wilby, M. J., Keller, C. U., Snik, F., Korkiakoski, V., and Pietrow, A. G. M. (2016). The coronagraphic Modal Wavefront Sensor: a hybrid focal-plane sensor for the high-contrast imaging of circumstellar environments. *ArXiv e-prints*.

Nederlandstalige samenvatting

Suppressing a Sea of Starlight Enabling technology for the direct imaging of exoplanets

De mensheid heeft vaak gefilosofeerd over het bestaan van planeten rond andere sterren. Al zo vroeg als 300 v. Chr. zei Epicurus in een brief aan zijn discipel Herodotus dat ontelbare werelden moesten bestaan, zowel gelijkend als niet-gelijkend op het onze. In de moderne wereld kunnen wij hun filosofische argumenten vervangen door wetenschappelijke redeneringen en wij kunnen tevens gestructureerde vragen stellen zoals; hoe vormen planeten?; is ons zonnestelsel normaal of speciaal?; hoe uniek is de Aarde? en tot slot, de ultieme vraag; is er leven elders in het heelal? Om deze vragen te beantwoorden moeten we planeten rond andere sterren ontdekken en bestuderen.

De eerste planeten rond een andere ster (extrasolaire planeten / exoplaneten) werden ontdekt in 1992 door Wolszcan en Frail. Zij vonden twee planeten met een lage massa rond een restant van een gestorven ster (pulsar). Dit was een belangrijke ontdekking in een eeuwenlange zoektocht naar planeten rond andere sterren. Deze zoektocht had immers al meerdere planeetvondsten gekend, die later fout bleken.

In 1995 werd de exoplaneet 51 Pegasi b gevonden rond een zonachtige ster met behulp van de radiale snelheidsmethode. De radiale snelheidsmethode gebruikt het snelheidscomponent van de ster naar de aarde toe om de aanwezigheid van planeten af te leiden. De aanwezigheid van een planeet verschuift het zwaartepunt van het planetenstelsel. De ster draait ook om dit gezamenlijke middelpunt heen en de beweging van de ster kan door astronomen met spectrografen worden vastgelegd als een schijnbare periodieke verschuiving van de spectraallijnen.

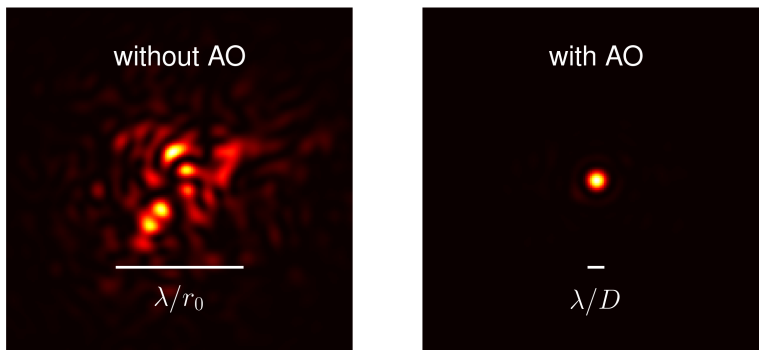
Een onverwacht resultaat was dat de meerderheid van de eerste ontdekkingen Jupiterachtige planeten waren in omloopbanen vergelijkbaar met die van Mercurius. Met behulp van langdurige studies van dezelfde ster en verbeterde nauwkeurigheid en stabiliteit van instrumenten zijn deze ontdekkingen opgeschoven naar Neptunusachtige planeten in Aardachtige banen. Conventionele radiale snelheidsmethode zien alleen het licht van de ster en geven dus slechts beperkte informatie over de planeet.

De meest succesvolle techniek (qua aantal ontdekkingen) is de planeetovergangsmethode, die voor het eerst is toegepast in 2000 door het team van Charbonneau om de reeds gedetecteerde planeet HD 209458 b te bevestigen. Een planeet die precies voor zijn moederster langsgaat (zoals gezien vanaf de Aarde) zal een klein deel van het licht van de ster met vaste regelmaat blokkeren. Onbekende planeten zijn op deze manier relatief gemakkelijk te vinden door gelijktijdig de helderheid van een groot aantal sterren bij te houden.

De meerderheid van de ongeveer 1600 huidige bevestigde exoplaneten werden gevonden met de planeetovergang en radiale snelheidsmethodes. Beide methodes hebben gemeen dat ze indirecte methode zijn om de aanwezigheid van planeten en hun eigenschappen (zoals grootte, massa en

omloopbaan) af te leiden. Door de schijnbare grootte van de planeet op meerdere golflengtes te meten kunnen chemische vingerafdrukken gedetecteerd worden in mogelijke planeetatmosferen. Jammer genoeg is slechts een klein aantal van de ontdekte planeten in een omloopbaan rond een ster die helder genoeg is om deze meting mogelijk te maken.

Iets recenter is de direct waarneemmethode tot wasdom gekomen. Hierdoor zijn astronomen in staat om rechtstreeks de atmosferen van planeten te bestuderen. Het idee om met een telescoop naar planeten rond een andere ster te kijken klinkt simpel maar is in de praktijk ontzettend lastig. Dit is vooral ingewikkeld als men een telescoop op Aarde gebruikt (in vergelijking met een ruimtetelescoop). De invloed van de turbulentie van de aardatmosfeer op de beeldkwaliteit heeft een belemmerende invloed bij het direct waarnemen van exoplaneten. Enkel toen Adaptieve Optica (AO) beschikbaar kwamen, waren astronomen in staat om de beeldkwaliteit in de ruimte te evenaren. Een gesimuleerde vergelijking in beeldkwaliteit voor en na Adaptieve Optica is te zien in Figuur 7.1. Dit laat de revolutionaire invloed zien van AO op het oplossend vermogen van de telescopen.

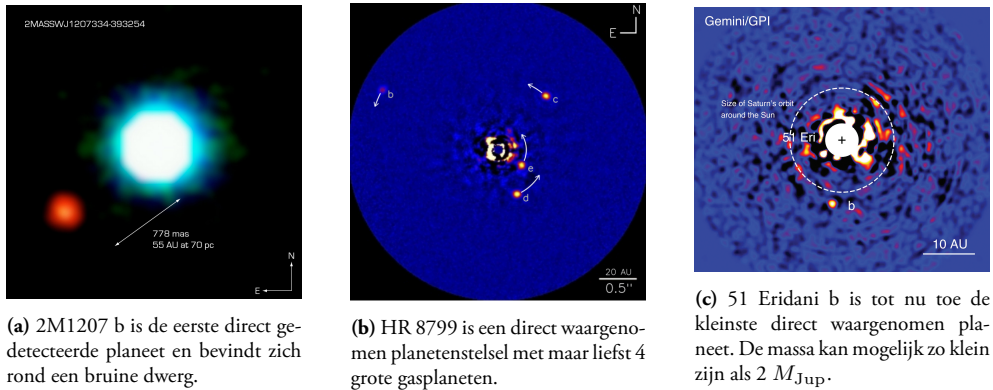


Figuur 7.1: Simulaties pre- en post-AO die de immense toename laten zien in de waargenomen scherpte van een puntbron.

Zelfs met AO is het moeilijk om planeten rechtstreeks te detecteren; zowel door de kleine hoekafstand tussen een potentiële planeet en zijn moederster, en het immense helderheidsverschil tussen hen. Software en hardware technieken zijn ontwikkeld om sterlicht te kunnen scheiden van het planeetlicht. Softwaremethodes omvatten bijvoorbeeld het gebruik van combinaties van referentiebeelden van sterren zonder een bekende planeet om optimaal het sterlicht af te trekken. Als voorbeeld van hardware methodes bestaan er coronagrafen waarmee men sterlicht kan onderdrukken in de telescoop voordat het de camera bereikt. Dit kan zo simpel zijn als een blokkerend element voor de ster, of door de fase van het inkomende licht aan te passen in het pupilvlak van het optische systeem (zoals een bril), wat ook de basis is van het werk in dit proefschrift. Deze laatste methode wordt gebruikt in de zogenoemde Apodizerende Faseplaat (APP) coronograaf.

Door steeds ingewikkeldere sterlichtaftrektechnieken en/of coronagrafen te gebruiken zijn astronomen in staat geweest om meer dan een dozijn planeten rechtstreeks waar te nemen. Een

selectie hiervan is te zien in Figuur 7.2.



Figuur 7.2: Een selectie van bekende direct waargenomen planeten.

Zelfs met deze technieken is het vermogen om planeten dichtbij een ster te zien beperkt door tweede-order effecten (zoals achterblijvende turbulentie, trillingen en mechanische doorbuigingen van de telescoop en het instrument). Dit zorgt voor een imperfecte verwijdering van het sterlicht en het overblijvende signaal kan zelfs kunstmatig op planeten lijken. Het direct waarnemen van planeten heeft dus nog betere manieren nodig om het sterlicht te onderdrukken.

Dit proefschrift

In dit proefschrift presenteren wij ontwikkelingen in coronagrafen die ertoe dienen om de sterlichtonderdrukking en de kleurafhankelijkheid te verbeteren.

Na een introductie in Hoofdstuk 1, presenteren we de Leidse AO laboratoriumopstelling in Hoofdstuk 2. Deze opstelling is ontworpen om een telescoop na te bootsen die een enkele ster direct waarneemt. Twee laserbronnen worden gebruikt om een ster na te bootsen op 2 verschillende golflengtes en een golffrontsensor en golffrontcorrigerend element zijn aanwezig voor de Adaptive Optica. Deze opstelling is in dit proefschrift gebruikt om onze nieuwe versies van coronagrafen gedeeltelijk te testen. Verder zijn wij van plan om in de toekomst deze opstelling te gebruiken voor veelbelovende technieken voor het meten en corrigeren van instrumentele fouten (o.a., veroorzaakt door mechanisch doorbuigen en temperatuurfuctuaties van de telescoop/instrument).

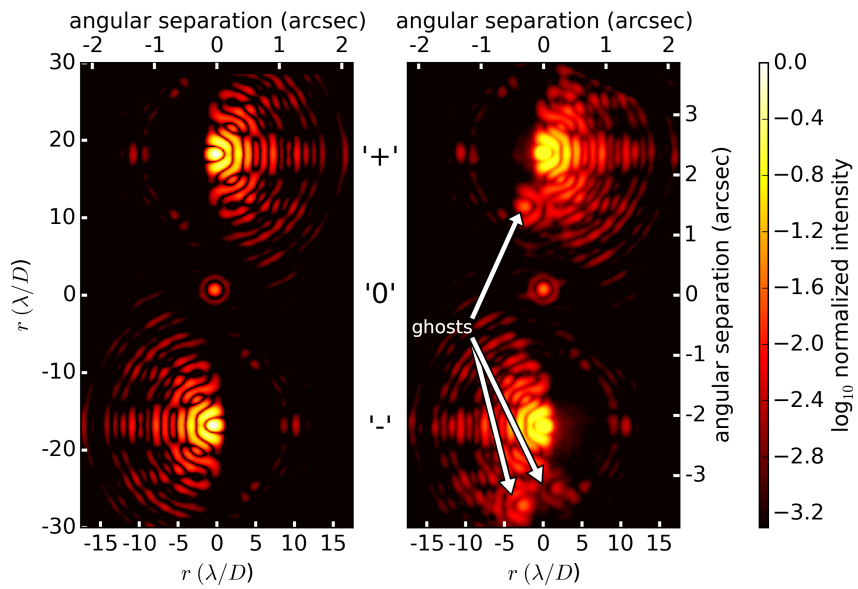
Een verbeterde versie van de Apodizerende Faseplaat coronagraph (de zogenaemde vector-APP of vAPP coronagraaf) gebruikt vloeibare kristaltechnologie, die ook wordt gebruikt in moderne televisie- en computerbeeldschermen, om een kleuronafhankelijk gedrag en elk mogelijk fasepatroon te kunnen realiseren. In Hoofdstuk 3 presenteren we de karakterisatie van de eerste breedband vector-APP (vAPP) coronagraaf, geoptimaliseerd voor het zichtbare licht. De karakterisatie is uitgevoerd in het Optische laboratorium te Leiden. De transmissie van licht van de coronagraaf tussen twee polarizatoren werd gebruikt om drie fundamentele eigenschappen te bepalen: de transmissie, retardatie en orientatie van de snelle as van de coronagraaf. Deze drie eigenschappen worden gebruikt in een simpel model om te voorspellen hoe goed de coronagraaf

werkt en vergeleken met opnames van een kunstster. Dit werd herhaald op meerdere golflengtes en bevestigde het achromatische gedrag van de coronagraaf. Deze vergelijking liet ook zien dat de belangrijkste limiterende factor de retardatie van de coronagraaf is.

In Hoofdstuk 4 presenteren we enkele ideeën voor de vector Apodizing Phase Plate die geïmplementeerd kunnen worden met de vloeibare kristalfabricagetechniek. Wij realiseerden ons dat door een continu veranderende fasegradient toe te voegen aan de coronagraaf, deze sterk vermindert last heeft van de retardatie van de coronagraaf. Dit zou ook het aantal optische elementen in de telescoop verminderen tot slechts één, waardoor fabricage en installatie in bestaande telescopen gemakkelijker wordt. Deze simpele toevoeging geeft daardoor een simpele en robuuste breedband coronagraaf. Ten tweede kunnen met de verhoogde schrijfresolutie van deze methode exotische fasepatronen gemaakt worden met hogere contrasten, en met totaal 360 graden onderdrukking rondom de ster.

In Hoofdstuk 5 demonstreren we het eerste nabij-infrarode smalbandige vAPP prototype met waarnemingen op de Large Binocular Telescope. Het coronagrafische ontwerp met de fasegradient beschreven in Hoofdstuk 4 is geïmplementeerd om de installatie mogelijk te maken met minimale aanpassingen. De eerste waarnemingen lieten zien dat het concept werkt, maar dat het gedrag van de coronagraaf niet geheel zoals verwacht is. Dit is te relateren aan twee factoren: een statische golffrontfout en een verkeerde uitlijning van de pupil van de telescoop op de coronagraaf. Beide problemen kunnen opgelost worden door de telescoop en het instrument opnieuw te calibreren.

De bemoedigende resultaten van Hoofdstuk 5 zetten aan tot de ontwikkeling van een nabij-infrarode breedband coronagraaf voor de 6.5 meter Clay telescoop in Chili. In Hoofdstuk 6 beschrijven wij de vAPP die is ontwikkeld voor het MagAO instrument, beschrijven de installatie en laten de waarneemresultaten zien (zie Fig. 7.3). We laten tevens zien hoe de twee afbeeldingen van de ster gebruikt kunnen worden om de sterlichtonderdrukking te verbeteren, alsook de bijhorende verbetering in de detectiegevoeligheid voor mogelijke planeten. In een vergelijking tussen andere studies laten we zien dat voor heldere sterren de vAPP coronagraaf beter werkt dan de competitie.



Figuur 7.3: Vergelijking tussen theoretische simulatie (links) en waarneming van een ster met de vAPP coronagraaf op MagAO (rechts).

Gäölse saamevatting

Euverzétter: Jos Tilmans

Suppressing a Sea of Starlight Enabling technology for the direct imaging of exoplanets

De minsjdôm haet dék gefillesoofeert euver öt bestaon van pleneete rônt anger sterre. Al zwoi vreug es 300 jaor veur Kristus zag Epicurus in eine brief aan ziene liërling Herodotus dat òntél-baare waerelde mooste bestaon, zwoiwaal geliekt es neet-geliekt op de ôzze. In de méderne waerelt kinne veer hun fillesoofiese raeje vervange door weitesjappelikke reedenaasje en veer kinne aeveziër euverzigtelikke vraoge stéle zwoi es; Wie vörme zich de pléneete ? Is òs zónnestéssel normaal of spissjaal ? Wie einmaalig is de Aerd ? En oeteindelik, de uuterste vraog; Is dao urregés anders laeve heemelswhoig ? Um op al dees vraoge ein antwoord te kinne gaeve moote veer de pléneete rônt anger sterre òntdékke en bestedeere.

De iëste pléneete rônt ein anger ster (extrasolaire pléneete / exopléneete woore òntdék in 1992 door Wolszcan en Frail. Zie vônge twië pléneete mét eine liëge massaa rônt ein restant van ein gestorréve ster. (pulsar). Dit waor ein belangrieke òntdékking in de iëwiglange zeuktoch nao pléneete rônt anger sterre. Dees zeuktoch hou ummers al miërdere pléneetvônste gekosj, die laater ònsjus bleeke te zin.

In 1995 woor de exopléneet 51 Pegasi b gevônge rônt ein zònechtige ster mét biestand van de radiele snelheidsmétoode. De radiele snelheidsmétoode gebruk òt snelheidskômponent van de ster nao de Aerd toe um de présensie van pléneete aaf te leije. De présensie van ein pléneet versjuuf òt zwoörtepunt van òt pléneetéstéssel. De ster driëjt oug um dit gezaamelikke middelpunt heen en de bewaeging van de ster kint door astroonome mét spektroograafe waere vasgelag es ein sjenbare versjuuving van de spektraalliene.

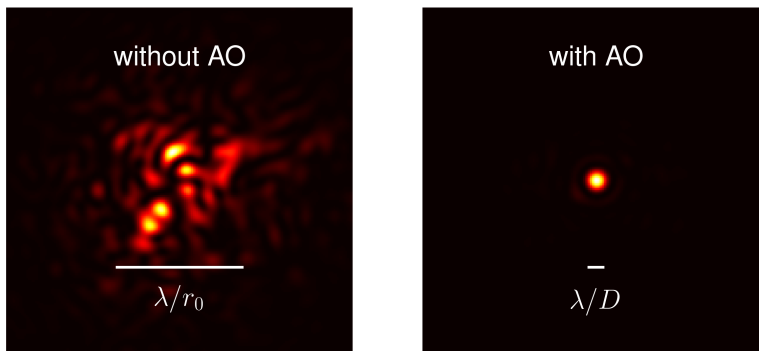
Ein ònverwachs rissultaat waor dat de miërderheit van de iëste òntdékkinge Jupiterrechtige pléneete waore in umluipbaane vergeliekbear mét die van Mercurius. Mét behulp van lang stuedies van dezelfde ster en verbaeterde akkeraatesse en staabieliëteit van instréménte zin dees òntdékkinge opgesjoove nao Neptunisechtige pléneete in Aerdechtige baane. Konvensiooneele radiele snelheidsmétoodes zeen allein òt leeg van de ster en gaeve dus slechs beperkte informaasje euver de pléneet.

De meis suuksesvolle techniek (wat òt aantal òntdékkinge betref) is de pléneeteuverganksmétoode, die veur òt iës is toegepas in 2000 door de ploog van Charbonneau um de alvas gedeekteerde pléneet HD 209458 b te bevestége. Ein pléneet welke sjus veur zien mooderster langsgéit (zwoi es gezeen vanaaf de Aerd) zal ein klein deil van òt leeg van de ster mét vaste reigelmaot blokkeere. Ònbekénde pléneete zin op dees meneer relatief gemaekelik te vénge door te geliektied de helderheit van ein grwoit aantal sterre bie te hauwe.

De miërderheit van de òngevaer 1600 véndaag den daag bevestigde eksoopléneete woore gevônge mét de pléneeteuvergank en radiele snelheidsmétoodés. Allebei de métoodés kômme euverei

dat ze neet drekte métoodés zin um de présensie van pléneete en hun eigesjappe (zwoi es grwuöte, massaa en umloupbaan) aaf te leije. Door de sjenbaare grwuöte van de pleneet op miêrdere golf-lengdés te maete kinne sjeikundige vingeraafdrökke gedeetekteert waere in mäögelékke pléneet-atmosfeere. Jaomer genôg is slechts ein klein aantal van de ôntdékte pléneete in ein umloupbaan rônt ein ster die helder genôg is um dees maeting mäögelik te maake.

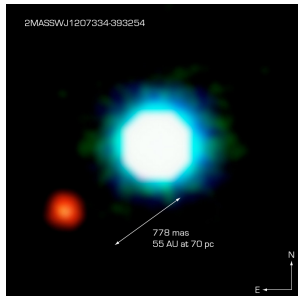
Get réserter is de drek woirnummétoode tot ôntwikkeling gekômme. Hiedoor zin astroonoo-me in staot rechstreeks de atmôsfeere van pléneete te bestedeere. Ôt idee um mét eine tilléskoop nao pléneete rônt ein anger ster te kieke klink sumpel mae is doelmaotig ôntzétént lestig. Dit is veural ingewikkelt es mén eine tilléskoop op Aerd gebruik (in vergelieking mét eine ruimte-tilléskoop). De invloot van de turbielensie van de Aerd atmôsfeer op de beeltkwoilleteit hat ein belemmerende invloot bie ôt drek waornomme van eksoopléneete. Élein toen Aadaptieve Optiekaa (AO) vécant kaome, waore astroonoo-me in staot um de beeltkwoilleteit in de ruimte te aevenaare. Ein gesiemuuleerde vergelieking in beeltkwoilleteit veur en nao Aadaptieve Optiekaa is te zeen in Feguur 7.4. Dit liêt de baanbraekende invloot zin van AO op ôt oplossént vermooge van de tilléskoope.



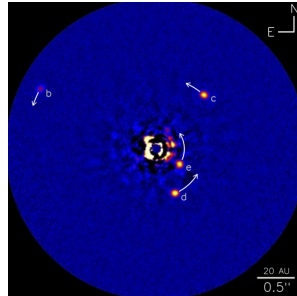
Figuur 7.4: Siemuulaasje veur- en nao-AO die de kollosaale aangreuj laote zin in de woirgenômme sjerrépte van ein puntbrôn.

Zellefs mét AO is ôt lestig um pléneete drek op te spaore; Zwoiwaal door de kleine hook-aafstant tösje ein mäögelékke pléneet en zien mooderster, en ôt kollosaale helderheidsversjil tösje die. Software en hardware métoodes zin ôntwikkel't um sterleeg te kinne sjeije van ôt pléneetleeg. Softwamétoodés behelse bieveurbeelt ôt gebruik van saamestélling van reférénsiebeelde van sterre zônger ein bekénde pléneet um optiemaal ôt sterleeg aaf te trékke. Es veurbeelt van hardwa-reméneere bestaon dér kooroonaagraafe woimét mén sterleeg kint ôngerdrökke in de tilléskoop veurdat ôt de kaameraa bereik. Dit kint zwoi sumpel zin es ein blokkeerént illemént veur de ster of door de faaze van ôt binnekômment leeg aan te passe in ôt puupilvlak van ôt optiese siesteem (wie eine bril), wat oug ôt fundament is van ôt wérk in dit proofsjrif. Dees léste métoode weurt gebruik in de zwoigheite Aapodieseerende Faazeplaat (APP) kooroonaagraaf.

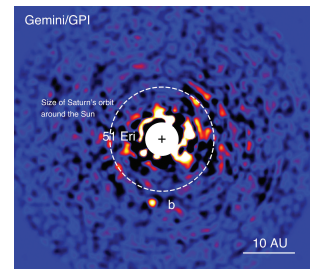
Door ummer miër gekompléseerde sterleegaaftréktechnieke en/of cooroonaagraafe te gebruke zín astronoomen in staot gewaes um miër dan ein twelléftal pléneete rechstreeks woir te numme. Ein séleksie hievan is te zéen in Feguur 7.5.



(a) 2M1207 b is de iëste drek ge-deetekterede pléneet en bevunk zich rönt eine broene dwerrég.



(b) HR 8799 is ein drek woirgenómme pléneetestétsel mét maer leefs 4 grwoite gaaspléneete.



(c) 51 Eridani b is tot noe toe de kleinste drek woirgenómme pléneet. De massaa kint mäögelik zwoi klein zin es $2 M_{\text{JUP}}$.

Figuur 7.5: Ein séleksie van bekénde drek woirgenómme pléneete.

Zellefs mét deeze technieke is öt vermaoge um pléneete kortbie ein ster te zin beperk door twiëde-order effekte (zwoiwie achterblijvende turbuulensie, trillinge en meechaaniese doorbuinge van de tilléskoop en öt instrémént). Dit zörg veur ein imperfekte eeliemienaasie van öt sterleeg en öt euverbliévént sinjaal kint zellefs kunsmaotig op pléneete lieke. Öt drek woirnumme van pléneete haet dus nog baetere meneere nwüdig um öt sterleeg te öngerdrökke.

Dit proefsrijf

In dit proefsrijf présenteere veur öntwikkelinge in kooroonaagraafe die de veur deene um de sterleegöngerdrökking en de kleuraafhankelékheit te verbaetere.

Nao ein introduksie in Sjapieter 1, présenteere veur de Leidse AO laabooraatoorie-umöpstélling in Sjapieter 2. Dees opstélling is öntworpe um eine tilléskoop nao te bootse welke ein énkele ster drek woirnump. Twië laazerbrönne waere gebruke um ein ster nao te bootse op twië versjillende golflengdés en ein golffröntkorriesjeerént illemént is aanwezig veur de Aadaptieve Optiekaa. Dees opstélling is in dit proefsrijf gebruke um özze nuuje verzies van kooroonaagraafe gedeiltelék te teste. Wier zin veur van plan um in de toeköms dees opstélling te gebruke veur väölbelaovende technieke veur öt maete en verbaetere van instréméntaale foute (önger angere veroiwrzaak door meechaaniese doorbuige en températuurfluktuu-aaties van de tilléskoop/instrémént).

Ein verbaeterde verzie van de Aapoodieseerende Faazeplaat kooroonaagraaf (de zwoigenaampde vector-APP of vAPP kooroonaagraaf) gebruke vloejbaare kristaltechnoologie, dae oug weurt gebruke in méderne teelevisie- en kómpjoeterbeeltsjerme, um ein kleurónafhanklik gedraag en eeder mäögelik faazepétrwoin te kinne bewérkstéllige.

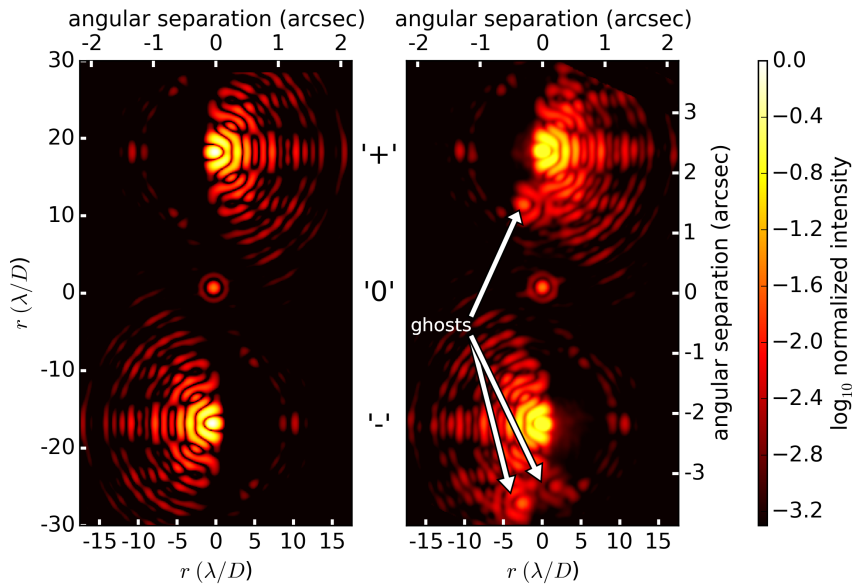
In Sjapieter 3 présenteere veur de karakterézasie van de iëste breitbart vAPP kooroonaagraaf, ge-optiemaalieseert veur öt zichbaare leeg. De karakterézasie is oetgeveurt in öt Optiese laabooraatoorie-um te Leiden. De doarlaoting van leeg van de kooroonaagraaf tösje twië pool-

aariezaatoore waere gebruik um drie fundaménteetele eigesjappe te bepaale: de doorlaoting, reetardasie en gerichheit van de snelle as van de kooroonaagraaf. Dees drie eigesjappe waere gebruik in ein sumpel médel um te veurspelle wie goot de kooroonaagraaf wérk en vergeleeke mét opnaames gemaak van ein kunsster. Dit weurt herhaolt op mièrdere golflengdés en bevestigde öt achroomaatiese gedraag van de kooroonaagraaf. Dees vergeliëking leet oug zeen dat de belangriekste liemieteerende faktor de reetardaasie van de kooroonaagraaf is.

In Sjapieter 4 presénteere veer einige iedeeje veur de Vector Apodizing Phase Plate die in gebruik genômme kinne waere mét de vloejbaare kristalfabreseertechniek. Veer beseffe dat door ein kontinuu verangerénde faazegradiejent toe te vooge aan de kooroonaagraaf, deze stérk vermindert las haet van de reetardaasie van de kooroonaagraaf. Dit zou oug öt aantal optiese eleménten in de tilléskoop vermindere tot slechs ein, wodoor fabreseere en instélaasje in bestaonde tilléskoope gemaekelékker weurt. Dees sumpele toevooging geuf daodoor eine sumpele en robuuste breitbant kooroonaagraaf. Ten twiède kinne mét de verwhuögde sjriefrisseluisie van dees métoode eksootiese faazepétrwoine gemaak waere mét hwoigere kontraste en mét tot 360 graoje òngerdrökking rônt de ster.

In Sjapieter 5 deemonstreere veer öt ièste naobie-infraarwoie smaalbandige vAPP prootootiep mét woirnumminge op de Large Binocular Tilléskoop. Öt kooroonaagraafiese òntwerp mét de faazegradiejent besjreeve in Sjapieter 4 is in gebruik genômme um de instélaasje mét miëniemaale aanpassinge. De ièste woirnumminge leete zin dat öt kônsep wérk, mae dat öt gedraag van de kooroonaagraaf neet gans zwoi es verwach is. Dit is te relaateere aan twië faktoore: ein staatiese golfrôntfout en ein verkiërde oetliëning van de puupil van de tilléskoop op de kooroonaagraaf. Allebei de probleme kinne opgelos waere door de tilléskoop en öt instrémént opnuu te kaliebreere.

De opbäörende rissultaate van Sjapieter 5 zétte aan tot de òntwikkeling van ein naobie-infraarwoie breitbant kooroonaagraaf veur de 6.5 maeter Clay tilléskoop in Chili. In Sjapieter 6 besjrieve veer de vAPP dae is òntwikkelt veur öt MagAO instrémént, besjrieve de instélaasje en laote de woirnumresultaate zin (zie Feguur 7.6). Veer laote aug zin wie de twië aafbeeldinge van de ster gebruik kinne waere um de sterleegòngerdrökking te verbaetere, es oug de biebehwuörénde verbaetering in de deeteksiegeveuligheit veur mäögelike pléneete. In ein vergeliëking tösje angere studies, laote veer zin dat veur heldere sterre de vAPP kooroonaagraaf baeter wérk dan de kômpetiesie.



Figuur 7.6: Vergelieking tösje teejooretiese siemuulaasje (leinks) en woirnumming van ein ster mét de vAPP kooroon-aagraaf op MagAO (rechts).

English summary

Suppressing a Sea of Starlight

Enabling technology for the direct imaging of exoplanets

Mankind has often philosophized about the existence of planets around other stars. It has been recorded as early as 300 BC when Epicurus argued in a letter to his disciple Herodotus, that innumerable worlds must exist, both similar and dissimilar to ours. In the modern world these philosophical arguments have been replaced by scientific reasoning and we can ask more structured questions such as; how do planets form?; is our solar system normal or special?; how unique is planet earth? and finally, the ultimate question; is there life elsewhere in the universe? To answer these questions we need to discover and study planets around other stars.

The first planets around another star (extrasolar planets / exoplanets) were discovered in 1992 by Wolszczan and Frail who found two low mass planets around a stellar remnant (pulsar). This was a crucial find in a century long quest for planets around other stars. This quest included many claims of detections which were later proven to be false.

In 1995, the exoplanet 51 Pegasi b was found around a solar-like star using the radial velocity method. The radial velocity method uses the line of sight velocity of the star to derive the presence of planets. A planet offsets the center of mass of the system from the center of the star. The star orbits around this common center of mass and this motion can be tracked by astronomers using spectrometers through an apparent periodic color shift of spectral lines. Remarkably, the majority of initially detected planets were Jupiter-mass objects in unexpected Mercury-like orbits. With extensive monitoring of the same star and increased accuracy and stability of the instruments this has since been extended to Neptune-mass planets with Earth-like orbits. Conventional radial velocity methods only see the light of the star and this method therefore offers limited information on the planet.

The currently most prolific discovery technique is the transit method, that was first used in 2000 by Charbonneau to confirm the planet HD209458 b previously discovered with the RV technique. A planet transiting directly in front of its parent star will block a tiny portion of the light with regular intervals. Unknown planets are relatively easy to detect by simultaneously monitoring the intensity of large numbers of stars.

The majority of the approximately 1600 currently confirmed exoplanets were found using the transit and radial velocity techniques. Both techniques have in common that they are indirect ways of determining the presence of planets and properties such as size, mass and orbit. By measuring the apparent size of the planet at different wavelengths, chemical signatures can be detected in potential planetary atmospheres. But unfortunately, only a fraction of these detected planets orbit sufficiently bright stars to reach the sensitivity needed for this characterization.

More recently, direct imaging has entered the field as a way to directly study the light of the planets. This allows astronomers to directly study the atmospheres of planets. While the idea to

point a telescope at a star and look at any orbiting planets is very simple, it is extremely hard in practice. This is especially hard when using ground-based telescopes (as opposed to space-based). The impact of atmospheric turbulence on the image quality is a prohibitive factor in direct imaging. Only when Adaptive Optics (AO) became available astronomers were able to reach the image quality that is seen in space. A simulated comparison of images taken before and after adaptive optics correction can be seen in Figure 7.7. This shows the revolutionary impact of AO to the resolution of telescopes.

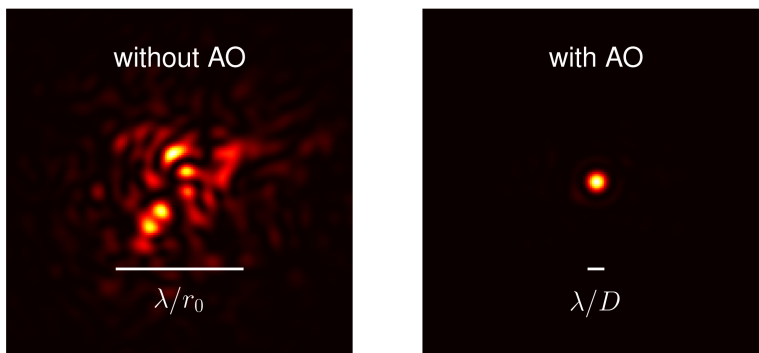
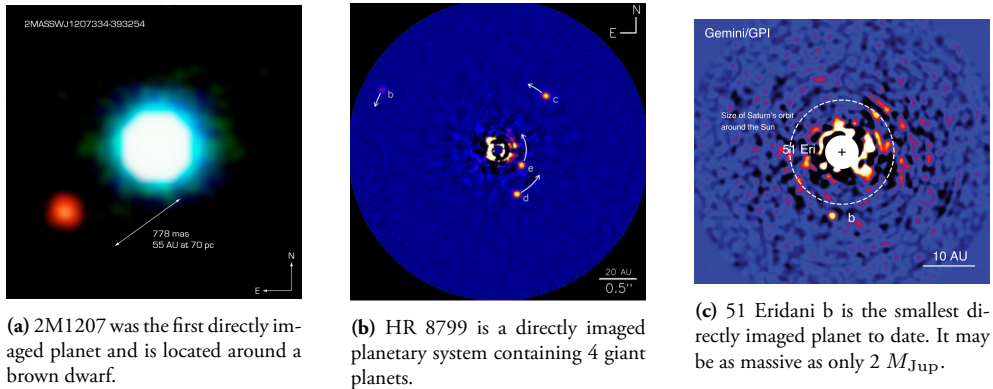


Figure 7.7: Pre- and Post-AO simulations showing the massive increase in sharpness of an imaged point source.

Even with AO it is difficult to detect planets; both due to the small separation between any potential planet and its parent star, and the massive difference in brightness between them. Software and hardware techniques have been developed to remove the starlight from the images in order to isolate the reflected and/or thermal light of the planet. Software techniques include using combinations of reference images of stars without a known planet to optimally subtract the starlight. Hardware methods include coronagraphs that suppress the starlight before it reaches the detector. This can be as simple as a blocking device that is placed in front of the star, or by changing the phase of the incoming light in the telescope across its pupil which is the basis of the work done in this thesis. This final technique is used in the so-called Apodizing Phase Plate coronagraph.

Through the use of increasingly complicated stellar subtraction techniques and coronagraphs astronomers have been able to directly image more than a dozen extrasolar planets. A selection is seen in Figure 7.8.

Yet even with these techniques the detection sensitivity of planets close to the star is limited by second-order effects (such as residual turbulence, vibrations and mechanical flexing of the telescope) that create an imperfect subtraction of the star and even mimic planetary signals. Direct imaging needs even better ways to suppress the starlight.



(a) 2M1207 was the first directly imaged planet and is located around a brown dwarf.

(b) HR 8799 is a directly imaged planetary system containing 4 giant planets.

(c) 51 Eridani b is the smallest directly imaged planet to date. It may be as massive as only $2 M_{\text{Jup}}$.

Figure 7.8: A selection of famous directly imaged planets.

This thesis

In this thesis we present developments to coronagraphs that are intended to increase their performance in terms of starlight suppression and achromatic behavior.

After an introduction in Chapter 1, we present our Leiden AO laboratory setup in Chapter 2. This setup is designed to mimic a real telescope directly imaging a star. Two laser sources are used to mimic a star at two wavelengths and both a wavefront sensor and a wavefront correcting element are present. This setup was used in this thesis to partly test our new models of coronagraphs. Furthermore we intend to use this setup in the future to test promising techniques for sensing and correcting the errors associated with the instrument (such as mechanical flexing and temperature variation induced wavefront errors).

An improved version of the Apodizing Phase Plate coronagraph (the vAPP coronagraph) uses liquid crystal technology, which is also found in modern televisions and computer monitors, to produce a device with an achromatic response and a custom phase design. In Chapter 3 we present the characterization of the first broad-band vAPP coronagraph optimized for visible light that was manufactured according to our specifications. Its characterization was done in the optical lab in Leiden. The transmission of the coronagraph between polarizers was used to reconstruct three fundamental properties: its transmission, retardance and fast axis orientation. These three parameters were used in a simple model to predict the coronagraph performance and compared to images that were taken of a point source to mimic a telescope imaging a star. This was repeated for many different wavelengths and confirms the achromatic nature of the coronagraph. This comparison also shows that the main limitation of the coronagraph is its dependence on the retardance of the plate.

In Chapter 4 we present several ideas for the vector Apodizing Phase Plate that can be implemented using the liquid crystal manufacturing technique. We realized that by adding a continuous phase ramp to the coronagraph we could severely reduce the impact of the retardance on the coronagraph performance. This would also reduce the amount of optical elements that we needed to introduce into the telescope to only one, thereby simplifying the manufacturing and installation into existing telescopes. This simple addition therefore creates a simple and robust broad-band

coronagraph. Secondly, the manufacturing technique also allows us to increase the writing accuracy of the phase patterns. The improved writing accuracy can be used to build exotic phase designs with higher contrasts and a region with 360 degree suppression around the star.

In Chapter 5 we demonstrate the first near-infrared narrow-band prototype of the vAPP coronagraph on-sky at the Large Binocular Telescope, which has twin 8.2 meter telescopes. The coronagraphic design with phase ramp described in Chapter 4 is implemented to facilitate the installation into the telescope with only trivial modifications. The first observations show that the concept works but its performance is less than was expected. The reduced performance is linked to two factors; a static wavefront error and a misalignment of the pupils of the telescope with respect to the coronagraphs. Both issues are deemed to be resolvable by recalibration of the telescope.

The encouraging results of Chapter 5 triggered the development of a near-infrared broadband vAPP coronagraph for the 6.5 meter Clay telescope in Chile. In Chapter 6 we describe the vAPP that was developed for the MagAO instrument, and report on its installation and on-sky demonstration (see Fig. 7.9). We show how the two PSFs of the vAPP can be used to increase the suppression of starlight and the corresponding increase in detection sensitivity for potential planets. By comparing with other direct imaging studies we show that for bright stars the vAPP coronagraph outperforms the competition.

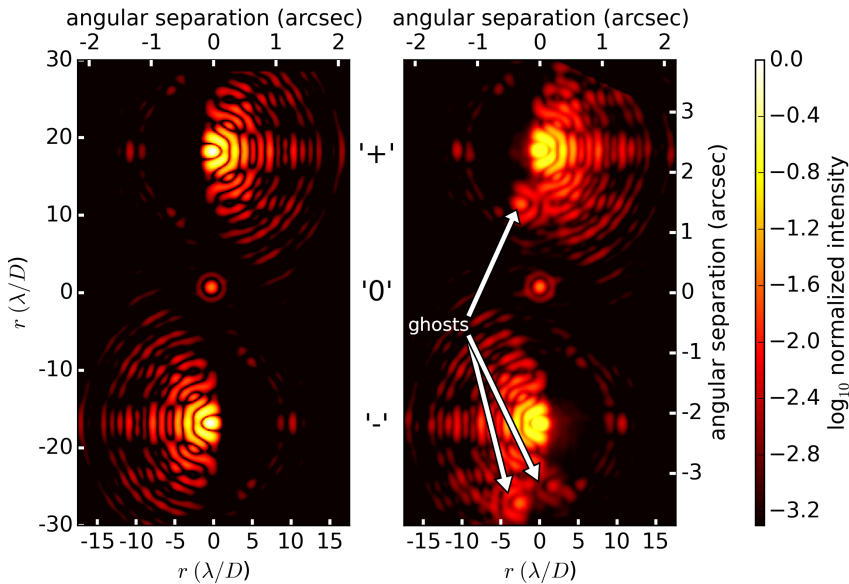


Figure 7.9: Comparison of theoretical simulation (left) with observed on-sky image of star (right).

Curriculum Vitae

I was born on May 11th, 1987 in Geulle, Meerssen and as a kid went to the local primary school 'in 't Riet'. As long as I can remember I loved astronomy, technology and history. In 1999 I went to high school at the Stella Maris College in Meerssen with a specialization on Science and Technology in the final few years and graduated in 2005. I had claimed for many years that I was going to study Archeology but decided in my fifth year of high school to study my other passion, Astronomy, in Leiden. In retrospect, I couldn't have made a better decision.

During my Bachelor's research project I worked with Henk Hoekstra on the impact of the combination of intrinsic alignments in galaxy clusters and foreground/background galaxy contamination on weak-lensing based mass estimates of the galaxy clusters. I received my Bachelor's degree in 2009. During my Master's study I first worked under supervision of Jarle Brinchmann on determining the dependence of stellar mass estimates of SDSS galaxies on the assumed star formation history. Secondly, I worked under supervision of Ignas Snellen and Ernst de Mooij on testing the use of consumer cameras for accurate photometry of the brightest stars in the sky. This was essentially a feasibility study for the later MASCARA project. During this time, Ernst and Ignas provided the opportunity to go on (my first) observing run with the 4 meter William Herschel Telescope in La Palma, Spain to take photometric observations of secondary transits of exoplanets in the NIR. I received my Master's degree in October 2011. While I was a student I also gave many tours at the Old Observatory and was co-chair of the student association for astronomy 'L.A.D. F. Kaiser'.

In November 2011 I started my PhD under supervision of Matthew Kenworthy. He was quickly joined by Frans Snik and Christoph Keller after the dissolution of Sterrenkundig Instituut Utrecht. Initially my work focused on building an Adaptive Optics testbed to test focal-plane wavefront sensing techniques but the focus quickly shifted to the very promising application of liquid crystal manufacturing techniques to the Apodizing Phase Plate coronagraph. I collaborated with the Geometric-Phase Photonics Lab at North Carolina State University to get multiple iterations of broad-band coronagraphs manufactured and also spent one week working in their lab to test the coronagraph. Furthermore, in the process of getting the coronagraph on-sky at the Large Binocular Telescope (USA) and the Clay Telescope (Chile) I collaborated with a team of astronomers at the University of Arizona. Finally, I spent several nights observing at the Clay telescope to test the coronagraph on-sky.

I presented my work at conferences, workshops and schools in Leiden, Noordwijk, Amsterdam, Groningen and Montreal (in both 2014 & 2015) and at seminars in Raleigh, USA and Santiago, Chile. Furthermore I attended the CfAO Adaptive Optics Summer School in Santa Cruz, California in 2012. As part of my teaching duties I assisted Henk Hoekstra with 'Sterrenkundig Practicum 2' for three years where we taught the second year students what to expect from professional astronomical research. This included three weeklong trips to the 2.5 meter Isaac Newton Telescope in La Palma where the students were familiarized with the observational aspect of astronomical research. Furthermore I assisted in assembling, testing and calibration of the new student telescope at the Old Observatory. Starting 2016 I will work as a Postdoc for one year with Ignas Snellen to construct and rollout the southern station of MASCARA on La Silla, Chile.

Acknowledgments

This thesis would not be possible without the assistance and support of many people in Leiden and abroad. First of all, I am grateful for the support given by colleagues around the world and in Leiden, including the support during my undergraduate studies. I thank Erik, David, Niels, Aart and Eric for their help with computers and offices. As well as the secretaries Anita, Liesbeth, Alexandra, and of course Jeanne to keep the observatory running. Evelijn's assistance on financial matters and travel support was invaluable.

I am grateful to Ernst and Ignas for giving me the opportunity to spend 11 days on La Palma as a rookie. My gratefulness also extends to Henk, whom I joined three consecutive years in the classroom and on La Palma. Remko's guidance on all things optical and mechanical was invaluable during this thesis. I would also like to thank Xander for sharing his knowledge and experience with PhD projects. The 'Gäölse' translation was done by Jos Tilmans as my own attempt resembled an inconsistent patchwork of dialects. His incredible feat deserves a special mention.

I am very thankful to my collaborators in Raleigh and Tucson for not only making our crazy ideas possible, but also getting the coronagraph on-sky within record time. Their support was crucial to get this done.

Sharing six different offices² over the years with numerous inhabitants was an inspiring experience. Officemates Carolina Ödman (outreach) and Martin Weiss (history) showed what an amazingly varied environment Leiden Observatory is to work in. Both Marissa's zeal in achieving her goals and knowing when to wind down & relax are admirable. I hope your dream of becoming an astronaut and going to space comes true. You deserve it. Many thanks go out to Jesse³ for allowing me to join him in his office. I never anticipated the great time we would have while sharing offices. Both in terms of practical jokes and solving scientific conundrums. My current office mates Stephanie, Jos, Christian, and Rob provide a very vibrant working environment and make it possible to get instant feedback on various topics.

Former group members Gerard, Tim, Maria, Laurens and Ritse still form a source of (comedic) relief. I was fortunate to be able to share thoughts and ideas with Tiffany during my PhD. Furthermore, I can not forget David Huijser's role during my undergraduate studies by challenging me in homework assignments, exams and videogames.

I am indebted to Harry Timmermans who guided me many years and introduced me to genealogical research. Sascha, thank you for your unwavering support throughout the years and in years to come. I would like to end by dedicating this thesis to my parents, and Maria and Leon. If one of you had been missing I would have been a different person.

²as a historical reference and in chronological order: Oort 454, 553, 462, 564, 568, 571

³future director of ESO

List of acronyms

8OPM: Eight-Octant Phase Mask
ADI: Angular Differential Imaging
AGPM: Annular Groove Phase Mask
ALC: Apodized Lyot Coronagraph
AMZ: Angel-Mach-Zehnder
AO: Adaptive Optics
APCMLC: Apodized Pupil Complex Mask Lyot Coronagraph
APP: Apodizing Phase Plate
AU: Astronomical Unit
BLC: Band-Limited Lyot Coronagraph
CCD: Charge Coupled Device
CMOS: Complementary Metal Oxide Semiconductor
DM: Deformable mirror
dOTF: Differential Optical Transfer Function
DPM: Disk Phase Mask
DZPM Dual Zone Phase Mask
E-ELT: European Extremely Large Telescope
EE: Encircled Energy
ELT: Extremely Large Telescope
EPICS: Exo-Planet Imaging Camera and Spectrograph
FFT: Fast Fourier Transform
FP: Focal Plane
FQPM: Four-Quadrant Phase Mask
FWHM: Full Width Half Maximum
GPI: Gemini Planet Imager
gvAPP: grating vector Apodizing Phase Plate
HARMONI: High Angular Resolution Monolithic Optical and Near
-infrared Integral field
HDR: High Dynamic Range
HLC: Hybrid Lyot Coronagraph
HST: Hubble Space Telescope
HWP: Half-Wave Plate
IFU: Integral Field Unit
LBT: Large Binocular Telescope
LHC: Left-handed Circular
LMIRCam: Large Binocular Telescope mid-infrared camera
LOCI: Locally Optimized Combination of Images

MagAO: Magellan Adaptive Optics
METIS: Mid-infrared E-ELT Imager and Spectrograph
MICADO: Multi-Adaptive Optics Imaging Camera for Deep Observations
MMTO: MMT Observatory
MTR: Multi-Twist Retarder
NACO: NAOS-CONICA
NCP: Non-common path
NCPA: Non-common path aberrations
NWO: Nederlandse Organisatie voor Wetenschappelijk Onderzoek
OVC: Optical Vortex Coronagraph
PCA: Principal Component Analysis
PDI: Polarization Differential Imaging
PG: Polarization Grating
PIAA(C): Phase Induced Amplitude Apodization (Coronagraph)
PIAACMC: PIAA Complex Mask Coronagraph
PP: Pupil Plane
PPA: Pupil Plane Apodization
PSF: Point spread function
PSI: Phase-Sorting Interferometry
QWP: Quarter-Wave Plate
RDI: Reference Differential Imaging
RHC: Righthanded Circular
RV: Radial Velocity
ScexAO: Subaru Coronagraphic Extreme Adaptive Optics
SD: Spectral Deconvolution
SDI: Simultaneous / Spectral Differential Imaging
SLM: Spatial Light Modulator
SP: Shaped Pupil
SPHERE: Spectro-Polarimetric High-contrast Exoplanet REsearch instrument
SR: Strehl Ratio
UV: Ultraviolet
IR: Infrared
vAPP: vector Apodizing Phase Plate
VLT: Very Large Telescope
VVC: Vector Vortex Coronagraph
WFS: Wavefront sensor